An Investigation of Mechanical Behavior and Failure Mechanisms of Composite T-Joints with Transverse Stitching

By

Patrick Bickford Stickler

A dissertation submitted in partial fulfillment of the requirements for the degree of

Doctor of Philosophy

University of Washington

2001

Program Authorized to Offer Degree: Mechanical Engineering

UMI Number: 3022898

UMI®

Bell & Howell Information and Learning Company
300 North Zeeb Road
P.O. Box 1346
Ann Arbor, MI 48106-1346

Doctoral Dissertation

Program Authorized to Offer Degree: Mechanical Engineering

University of Washington
Graduate School

This is to certify that I have examined this copy of a doctoral dissertation by

Patrick Bickford Stickler

and have found that it is complete and satisfactory in all respects,
and that any and all revisions required by the final
examining committee have been made.

Chair of Supervisory Committee:

Mamidala Ramulu

Reading Committee:

Albert S. Kobayashi

Mark E. Tuttle

Date: August 2, 2001

University of Washington

Abstract

AN INVESTIGATION OF MECHANICAL BEHAVIOR AND FAILURE MECHANISMS OF COMPOSITE T-JOINTS WITH TRANSVERSE STITCHING

by Patrick Bickford Stickler

Chairperson of the Supervisory Committee

Professor Mamidala Ramulu

Department of Mechanical Engineering

A new low cost damage tolerant method of joining load-bearing composite structures using two-dimensional dry fabric preforms with transverse stitching and a novel fiber insertion process with resin transfer molding has recently been developed. however. knowledge of strength prediction and failure mechanisms is not well understood. In this investigation. fundamental knowledge of T-joint mechanical behavior was developed through detailed experimental. numerical. and post failure analyses. Experiments were conducted under flexure. tension. and shear loads and failed specimens were examined to discern failure modes. T-joint constituent elastic and strength properties were experimentally determined. Elastic properties were used as input to the finite element analysis and strength properties were used as limiting values in the T-joint failure analysis. Linear elastic. nonlinear elastic. and progressive damage finite element models were developed under each load condition. T-joint numerical models are shown to predict experimental behavior through ultimate load. Damage accumulation was characterize based on experimental. numerical. and post failure analyses. A parametric finite element analysis was conducted and design curves were derived to demonstrate the effect of varying key T-joint interface parameters on mechanical behavior under each load condition. Results of this research enable the application of T-joints with transverse stitching to future products and predictive finite element models developed herein reduce the structural testing required to validate these designs.

TABLE OF CONTENTS

LIST OF FIGURES

Number *Page*

LIST OF TABLES

ACKNOWLEDGMENTS

The author would like to acknowledge the Boeing Company for providing research funding and Albany International Techniweave, Inc. for graciously donating the experimental panels and T-joints for this investigation. Specifically, I would like to thank:

- Professor Mamidala Ramulu for his indefatigable mentoring and outstanding guidance in pursuing this research.

- Members of the supervisory committee, Professors Albert S. Kobayashi, Mark E. Tuttle, Minoru Taya, and Dr. William J. Renton, Boeing, Director of Structures Technology for their continued support and encouragement throughout my study.

- Jim Crowford and Don Blackden of Albany International Techniweave, Inc. for their many technical discussions. Keith Burgess for the development of the novel T-forming process and his early insight and encouragement in pursuing this research.

- Colleagues Dr. Patrick S. Johnson and Dr. Barry P. Van West; Dr. Roy Ikegami, Boeing Supervisor, and Scott Coguill, University of Wyoming.

- Intec for providing experimental test facilities.

I would especially like to thank my wife Judy for her encouragement, sacrifice, and patience during the past several years. For without her continued support, this would not be possible.

Dedication

This work is dedicated to Mitchell G. Stickler, my father, who raised me with discipline and integrity, the foundation for the accomplishment of far reaching goals.

INTRODUCTION

Polymer matrix composites with their high specific strength and stiffness are finding increased use in structural applications throughout industry. Applications of composites may be found in the aerospace, marine, automobile, sporting goods, and medical devise industries to name just a few. Current emphasis of composite design is on increased performance with reduced material and manufacturing cost. Aerospace applications of composite materials include wing skins, spars, and ribs; fuselage bulkheads and longerons; and airplane access panels and doors. The efficient transfer of load through these structures and the requirement for reduced cost, dictates the need for innovative joining methods.

One common type of composite joint found throughout the aerospace industry is the structural T-joint. Aerospace applications of T-joints include wing spar-to-skin and stiffener-to-skin interfaces. T-joints are also used in fuselage bulkhead-to-skin and longeron-to-skin interfaces. Current T-joint designs are typically fabricated by one of two methods: (1) through the use of opposing C-channels with a radius filler and cap plies or (2) through the use of three-dimensional woven fiber preforms and resin transfer molding. These methods are structurally efficient but tend to have high manufacturing and/or material costs. T-joints using transverse stitching and two-dimensional dry fabric preforms with resin transfer molding have the potential of significantly reducing the cost of composite structure and improving the damage tolerance and ultimate failure strength.

However, a review of current knowledge of stitched composite T-joints reveals a significant gap in experimental analysis and numerical predictive capability for the characterization of mechanical behavior of this type of joint. In order to design primary and secondary structures using transverse stitched T-joints, experimental investigation and predictive modeling are required. This research investigated the mechanical behavior of stitched composite T-joints under representative load conditions of static flexure, tension, and rail shear at room temperature ambient conditions. Numerical models were developed to predict failure and experiments were conducted to validate these analyses. In-situ strain measurements were recorded using strain gages under each experimental condition and results were correlated with finite element predictions. A comprehensive post-failure analysis was conducted to discern failure modes. Results of this investigation may be used by designers to predict mechanical behavior and failure mechanisms in the application of composite T-joints with transverse stitching to future products. Numerical methods developed herein may be used as a design tool for predicting performance of varying T-joint geometric configurations, reducing the requirement for future validation. Parametric design curves are presented to demonstrate the effects of varying key geometric and material properties on T-joint mechanical behavior.

This dissertation contains a comprehensive documentation of the conducted research. Chapter 1 provides a review of current knowledge in the area of stitched composite T-joints. In Chapter 2, the objectives of the research are presented. The experimental and numerical methods are given in Chapter 3. Chapter 4 provides a summary of T-joint results of experimentation and numerical evaluation under flexure loading using T-300/Shell 862. Chapter 5 provides a detailed characterization of the physical, mechanical, and strength properties of the T-joint constituent laminates using T-300/PR520. In Chapter 6, experimental T-joint results are presented under flexure, tension, and rail shear loading. Detailed linear elastic, nonlinear elastic, and progressive damage finite element analysis results are presented in Chapter 7. A discussion of T-joint failure, mechanical behavior, and parametric analysis is provided in Chapter 8. Chapter 9 presents the research conclusions and recommendations for future study.

CHAPTER 1
LITERATURE REVIEW

1.1 Polymer Matrix Composite Design

Polymer matrix composites with their high specific strength and stiffness are finding increased use throughout industry. A composite may be defined as a macroscopic combination of two or more materials consisting of a reinforcing material and a binder.[1] In the case of advanced composite materials, the reinforcement is a continuous fiber and the binder is a resin. Types of continuous fibers include glass, carbon, graphite, and aramid. Advanced composite resins are classified as either thermosets or thermoplastics. Thermosets are polymers that undergo cross-linking during curing and may not be reformed after curing. Typical thermoset resin types used in practice include epoxy, vinyl ester, bismaleimide (BMI), and polyimide. Thermoplastic resins, on the other hand are polymers that have a distinct melt temperature and may be reformed after curing. Types of thermoplastic resins include polyether ether ketone (PEEK), polyphenylene sulfide (PPS), and polysulfone.[2] Advanced composite material product forms include unidirectional prepreg tape, woven prepreg fabric, dry two and three-dimensional woven preforms, and stitched two-dimensional preforms.

Composites are classified as engineered materials because they allow the designer to tailor the properties to insure optimal strength in the primary direction of loading. This tailorability is due to the anisotropic nature of composites and requires specialized analysis techniques such as classical lamination theory or numerical analysis techniques such as the finite element method.[3-5] With the advent of high modulus fibers and toughened epoxy resin systems, composite materials have found wide use in many applications that traditionally were designed using metallic materials. Advanced composites materials may be found in commercial and military aircraft, launch vehicles and satellite buses, automobile components, boats, sporting equipment, and medical prostheses.[6] In large complex assemblies, composite materials require methods of attachment. Unlike metals, composites are not readily welded, at least not in the traditional sense, but instead must be joined using either mechanical fastening, adhesive bonding, or transverse stitching.

1.2 Composite Joints

Design of complex composite structures dictates the need for efficient joining methods. This is due in part to the inadequacy of structural joints to carry loads comparable to that of the base materials and in part due to the high cost of fabrication. There are two traditional types of structural joining methods found throughout industry, mechanical fastening and adhesive bonding.[7-8]

1.2.1 Bolted Joints

In practice, bolted or riveted joints experience complex load conditions including flexure, tension, and shear. These load conditions create a variety of failure modes. Figure 1.2.1-1 depicts typical failure modes for bolted joints in advanced composites. Tensile failure modes include net section failure, bearing failure, and shear failure. Mixed mode failures include cleavage tension, combined tension and shear, bolt pull-through, a problem in countersunk holes, and bolt bearing failure. Cleavage failures are most common in laminates with a high percentage of zero degree plies.[9]

There are many factors that influence the failure mode in bolted composite joints. These include laminate thickness and ply orientation, hole tolerance and quality, type of loading, hole diameter and pitch, bearing area, and environmental conditions including moisture and temperature. Local stress concentrations at the hole interface tend to be the leading cause of reduced performance for fastened joints.

Methods have been developed for reducing this undesirable stress concentration. Mechanical joint strength may be improved by adding local pad-ups to the laminate at the interface, local reinforcement with stiffer fibers, local softening by using low modulus fiber reinforcement, or by adding ±45° fibers.[10] Additional methods of improving fastener performance in composites include tailored fiber placement, the use of elliptically shaped bolts, and bonded metallic inserts.[11-14] However, these methods tend to drive up the manufacturing cost and increase the structural weight.

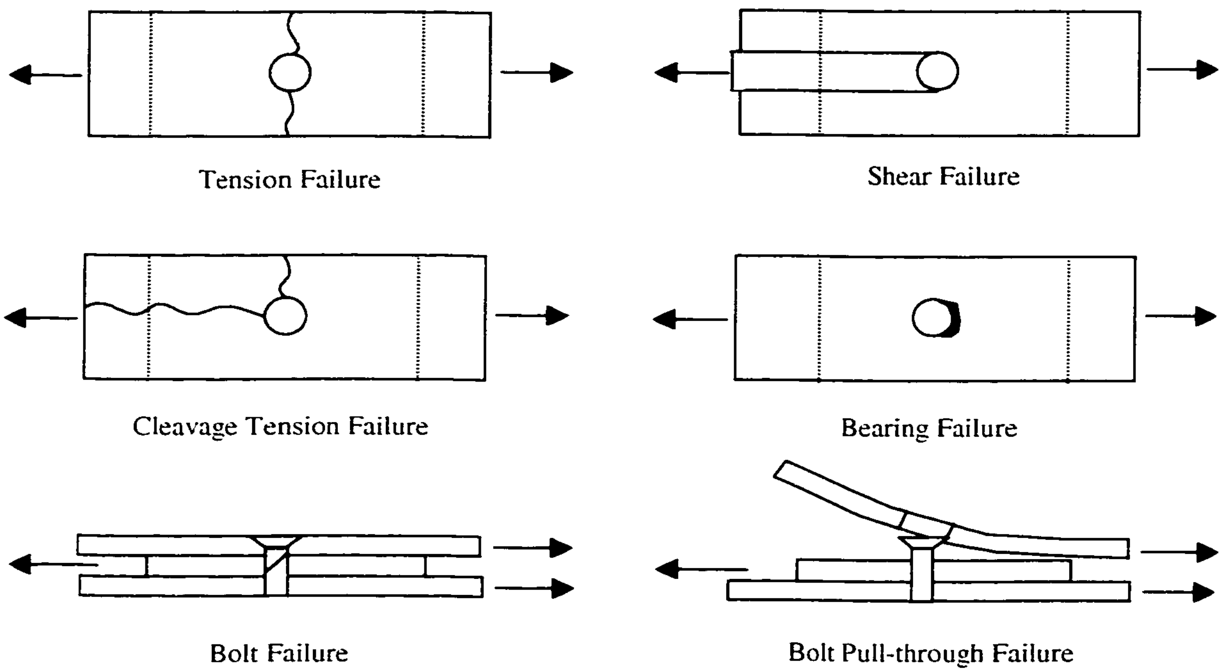

Figure 1.2.1-1. Failure Modes for Bolted Joints in Advanced Composites.[9]

1.2.2 Adhesive Bonded Joints

Adhesive bonded joints are finding greater use in advanced composite design for weight critical applications. Analytical and numerical methods have been developed for the analysis of bonded joints. Early pioneers in the development of analytical methods for bonded joints are Volkersen[15] and Goland and Reissner.[16] They developed closed form solutions for the stresses in single lap joints. Renton and Vinson[17] developed analytical methods for the static and fatigue analysis of single lap joints with special consideration of the anisotropic properties of the adherends, ply orientation, adhesive thickness, lap length, and the mechanical properties of the adhesive.

Numerical methods including finite element analysis have been employed for the analysis of bonded joints as well. Hart-Smith[18] developed a set of numerical tools for the analysis of bonded joints. These analytical tools incorporate nonlinear adhesive behavior. Adams and Peppiatt[19] successfully used the finite element method to analyze single lap joints. They employed constant strain two-dimensional triangular elements and a plane strain assumption in their analysis.

Types of adhesive bonded joints found in practice include in-plane single lap, double lap, tapered lap, scarf, joints and out-of-plane T-joints. Figure 1.2.2-1 shows the load-carrying capability of several bonded joints and associated failure modes. Single lap joints have eccentric loading that induces bending at the adherend/adherent interface causing the joint to fail at low loads. Double lap joints have improved load-carrying capability because of the eccentric loading. The failure mode for double lap joints is typically due to peel stresses. Tapered lap joints have a greater strength due to the reduction in peel stresses and failures are typically in shear. Scarf lap joints tend to be the strongest lap joint configuration but are very costly to fabricate.

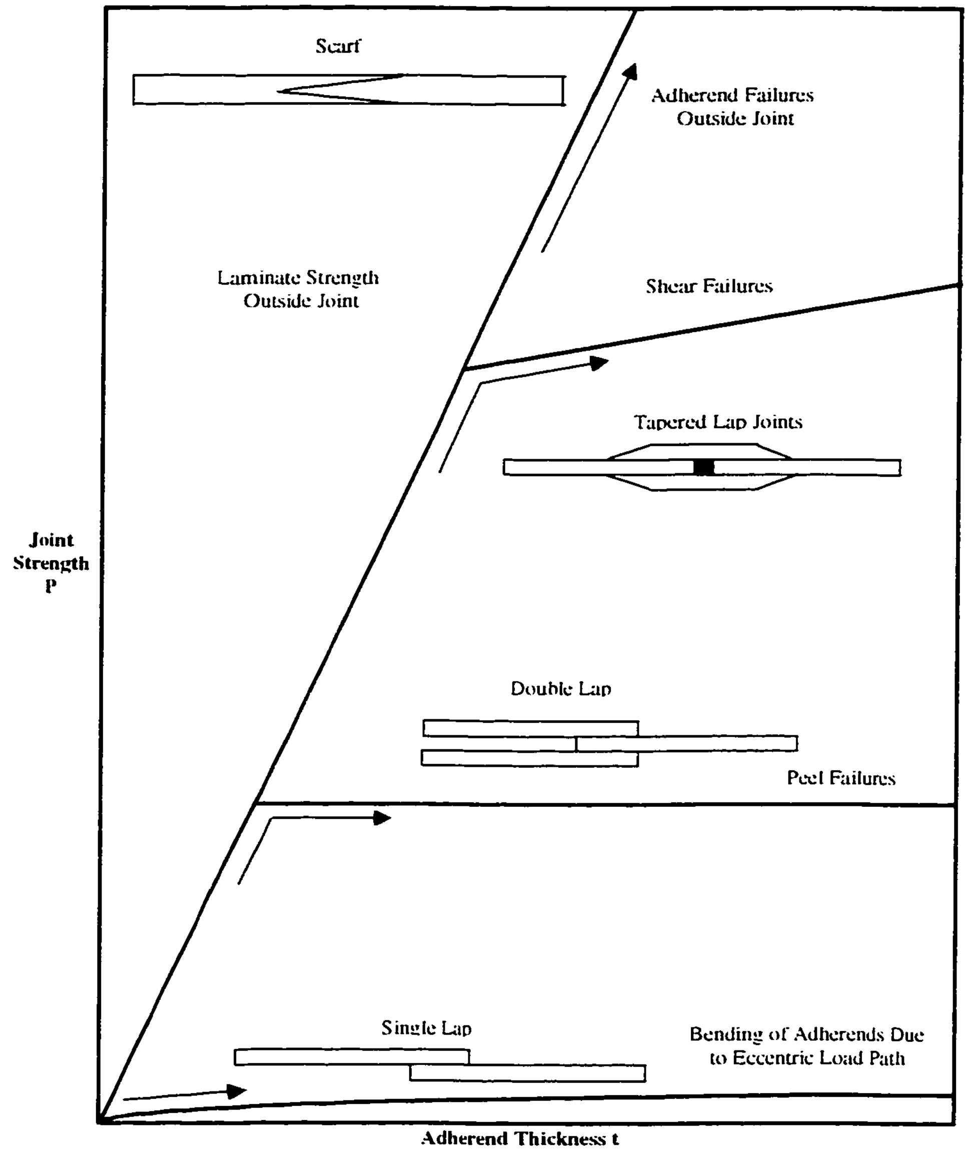

Figure 1.2.2-1. Load-Carrying Capacity of Adhesive Joints. [9]

Table 1.2.2-1 shows the advantages and disadvantages of mechanically fastened and adhesive bonded joints. Mechanical joints are easier to manufacture but develop large stress concentrations at the fastener hole locations and are less structurally efficient. Adhesive bonded joints tend to be more structurally efficient and have excellent fatigue properties but have the disadvantage of being sensitive to peel in the through-the-thickness direction and have relatively low damage tolerance.

Table 1.2.2-1. Comparison of Mechanically Fastened and Adhesive Bonded Joints.[7]

Advantages	Disadvantages
Adhesive Bonded Joints	
• Small stress concentration in adherends • Stiff connection • Excellent fatigue properties • No fretting properties • Sealed against corrosion • Smooth surface contour • Relatively lightweight • Damage tolerant	• Limits to thickness that can be joined with simple joint configuration • Inspection difficult other than for gross flaws • Prone to environmental degradation • Sensitive to peel and through-the-thickness stresses • Residual stress problems when joined to metals • Cannot be disassembled • May require costly tooling and facilities • Requires high degree of quality control • May be environmental concerns
Bolted Joints	
• Positive connection • Can be disassembled • No thickness limitation • Simple joint configuration • Simple manufacturing process • Simple inspection procedure • Not environmentally sensitive • Provides through-the-thickness reinforcement. not sensitive to peel stresses • No major residual stress problem	• Considerable stress concentration • Prone to fatigue cracks in metallic components • Hole formation can damage composite • In composites. relatively poor bearing properties • Prone to fretting in metal • Prone to corrosion in metal • May require extensive shimming with thick composites

One method for reducing the peel failure of lap joints and increasing the damage tolerance is to use through-the-thickness reinforcement in the form of transverse stitching. Transverse stitching has been shown to provide a clamping force that increases the peel resistance of the joint during loading.[20]

1.3 Transverse Stitching of Composite Laminates and Joints

Transverse stitching has been used as a method for improving the damage tolerance and ultimate failure strength of composite laminates and joints. Mignery *et al.*[21] investigated the use of stitching to suppress delamination in laminated composites. Their investigation showed that stitching effectively arrested delamination in composite laminates as the crack approached the stitch line. Stitching was shown to have varying effect on ultimate strength depending on the layup orientation. Transverse stitching has also been shown to improve the damage tolerance of single lap joints. Tong *et al.*[22-25] analyzed and tested adhesive bonded composite lap joints with transverse stitching. Kevlar™ thread was used for the transverse stitching and specimens were fabricated using the resin transfer molding process. They showed that the ultimate tensile strength of stitched single lap joints is 20% greater than unstitched specimens. The axial displacement of stitched specimens is 25% greater than unstitched specimens indicating an appreciable damage tolerance or larger failure strain as shown in Figure 1.3-1. The observed failure modes of the stitched lap joint specimens were peel, fiber breakage, and fiber pullout.

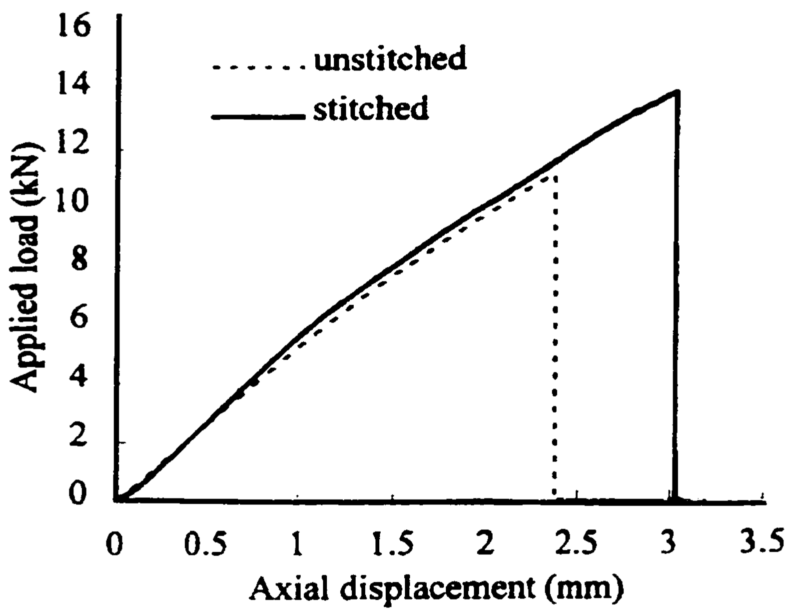

Figure 1.3-1. Load-Displacement of Stitched and Unstitched Single Lap Joint.[24]

Dransfield *et al.*[26-27] investigated the effect of transverse stitching on delamination toughness of polymer matrix composite materials. During this study, it was shown that the addition of through-the-thickness reinforcement significantly improved the mode I delamination toughness. The effect of stitching on both mode I and II delamination toughness was also investigated.[28-33] These studies showed improvements in both mode I and II delamination toughness through the use of transverse stitching. Typical advantages of stitched composite laminates over two-dimensional laminates sited by Mouritz *et al.*[34] include:

- inexpensive and simple to manufacture
- improved handling of preforms (plies are prevented from moving)
- improved impact damage tolerance
- improved delamination resistance to ballistic impact and blast pressure
- improved interlaminar fatigue resistance
- improved joint strength under monotonic and cyclic loading
- slight improvement in through-the-thickness tensile modulus and strength

1.4 Structural T-Joint Types

One type of structure prevalent in aircraft design is the composite "T" structure. Figure 1.4-1 shows typical aerospace applications of "T" structures include T-joints and T-stiffeners. T-joints consist of a flange, web, and radius filler. The flange interfaces with the substructure, the web provides an interface for attachment to the skin, and the radius filler provides continuity between the web and flange. T-joints are found at composite bulkhead-to-skin, rib-to-skin, and spar-to-skin interfaces. The purpose of the T-joint is to transfer flexural, tension, and shear loads to the skin. T-stiffeners are used extensively in aircraft wings. The purpose of the T-stiffener is to prevent buckling during wing loading.

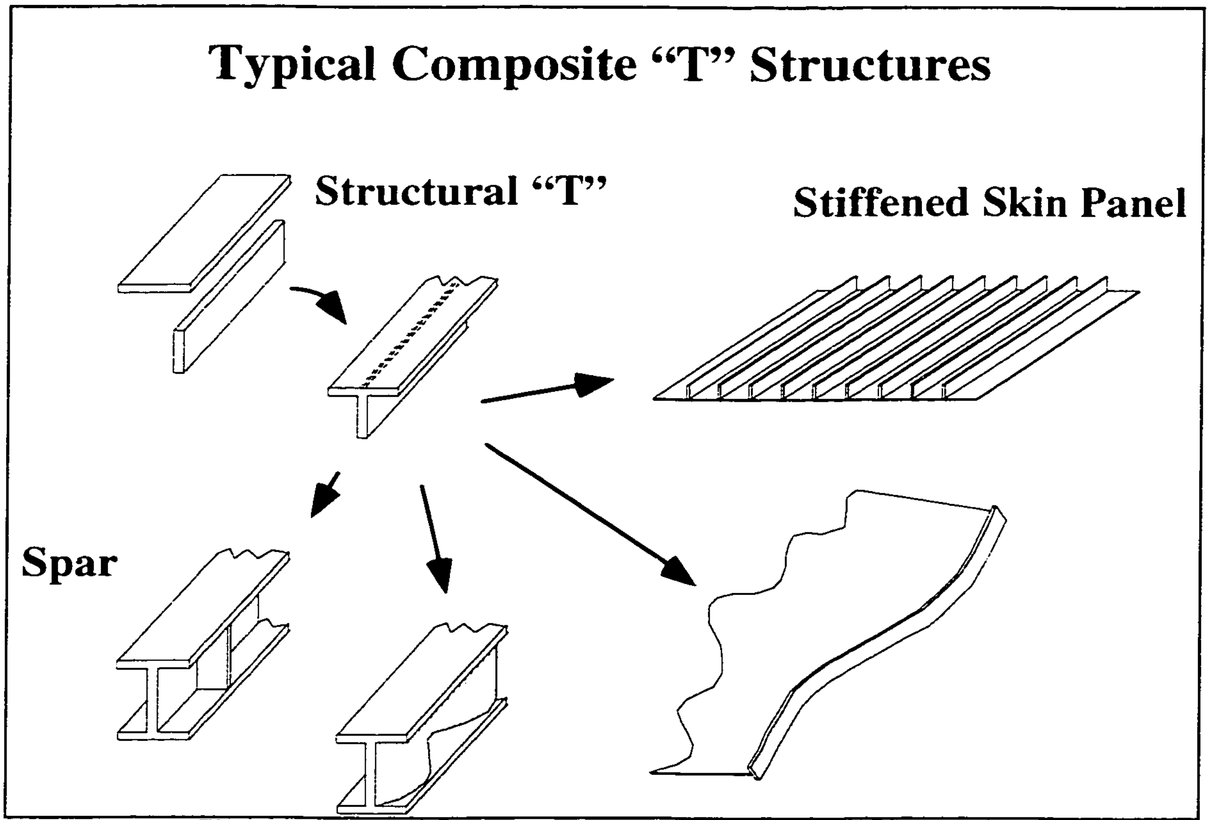

Figure 1.4-1. Structural T's Used in Aerospace Applications.

There are several types of composite structural T-joint configurations. Fastened T-joints are used extensively throughout the aerospace industry. The most common types of fastening mechanisms for T-joints are bolts and rivets. A typical bolted composite T-joint is shown in Figure 1.4-2. Fastener holes are drilled through the composite substructure and into the flange of the T-joint. In fastened T-joints, primary load transfer occurs through the bolt or rivet and peak stresses occur at the hole locations due to the high stress concentrations in this region. In the early stages of failure, these stress concentrations are relieved through composite laminate microcracking and delamination at the hole interface. As load increases, ultimate joint failure occurs by tension, shear, cleavage, bearing, or bolt pull-through as discussed previously.

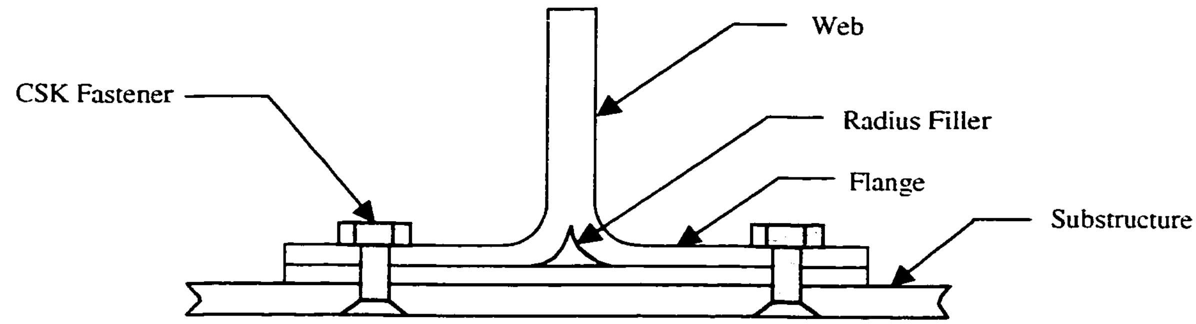

Figure 1.4-2. Bolted Composite T-Joint.

Another type of composite T-joint is the adhesive bonded T-joint. There are two types of adhesive bonded T-joints: hand layup with a radius filler and three-dimensional weave using resin transfer molding. Figure 1.4-3 shows a typical hand layup composite T-joint with opposing angle laminates and radius filler. This type of joint is used most often in the design of high performance aircraft structures. Typical failure modes for this joint are peel failure at the corner of the bonded interface, delamination of the radius plies, and cracking in the radius filler.

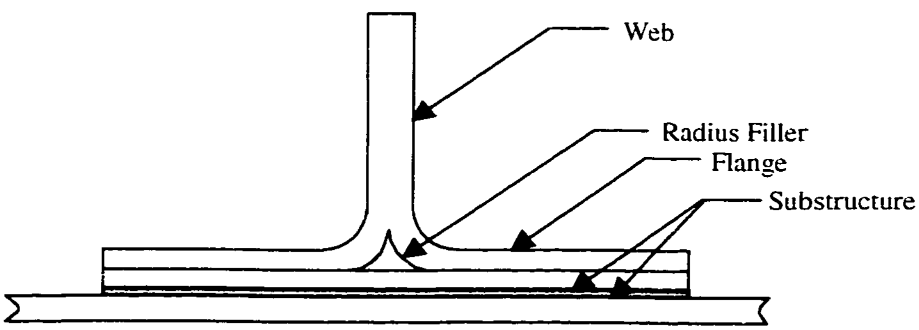

Figure 1.4-3. Adhesive Bonded Composite T-Joint With Radius Filler.

One method to improve the performance of composite structures and in particular composite T-joints is through the use of three-dimensional woven preforms.[35-37] The through-the-thickness reinforcement eliminates the need for a radius filler obviating the concern for early cracking as in the hand layup design. Three-dimensional woven preforms have been produced in a variety of complex shapes including I-beams for wing spars, T-sections for primary fuselage frames and wing stiffeners, and cylinders and turbine rotor shapes.[34] Examples of three-dimensional woven preform shapes are shown in Figure 1.4-4.

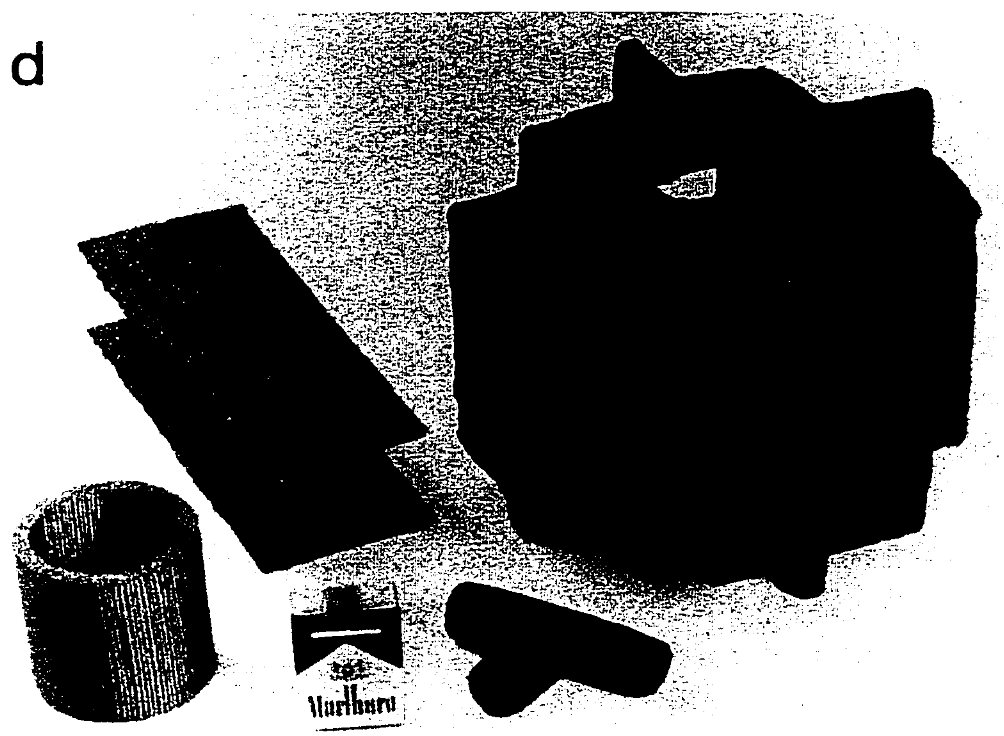

Figure 1.4-4. Various 3D Woven Preform Shapes.[34]

Three-dimensional woven preforms have many benefits including improved through-the thickness properties, the ability to produce near net shape parts, high impact damage tolerance, and high tensile strain to failure. Figure 1.4-5 shows a high performance T-joint configuration using three-dimensional woven dry fabric and resin transfer molding. This joint addresses the concerns with cracking in the radius filler found in hand layup joints. However, three-dimensional dry preform materials tend to be expensive.

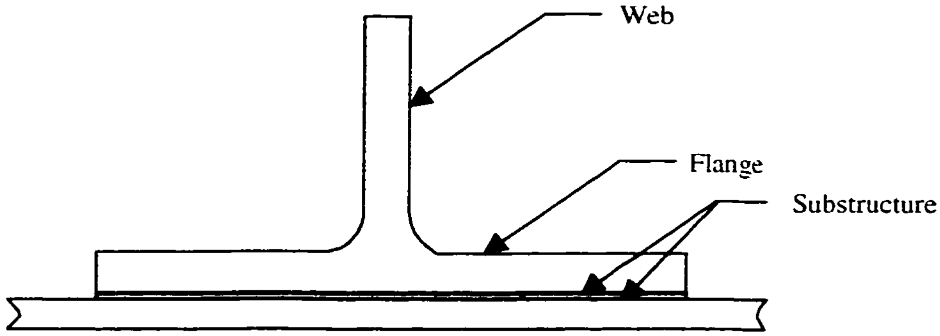

Figure 1.4-5. 3D Woven Composite T-Joint.

Additional issues impeding the use of three-dimensional woven preforms in practical design applications include: lower in-plane properties for tension, compression, shear, and torsion; lack of analytical methods for the prediction of failure; and lack of long-term characterization of durability and environmental aging.

Despite these issues, composite T-joints have found applications in industry. Composite T-joints are being used extensively in aerospace and marine applications. An experimental and numerical evaluation of the mechanical behavior of out-of-plane joints was accomplished by Gillespie and Pipes.[38] They investigated integral spar joints with no inserts, titanium inserts, and graphite-epoxy inserts under pull-off loading. A discussion of material properties and strength criteria was presented. A two-dimensional finite element model was developed to predict the integral joint mechanical response and strength. Predicted and experimental load-displacement plots were presented and good agreement was shown for the case on no inserts. For the case of no inserts, a linear-elastic response was observed up to failure. A bilinear response was observed for the titanium and graphite-epoxy insert concepts. Joint strength was predicted using the maximum stress and Tsai-Wu failure criterion. The Tsai-Wu failure criterion was shown to best predict the joint strength under out-of-plane loading.

Shenoi and Violette[39] studied structural composite T-joints in small boat applications. In their study they evaluated the influence of joint geometry on the out-of-plane load transfer for hull bulkhead joints. Experiments were performed on T-joints with foam inserts and radius fillers. An analytical model was presented and finite element analysis and experimentation were used to validate the model. The analytical model agreed well with experimentation. A further study by Shenoi and Hawkins[40] used finite element analysis and experimentation to investigate load dissipation and failure mechanisms in composite T-joints. Significant results of this study are that the behavior and failure modes of T-joints are dependent upon geometry and materials.

Phillips and Shenoi[41] studied the damage tolerance of laminated tee joints fabricated from fiber reinforced plastics for marine applications. Experiments were conducted on off-axis pull-off and three-point bend load conditions. The off-axis pull-off test simulates in-service combine web tension and flexure loading and the three-point bend test produces flange flexure. Load-deflection plots were recorded and desecrate events were indicative of damage inception and evolution as shown in Figure 1.4-6. Failures occurred as fillet ply delamination and matrix cracking at the flange-to-web interface as shown in Figure 1.4-7. A two dimensional finite element model was developed with a plane strain assumption. Progressive damage was modeled by including incrementally larger gaps in the geometry representing delamination growth under increased load. Reasonable agreement was shown between the experimental and numerical results as shown in Figure 1.4-8.

Junhou and Shenoi[42] investigated several types of joints including T-joints. This investigation focused on design synthesis, and static, impulse, creep, and fatigue loading. A finite element analysis was performed and experiments were conducted.

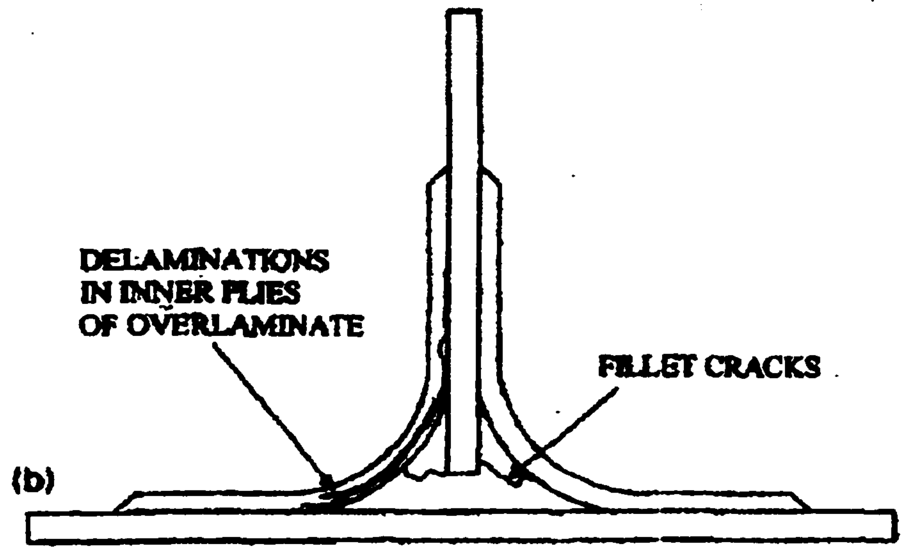

Figure 1.4-6. T-Joint Final Failure Modes.[41]

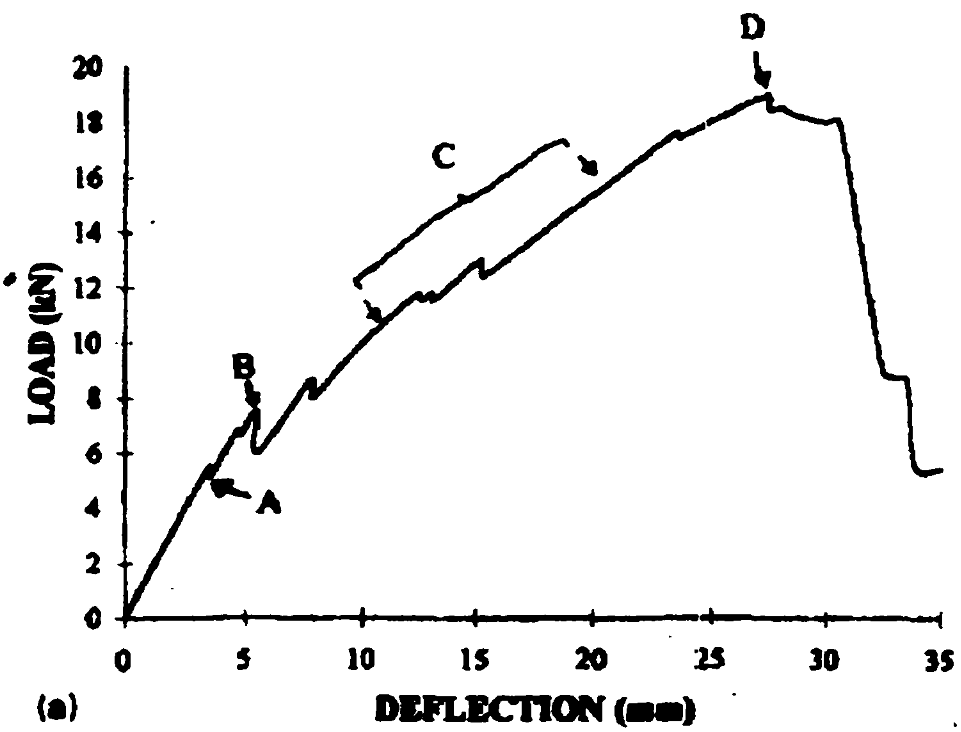

Figure 1.4-7. Experimental Load-Displacement Plot.[41]

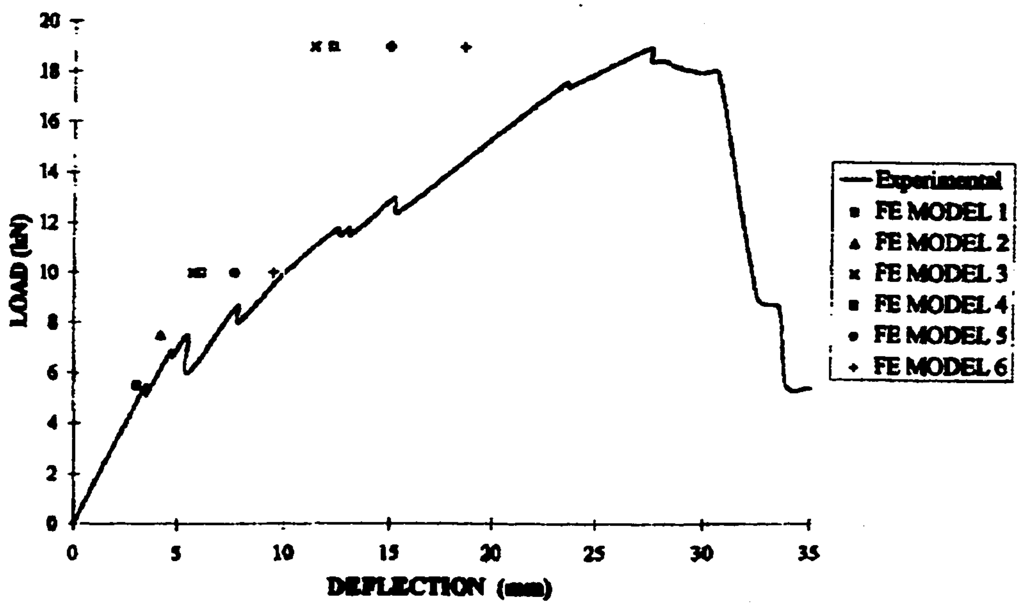

Figure 1.4-8. Comparison of Numerical and Experimental Load-Displacement.[41]

Theotokoglou[43-45] recently reported the strength of composite sandwich T-joints under pull-off load. Experimental and numerical analysis were performed. The elastic finite element analysis includes nonlinear core and adhesive properties and large displacement. A two-dimensional finite element model was created with a plane strain assumption. The nonlinear analysis more consistent agreement with experimental results. Failures occur due to shear fracture of the core. Dulieu-Smith *et al.*[46] performed a thermoelastic stress analysis of T-joints fabricated from graphite reinforced plastic. A two-dimensional finite element model was created using ANSYS software. The T-joint was modeled using two-dimensional plane elastic solid elements. Good agreement was shown between the thermoelastic response under experimental loading as compared to the finite element analysis results. Specimens failed by delamination at the T-joint interface. Although significant research has been conducted on through-the-thickness reinforcement of laminates and joints, research to date has not addressed the performance of T-joints with transverse stitching located directly at the web-to-flange interface.

1.5 Composite Joints with Transverse Stitching

The requirement for reduced structural weight and the ever-increasing demand for more efficient aerospace structures has driven the development of adhesive bonded T-joints. However, adhesive bonded T-joints are sensitive to peel and through-the-thickness stresses. A method of improving the performance of structural joints with reduced cost is through the use of transverse stitching.[47] T-joints with and without transverse stitching using resin transfer molding, epoxy resin, and fiber preforms was evaluated by Young and Chuang.[48] The primary failure mode in unstitched specimens was a delamination at the flange-to-skin interface. This investigation showed that transverse stitching along the rib at an offset distance from the web improved the pull-off strength of T-joints. Figure 1.5-1 shows the experimentally determined pull-off strength results of T-joint specimens with and without stitching.

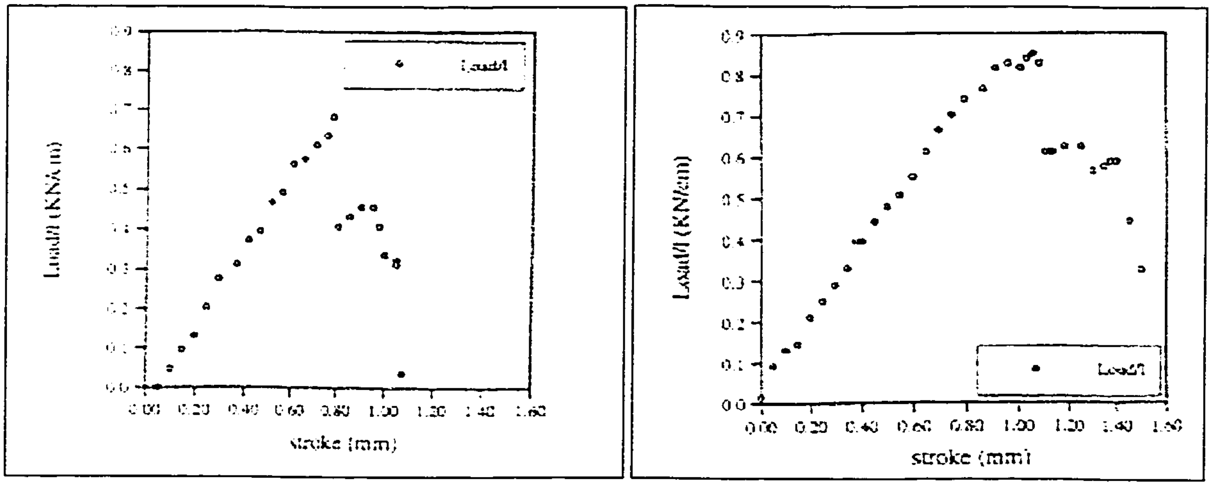

Figure 1.5-1. Composite T-Joint: (a) Without and (b) With Transverse Stitching. [48]

Rispler *et al.*[49] have investigated the failure analysis of composite T-joints with and without inserts (radius fillers) in tension using graphite/epoxy T-300/934 unidirectional prepreg tape (Figure 1.5-2). Unidirectional fiber tow was used for the insert.

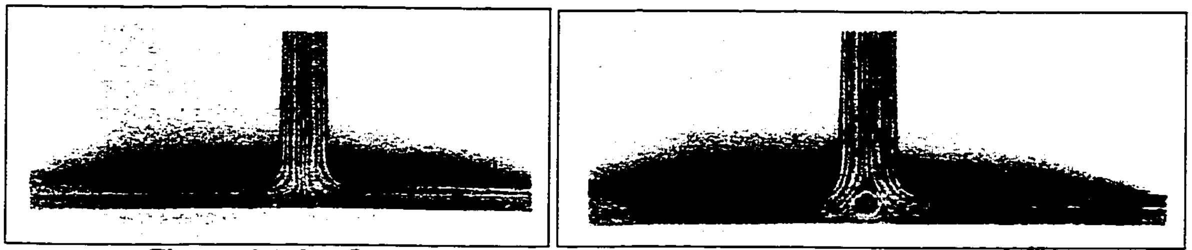

Figure 1.5-2. Composite T-Joint: (a) Without and (b) With Insert.[49]

A finite element analysis was performed using a plane strain assumption. A truncated quadratic delamination failure criterion was used. Failure was shown to initiate at and be dominated by the resin properties in the radius filler resin-rich area of the web-to-flange interface. The predicted and experimental load-displacement plot for the T-joint with and without insert is shown in Figure 1.5-3. Specimens behaved linearly up to first crack and the large drop in the load–displacement curve indicates the presence of an unstable crack. It was shown that the inclusion of an insert had a detrimental effect on pull-off strength. It was hypothesized that the insert introduced geometric discontinuities.

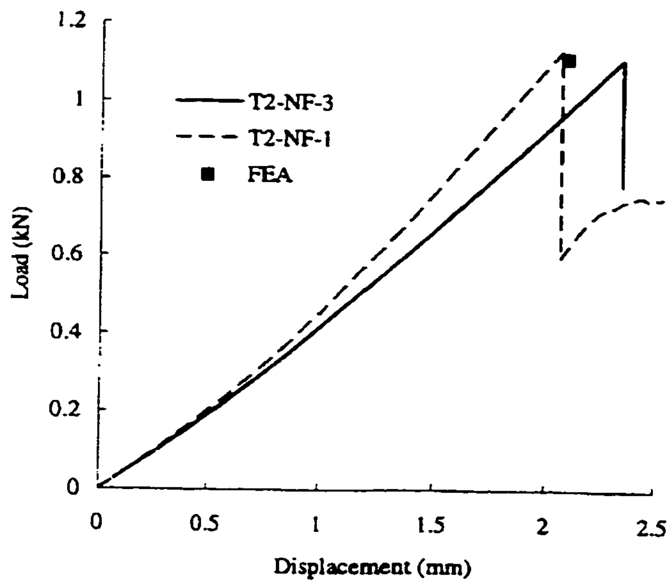

Figure 1.5-3. Load-Displacement Plot for T-Joint Without and With Insert.[49]

The effect of stitching on T-section stiffeners in compression fabricated from TORAY 7474 prepreg was evaluated by Tada and Ishikawa.[50] Stitched T-sections were shown to have a 4% increase in buckling load over unstitched T-sections. Freitas *et al.*[51] investigated T-stiffeners in tension using Z-fiber insertions in the flange interface and directly in the radius filler. Z-fiber reinforcements are discrete insertions whereas fiber insertion is continuous along the stitching direction. Results indicated an increase in initial and ultimate failure of the T-stiffeners in tension with the addition of Z-fiber insertions.

A new low cost damage tolerant method of fabricating T-joints is emerging using transverse stitching and two-dimensional fiber preforms (Figure 1.5-4). This joining method uses fiber insertions in the form of yarn or tow as the main load transfer mechanism through the mating surfaces of the dry fiber preforms. Fiber insertion differs from traditional transverse reinforcement in that for these joints the primary load transfer mechanism is through the stitches, whereas the traditional use of transverse stitches is to improve the damage tolerance of joints after initial damage occurs. Experimental and analytical investigations on T-joints using fiber insertion and RTM were conducted recently by Stickler *et al.*[52-54] Their study characterized stitched T-joint performance in flexure. In these experiments, Shell Epon 862/W and PR520 RTM resins were used for the fabrication of the specimens. T-joint parameters were varied to determine the effect on joint flexure strength and an analytical model was developed to predict linear elastic behavior. Results of this investigation showed that increasing the overall web thickness and number of rows of stitching increases the failure strength of the T-joint and that initial T-joint failure modes identified include matrix cracking initiated at the resin-rich corner fillet and fiber/matrix debonding at the transverse stitch locations. A damage progression model was established for failure of the T-joint in flexure.

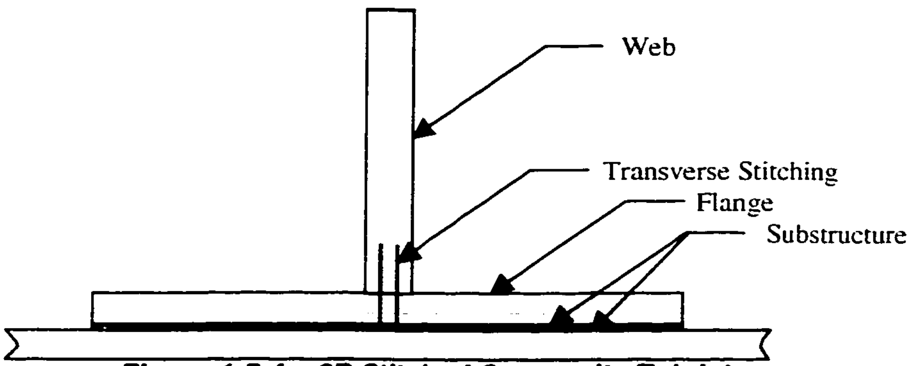

Figure 1.5-4. 2D Stitched Composite T-Joint.

Finite element analysis has been used to model damage accumulation in composite materials. Kermanidis *et al.*[55] developed a progressive damage finite element model for bolted composite lap joints under incremental loading. Failure analysis was performed that included material property degradation. A matrix dominated failure mode was observed at ultimate failure. Camanho and Matthews[56] also utilized finite element analysis to model the progressive damage in mechanically fastened joints. A three-dimensional failure criterion was used to predict damage. Comparisons were made between experimental and predicted load-displacement relations. Good agreement was shown under shear, tension and bearing loads.

The effect of nonlinear material properties has been considered by several investigators. Chiu *et al.*[57] investigated the nonlinear matrix dominated response of composite materials under loading. The shear stress-shear strain behavior of graphite epoxy composites was investigated. Time-dependent nonlinear behavior was observed at room temperature. Jones and Alesi[58] investigated material and geometric nonlinearities in blade-stiffened panels. Measured strains were compared to finite element predictions and good correlation was shown. Potter *et al.*[59] performed an experimental and numerical evaluation of composite "I" beams. Geometric and material property nonlinearities were applied to the adhesive layer and the laminate was modeled using linear properties. Good accuracy was shown between the experimental and analytical results at the failure load.

1.6 Summary

A literature review is presented in this chapter. Two traditional joining methods are reviewed: mechanical fastening and adhesive bonding. A detailed review of experimental and numerical research in the stitching of composite laminates and joints is also presented. A new low cost damage tolerant T-joint is proposed using fiber insertions as the primary load caring mechanism. A summary of the significant conclusions is presented below:

- Bolted joints are expensive to produce and complex load conditions give rise to local stress concentrations at the hole interface which tend to reduced performance and increase weight.

- Bonded joints are structurally efficient but are costly to produce and are susceptible to peel failure and impact damage.

- T-joints using the hand layup process are expensive to produce and experience cracking in the radius filler during loading which reduces their performance.

- Three-dimensional woven T-joints are structurally efficient and the through-the-thickness reinforcement of these preforms improves damage tolerance. However, three-dimensional woven dry preform materials are costly to produce.

- Transverse stitched T-joints using an automated fiber insertion process, two-dimensional dry fabric preforms, and resin transfer molding are low cost, have good structural performance, and are inherently damage tolerant. However, mechanical behavior and failure mechanisms are not well understood.

No investigation in the open literature was applicable to the mechanical behavior of composite T-joint with transverse stitching and numerical models for the prediction of failure and characterization of failure modes under typical aerospace load conditions do not existent.

CHAPTER 2
OBJECTIVES

This research evaluates the performance of a new low cost, damage tolerant, stitched composite T-joint configuration using fiber insertion, two-dimensional dry preforms, and resin transfer molding with PR520 toughened epoxy resin. Mechanical experiments are conducted under three separate loading conditions: flexure, tension, and shear. These conditions are selected as representative of the in-service loads found in the application of this type of joint to aerospace structures. All experiments are conducted under room temperature ambient conditions. Experimental analysis is performed to determine initial and ultimate failure loads and finite element analysis is employed to model mechanical behavior and to predict failure. The numerical models developed herein provide predictive capability for determining the failure strength of similar joint configurations. Results may be used to assist in the design of structural T-joints for application in a broad range of future products. Parametric design curves are presented using the models developed herein.

The following are the specific objectives of the research:

Experimental Work

- Develop web and flange in-plane and out-of-plane laminate elastic and strength properties.
- Develop experimental procedures including fixture fabrication and strain gage instrumentation.
- Perform experimental analysis to determine initial and ultimate failure strength of the stitched composite T-joint under flexure, tension, and shear loading.
- Measure far field strains using strain gages and correlate measured values with finite element model predictions.

Numerical Modeling

- Perform numerical analysis to develop predictive linear elastic, non-linear elastic, and progressive damage finite element models for the stitched T-joint flexure, tension, and shear configurations.
- Develop parametric design curves for T-joint fiber insertion properties under flexure, tension, and rail shear loading.

Identification of Failure Mechanisms

- Perform a comprehensive post failure analysis including optical micrographic examination to determine T-joint failure modes.
- Develop a progressive damage models for each load condition based on experimental observations and post failure analysis.

CHAPTER 3
EXPERIMENTAL AND NUMERICAL METHODS

The experimental and numerical methods for the investigation of mechanical behavior of the composite transverse stitched T-joints will be discussed in this chapter. Specimen configuration, constituent material properties, fabrication method, experimental setup, numerical analysis, and post failure analysis procedures are presented.

3.1 Materials and T-Joint Specimen Configurations

The T-joint specimens used in this evaluation are fabricated using T-300-3k-4h satin weave (crow foot) two-dimensional dry fabric preforms manufactured by Albany International Techniweave, Inc. The two-dimensional dry preforms are fabricate from T-300 fibers manufactured by BP Amoco.[60] The individual preform plies are balanced with 4.9 fiber tows per cm in each direction. Figure 3.1-1 shows a sample of 4HS or crowfoot satin weave. In 4HS satin weave, the fill thread passes over three warp threads and under one. This is a more pliable fabric than that of plain weave and consequently easier to form around curves.

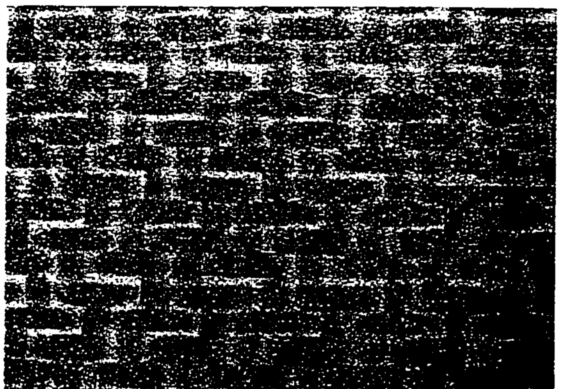

Figure 3.1-1. Typical 4HS Satin Weave (Crowfoot Satin).

Hexcel fabricated the IM7 6k fiber insertion tows used for transverse stitching.[61] Two types of RTM resin systems were selected for this investigation: Shell Epon 862/W[62] and 3M PR520.[63] The Shell 862 resin, a low cost epoxy resin system, was selected for early investigations. The PR520, a toughened epoxy resin, was selected for more detailed investigation. Table 3.1-1 shows a comparison of the T-joint resin mechanical properties. As shown, the 3M PR520 toughened epoxy has superior mechanical properties to that of the Shell 862 resin system.

Table 3.1-1. T-Joint Resin Mechanical Properties.

T-joint Material	E (GPa)	Tensile Strength (MPa)	Elongation (%)
Shell Epon 862/W Resin[62]	2.81	68.9	4.70
3M PR520 Resin[63]	3.55	91.0	5.00

Fiber insertions are stitched through the dry preform of the T-joint flange and penetrate the preform web to a depth of 12.7 mm providing a continuous fiber stitch path. Resin transfer molding is used to consolidate the specimens. A typical T-joint specimen configuration is shows in Figure 3.1-2.

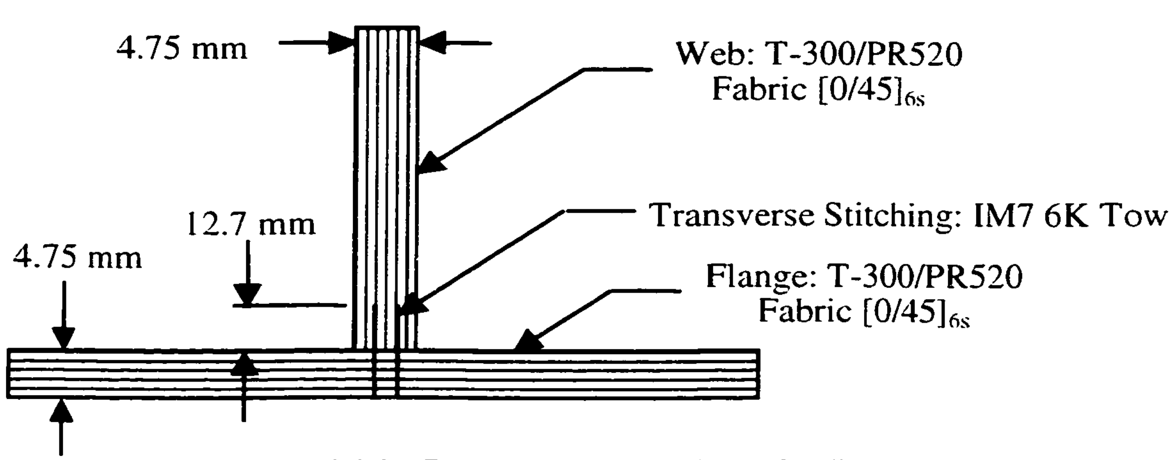

Figure 3.1-2. Typical T-Joint Specimen Configuration.

Table 3.1-2 provides a detailed summary of the T-joint constituent properties. Individual material properties were captured from vendor provided data sheets.

Table 3.1-2. T-Joint Constituent Properties Summary.

Property	T-300 3k Carbon Fiber[60]	IM7 6k Carbon Fiber[61]	Epon 862/W Resin[62]	PR520 Resin[63]
Manufacturer	BP Amoco Chemicals	Hexcel	Shell	3M
Tensile Modulus (GPa)	231	276	2.81	3.55
Tensile Strength (GPa)	3.75	5.15	0.069	0.091
Shear Modulus (GPa)	22	19	-	0.33
Poisson's Ratio	0.20	0.20	-	0.38
Density (g/cc)	1.76	1.78	1.12	1.25
Strain to Failure (%)	1.40	1.81	4.7	6.0
Filament Diameter (μm)	7.0	5.0	N/A	N/A
Thermal Conductivity (W/mK)	8.0	10	-	-
CTE at 21°C (μm/m-K)	-0.17	-0.17	-	-

Figure 3.1-3 shows key T-joint specimen geometric parameters. Parameters include web height, $\mathbf{H_w}$ and thickness, $\mathbf{t_w}$, flange width, $\mathbf{W_f}$ and thickness, $\mathbf{t_f}$, fiber insertion depth, $\mathbf{h_s}$, number of rows of fiber insertions, **N**, fiber insertion spacing, **S** and pitch **P**, and specimen width, **W**. Figure 3.1-4 shows a polished T-joint transverse cross-section revealing the continuous nature of the IM7 fiber insertion tow loops.

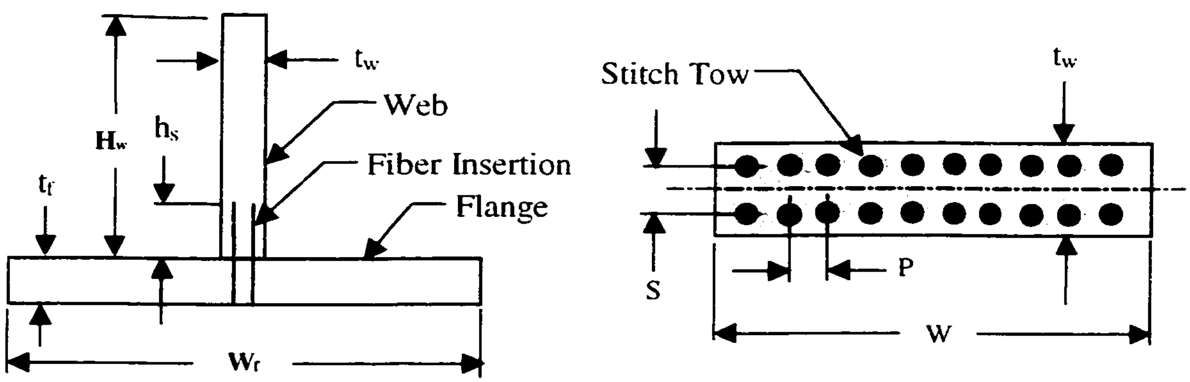

Figure 3.1-3. T-Joint Specimen Parameters.

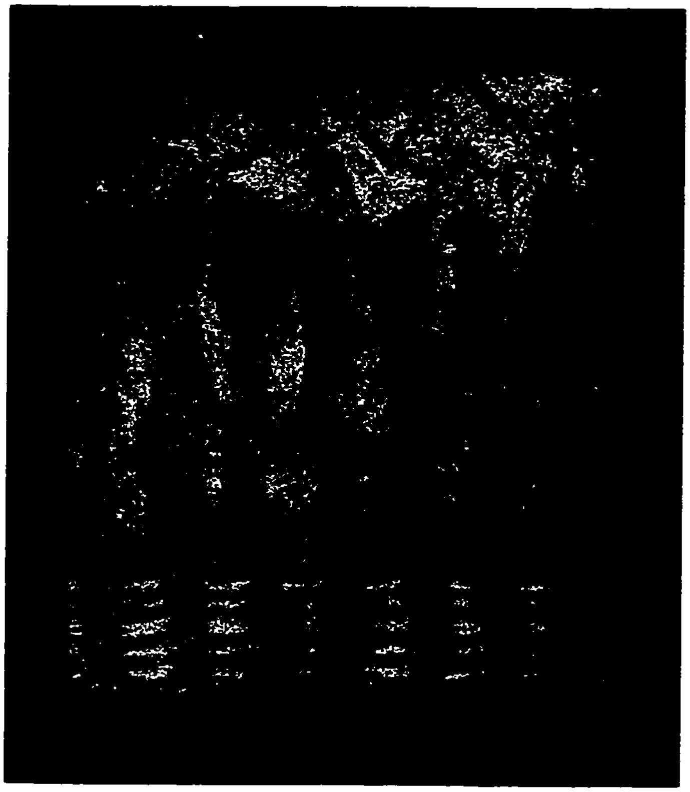

Figure 3.1-4. T-joint Transverse Section Showing Continuous IM7 Fiber Insertion Tow Loops.

3.2 Material Properties Development

An experimental investigation was undertaken to develop the T-joint T-300/PR520 web and flange laminate physical, elastic, and strength properties. Table 3.2-1 summarizes the material properties development matrix for this investigation. Both in-plane and out-of-plane properties are experimentally determined. The T-joint web and flange layup used in this investigation is quasi-isotropic. Based on the quasi-isotropic nature of the T-joint web and flange, it is assumed that the in-plane transverse material and strength properties are equal to the longitudinal properties. In order to limit the number of specimens required, the longitudinal properties are experimentally determined, and the transverse properties are assumed to be equal.

Table 3.2-1. Laminate Material Properties Development Matrix.

T-300/PR520 Composite Laminate Material Properties Experimental Matrix Quasi-isotropic Layup $[0/45]_{6s}$					
Test Type	**Reference**	**T-300/PR520**	**Temperature**	**Specimen Size (mm)**	**Measured Properties**
Tension	ASTM D3039	6	RTA	19.05 W x 292.1 L x 5.08 T	$E_{xx} = E_{yy}$, ν_{xy}, $X_t = Y_t$
Compression	ASTM D3410	6	RTA	12.7 W x 139.7 L x 5.08 T	$X_c = Y_c$
In-Plane Shear	ASTM D4255 Method A	6	RTA	69.85 W x 107.95 L x 5.08 T	G_{xy}, S_{ll}
Out-of-Plane Tension	Draft ASTM	6	RTA	25.4 W x 25.4 L x 5 T, r = 3.175	E_{zz}, ν_{zx}, ν_{zy}
	Draft ASTM	6	RTA	25.4 diameter, t = 19.05	Z_t
V-notch Beam	ASTM D5379	6	RTA	19.05 W x 76.2 L x 7.62 T	$G_{xz} = G_{yz}$
Fiber, Matrix, Void Content	ASTM D3171 Method I A6	3	RTA	25.4 W x 25.4 L x 5.1 T	V_f, V_m, V_v

Table 3.2-2 summarizes the Micro-measurements Group strain gages selected for use in determination of the elastic material properties.[64] The appropriate strain gages are used as indicated in the appropriate ASTM specification with special consideration of their application to composite materials as outlined by Tuttle and Brinson.[65]

Table 3.2-2. Experimental Strain Gage Selection.

Test Type	Type	Micro-Measurements Gage ID[64]
Tension	Two-element 90° tee rosette	CEA-06-125UT-350
Compression	Uniaxial	EA-06-125AC-350
In-Plane Shear	Two-element 90° tee rosette	CEA-06-125UT-350 (45°)
Out-of-Plane Tension	Two-element 90° tee rosette	CEA-06-125UT-350
V-notch Beam	Iosipescu specialty gage	N2A-00-C032A-500

3.3 T-Joint Specimen Fabrication

T-joint specimens are fabricated using two-dimensional fiber preforms consisting of multiple layers of 3k 4HS satin woven fabric. Prior to T-joint consolidation, fabric plies are cut for both the web and flange elements. Next, web plies are stacked using a quasi-isotropic $[0°/45°]_{6s}$ and tacked by heating and cooling (the flange element was made the same way as the preform web element). Then the web element is placed into the molding tool and compacted to final dimensions as the tool is bolted together. Next, the flange element of the preform is placed in the tool and compacted with metal tool inserts. The tool insert directly above the joint is then removed while the inserts on the rest of the flange are maintained in their final position. This provides access to the joint so that the carbon tows can be inserted through the flange and into the web element. The fiber insertion process is then performed using IM7 6k tow. After the insertion process is completed, the mold is sealed (bolted) and the RTM process is initiated.

Again, two resin systems were investigated Shell 862/W and PR520. During RTM processing, the Shell 862/W resin is degassed at 40°C and preheated to 50°C. The mold is then preheated to 100°C. Next, the resin is transferred at 138 kPa while the mold is under vacuum. Then the specimens are initially cured for four hours at 120°C, demolded, and post-cured for 2.5 hours at 175°C.

The PR520 RTM specimens are cured by preheating the resin to 80°C and then sending it through a heat exchanger to reach an injection temperature of 163°C. The RTM mold is preheated to 163°C. Next, the resin is transferred at 517 kPa while the mold is under vacuum. After fiber wet-out is ensured, the specimens are cured for two hours at 180°C, and demolded. The typical cured specimen fiber volume fraction is 55%. A completed PR520 T-joint subcomponent is shown in Figure 3.3-1.

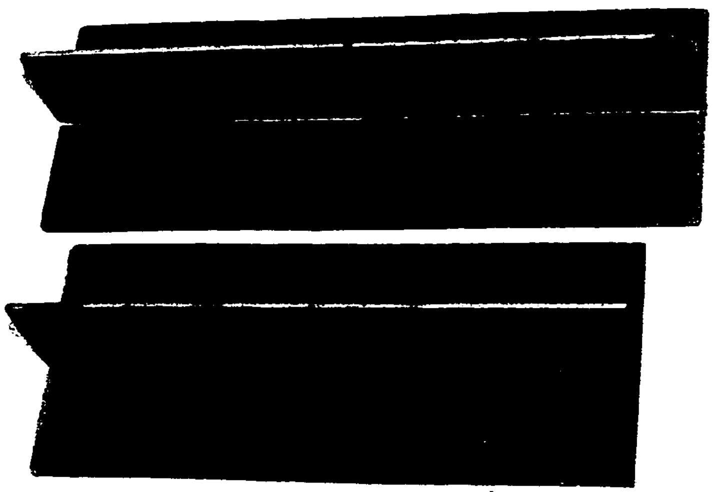

Figure 3.3-1. PR520 Subcomponent Prior to Machining Into T-Joint Specimens.

A vendor provided PR520 neat resin stress-strain plot is shown in Figure 3.3-2 (Shell 862 stress-strain data was not available). Data is measured using a tensile specimen and a biaxial strain gage. The neat resin is slightly ductile as shown by the nonlinearity in the stress-strain curve. This nonlinear behavior indicates a small amount of matrix yielding prior to ultimate tensile failure for the unconstrained matrix. The average matrix strain at failure is 5.0% and the average failure stress is 91.0 MPa. The average modulus determined from the slope of the stress-strain plot is 3.55 GPa.

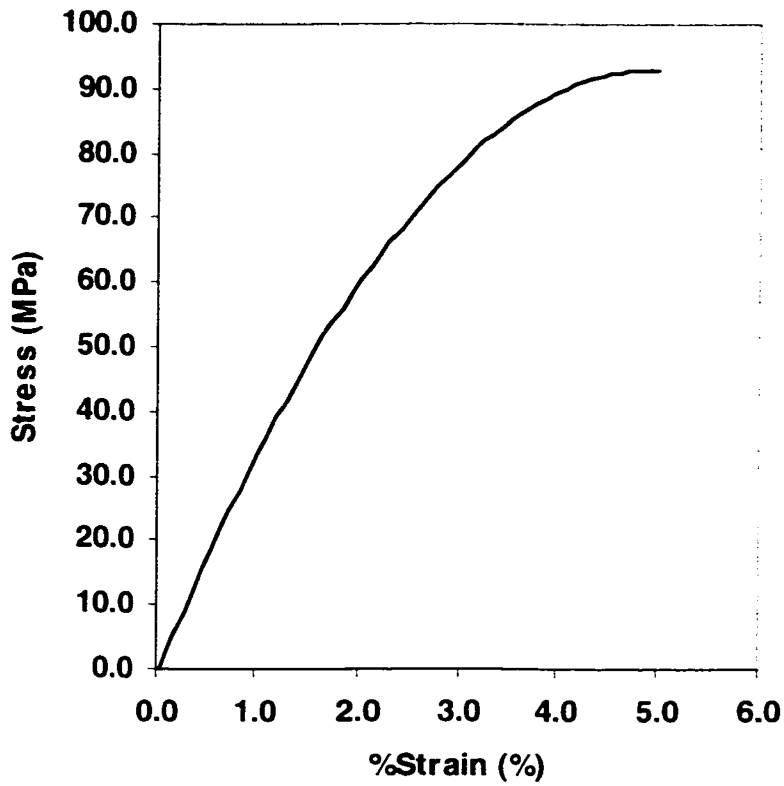

Figure 3.3-2. 3M PR520 Neat Resin Stress-Strain Plot.[63]

3.4 Experimental Methods and Procedures

The following sections discuss the experimental methods for the T-joint investigation. Section 3.4.1 discusses the flexure experimental methods, Section 3.4.2

discusses the tensile specimen experimental methods and Section 3.4.3 discusses the rail shear experimental methods.

Flexure, tension, and rail shear experiments are conducted using a 245 kN MTS static load frame with a built-in cross-head displacement. The cross-head displacement uses an optical encoder to measure the displacement. A built-in load cell with strain gages is used to measure the applied load. All specimens are loaded at a rate of 1.25 mm/min. All experiments continue through initial damage and T-joint catastrophic failure. Catastrophic failure is defined as a permanent drop in the load carrying capability of the joint. Failed T-joints are then sectioned to establish the failure mechanisms or if necessary terminated prior to complete failure and then sectioned in order to establish the evolution of damage leading to failure.

3.4.1 Flexure Experiments

Flexure experimental analysis was accomplished on the T-joints. A fixed support flexure experimental fixture was designed and fabricated. The upper flange of each T-joint specimen was bolted to a steel support fixture at two locations along the width as shown in Figure 3.4.1-1. Prior to attachment to the support fixture, a 1.27 cm thick aluminum backing plate was bonded to each specimen using a AF 163 epoxy film adhesive at 120°C. During each experiment, load is applied normal to the web 2.54 cm from the flange-to-web interface. A 3.175 mm diameter load pin was used to apply force normal to the web.

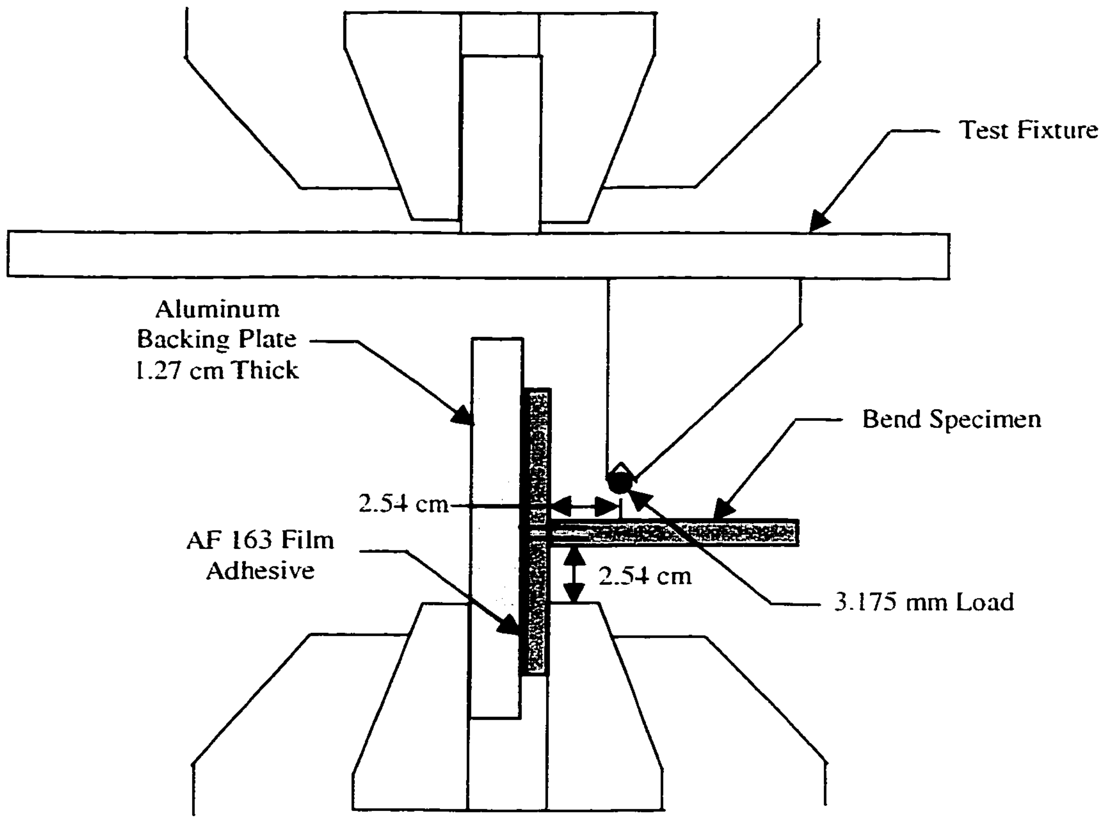

Figure 3.4.1-1. Flexure Experimental Fixture.

3.4.2 Tension Experiments

3.4.2.1 Fixed Supports

Fixed support tension experiments were accomplished on the T-joint specimens. A Tension experimental fixture was designed and fabricated. The flange of each T-joint specimen was clamped to a steel support fixture at each end as shown in Figure 3.4.2.1-1. Prior to attachment to the support fixture, an aluminum backing plate is bonded to each specimen using AF 163 film adhesive at 120°C. The bondline thickness was nominally 0.125 mm. The bondline is masked using Kapton under the web-to-flange interface to ensure the stitches are free at this boundary.

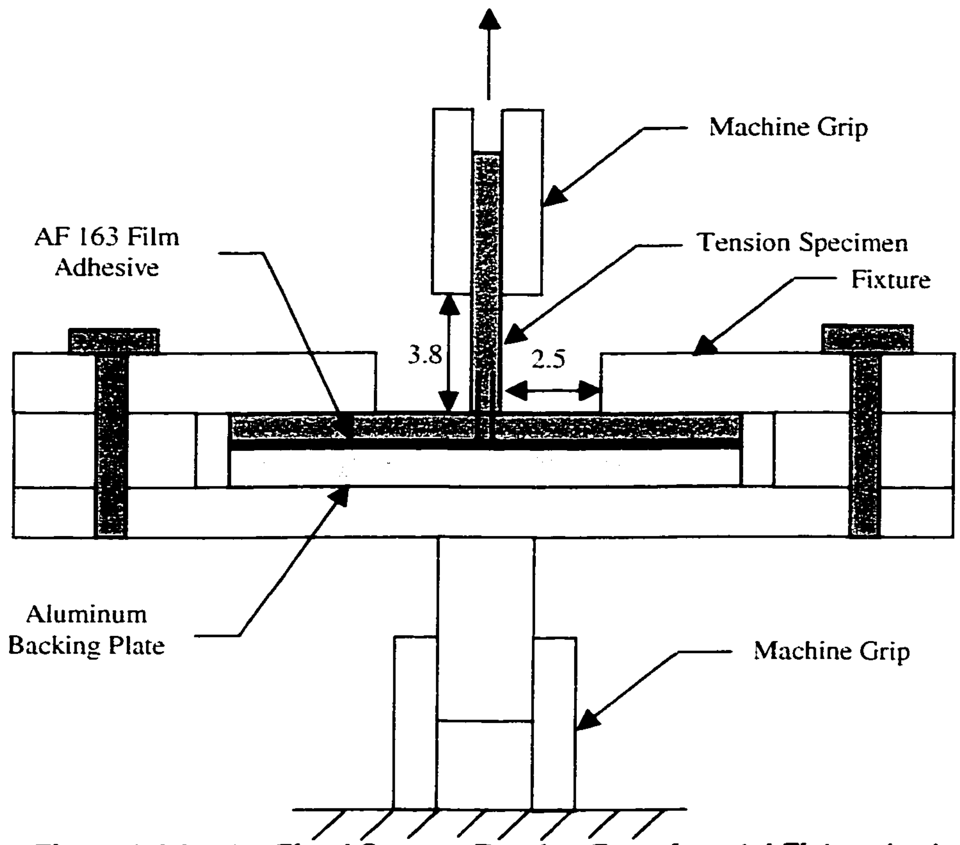

Figure 3.4.2.1-1. Fixed Support Tension Experimental Fixture (cm).

3.4.2.2 Simple Supports

Simple support tension experiments are accomplished on T-joint. A tension experimental fixture was designed and fabricated as shown in Figure 3.4.2.2-1. Specimens are gripped on the web 3.8 cm from the web-to-flange interface. Simple supports are located 4.5 cm from the web centerline.

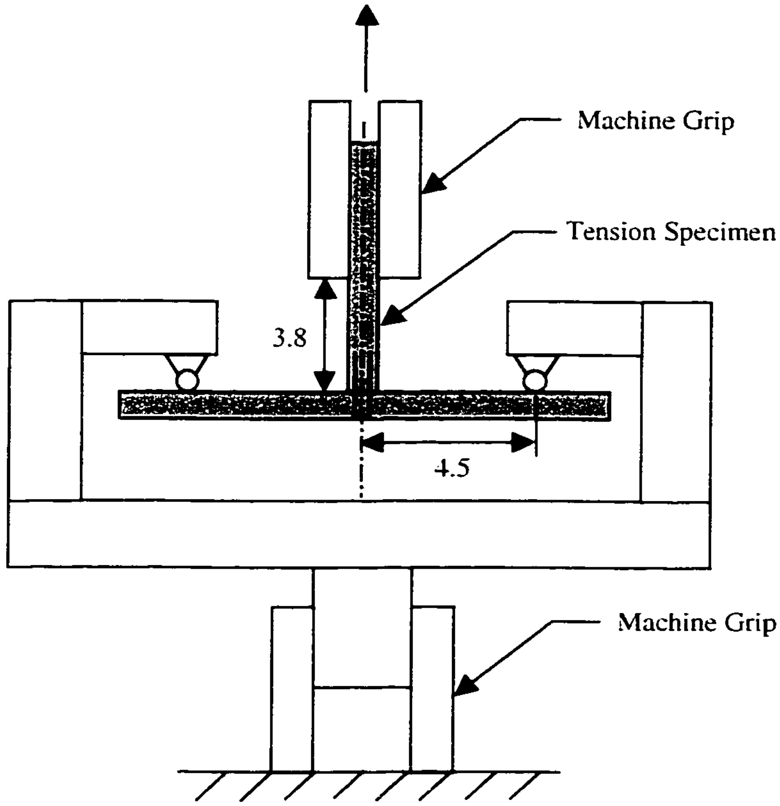

Figure 3.4.2.2-1. Simple Support Tension Experimental Fixture (cm).

3.4.3 Rail Shear Experiments

Rail shear experiments are accomplished on T-joint specimens with PR520 toughened epoxy resin. A rail shear test experimental fixture was designed and fabricated. The flange of each T-joint specimen is bolted to a steel support fixture at four locations along the width on each side of the web and at four locations near the top of the web as shown in Figure 3.4.3-1. During experiments, load is applied parallel to the longitudinal axis of the specimen.

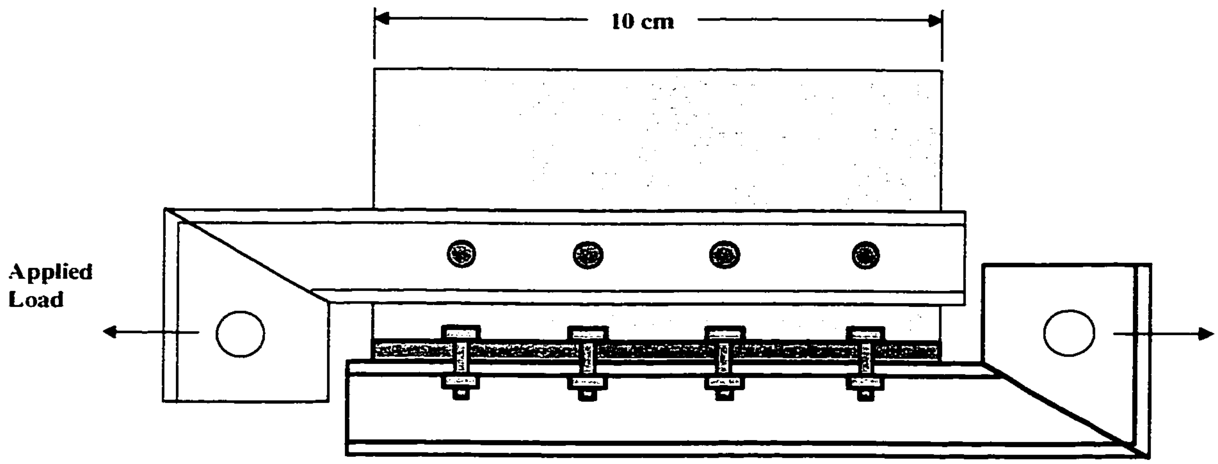

Figure 3.4.3-1. Rail Shear Experimental Fixture.

3.5 Data Collection and Reduction

The data acquisition system is shown in Figure 3.5-1. Both load-displacement and strain-load measurements are recorded for all specimen configurations. The specimens are tested in an MTS 810 static load frame. Load displacement data is measured using an MTS load cell 661-22C-01. Processing of load-displacement data is accomplished using an MTS model 458.20 controller and a National Instruments model SCXI-1000 conditioner. Strain measurements are taken using Micro-measurements strain gages and data is conditioned using the National Instruments model SCXI-1000 conditioner. Data is then read using a PC input port and LabView Version 5.1 software is used for data recording.

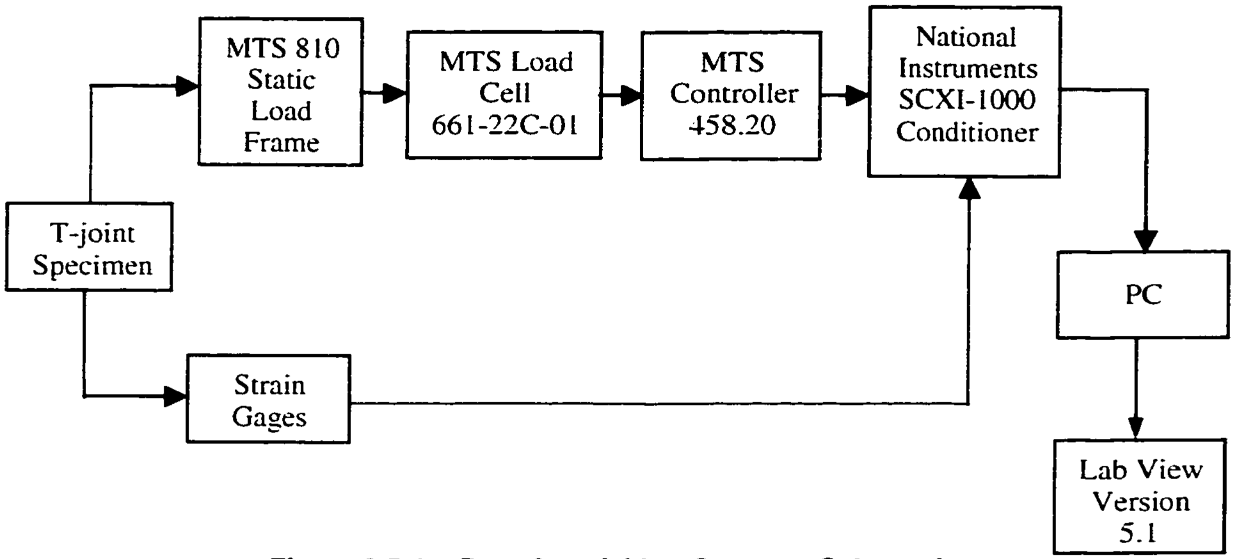

Figure 3.5-1. Data Acquisition Systems Schematic.

Micro-measurements uniaxial and three-element stacked rosette strain gages are bonded to the specimens using M-bond 200 cement. The anisotropic nature of composite laminates requires special consideration of transverse-sensitivity effects, gage-misalignment errors, and temperature-compensation methods. A detailed description of strain gage technologies and application to orthotropic materials is given by Tuttle and Brinson.[65]

Figure 3.5-2 shows the strain gage layout for the flexure specimens. The flexure specimens use two EA-06-062AQ-350 uniaxial gages and four WA-06-120WR-350 three element 45° rectangular stacked rosettes. Figure 3.5-3 shows the strain gage layout for the tension specimens. The tension specimens use two EA-06-062AQ-350 uniaxial gages and two WA-06-120WR-350 three element 45° rectangular stacked rosettes. A reduction in gage count is possible with the tension specimens due to the symmetric nature of the loading. Figure 3.5-4 and 3.5-5 show the strain gage layout for the rail shear specimens in isometric and plan view, respectively. The rail shear specimens use four WA-06-120WR-350 three element 45° rectangular stacked rosettes. All gages have a resistance of 350 ohms and a gage factor of 2.1.[64] Additional strain gage specifications are contained in Appendix A.

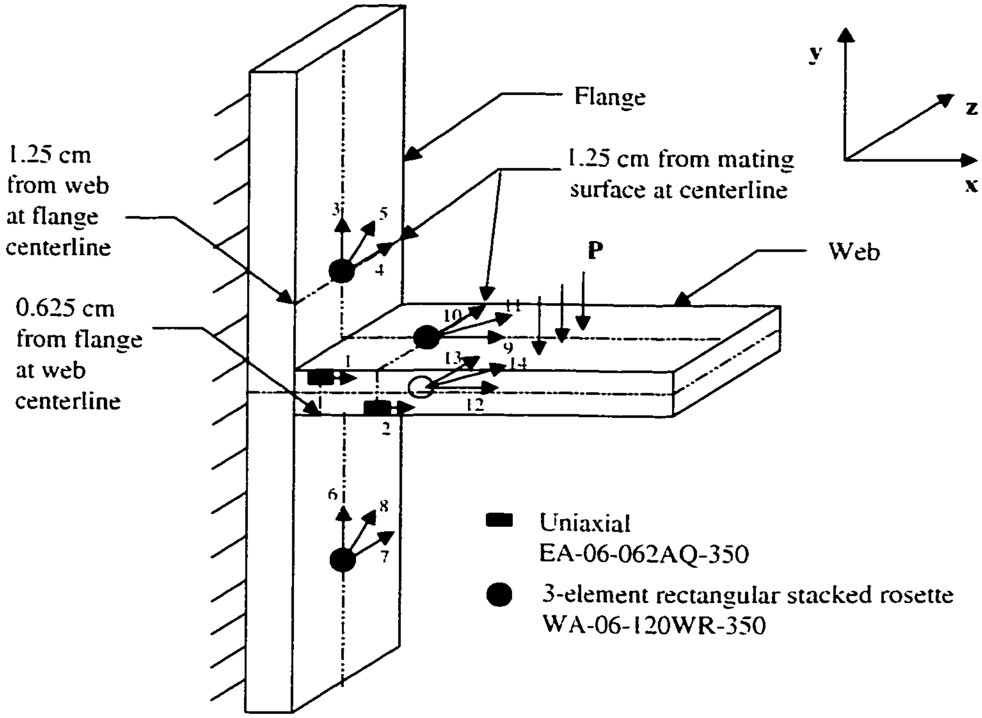

Figure 3.5-2. Flexure Specimen Instrumentation Layout.

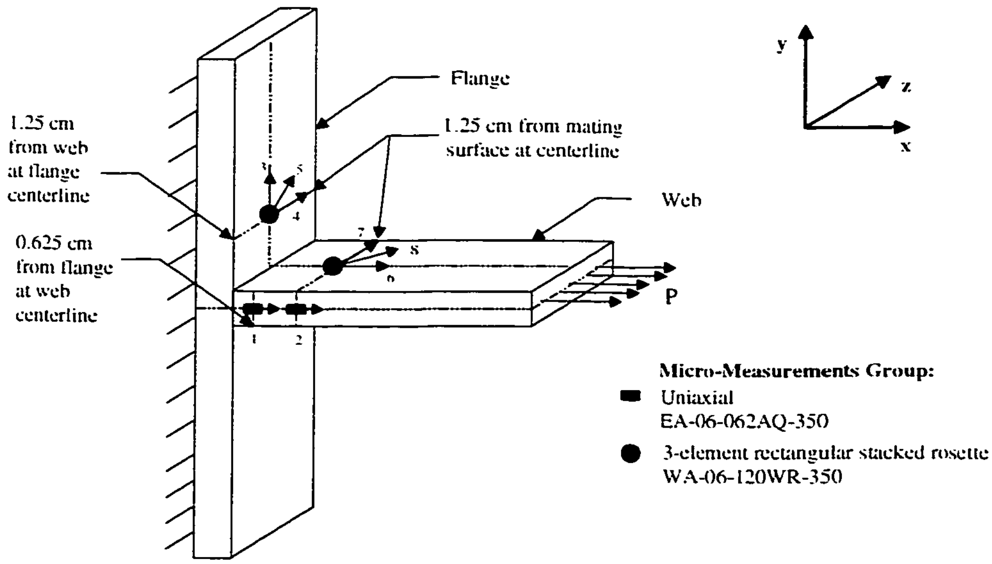

Figure 3.5-3. Tension Specimen Instrumentation Layout.

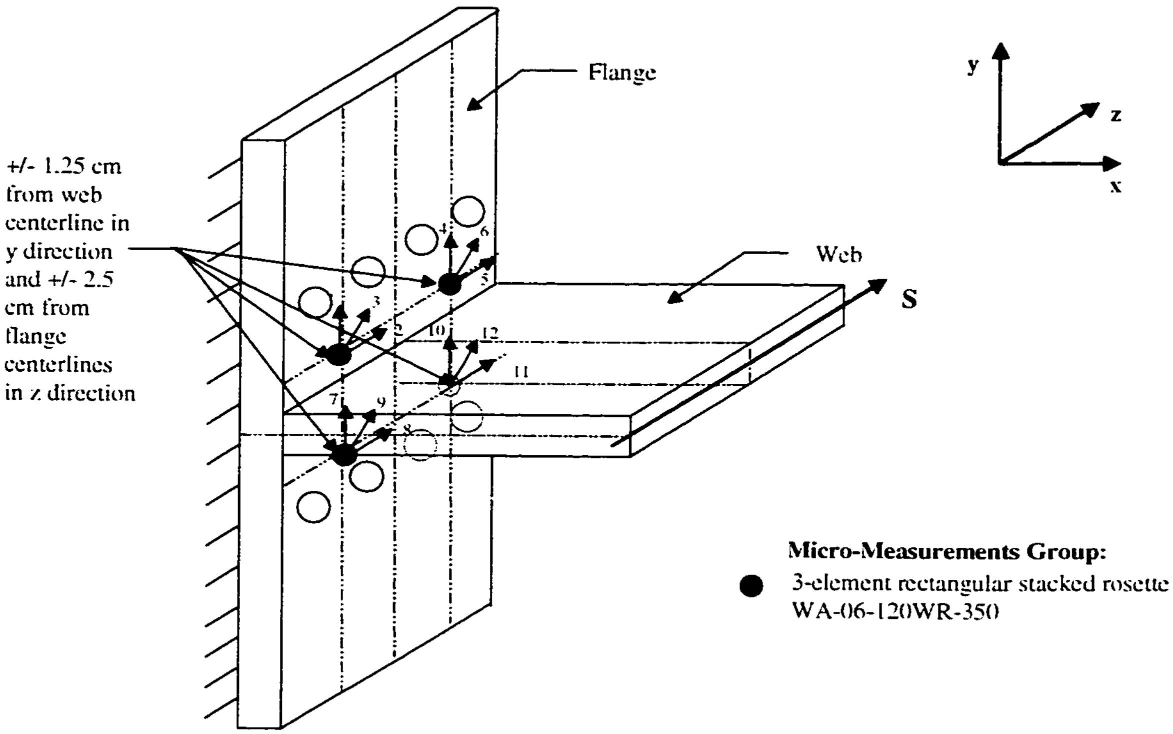

Figure 3.5-4. Rail Shear Specimen Instrumentation Layout Isometric.

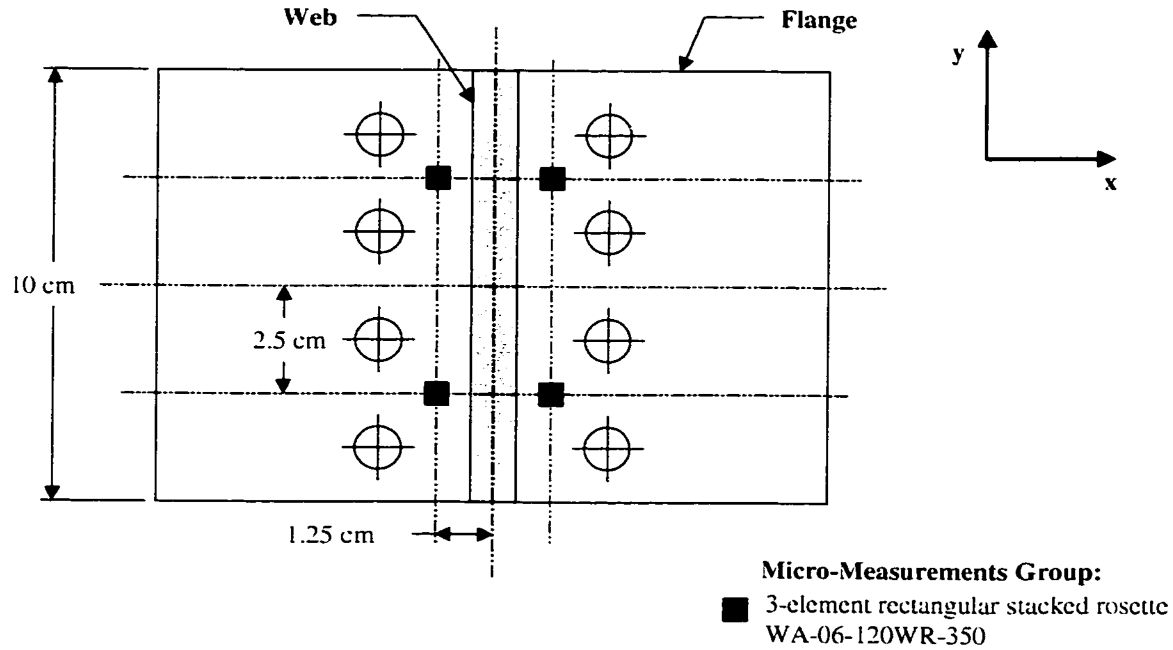

Figure 3.5-5. Rail Shear Specimen Instrumentation Layout Plan View.

Recorded strain measurements are used to characterize T-joint laminate failure. Comparisons are made between experimentally determine allowable strains and T-joint measured strains. Strain measurements are also used in the development of numerical models to predict load-displacement response. Comparisons are made between predicted and actual surface strains under flexure, tension, and rail shear loading.

3.6 Analytical and Numerical Modeling of Stitched T-joints

3.6.1 Strength of Materials

A strength of materials approach, using simple beam theory, is used to calculate deflections and stresses in resin-rich fillet regions of tension, flexure, and rail shear specimen. A sensitivity analysis is conducted to evaluate the effect of resin interface thickness on the T-joint displacement.

3.6.2 Finite Element Analysis

Linear elastic, non-linear elastic, and damage progression finite element analyses are performed using ANSYS version 5.6 software[66] on the geometry of the T-joint in flexure, tension, and rail shear. Table 3.6.2-1 shows a summary of the T-joint numerical models. A two-dimensional analysis is performed on the flexure and tension specimens. For the two-dimensional analysis, a plane strain condition is assumed. Plane strain is assumed because the specimen width is significantly greater than the flange or web thickness. The flexure analysis includes both linear elastic and nonlinear elastic modeling with fixed boundary conditions. The tension analysis is linear elastic with simple support boundary conditions. The rail shear specimens are modeled using three-dimensional finite element analysis. Fixed support boundary conditions are applied to the flange and displacement is applied to the web.

Table 3.6.2-1. T-Joint Numerical Model Attributes.

Attribute	Flexure	Tension	Rail Shear
Model Type	2D Linear Elastic. Nonlinear Elastic. and Damage Progression Plane Strain	2D Linear Elastic and Damage Progression Plane Strain	3D Linear Elastic -
ANSYS Element	LINK1 – 2D Spar PLANE2 – 2D 6-Node Triangular Structural Solid PLANE183 – 2D 8-Node Structural Solid	LINK1 – 2D Spar PLANE2 – 2D 6-Node Triangular Structural Solid PLANE183 – 2D 8-Node Structural Solid	LINK8 – 3D Spar SOLID187 – 3D 10-Node Tetrahedral Structural Solid SOLID185 – 3D 8-Node Structural Solid
Boundary Conditions	Fixed Support Flange	Simple Support Flange	Fixed Support Flange

Figure 3.6.2-1 shows the finite element mesh for a typical flexure T-joint specimen. The resin-rich fillet region 2 is modeled using 6-node triangular elements. The quasi-isotropic two-dimensional woven fiber preform regions 3 and 4 are modeled using 8-node quadrilateral elements. The two fiber insertions in region 1 are modeled using one-dimensional bar elements. A finer mesh is used at the web-to-flange interface and in the fillet areas and a courser mesh was used at the distal ends of the web and flange.

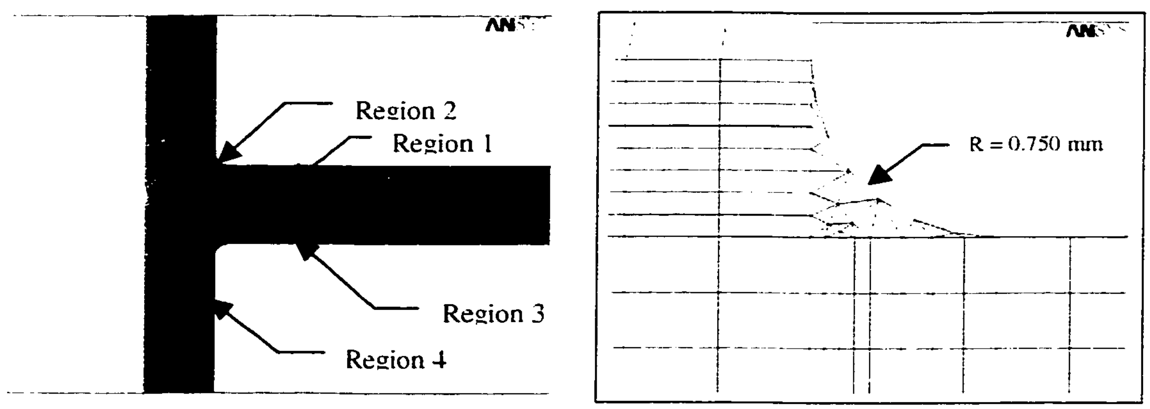

Figure 3.6.2-1. Finite Element Mesh for Stitched T-Joint Flexure Specimen.

3.7 Post Failure Analysis

A detailed post failure analysis was performed on the failed flexure, tension, and rail shear specimens. Macro and microscopic examination of the sectioned T-joints is conducted to delineate the failure modes and damage progression. Optical micrographs were taken using an Olympus BH-2 metallurgical microscope with a magnification of 20x. Digital images were acquired using a Nicon COOLPIX 950 camera. Prior to examination, specimens were potted using Buehler SAMPL-KWICK compound. An Automet 2 polisher and a staged polishing process was used to prepare specimens for optical micrograph. A series of diamond suspension fluids were used with grit sizes of 15, 9, 3, and 0.5 micrometers.

A post failure analysis is conducted to discern modes of failure. An applicable failure criterion is selected for the prediction of T-joint failure. Particular attention is paid to the resin-rich fillet region and interface between the web and flange. The resin-rich region is assumed to be isotropic. Experimental analysis is used to discern failure mechanisms. A summary of failure criteria applicable to composite joints and laminates is given in Appendix B.

CHAPTER 4

T-300/SHELL 862 T-JOINT EVALUATION

Preliminary experimental, numerical, and post failure analysis are conducted on the T-300/Shell 862 T-joints under flexure loading. Section 4.1 provides a T-joint experimental analysis under flexure loading, Section 4.2 includes a T-joint linear elastic finite element analysis under flexure loading, and Section 4.3 provides a post failure analysis of the T-joints.

4.1 T-300/Shell 862 Experimental Analysis Under Flexure Loading

Figure 4.1-1 shows the T-joint configuration used in this investigation. The specimen geometry including web thickness, flange thickness, and fiber insertion location are shown schematically in Figure 4.1-1 (a) and a typical structural T-joint is shown in Figure 4.1-1 (b). The transverse stitches for all specimens entered the web to a depth of 1.27 cm.

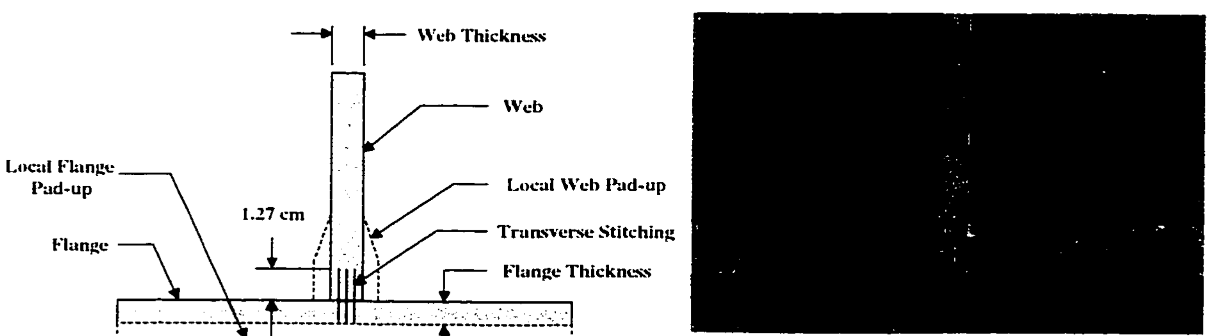

Figure 4.1-1. Flexure Specimen: (a) Showing Local Web and Flange Pad-up and (b) Typical Structural T-Joint.

An experimental matrix was designed to determine the effect of varying key T-joint geometric parameters on the load-carrying capacity of the composite joint and is shown in Table 4.1-1. The geometric parameters that were varied include local web thickness, number of rows of stitching, flange thickness, and specimen width. Four specimens of each condition were loaded to failure and average values were recorded. Specimens 1A and 1B were the baseline (no local pad-ups) from which geometric parameters were varied. Specimens 1A contained two rows of transverse stitching and specimens 1B contained three rows of stitching. Specimens 2A and 2B included the use of a local web pad-up and contained six rows of stitching each. Specimens 3A and 3B contained a flange pad-up. Specimens 3A contained two rows of stitching and specimens 3B contained three rows of stitching.

Table 4.1-1. T-Joint Flexure Test Matrix.

Specimen Configuration	Configuration Description	Number of Specimens	Web Thickness (mm)	Flange Thickness (mm)	Specimen Width (mm)
1A	Baseline	4	4.99	3.81	50.8
2A	Local Web Pad-up	4	9.65	3.81	50.7
3A	Local Flange Pad-up	4	4.63	6.35	50.8
1B	Baseline	4	7.71	3.81	50.8
2B	Local Web Pad-up	4	12.7	3.81	50.7
3B	Local Flange Pad-up	4	7.65	6.35	50.8

Figure 4.1-2 shows the typical load-displacement curve for a T-300/Shell 862 flexure specimen. The initial load-displacement curve is nearly linear until the onset of matrix cracking and fiber insertion debonding. At the point of initial joint failure, a leveling of the load-displacement curve is observed. After the initial failure, the specimens continue to carry load and the behavior is nearly linear with a reduced slope. Just prior to the final failure, load-displacement curves were associated with a slight amount of non-linearity. This observation was believed to be due to geometric non-linearities and/or local yielding of the matrix prior to cracking. Upon further loading, failure progressed from initial matrix cracking to final failure as indicated by the final drop in the load-displacement curve.

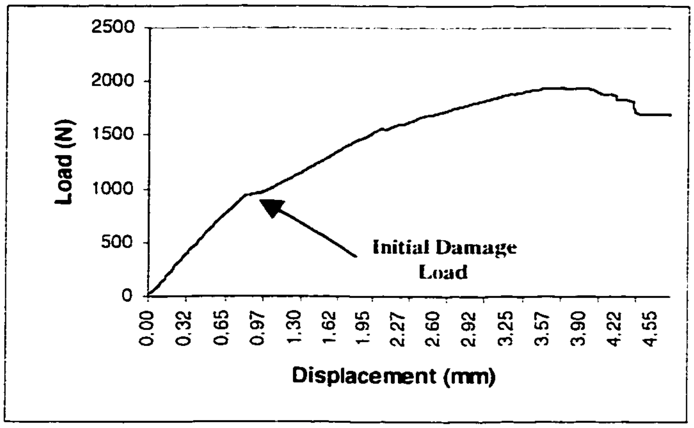

Figure 4.1-2. Typical Load-Displacement for T-300/Shell 862 Flexure Specimen.

The linear portion of the load-displacement curve for each specimen was used to determine the flexural modulus for the T-joint specimens. The flexural modulus, E_b of the specimens was approximated using equation 4-1:

$$E_b = \left(\frac{P}{y}\right)\left(\frac{L^3}{3I}\right) \qquad 4\text{-}1$$

where **P** is the applied load, **y** is the web displacement at the applied load, **L** is the distance from the applied load to the web-to-flange interface, and **I** is the web moment of inertia. Table 4.1-2 summarizes the calculated average values of the proportional limit and flexural modulus for the T-joint specimens. As expected, increasing the T-joint web thickness increases the proportional limit and reduces the flexural modulus. Also, increasing the flange thickness had the effect of increasing the proportional limit and had little effect on the flexural modulus.

Table 4.1-2. Average T-Joint Flexural Proportional Limit and Flexural Modulus.

Specimen ID	Proportional Limit (kN)	Flexural Modulus E_b (GPa)
1A-1	0.66	15.5
2A-1	2.08	5.90
3A-1	1.04	15.9
1B-1	1.23	7.20
2B-1	3.41	4.40
3B-1	2.20	7.20

The flexure experimental results in terms of flexure moment per specimen width are presented in Figure 4.1-3 for the six T-joint configurations. Both initial damage moment and maximum moment are shown. These values are used as the basis of design loads for calculating maximum joint flexure moments. As shown, the baseline specimens (1A and 1B) had an initial damage moment of 392 and 573 N-mm/mm and a maximum moment of 901 and 1616 N-mm/mm respectively. The addition of the local web pad-up (2A and 2B) had the effect of increasing the initial damage moment by 277% and 424% and the maximum moment by 210% and 309% respectively. Improvement in the flexure moment of specimens 2A and 2B over that of the baseline may be attributed in part to the additional rows of stitching and in part to the larger moment of inertia of the local web cross-section. The addition of a local flange pad-up (3A and 3B) had the effect of increasing the initial damage moment by 162% and 289% and the maximum moment by 108% and 221% respectively. In this case, the results are less dramatic. Improvements over the baseline may be attributed to the thicker flange providing additional fiber matrix shear area at the fiber insertions.

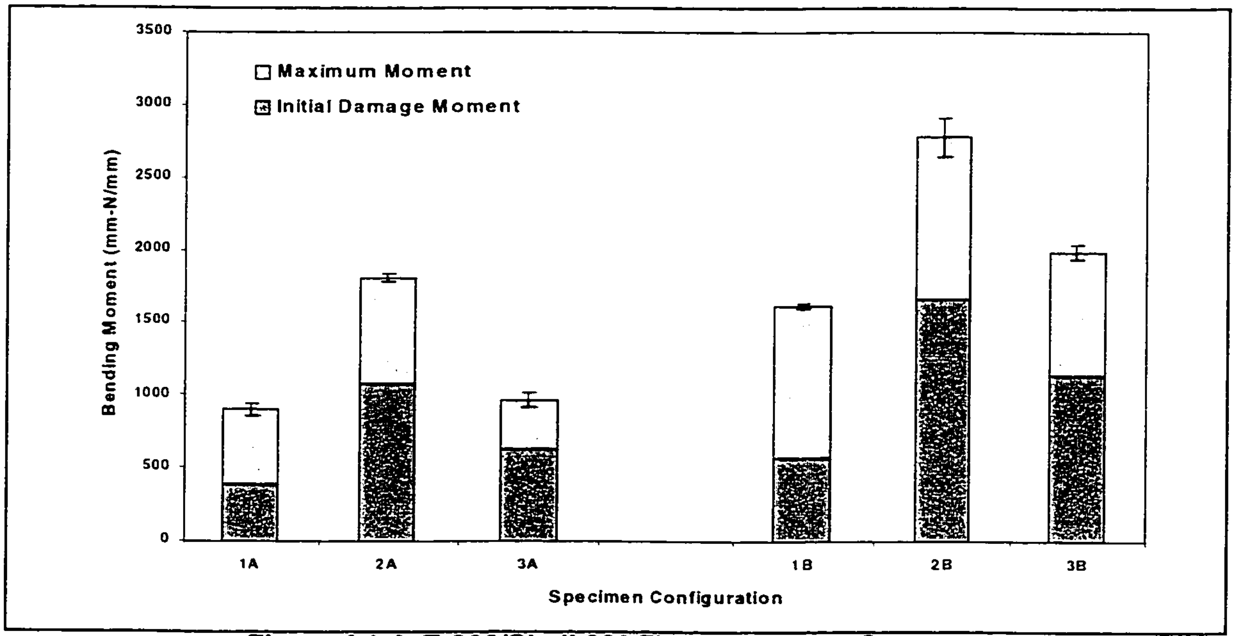

Figure 4.1-3. T-300/Shell 862 Flexure Results Summary.

4.2 T-300/Shell 862 Linear Elastic Flexure Numerical Modeling

A linear finite element analysis was performed using ANSYS version 5.6 software[66] on the geometry of T-joint 1A and 1B. For this analysis, a two-dimensional plane strain condition was assumed. Plane strain was assumed because the specimen width is significantly greater than the flange or web thickness. The flexure finite element model is divided into several regions as same shown previously in Figure 3.6.2-1. For the flexure analysis, the resin-rich fillet region 2 was modeled using 6-node triangular elements. The quasi-isotropic two-dimensional woven fiber preform regions 3 and 4 were modeled using 8-node quadrilateral elements. The two fiber insertions in region 1 were modeled using one-dimensional bar elements. A finer mesh was used at the web-to-flange interface and in the fillet areas and a courser mesh was used at the distal ends of the web and flange. The finite element model used in this analysis contains 3935 8-node quadrilateral elements, 54 6-node triangular elements, and 116 bar elements.

Table 4.2-1 shows the mechanical properties used for the finite element model for the various regions of the mesh. Orthotropic material properties were used for the composite web and flange and isotropic material properties were used for the resin-rich fillet and web-to-flange interface. The tow rows of fiber insertions were modeled using fiber tow properties. A nodal force of 659 N or the average proportional limit for specimens 1A was applied normal to the web 2.54 cm from the web-to-flange interface. Fixed boundary conditions (zero displacement) were assumed at the flange interface to represent the bolted flange-to-fixture attachment constraint.

Table 4.2-1. Material Properties for Finite Element Analysis.

Material	Region*	E_x (GPa)	E_y (GPa)	E_z (GPa)	G_{xy} (GPa)	G_{xz} (GPa)	G_{yz} (GPa)	ν_{xy}	ν_{xz}	ν_{yz}
IM7 6-k Tow	1	275	275	275	106	106	106	0.3	0.3	0.3
862/W Resin	2	2.7	2.7	2.7	0.98	0.98	0.98	0.38	0.38	0.38
T-300/862W	3 & 4	45.9	45.9	5.5	15.4	2.0	2.0	0.22	0.22	0.32

* *FEA regions defined previously in Figure 3.6.2-1.*

A similar modeling approach was used for the finite element analysis of specimens 1B. In this case, the finite element analysis used 2188 8-node quadrilateral elements, 38 6-node triangular elements, and 105 bar elements. The three fiber insertions were modeled using one-dimensional bar elements. A nodal force of 1227 N or the average proportional limit for specimens 1B was applied normal to the web 2.54 cm from the web-to-flange interface.

Detailed results of the finite element analysis at the flange to web interface for specimen configuration 1A is shown in Figure 4.2-1. Local stresses are shown as contour lines with labels indicating the magnitude of the stress in units of MPa. For this analysis, a nodal force of 659 N or the average proportional limit for specimens 1A was applied. The discontinuities in the contour lines may be attributed to the differences in material properties in regions 1 through 4.

The local tensile stress in the web direction, σ_x is shown in Figure 4.2-1 (a). The predicted stress in the matrix is shown to just exceed the Shell 862 matrix allowable tensile strength of 78.6 MPa. The local tensile stress in the flange direction, σ_y is shown in Figure 4.2-1 (b). The local stress just exceeds the tensile strength of the cured matrix. The local shear stress, τ_{xy} is shown in Figure 4.2-1 (c). This value is below the failure strength of the matrix in shear. The equivalent or effective stress, σ_{eff} is shown in Figure 4.2-1 (d). The effective stress also just exceeds the Shell 862 matrix allowable strength at the onset of failure. As indicated by the leveling off of the load-displacement curve, the limiting stresses occur in the resin-rich area in the fillet and under the web-to-flange interface indicating matrix cracking and fiber debonding.

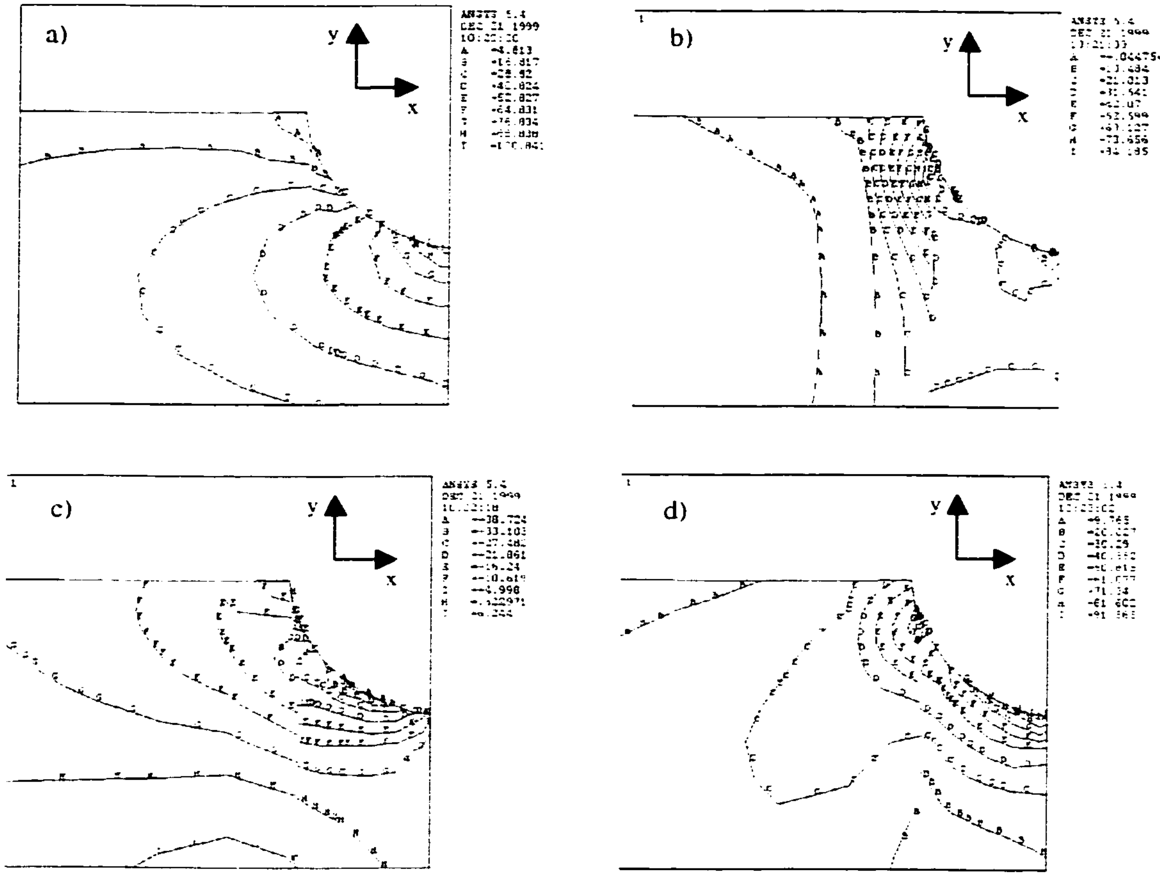

Figure 4.2-1. Finite Element Analysis for Stitched Joint Fillet Flexure Stress (MPa) With an Applied Load of 659 N for Specimens 1A: (a) Normal Stress, σ_x, (b) Normal Stress, σ_y, (c) Shear Stress, τ_{xy}, and (d) Effective Stress, σ_{eff}.

Detailed results of the finite element analysis at the flange to web interface for specimen configuration 1B is shown in Figure 4.2-2. For specimens 1B a nodal force of 1227 N or the average proportional limit was applied normal to the web 2.54 cm from the web-to-flange interface. The local tensile stress in the web direction, σ_x is shown in Figure 4.2-2 (a). Again, the predicted stress in the matrix is shown to just exceed the Shell 862 matrix allowable tensile strength. Similar trends as indicated above are shown for tensile stress in the flange direction Figure 4.2-2 (b), the shear stress Figure 4.2-2 (c) and the effective stress Figure 4.2-2 (d).

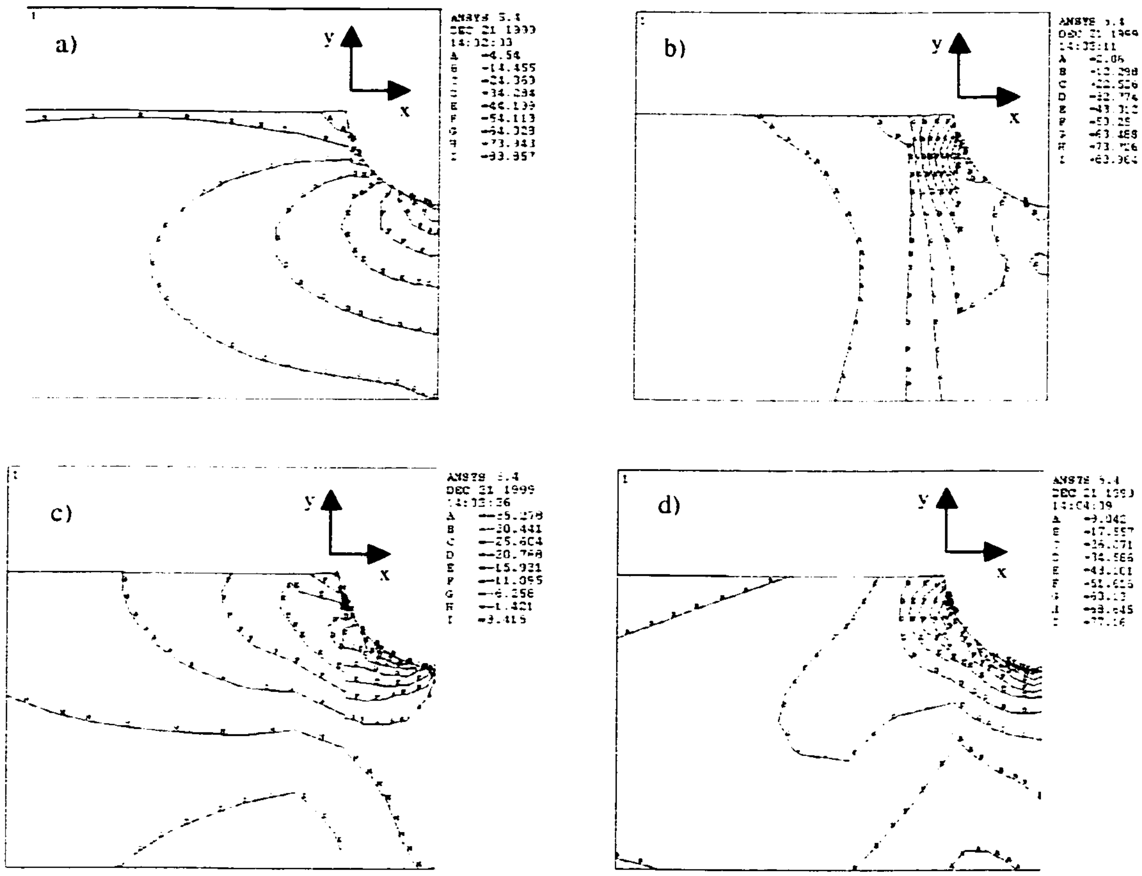

Figure 4.2-2. Finite Element Analysis for Stitched Joint Fillet Flexure Stress (MPa) With an Applied Load of 1227 N for Specimens 1B: (a) Normal Stress. σ_x, (b) Normal Stress, σ_y, (c) Shear Stress, τ_{xy}, and (d) Effective Stress, σ_{eff}.

Predicted and average experimental displacement values for T-joint configurations 1A and 1B are shown in Figure 4.2-3. The finite element analysis results agree well with the average experimental values up to the point of matrix cracking and fiber matrix debonding for specimens 1A. Just prior to the onset of matrix cracking, the experimentally determined displacement is slightly nonlinear indicating a local yielding or cracking of the matrix. Again, this may also be observed in the load-displacement curve. As shown in Figure 4.2-3, the predicted values for specimens 1B are less consistent then that of specimen 1A. The experimental data indicates a more pronounced nonlinearity in the average load-displacement curve. This may in part account for the difference in predicted and experimental results for specimens 1B.

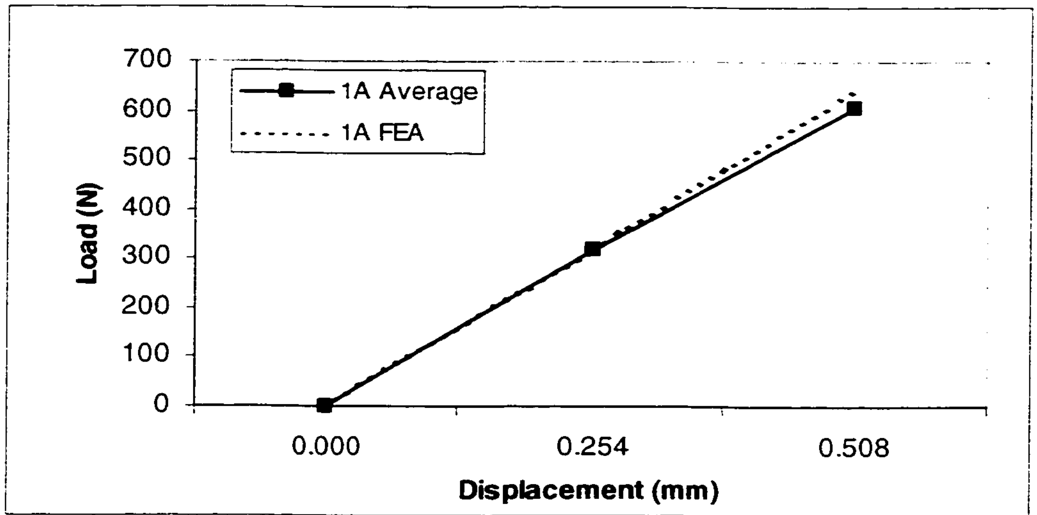

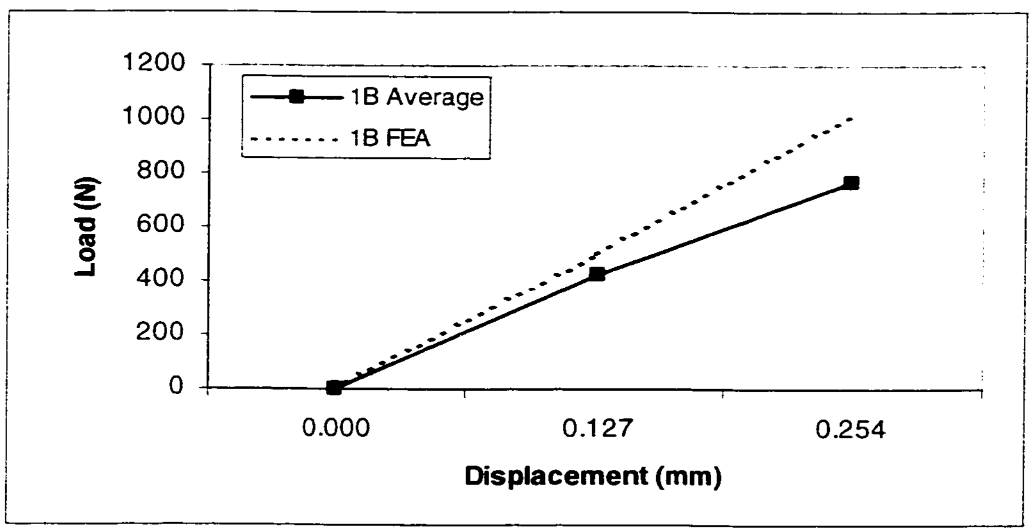

Figure 4.2-3. Displacement Predictions & Experimental Results: Specimens 1A & 1B.

4.3 T-300/Shell 862 T-Joint Flexure Post Failure Analysis

Figure 4.3-1 shows a typical failed T-300/Shell 862 T-joint flexure specimen including a close-up view of the failure region. The rows of transverse stitches are clearly visible. Fiber pullout and fiber breakage can be observed at the web-to-flange interface. Fiber insertion tuffs are visible indicating that the continuous fiber insertion loops broke prior to pull-out.

Figure 4.3-1. Failed Specimen Showing Fiber Pullout and Fiber Breakage.

Figure 4.3-2 shows optical micrographs for typical T-300/Shell 862 flexure specimens at a magnification of 20x. The two micrographs of specimens 1A show cracks at the resin-rich corner fillet of the T-joint, a crack along the web-to-flange interface, and a crack running parallel to the fiber insertions. Similar cracking is shown for specimens 1B, 2A, 2B, 3A and 3B. Other observed mechanisms of failure for the T-joint specimens in flexure include fiber breakage, fiber-matrix debonding, and fiber bridging. Identified mechanisms of failure included crack initiation at the corner of the web-to-flange interface and at the core-to-flange interface. All specimens failed in a similar manner.

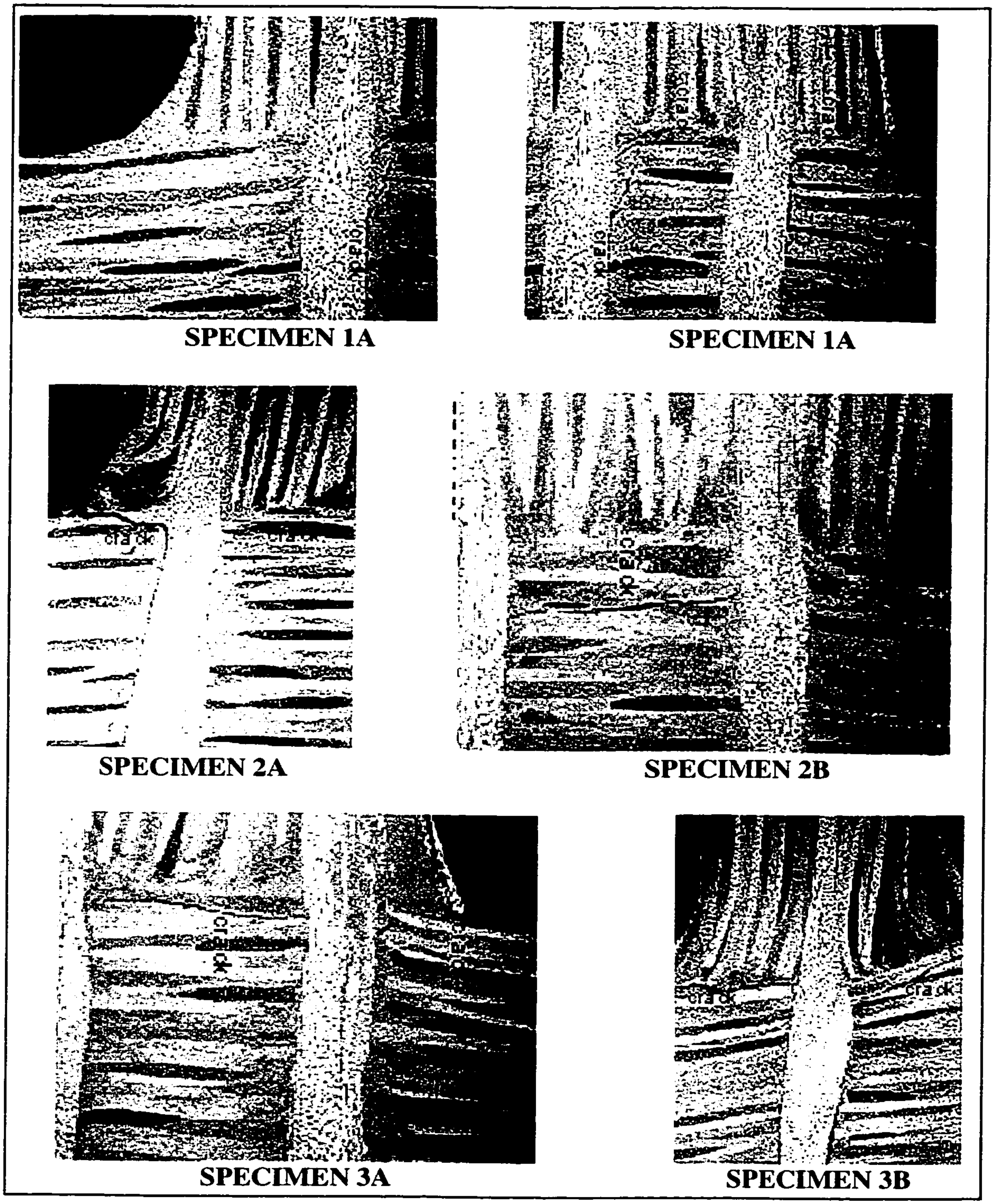

Figure 4.3-2. Optical Micrograph of Failed Specimens.

Based on the optical micrographs of the failed specimens, the damage progression in the transverse stitched T-joints subjected to flexure loads is shown schematically in Figure 4.4-3. As shown, damage progresses in a series of steps coinciding with increased load. As sufficient load is applied to the specimen, the local stress in the matrix exceeds the matrix tensile strength and a crack initiates at the fillet or flange-to-web interface (a). Increased loading beyond this point then causes the crack to propagate to the neighboring fiber insertion (b). The crack is initially arrested at the fiber insertions until the load is increased further, where fiber matrix-debonding and fiber bridging occur due to high shear stresses at the fiber-to-matrix interface (c). Next the crack arrests due to fiber bridging at the fiber insertion. This has the effect of reducing the crack stress intensity. This fiber bridging gives the T-joint an increased damage tolerance or an ability to carry additional load after first failure occurs. Increased loading then causes fiber elongation, followed by fiber breakage and fiber pullout (d). Further loading causes additional matrix cracking and propagation to the next fiber insertion (e). Loading beyond this point leads to catastrophic failure of the T-joint.

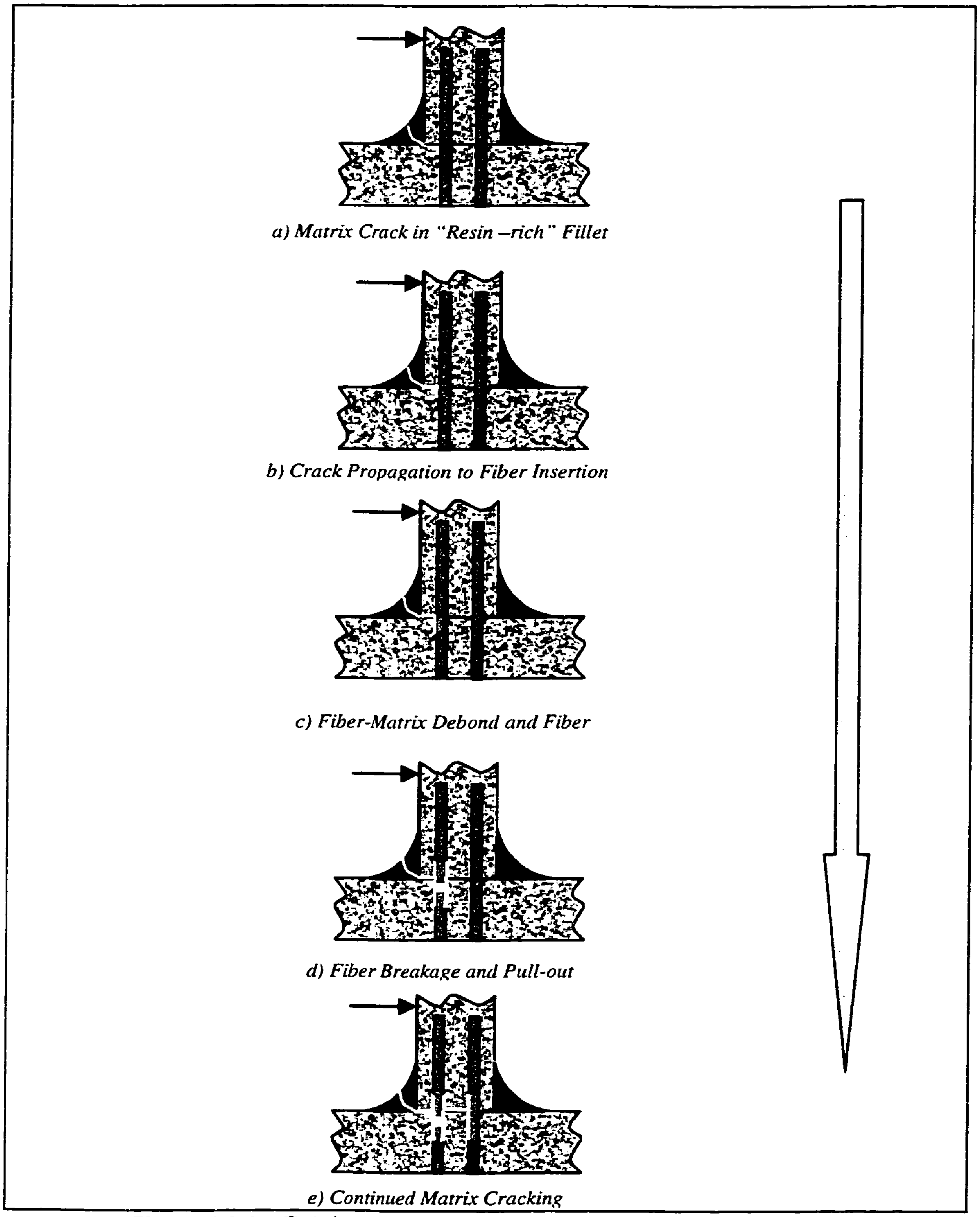

Figure 4.3-3. T-Joint Damage Progression Under Flexure Loading.

CHAPTER 5

T-300/PR520 MATERIAL PROPERTIES

An experimental investigation was undertaken to determine the T-300/PR520 T-joint web and flange laminate physical, elastic, and strength properties.[67] The elastic properties are used as input to the T-joint linear, nonlinear, and progressive damage finite element analyses presented in Chapter 7. The strength properties are used as limiting values in the T-joint laminate failure analysis as presented in Chapter 8.

5.1 Laminate Material and Strength Properties Experimental Matrix

Table 5.1-1 shows the experimental material properties development matrix. A quasi-isotropic layup is used for the experimental panels. Based on this quasi-isotropic layup, it is assumed that the in-plane transverse material and strength properties are equal to the longitudinal properties. In order to limit the number of specimens required, the longitudinal properties are experimentally determined, and the transverse properties are assumed to be equal as indicated in Table 5.1-1.

Table 5.1-1. Laminate Material Properties Development Matrix.

T-300/PR520 Composite Laminate Material Properties Experimental Matrix Quasi-isotropic Layup $[0/45]_{4s}$					
Test Type	**Reference**	**T-300/PR520**	**Temperature**	**Specimen Size (mm)**	**Measured Properties**
Tension	ASTM D3039	6	RTA	19.05 W x 292.1 L x 5.08 T	$E_{xx} = E_{yy}, \nu_{xy}, X_t = Y_t$
Compression	ASTM D3410	6	RTA	12.7 W x 139.7 L x 5.08 T	$X_c = Y_c$
In-Plane Shear	ASTM D4255 Method A	6	RTA	69.85 W x 107.95 L x 5.08 T	G_{xy}, S_{lt}
Out-of-Plane Tension	Draft ASTM	6	RTA	25.4 W x 25.4 L x 5 T, r = 3.175	$E_{zz}, \nu_{zx}, \nu_{zy}$
	Draft ASTM	6	RTA	25.4 diameter, t =19.05	Z_t
V-notch Beam	ASTM D5379	6	RTA	19.05 W x 76.2 L x 7.62 T	$G_{xz} = G_{yz}$
Fiber, Matrix, Void Content	ASTM D3171 Method I A6	3	RTA	25.4 W x 25.4 L x 5.1 T	V_f, V_m, V_v

Table 5.1-2 summarizes the Micro-measurements Group strain gages selected for use in the determination of the elastic material properties.[64] Again, the appropriate strain gages are used as indicated in the appropriate ASTM specification with special consideration of their application to composite materials as outlined by Tuttle and Brinson.[65]

Table 5.1-2. Experimental Strain Gage Selection.

Test Type	Type	Micro-Measurements Gage ID[64]
Tension	Two-element 90° tee rosette	CEA-06-125UT-350
Compression	Uniaxial	EA-06-125AC-350
In-Plane Shear	Two-element 90° tee rosette	CEA-06-125UT-350 (45°)
Out-of-Plane Tension	Two-element 90° tee rosette	CEA-06-125UT-350
v-notch Beam	Iosipescu specialty gage	N2A-00-C032A-500

5.2 Panel Fabrication

The experimental panels were fabricated using plain weave fabric plies consisting of T-300 fibers and PR520 toughened epoxy resin matrix. Table 5.2-1 shows the panel requirements for the material property development program. Based on the specimen sizes, four panels are required. Quasi-isotropic laminates were used with the general stacking sequence $[0°/45°]_{ns}$, where the angles denote the warp direction of individual fabric plies. Two panel thicknesses were used: $[0°/45°]_{6s}$ panel with a nominal thickness of 5.1-mm and a $[0°/45°]_{22s}$ panel with a nominal thickness of 18.6 mm. The 5.1-mm panel corresponds to the web and flange thickness while the 18.6 mm panel is approximately four times the web and flange thickness. The tension, compression, shear, and constituent specimens used the 5.1-mm thick panels 1 through 3 and the out-of-plane tension and v-notch beam or out-of-plane shear specimens used the 18.6-mm thick panels 4 and 5. The panels for the determination of out-of-plane properties are thicker to ensure adequate space for mounting strain gages to the sides of the specimens.

Table 5.2-1. Material Properties Development Panel Requirements.

Panel Requirements		
Test Type	**Panel Dimensions (mm)**	**Panel Requirements**
Tension	305 W x 305 L x 5.1 T	0.75
Compression	305 W x 305 L x 5.1 T	0.75
Shear	305 W x 305 L x 5.1 T	1.25
Out-of-Plane Tension	305 W x 305 L x 19 T	0.5
V-notch Beam	305 W x 305 L x 19 T	0.5
Fiber, Matrix, Void Content	305 W x 305 L x 5.1 T	0.25
Total Panels		**4**

The as fabricated experimental test panels 1 through 3 are shown in Figure 5.2-1 and panels 4 and 5 are shown in Figure 5.2-2, respectively.

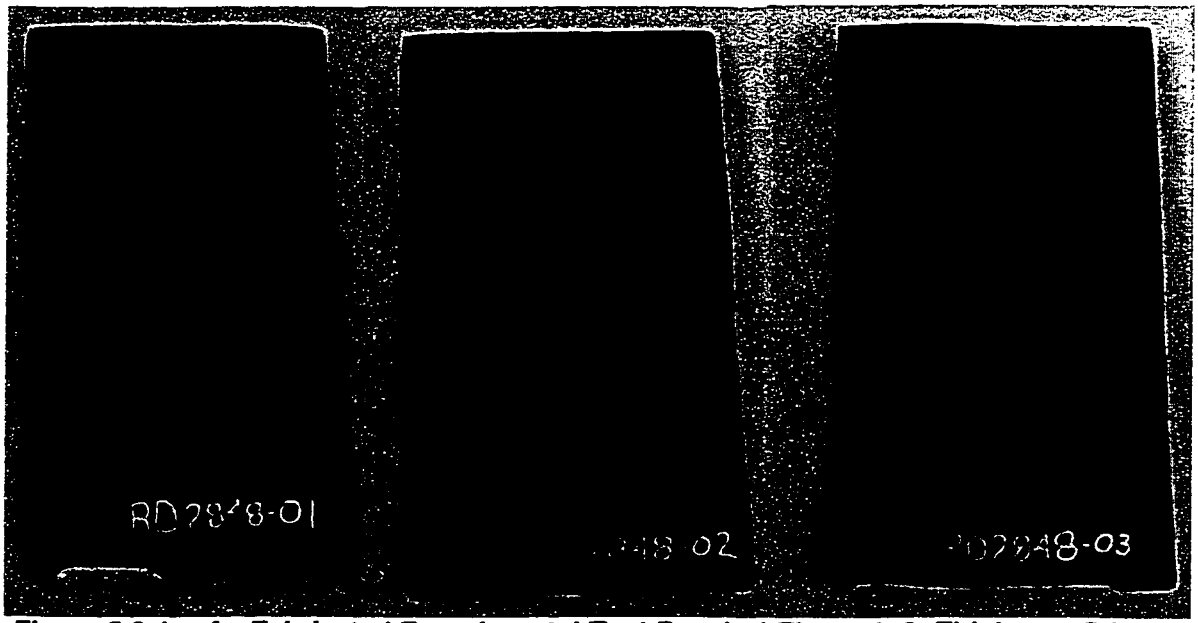

Figure 5.2-1. As Fabricated Experimental Test Panels 1 Through 3: Thickness 5.1 mm.

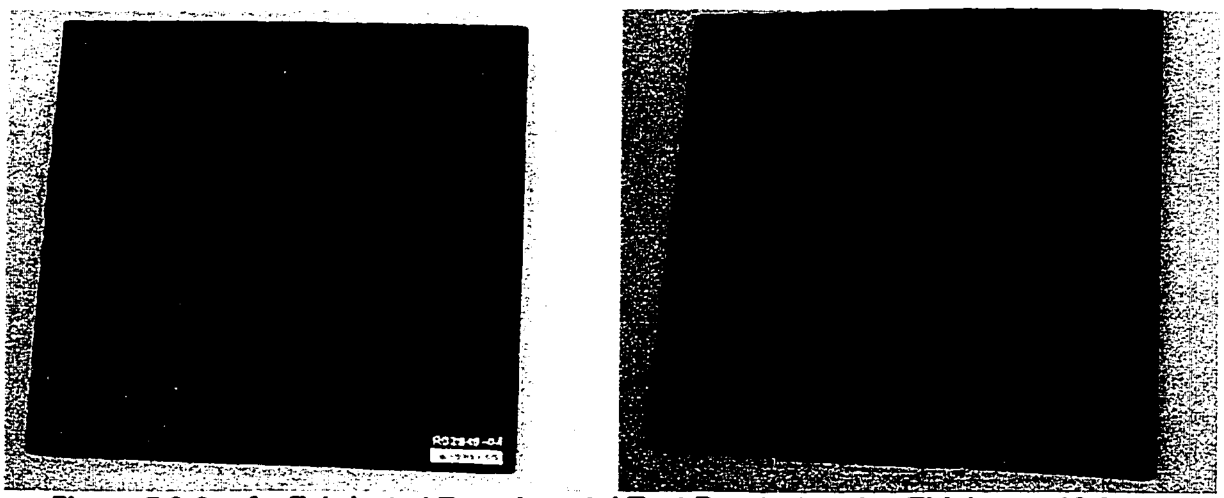

Figure 5.2-2. As Fabricated Experimental Test Panels 4 and 5: Thickness 18.6 mm.

5.3 Nondestructive Evaluation

The T-300/PR520 panels were inspected using an SONDA-007 400 KHz focused airborne UT. at 1 mm indexing. A typical through transmission ultrasound (TTU) device uses elastic waves as a method of detecting flaws in composite laminates. With TTU a transducer is located on one side of the panel and a receiver is located on the other. Water or air is used as the coupling media for the ultrasonic wave. Defects are measured as a local attenuation of the transmitted signal. Defects including porosity. voids. delamination. inclusions. incorrect cure conditions. and poor fiber wetout may be readily detected.[68-69] Ultrasonic readings are compared to a known defect free standard.

The SONDA 007CX AIRSCAN is an air-coupled ultrasonic flaw detector. The ambient air is used as the couplant. The system drives transducers with tonebursts of 50 kHz. 200 kHz. 400 kHz. and 1 MHz.[70] The receiver includes a narrow band low-noise and high-gain preamplifier. The QMI UT was used in conjunction with a cocure robotic scanner. Figure 5.3-1 (a) shows the TTU inspection setup and (b) a typical panel during inspection.

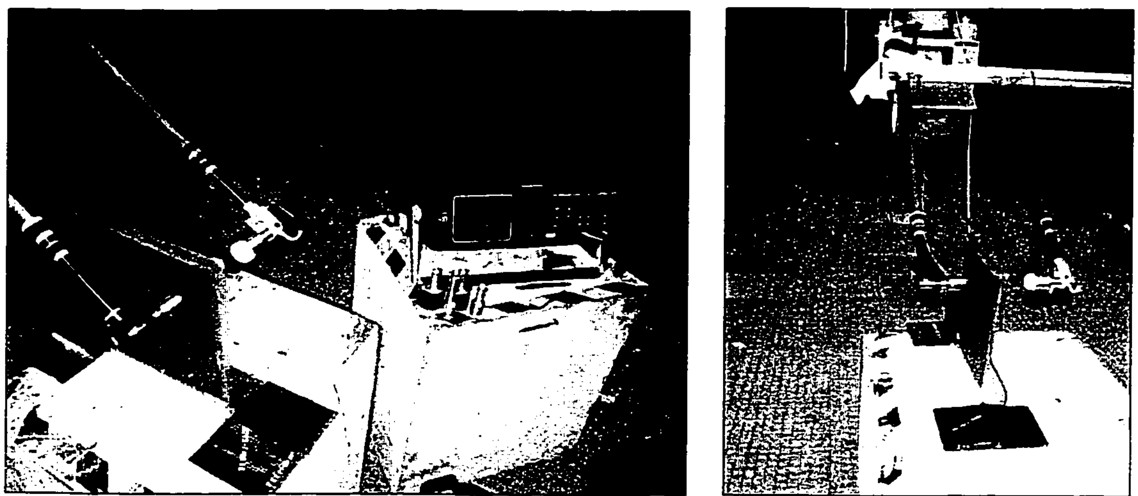

Figure 5.3-1. TTU Inspection Systems Setup: (a) SONDA-007CX AIRSCAN and (b) Typical Panel Inspection.

Figure 5.3-2. shows the C-scan of the 5.1-mm experimental panels 1 through 3 at 400KHz and 1-mm indexing. Panels 1 and 3 were shown to be consolidated and uniform, but panel 2 was uniformly porous. It was noted prior to scanning that surface voids or porosity were visible on panel 2. This panel was not used in the experimental investigation. Figure 5.3-3 shows the C-scan of the 18.6-mm experimental panels 4 and 5 at 400KHz and 1-mm indexing. These samples are shown to be consolidated and uniform. The lines shown on panel 4 of Figure 5.3-3 represent missing data.

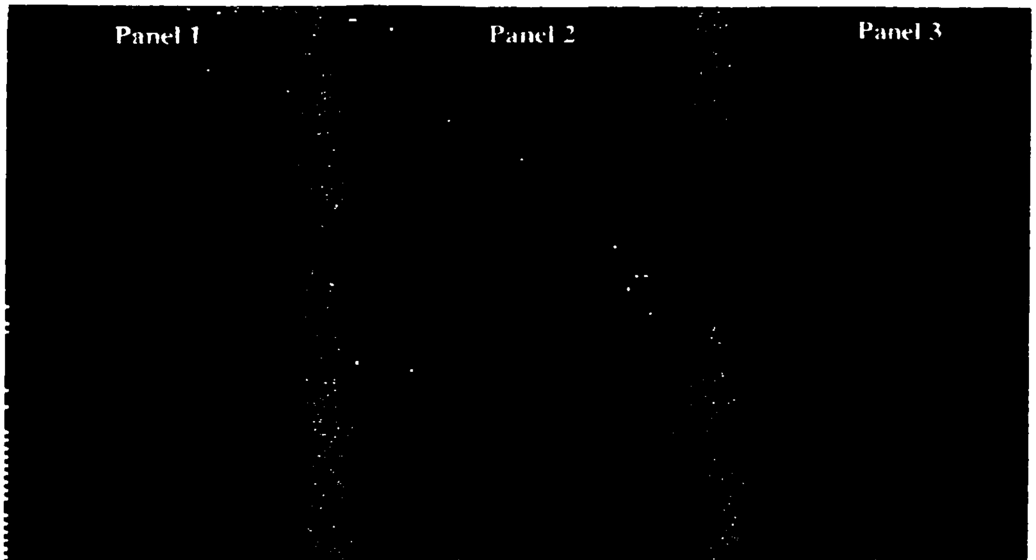

Figure 5.3-2. C-scan of Experimental Panels 1 Through 3: 400 kHz and 1 mm Indexing.

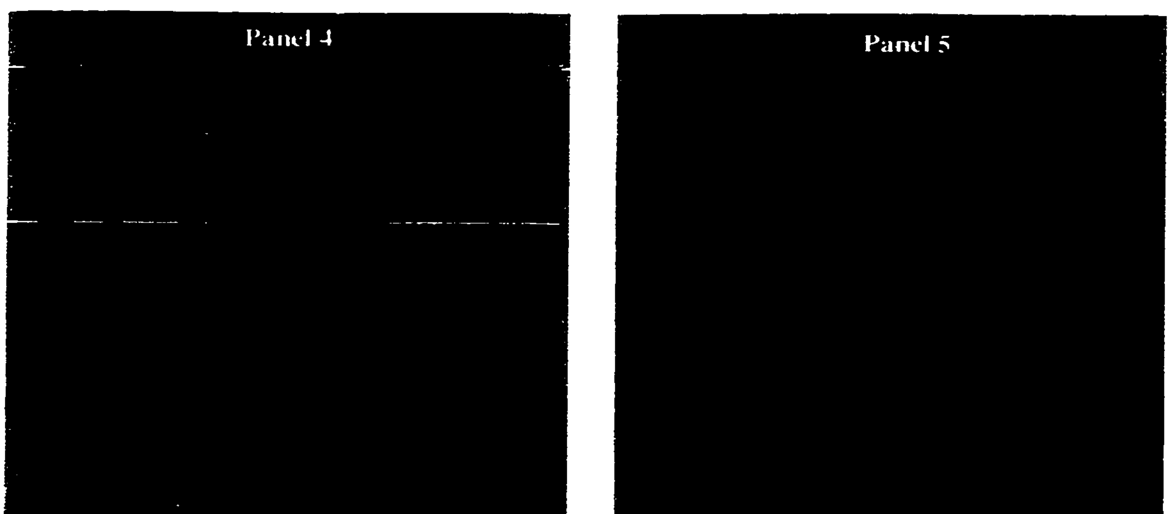

Figure 5.3-3. C-scan of Experimental Panels 4 and 5: 400 kHz and 1 mm Indexing.

Figure 5.3-4 (a) and (b) show the C-scan mean value and standard deviation for the known graphite/epoxy prepreg standard step wedges and the experimental panels. The mean value is represented as an arbitrary range from 0-255. The low end of the range indicates very little energy passing through the panel and hence poor panel consolidation and the high end of the range represents a large amount of energy passing through the panel or excellent panel consolidation. The standard is set at approximately the 80th percentile of the range. The standard deviation is shown as upper and lower limits on the data bars. The mean value and standard deviation are shown to be within acceptable limits for all panels except panel 2 which has a mean value significantly below that of standard 1 and a large standard deviation. Panel 1, 4, and 5 are shown to be better than the standard. Panel 3 is only slightly less than the standard.

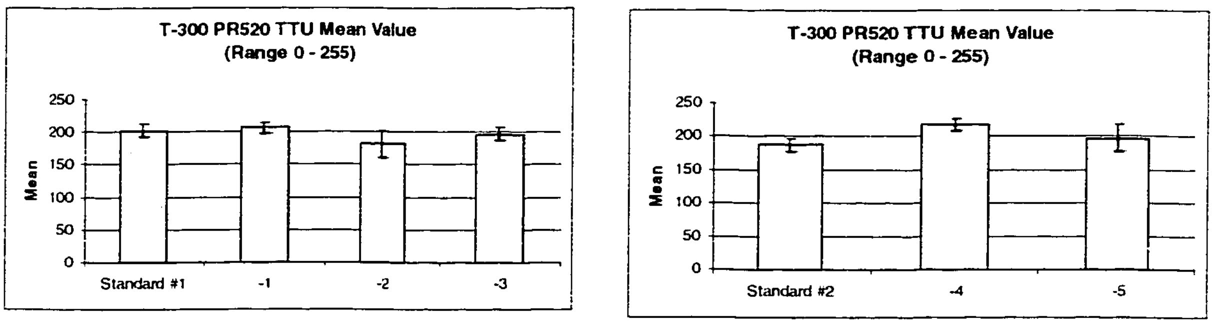

Figure 5.3-4. C-scan Mean Value: (a) Panel 1 Through 3 and (b) Panel 4 and 5.

5.4 Specimen Preparation

A panel cutting diagram is shown in Figure 5.4-1. All specimens were trimmed to their final dimensions using a standard surface grinder equipped with a water cooled, 10-mm thick aluminum oxide abrasive wheel. This provided specimens with a dimensional tolerance of ± 0.125 mm. The load bearing edges of the v-notch beam specimens were ground flat and parallel to within 0.05 mm using a standard surface grinder equipped with a 19-mm wide 60 grit aluminum oxide grinding wheel. The v-notches were machined into the specimen using a specially dressed grinding wheel. The sides of the out-of-plane tension specimens were also ground to these same tight tolerances. The notches in the in-plane shear specimens were fabricated by routing with a high-speed diamond router bit. When specimens were tabbed, G-10 glass/epoxy tabbing material was adhered using Techkits A-12 epoxy adhesive, cured for 1 hour at 65°C. The steel pull-tabs used for the out-of-plane tension specimens were also adhered with the A-12 epoxy. All strain gages were adhered using M-Bond 200 methyl-2-cyanoacrylate.

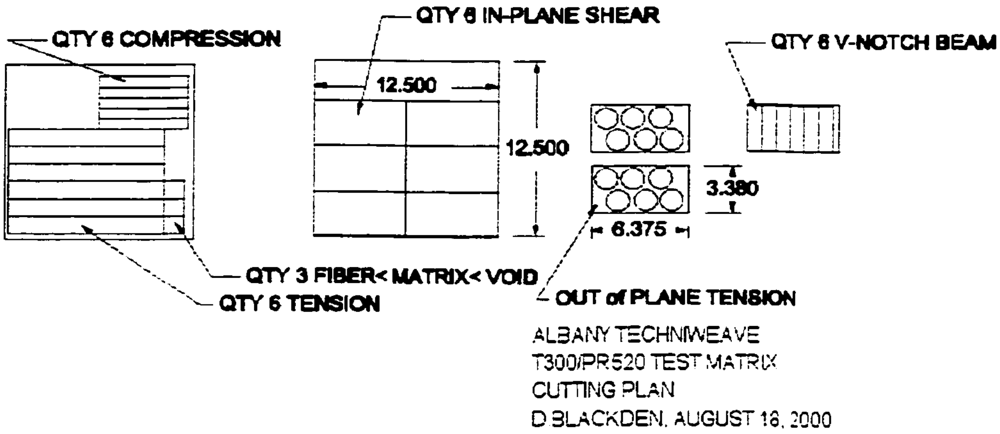

Figure 5.4-1. Panel Cutting Diagram.

5.5 Experimental Results

5.5.1 Laminate Constituent Fiber, Matrix, and Void Volume Fraction

Laminate fiber volume, resin content, and void content were experimentally determined according to ASTM D 3171-99 Method A1 procedure A – matrix digestion using nitric acid.[71] Fiber volume specimens were weighed on a Mettler precision balance to a resolution of 0.0001 grams. Next, the specimens were re-weighed while suspended in water allowing for a direct density measurement. The specimens were then placed in boiling nitric acid for one hour to remove all the organic components. Finally, the acid was drained from the fibers and rinsed clean with distilled water. The fibers were placed in a drying oven over night and a final dry weight was measured. These weights as well as the density of the fiber and the density of the resin were used to calculate the fiber and void volume of the panels. Table 5.5.1-1 shows details of the laminate constituent content and Table 5.5.1-2 shows a summary of the laminate physical properties. Average fiber volume, V_f was determined to be 55.0% and average resin volume, V_m was 45.0%. The average void volume, V_v was determined to be 1.1% however a large coefficient of variation was noted. Additional physical properties data is provided in Appendix D.

Table 5.5.1-1. T-300/PR520 Laminate Constituent Content.

Specimen	Dry Composite Weight (g)	Wet Composite Weight (g)	Fiber Weight (g)	Resin Weight (g)	Composite Density (g/cc)	Fiber Volume V_f (%)	Resin Volume V_m (%)	Void Volume V_v (%)	Resin Content (%)
5A	2.42	0.82	1.56	0.87	1.51	55.3	44.7	1.5	35.7
5B	2.42	0.83	1.54	0.88	1.52	54.8	45.2	1.0	36.4
5C	2.40	0.82	1.52	0.88	1.52	54.8	45.2	0.7	36.5
					Average	**55.0**	**45.0**	**1.1**	**36.2**
					STDEV	**0.3**	**0.3**	**0.4**	**0.4**
					CV(%)	**0.5**	**0.6**	**36.7**	**1.2**

*Composite Density = (Dry Weight/(Dry Weight-Wet Weight))*Water Density*
*Fiber Volume = ((Fiber Weight/Fiber Density)/(Dry Weight/Composite Density))*100%*

Table 5.5.1-2. T-300/PR520 Laminate Constituent Content Summary.

Resin	V_f (%)	V_m (%)	V_v (%)
T-300/PR520	55.0	45.0	1.1

5.5.2 Laminate Tensile Properties

Laminate tensile experiments were performed according to ASTM D 3039, using an Instron Model 1334 universal servo-hydraulic test frame with a 450 kN load capacity.[72] The test frame was equipped with hydraulically actuated grips. A blunt-ended tab configuration was selected. The specimens were cut 25.4 mm wide then routed in a dogbone configuration to a final gage section width of 12.7 mm. The further reduced gage section was required due to the specimen thickness of 5 mm. Specimens were instrumented with Micro-measurements Group two-element 90° tee rosette strain gages CEA-06-125UT-350. Figure 5.5.2-1 shows the compression specimen configuration.

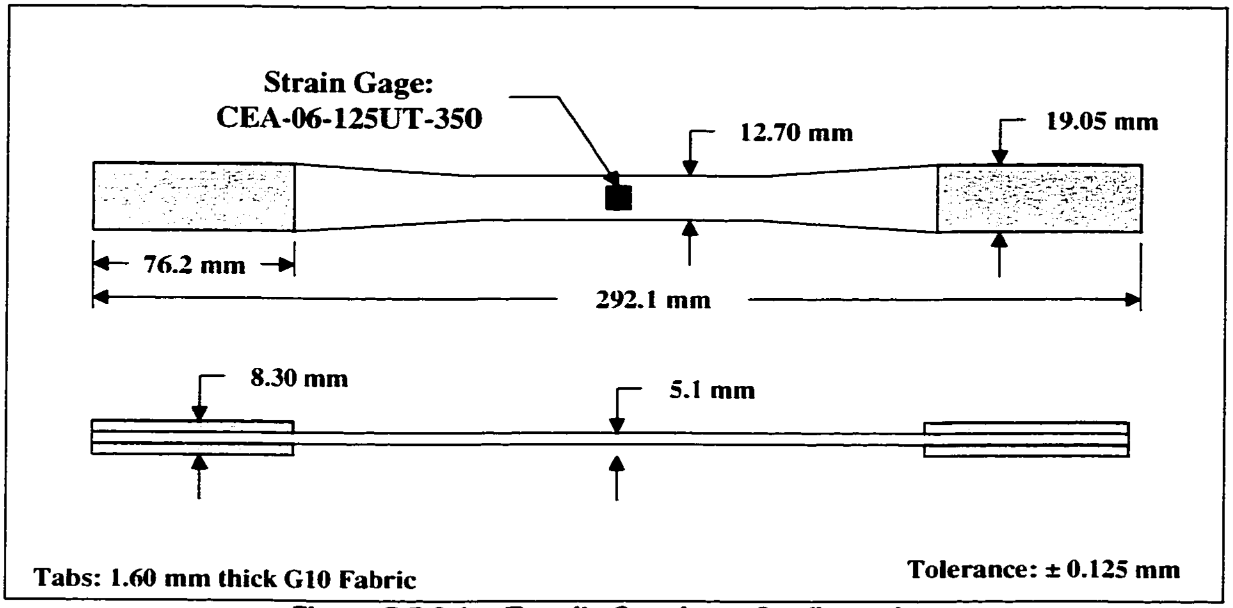

Figure 5.5.2-1. Tensile Specimen Configuration.

The tensile strength F^{tu} was determined using the following expression:

$$F^{tu} = \frac{P^{max}}{A}$$

where **P** is the maximum load prior to failure and **A** is the average cross-sectional area. The tensile modulus of elasticity was determined at 1000 με and 3000 με. The Poisson's ratio was determined using the following expression:

$$v = -\frac{\Delta\varepsilon_t}{\Delta\varepsilon_l}$$

where $\Delta\varepsilon_t$ is the transverse strain and $\Delta\varepsilon_l$ is the longitudinal strain. Figure 5.5.2-2 (a) shows the instrumented tensile specimens and (b) the experimental test setup. The tensile load was applied using a constant displacement rate of 2.5 mm/min. All data was collected digitally and stored as ASCII files.

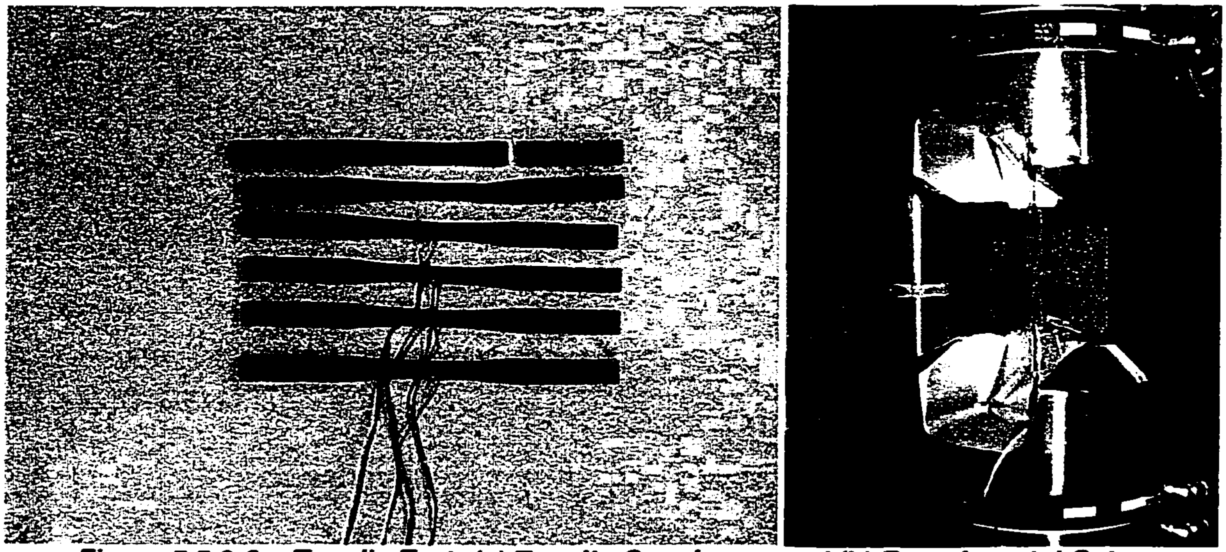

Figure 5.5.2-2. Tensile Test: (a) Tensile Specimens and (b) Experimental Setup.

Figure 5.5.2-3 shows a typical load-displacement plot. Load-displacement is shown to be linear up to ultimate failure. A typical failed specimen is shown in Figure 5.5.2-4. All specimens failed laterally in the middle of the gage section. Individual tensile specimen load-displacement plots are provided in Appendix D.

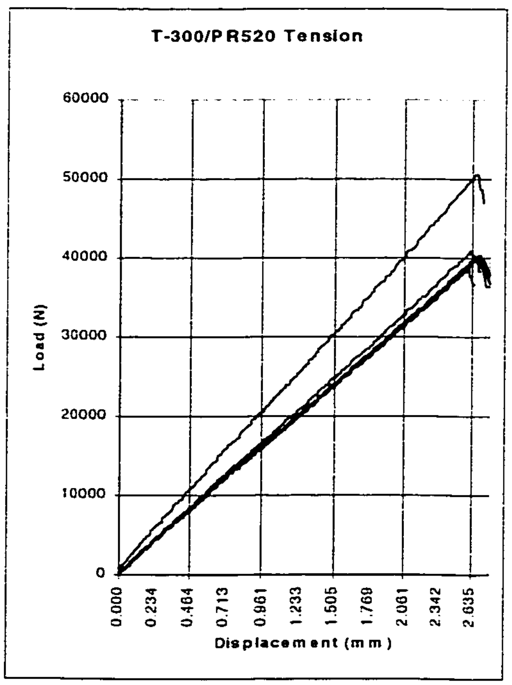

Figure 5.5.2-3. T-300/PR520 Laminate Tensile Load-Displacement Plot.

Figure 5.5.2-4. Typical Failed T-300/PR520 Laminate Tensile Specimen.

Table 5.5.2-1 shows a summary of the laminate properties. The average tensile modulus was determined to be 44.2 GPa. The average tensile strength was 616 MPa and the average in-plane Poisson's ratio was 0.31. The Coefficient of Variation (CoV) was within 5% indicating excellent data consistency.

Table 5.5.2-1. T-300/PR520 Laminate Tensile Properties Summary.

Tensile Test Results ASTM D3039						
SPECIMEN ID RATIO	WIDTH (mm)	THICKNESS (mm)	STRESS (MPa)	MODULUS (GPa)	Strain (micro)	POISSON'S RATIO
T-4	12.7	5.13	612	44.8	13662	0.32
T-5	13.0	5.13	616	44.8	13738	0.30
T-6	12.7	5.05	599	44.8	13369	0.31
T-7	12.8	5.05	621	43.4	14286	0.32
T-8	15.9	5.13	621	43.4	14286	0.30
T-9	12.8	5.03	629	44.1	14266	0.31
		Average	**616**	**44.2**	**13934**	**0.31**
		SD	**10.2**	**0.68**	**397**	**0.01**
		CV(%)*	**1.66**	**1.53**	**2.85**	**2.89**

** CV < 5% indicates excellent data consistancy*

5.5.3 Laminate Compressive Properties

Laminate compression experiments were conducted according to ASTM D3410 using the IITRI fixture.[73] The wedges in the fixture had serrated faces. The specimens were tabbed with 1.6 mm G10 allowing a 12.7 mm gage section. The specimens were instrumented with Micro-measurements Group uniaxial EA-06-125AC-350 strain gages. Figure 5.5.3-1 shows the compression specimen configuration.

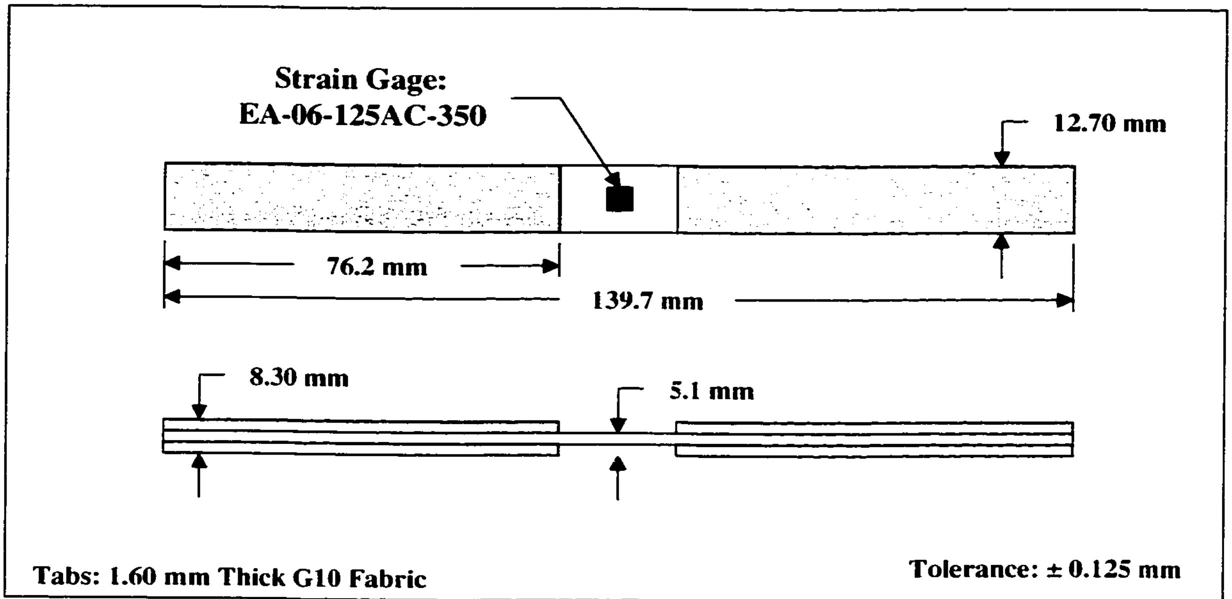

Figure 5.5.3-1. Compression Specimen Configuration.

The tensile strength F^{cu} was determined using the following expression:

$$F^{cu} = \frac{P^{\max}}{A}$$

where **P** is the maximum load prior to failure and **A** is the average cross-sectional area. The compression modulus of elasticity was determined at 1000 $\mu\varepsilon$ and 3000 $\mu\varepsilon$. Experiments were conducted in an Instron Model 1321 universal test frame with a 90 kN load capacity using the IITRI compression test fixture.[74] The compression loads were applied using a constant displacement rate of 1.25 mm/min. Figure 5.5.3-2 (a) shows the test specimens and (b) the experimental setup using the IITRI test fixture.

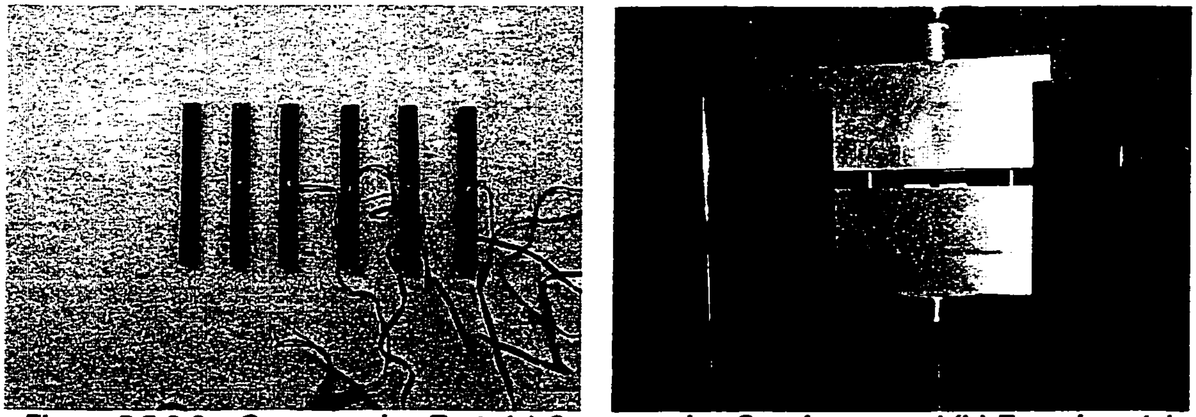

Figure 5.5.3-2. Compression Test: (a) Compression Specimens and (b) Experimental Setup Using IITRI Fixture.[74]

Figure 5.5.3-3 shows the compression specimen load-displacement plot. The load-displacement is nearly linear up to ultimate failure. A typical failed specimen is shown in Figure 5.5.3-4. All specimens failed through the thickness in the gage section with partial brooming. Individual compression specimen load-displacement plots are provided in Appendix D.

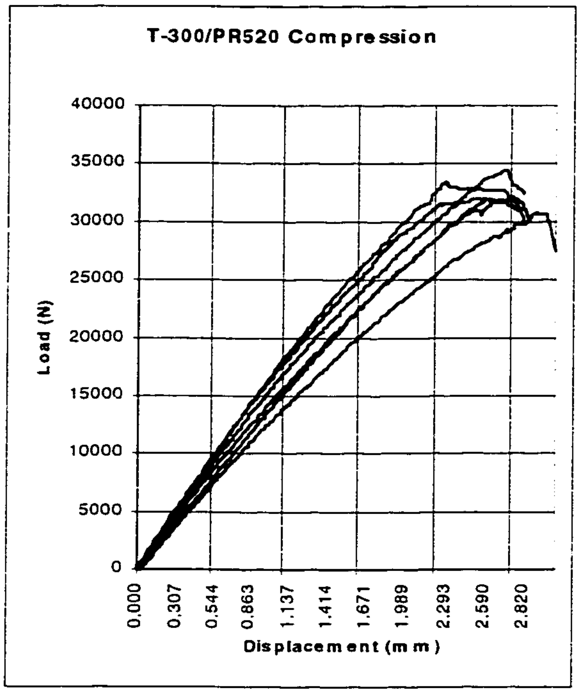

Figure 5.5.3-3. T-300/PR520 Laminate Compression Load-Displacement Plot.

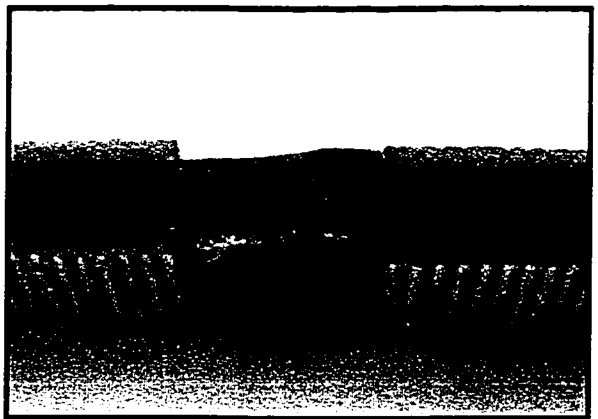

Figure 5.5.3-4. Typical Failed T-300/PR520 Laminate Compression Specimen.

Table 5.5.3-1 shows a summary of the laminate properties. The average compression modulus was determined to be 40.5 GPa with a CoV of 1.20% and the average compression strength was determined to be 504 MPa with a CoV of 3.42%. The percent bending was below the 10% ASTM specification requirement.

Table 5.5.3-1. T-300/PR520 Laminate Compression Properties Summary.

Compression Test Results ASTM D3410 IITRI Test Fixture						
SPECIMEN ID	**WIDTH (mm)**	**THICKNESS (mm)**	**STRESS (MPa)**	**MODULUS* (GPa)**	**Strain (micro)**	**BENDING** (%)**
C-1	12.7	4.98	481	39.9	12055	4.90
C-2	12.7	5.03	501	40.1	12513	6.50
C-3	12.8	5.13	512	41.2	12408	9.00
C-4	12.7	5.05	498	40.4	12321	1.30
C-5	12.7	5.08	533	40.5	13169	0.10
C-6	12.7	5.05	499	40.8	12230	2.60
		AVERAGE	**504**	**40.5**	**12449**	
		STDEV	**17.2**	**0.48**	**386**	
		CV(%)***	**3.42**	**1.20**	**3.10**	

* Average of back-to-back strains.

** Percent bending must be < 10% to be valid

*** *CV < 5% indicates excellent data consistency*

5.5.4 Laminate In-Plane Shear Properties

In-plane shear experiments were performed according to ASTM D 4255, Method A, using a modified two-rail shear fixture.[75] Instead of drilling holes along the edges of the specimen, the specimen was clamped in the fixture using 5 grade 8 bolts each with a torque of 41 N-m.[76] Specimens were cut to a final width of 70 mm wide by 108 mm long. Notches were routed to reduce the cross-section length to a nominal value of 50 mm. Specimens were instrumented with Micro-measurements Group two-element 90° tee rosette strain gages, CEA-06-125UT-350, oriented at 45°. Figure 5.5.4-1 shows the in-plane shear specimen configuration.

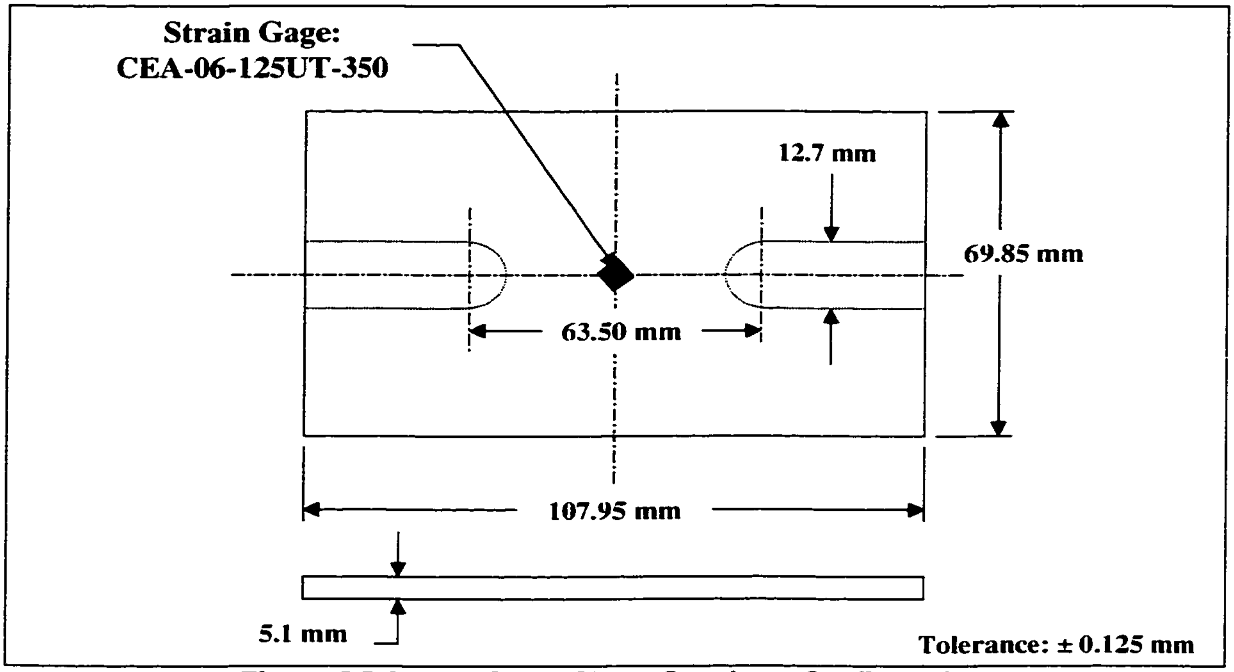

Figure 5.5.4-1. In-Plane Shear Specimen Configuration.

The in-plane shear strength **S** was determined using the following expression:

$$S = \frac{P^{\max}}{bh}$$

where **P** is the maximum load prior to failure, **b** is the total gage length, and **h** is the specimen thickness. The shear modulus of elasticity **G** was determined at 1000 με and 3000 με using the following expression:

$$G = -\left(\frac{\Delta P}{\Delta e}\right) / 2bh$$

where **ΔP/Δe** is the slope of the load-displacement plot in the linear region, **b** is the total gage length, and **h** is the specimen thickness. Experiments were performed in a Model 1321 test frame at a constant displacement rate of 1.25 mm/min. Figure 5.5.4-2 shows the shear specimens set and Figure 5.5.4-3 shows the experimental test setup. Visible are the two rails of the shear fixture.

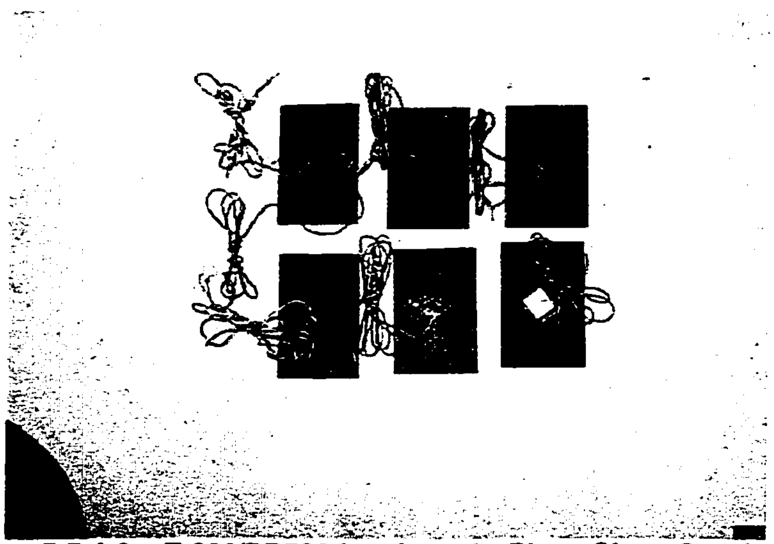

Figure 5.5.4-2. T-300/PR520 Laminate In-Plane Shear Specimens.

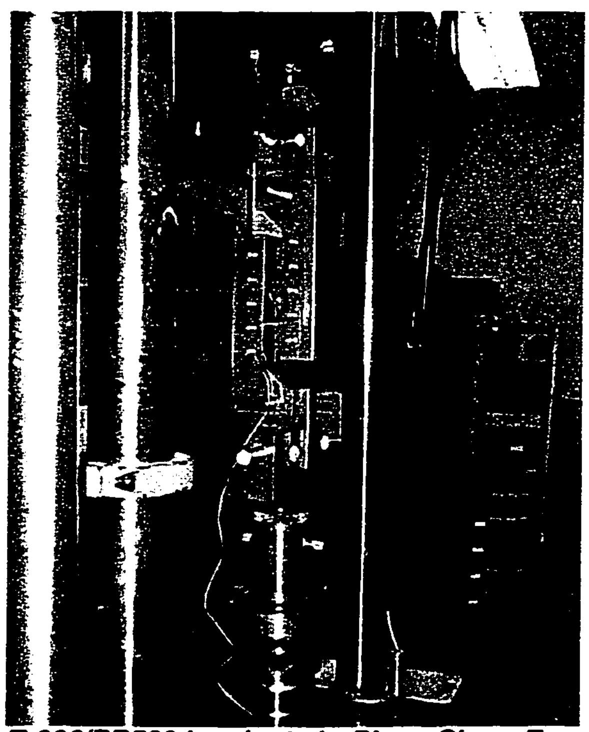

Figure 5.5.4-3. T-300/PR520 Laminate In-Plane Shear Experimental Setup.

Figure 5.5.4-4 shows the in-plane shear load-displacement plot. Again, the load-displacement plot is linear up to ultimate failure. A typical failed specimen is shown in Figure 5.5.4-5. All specimens failed in a nearly circular pattern. This failure mode is unusual and warrants further investigation under a future study. Individual in-plane shear specimen load-displacement plots are provided in Appendix D.

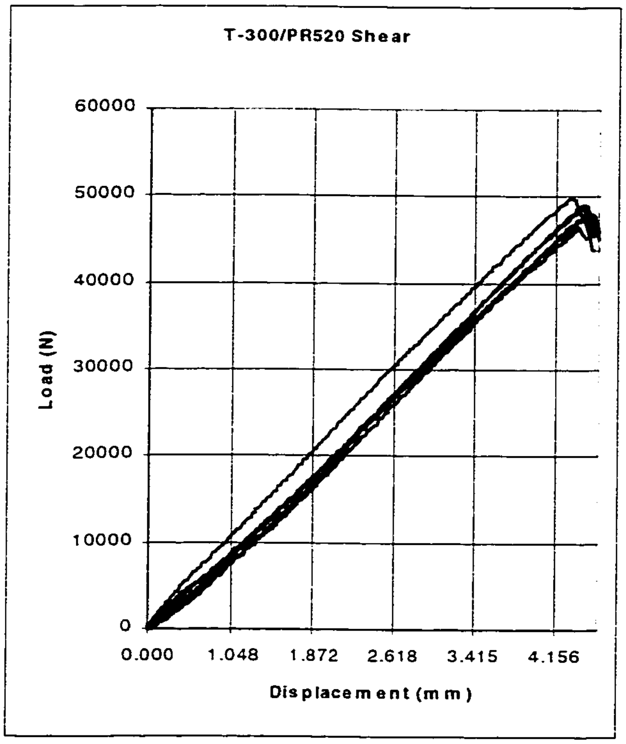

Figure 5.5.4-4. T-300/PR520 Laminate In-Plane Shear Load-Displacement Plot.

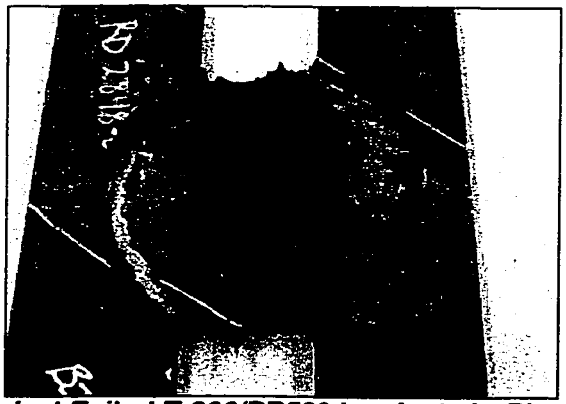

Figure 5.5.4-5. Typical Failed T-300/PR520 Laminate In-Plane Shear Specimen.

Table 5.5.4-1 shows the laminate shear modulus and strength data. The average shear modulus was determined to be 16.5 GPa and the average shear strength was 196 MPa. The coefficient of variation was high for the modules data indicating relatively high data scatter.

Table 5.5.4-1. Laminate In-Plane Shear Properties Summary.

In-Plane Shear Test Results ASTM D4255 Method A					
Specimen ID	**Width (mm)**	**Thickness (mm)**	**Stress (MPa)**	**Modulus (GPa)**	**Strain (micro)**
BIP-1	48.4	5.00	205	20.8	9868
BIP-2	48.1	5.13	197	13.1	15053
BIP-3	48.3	5.13	198	13.7	14495
BIP-4	48.3	5.11	194	15.8	12288
BIP-5	48.2	5.08	194	17.5	11102
BIP-6	48.6	5.13	186	18.3	10189
		Average	**196**	**16.5**	**12166**
		STDEV	**6.27**	**2.93**	**2195**
		CV(%)	**3.20**	**17.7**	**18.0**

** CV < 5% indicates excellent data concistancy*

5.5.5 Laminate Out-of-Plane Tensile Properties

Out-of-plane tension experiments were performed according to a draft ASTM standard.[77] Specimens were prepared in two ways. The specimens used for the strength experiments were first cut then ground into 25.4 mm square cubes that were adhered to 31.75 mm diameter steel cylinders using A-12 adhesive. These specimens were then put on a lathe and had the mid-section reduced to a final diameter of 12.7 mm using a 2.5 mm radius, water-cooled tool post grinder. The specimens used for modulus determination were prepared in the same manner as the strength specimens except the mid-section was not reduced. Instead, the corners of the cube were radiused to match the steel cylinder diameter. These specimens were instrumented with Micro-measurements Group two-element 90° tee rosette strain gages, CEA-06-125UT-350. Figure 5.5.5-1 shows the out-of-plane tension specimens for the modulus and strength determination.

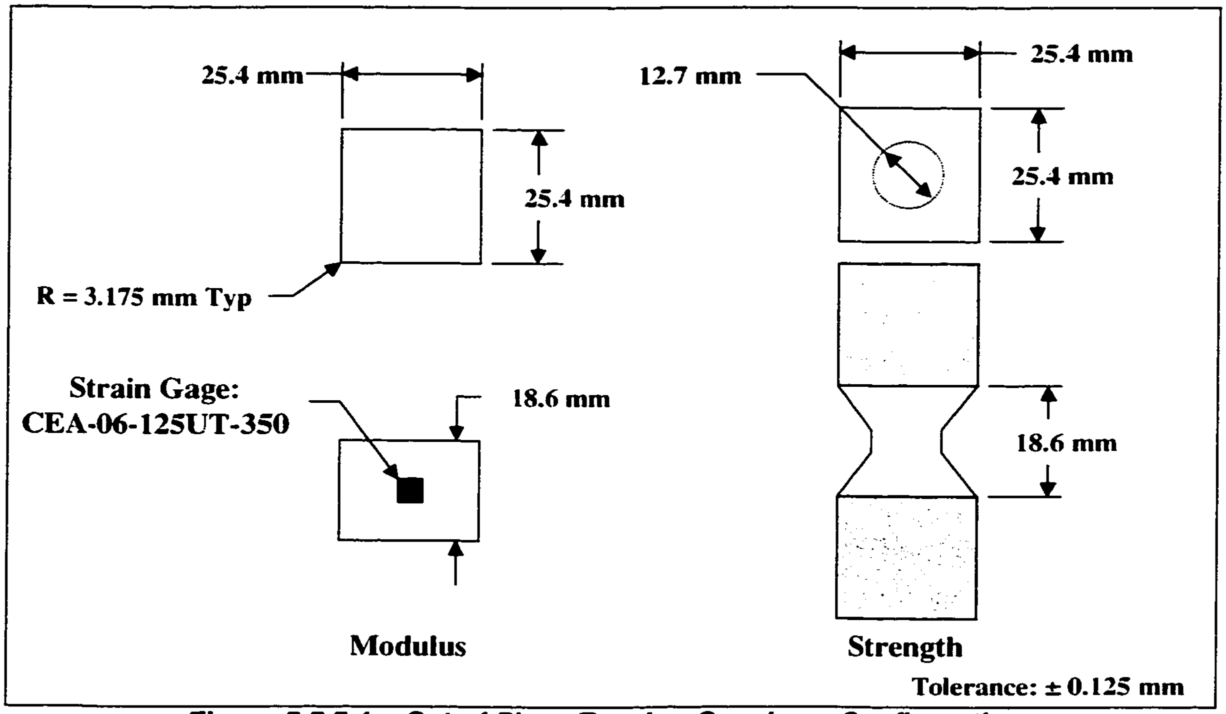

Figure 5.5.5-1. Out-of-Plane Tension Specimen Configuration.

The out-of-plane tensile strength F^{tu} was determined using the following expression:

$$F^{tu} = \frac{P^{max}}{A}$$

where **P** is the maximum load prior to failure and **A** is the average cross-sectional area. The tensile modulus of elasticity was determined at 1000 με and 3000 με. The Poisson's ratio was determined using the following expression:

$$\nu = -\frac{\Delta\varepsilon_t}{\Delta\varepsilon_l}$$

where $\Delta\varepsilon_t$ is the transverse strain and $\Delta\varepsilon_l$ is the longitudinal strain. The modulus specimens were not tested to failure. All specimens were attached to the test frame via a rod that was screwed onto the ends of the steel cylinders, then clamped in wedge grips. Experiments were conducted on a MTS 20 kN capacity servo-hydraulic universal test frame at a rate of 1.25 mm/min for the strain measurements and at 2 mm/min for the strength tests. Figures 5.5.5-2 and 5.5.5-3 show the out-of-plane tension specimens and experimental test setup.

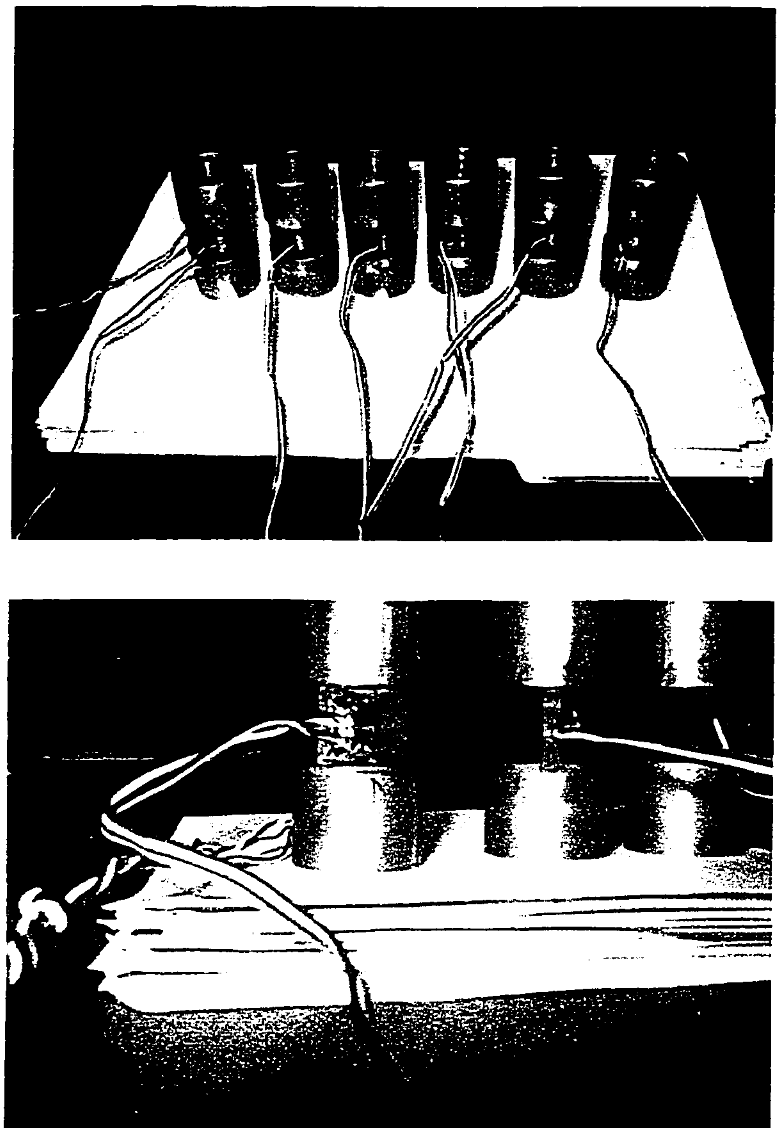

Figure 5.5.5-2. Out-of-Plane Tension Test: (a) Specimens and (b) Strain Gage Instrumentation.

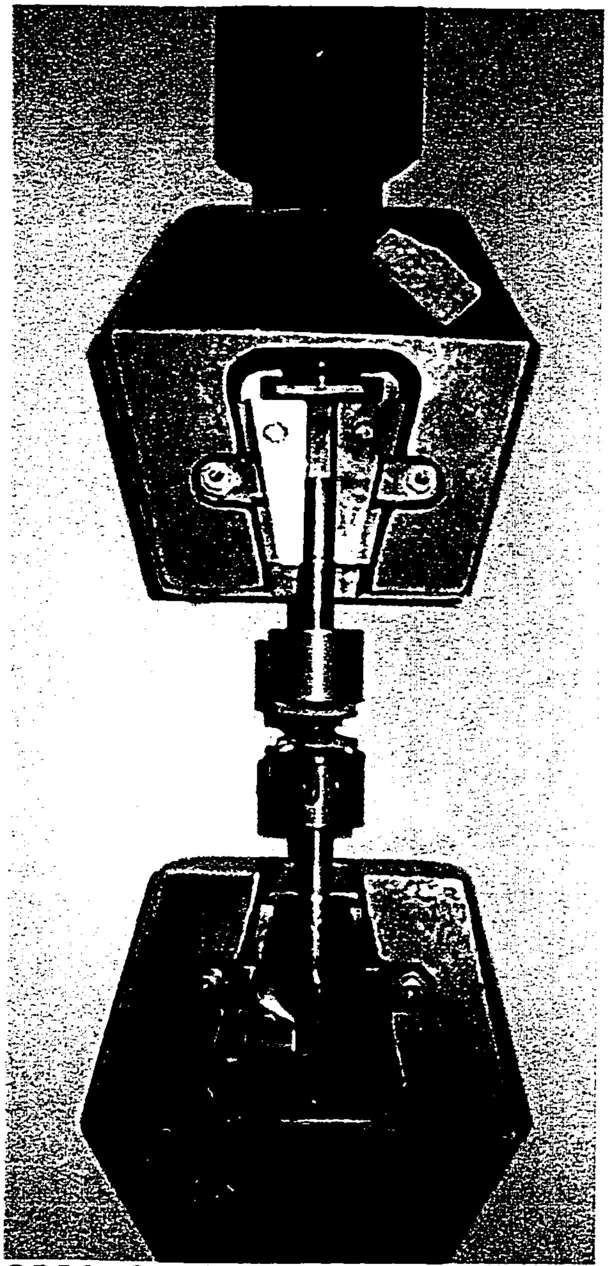

Figure 5.5.5-3. Out-of-Plane Tension Experimental Setup.

Figure 5.5.5-4 shows the out-of-plane load-displacement plot. The load-displacement is shown to be linear up to ultimate failure. A typical failed specimen is shown in Figure 5.5.5-5. Specimens failed in interlaminar tension in the reduced gage section. Individual out-of-plane tension specimen load-displacement plots are provided in Appendix D.

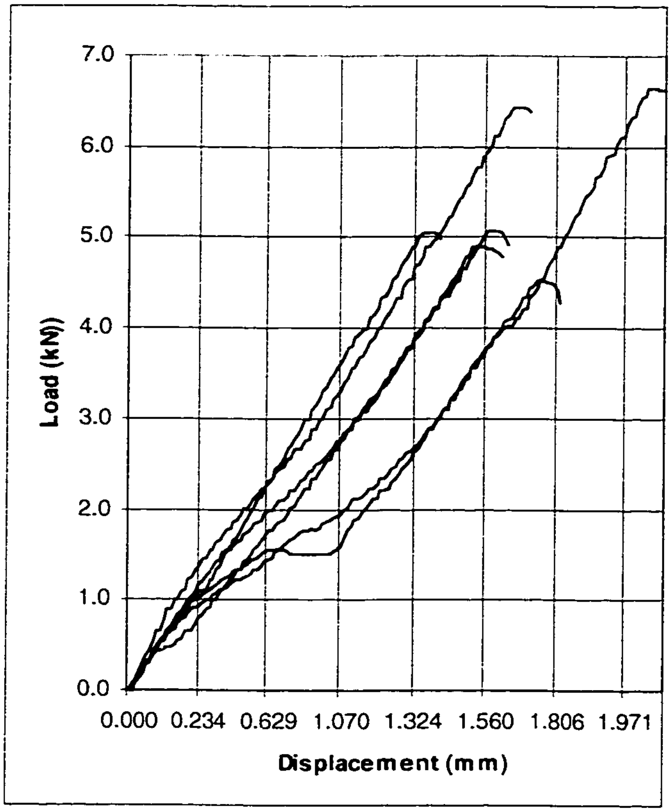

Figure 5.5.5-4. T-300/PR520 Laminate Out-of-Plane Tension Load-Displacement Plot.

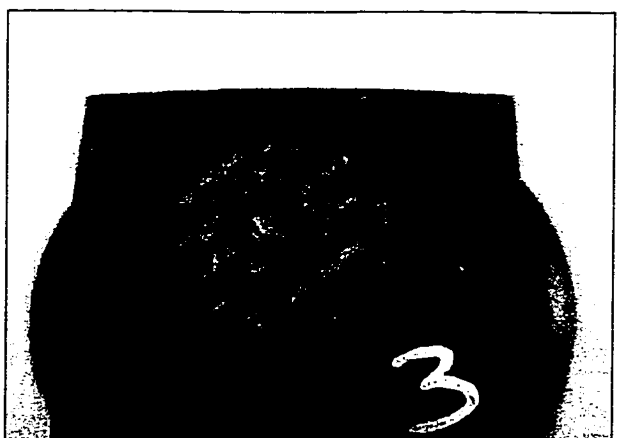

Figure 5.5.5-5. Typical Failed T-300/PR520 Laminate Out-of-Plane Tension Specimen.

Table 5.5.5-1 shows the laminate out-of-plane tension modulus and strength data. The average out-of-plane tension modulus was determined to be 9.73 GPa and the average out-of-plane tensile strength was 46.3 MPa. The average Poisson's ratio was determined to be 0.082.

Table 5.5.5-1. T-300/PR520 Out-of-Plane Tension Properties Summary.

Out-of-Plane Tensile Test Results
Draft ASTM Working Document

Specimen ID	Width (mm)	Thickness (mm)	Modulus (GPa)	Poisson's Ratio
OPT-1	25.3	25.6	9.00	0.08
OPT-2	25.3	25.3	7.79	0.07
OPT-3	25.3	25.4	8.76	0.07
OPT-4	25.4	25.3	8.89	0.08
OPT-5	25.4	25.4	11.72	0.08
OPT-6	25.5	25.5	12.20	0.11
		Average	**9.73**	**0.08**
		STDEV	**1.79**	**0.01**
		COV(%)	**18.4**	**18.0**

** CV < 5% indicates excellent data consistancy*

Specimen ID Strength	Diameter (mm)	Load (N)	Stress (MPa)	Strain (micro)
OPT-1	12.9	5204	39.9	4429
OPT-2	12.8	6566	52.1	6686
OPT-3	12.8	6272	48.9	5580
OPT-4	12.8	6552	51.3	5768
OPT-5	11.4	4755	46.6	3979
OPT-6	12.8	5013	39.2	3214
	Average	**5727**	**46.3**	**4943**
	STDEV	**826**	**5.60**	**1289**
	COV(%)	**14.4**	**12.1**	**26.1**

** CV < 5% indicates excellent data consistancy*

5.5.6 Laminate Out-of-Plane Shear Properties by Iosipescu (V-notched Beam) Shear

Laminate out-of-plane shear experiments were conducted according to ASTM D5379.[78] Specimens were instrumented with Micro-measurements Group N2A-00-CO32A-500 Iosipescu specialty gages. Experiments were performed using an MTS 20 kN capacity universal test frame at a rate of 1.25 mm/min. Figure 5.5.6-1 shows the out-of-plane shear specimen configuration.

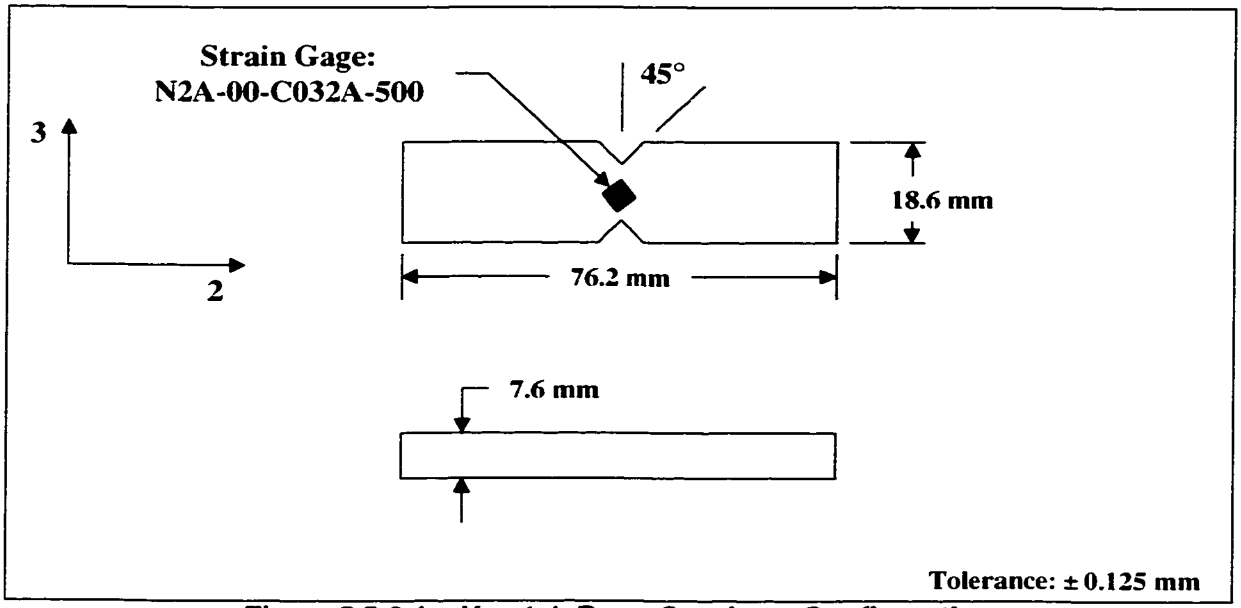

Figure 5.5.6-1. V-notch Beam Specimen Configuration.

The out-of-plane shear strength F_u was determined using the following expression:

$$F_u = \frac{P^u}{A}$$

where **P** is the ultimate load prior to failure and **A** is the average cross-sectional area. The out-of-plane shear modulus of elasticity is determined at 1000 με and 3000 με. Figure 5.5.6-3 (a) shows the out-of-plane shear specimens and (b) the experimental test setup using the Iosipescu shear fixture.[79] A 90° notch angle was used. This test method was originally developed for isotropic materials by N. Iosipescu[80] and was subsequently adapted for use with composites by Adams and Walrath.[81] The advantage of this test method is that a large area of uniform shear is developed in the gage area.

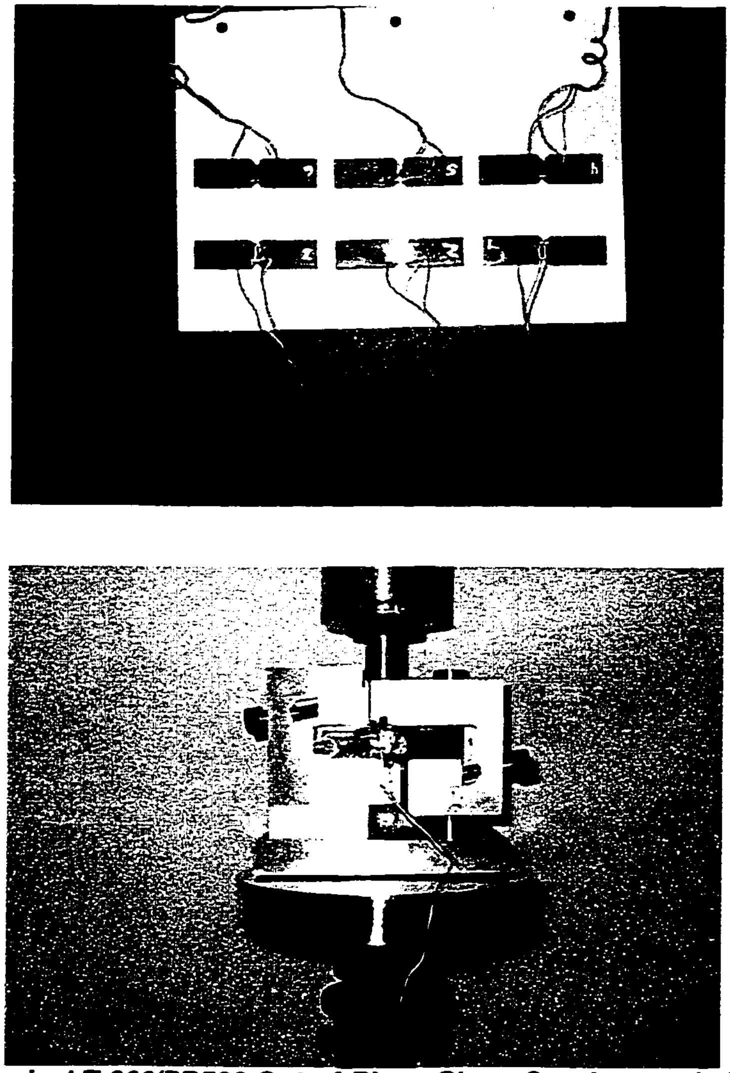

Figure 5.5.6-2. Typical T-300/PR520 Out-of-Plane Shear Specimens via V-notch Beam: (a) Specimens and (b) Iosipescu Shear Fixture. [74]

Figure 5.5.6-3 shows the out-of-plane shear load-displacement plot. The load-displacement plot is nonlinear up to initial failure. The first drop in the load-displacement plot is indicative of a notch root crack development. Ultimate failure occurs with additional load. A typical failed specimen is shown in Figure 5.5.6-4. A crack may be observed extending transverse to the notch originating at the upper notch tip. This failure was consistently observed in all specimens. Individual out-of-plane shear specimen load-displacement plots are provided in Appendix D.

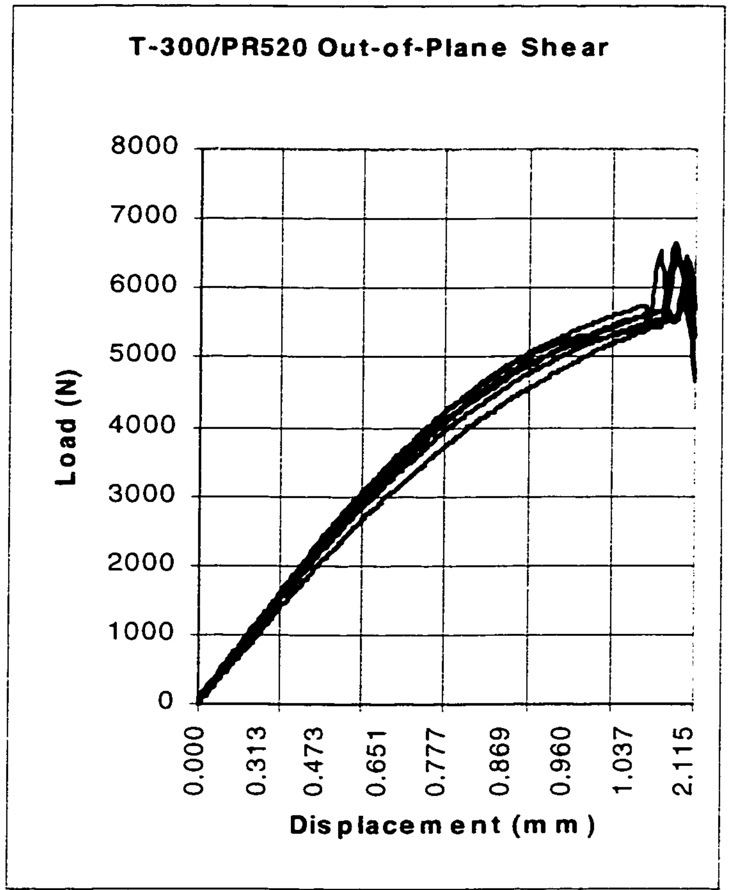

Figure 5.5.6-3. T-300/PR520 Laminate Out-of-Plane Shear Load-Displacement Plot.

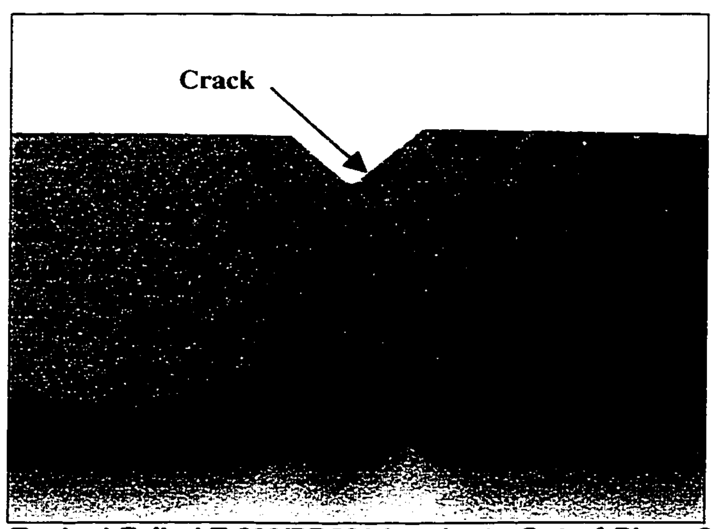

Figure 5.5.6-4. Typical Failed T-300/PR520 Laminate Out-of-Plane Shear Specimen.

Table 5.5.6-1 shows a summary of the laminate shear properties. The average out-of-plane shear modulus was determined to be 2.98 GPa and the average out-of-plane shear strength was 74.0 MPa. Again the low CoV indicated a high level of data consistency.

Table 5.5.6-1. T-300/PR520 Out-of-Plane Shear Properties Summary.

V-notch Beam Shear Test Results ASTM D5379 Iosipescu Shear Fixture				
SPECIMEN ID	**Width**	**THICKNESS**	**STRESS**	**MODULUS**
	(mm)	**(mm)**	**(MPa)**	**(GPa)**
I-1	11.5	7.65	74.5	2.96
I-2	11.4	7.70	74.5	2.96
I-3	11.5	7.70	75.8	2.90
I-4	11.4	7.57	74.5	3.03
I-5	11.4	7.49	72.4	3.10
I-6	11.4	7.62	72.4	2.90
		Average	**74.0**	**2.98**
		SD	**1.36**	**0.08**
		CV(%)*	**2.00**	**3.00**

** CV < 5% indicates excellent data consistancy*

5.6 Micromechanical Analysis

A micromechanical analysis was performed to predict the web and flange laminae and laminate elastic properties.[82] Micromechancial analysis is used to predict the in-plane elastic laminae properties and laminate effective properties are determined using laminated plate theory. Table 5.6-1 shows the vendor published PR520 neat resin properties[63] and T-300 reinforcing fiber properties used in the analysis.[60]

Table 5.6-1. T-Joint Constituent Properties.

Constituent	**Typical Diameter (μm)**	**Specific Gravity**	**Tensile Modulus (GPa)**	**Tensile Strength (GPa)**	**Strain to Failure (%)**	**Coefficient of Thermal Expansion (10^{-6}/°C)**	**Poisson's Ratio**
PR520 (3M)[63]	-	1.25	3.54	910	6.0	-	0.38
T-300 (Amoco)[60]	7	1.76	231	3.75	1.4	-0.6 (L)	0.2

5.6.1 Micromechanical Analysis of Laminae Elastic Properties

The in-plane elastic lamina properties are calculated using the simple rule of mixtures expressions for the apparent Young's modulus in the longitudinal, $\mathbf{E_{11}}$, and transverse, $\mathbf{E_{22}}$, directions, the apparent major Poisson's ratio, $\boldsymbol{\nu_{12}}$, and the apparent shear modulus $\mathbf{G_{12}}$:

$$E_{11} = E_f V_f + E_m V_m$$

$$E_{22} = (E_f E_m)/(E_f V_m + E_m V_f)$$

$$\nu_{12} = \nu_f V_f + \nu_m V_m$$

$$G_f = E_f/[2(1+\nu_f)]$$

$$G_m = E_m/[2(1+\nu_m)]$$

$$G_{12} = (G_f G_m)/(G_f V_m + G_m V_f)$$

where $\mathbf{E_f}$ and $\mathbf{E_m}$ are the modulus of the fiber and matrix, respectively, $\boldsymbol{\nu_f}$ and $\boldsymbol{\nu_m}$ are the Poisson's ratio of the fiber and matrix, respectively, $\mathbf{V_f}$ is the fiber volume fraction, $\mathbf{V_f}$ is the matrix volume fraction, $\mathbf{G_f}$ is the shear modulus of the fiber, and $\mathbf{G_m}$ is the shear modulus of the matrix.

5.6.2 Apparent Laminate In-Plane Elastic Properties

The laminate effective properties are determined using laminated plate theory. For a specially orthotropic lamina the stress-strain relations are given by:

$$\begin{pmatrix} \sigma_{xx} \\ \sigma_{yy} \\ \tau_{xy} \end{pmatrix} = \begin{bmatrix} Q_{11} & Q_{12} & 0 \\ Q_{21} & Q_{22} & 0 \\ 0 & 0 & Q_{66} \end{bmatrix} \begin{pmatrix} \varepsilon_{xx} \\ \varepsilon_{yy} \\ \gamma_{xy} \end{pmatrix}$$

where **[Q]** is the stiffness matrix. Individual elements of the stiffness matrix are given by:

$$Q_{11} = \frac{E_{11}}{1-\nu_{12}\nu_{21}} \qquad Q_{22} = \frac{E_{22}}{1-\nu_{12}\nu_{21}} \qquad Q_{12} = Q_{21} = \frac{\nu_{12}E_{22}}{1-\nu_{12}\nu_{21}} = \frac{\nu_{21}E_{11}}{1-\nu_{12}\nu_{21}} \qquad Q_{66} = G_{12}$$

The laminate extensional stiffness matrix **[A]** may then be determined using the following expressions for a symmetric quasi-isotropic laminate:

$$[A] = \begin{bmatrix} A_{11} & A_{12} & 0 \\ A_{12} & A_{22} & 0 \\ 0 & 0 & A_{66} \end{bmatrix}$$

where

$$A_{11} = A_{22}$$

$$A_{16} = A_{26} = 0$$

$$A_{66} = \frac{(A_{11} - A_{12})}{2}$$

The individual elements in the laminate extensional stiffness matrix **[A]** are determined using the following expression:

$$A_{mn} = \sum_{j=1}^{N} \left(\bar{Q}_{mn} \right)_j (h_j - h_{j-1})$$

where

N = total number of laminas in the laminate

$\left(\bar{Q}_{mn} \right)_j$ = elements of the $[Q]_{bar}$ matrix of the jth lamina

h_{j-1} = distance from the midplane to the top of the jth lamina

h_j = distance from the midplane to the bottom of the jth lamina

The effective laminate properties for a symmetric quasi-isotropic laminate are then determined using the following expressions:

$$E_{xx} = E_{yy} = \frac{A_{11}^2 - A_{12}^2}{hA_{11}}$$

$$\nu_{xy} = \frac{A_{12}}{A_{11}}$$

$$G_{xy} = \frac{A_{11} - A_{12}}{2h}$$

where **h** is the laminate thickness.

The calculated laminate effective elastic properties were determined to be between 5-7% higher than the experimentally determined values as shown in Table 6.6.2-1.

Unidirectional tape laminate stiffness properties are typically higher than that of woven fabric layups of similar stacking sequence and fiber orientation.[83] The slightly higher predicted values in this case may be attributed in part to the use of methods that do not take into account the waviness of the individual plain weave fabric plies and in part due to the fiber volume fractions obtainable using resin transfer molding. The presence of fiber waviness tends to reduce in-plane elastic properties over that of non-crimp fabrics and unidirectional prepreg tape. During loading, the crimped fibers tend to straighten causing local stress in the matrix that lead to microcracking of the matrix and reduced overall performance.[84]

Table 5.6.2-1. Predicted and Actual Elastic Properties.

Constituent	$E_{xx} = E_{yy}$ (GPa)	G_{xy} (GPa)	ν_{xy}
Predicted	47.68	17.98	0.33
Measured	44.24	16.53	0.31

5.7 Results Summary

Table 5.7-1 provides a summary of the laminate physical, elastic, and strength properties for the T-300/PR520 material as determined by the experimental test program. Again, based on the plain weave fabric quasi-isotropic layup, it is assumed that the transverse properties are equal to the experimentally determined longitudinal properties. As shown, the in-plane elastic compression modulus is approximately 9% lower than that of the elastic tensile modulus. The laminate compression strength is approximately 18% lower than that of the tensile strength.

Table 5.7-1. T-300/PR520 Laminate Properties Summary.

T-300/PR520 Plain Weave Fabric Laminate Elastic and Strength Properties Summary
Quasi-isotropic Layup $[0/45]_{6S}$

Average Laminate Elastic Property	Value	% CoV
E_{xxt}: Longitudinal Tensile Modulus (GPa)	44.24	1.5
E_{yyt}: Transverse Tensile Modulus (GPa)*	44.24	1.5
E_{xxc}: Longitudinal Compression Modulus (GPa)	40.48	1.2
E_{yyc}: Transverse Compression Modulus (GPa)*	40.48	1.2
ν_{xy}: In-plane Poisson's Ratio	0.31	2.9
G_{xy}: In-plane (Interlaminar) Shear Modulus (GPa)	16.53	17.7
E_{zzt}: Z-directional Tensile Modulus (GPa)	9.73	18.4
E_{zzc}: Z-directional Compression Modulus (GPa)	8.37	24.2
ν_{zx}: Transverse Poisson's Ratio	0.08	18.0
ν_{zy}: Transverse Poisson's Ratio*	0.08	18.0
G_{xz}: Transverse Shear Modulus (GPa)	2.98	3.0
Gyz: Transverse Shear Modulus (GPa)*	2.98	3.0

Average Laminate Physical Property		
V_f: Fiber Volume Fraction (%)	55.00	1.4
V_m: Resin Volume Fraction (%)	45.00	26.5
V_v: Void Volume Fraction (%)	1.10	2.4

Average Laminate Strength Property	Value	% CoV
X_t: Longitudinal Tensile Strength (MPa)	616.28	1.7
Y_t: Transverse Tensile Strength (MPa)*	616.28	1.7
X_c: Longitudinal Compressive Strength (MPa)	504.01	3.4
Y_c: Transverse Compressive Strength (MPa)*	504.01	3.4
S_s: In-plane (Intralaminar) Shear Strength (MPa)	195.93	3.2
Z_t: Z-directional Tensile Strength (MPa)	46.33	12.1
$X_{\varepsilon t}$: Longitudinal Tensile Strain (10^{-6})	13934	2.9
$Y_{\varepsilon t}$: Transverse Tensile Strain (10^{-6})*	13934	2.9
$X_{\varepsilon c}$: Longitudinal Compressive Strain (10^{-6})	12449	3.1
$Y_{\varepsilon c}$: Transverse Compressive Strain (10^{-6})*	12449	3.1
$S_{\varepsilon s}$: In-plane (Intralaminar) Shear Strain (10^{-6})	12166	18.0
$Z_{\varepsilon t}$: Z-directional Tensile Strain (10^{-6})	4943	26.1

* $E_{xxt} = E_{yyt}$, $E_{xxc} = E_{yyc}$, $\nu_{zx} = \nu_{zy}$, $G_{xz} = G_{yz}$, $X_t = Y_t$, $X_c = Y_c$, $X_{\varepsilon t} = Y_{\varepsilon t}$, $X_{\varepsilon c} = Y_{\varepsilon c}$

CHAPTER 6

T-300/PR520 T-JOINT EXPERIMENTAL RESULTS

An experimental investigation of mechanical behavior of the stitched T-300/PR520 T-joints with transverse stitching was performed under flexure, tension, and rail shear load conditions. Table 6.0-1 provides a summary of the T-joint experimental methods presented in Chapter 3. Section 6.1 presents results of the fixed support flexure experiments, Section 6.2 presents the tension results under fixed and simple support boundary conditions, and Section 6.3 presents the fixed support rail shear results.

Table 6.0-1. Summary of T-Joint Experiments.

Flexure	Fixed Support Tension	Simple Support Tension	Rail Shear
Section 6.1	Section 6.2.1	Section 6.2.2	Section 6.3
Fixed Support Flange	Fixed Support Flange	Simple Support Flange	Fixed Support flange
AF 163 Adhesive Bonded Flange	AF 163 Adhesive Bond Flange	None	Bolted Flange
Aluminum Backing Plate	Aluminum Backing Plate	None	Steel Fixture Backing Plate
Load Pin Applied Normal to Web	Hydraulic Gripped Web	Hydraulic Gripped Web	Bolted Web

6.1 Flexure Experiments

Experiments were conducted under flexure loading with fixed support boundary conditions. This section discusses the experimental results. Figure 6.1-1 (a) shows the five fixed support flexure specimens and Figure 6.1-1 (b) shows a typical specimen with a partial view of strain gage instrumentation and the aluminum backing plate bonded to the lower surface of the flange.

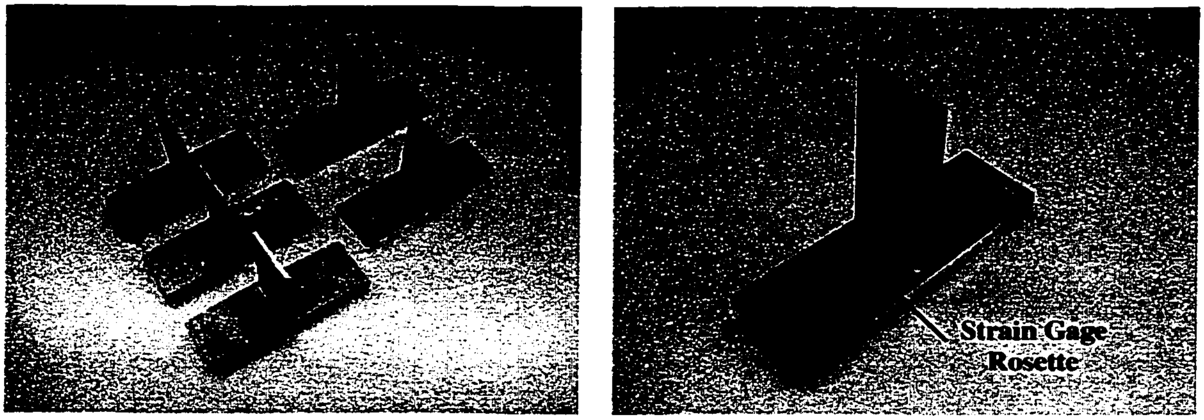

Figure 6.1-1. Typical T-300/PR520 T-Joint Fixed Support Flexure Specimens: (a) Specimen Set and (b) Typical Specimen Showing Instrumentation.

A typical T-300/PR520 T-joint flexure specimen just prior to loading is shown in Figure 6.1-2. Clearly visible are the aluminum backing plate, load pin, and upper specimen grip. Strain gage instrumentation lead wires are shown leading from the specimen to the data acquisition system. Figure 6.1-3 shows a specimen web deflecting under applied load.

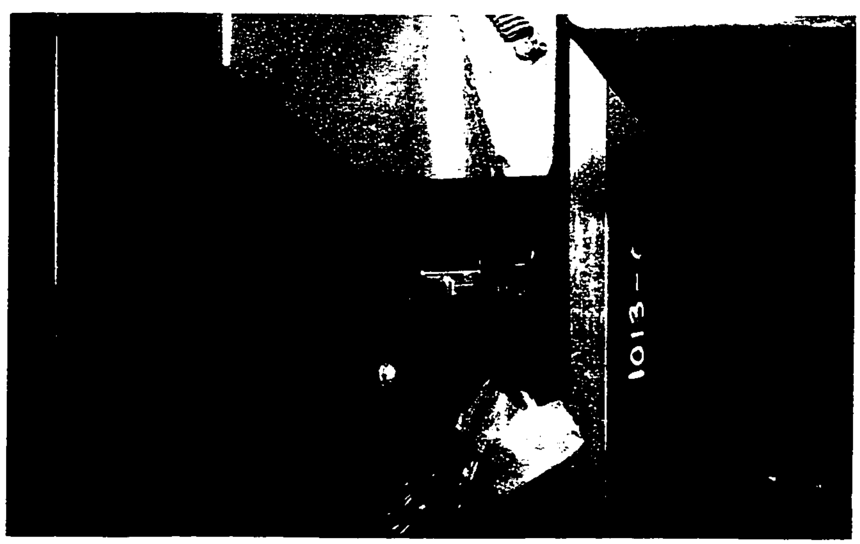

Figure 6.1-2. Typical T-300/PR520 T-Joint Flexure Specimen Experimental Setup

Figure 6.1-3. Typical T-300/PR520 T-Joint Flexure Specimen Showing Web Deflection Under Load.

The load-displacement plot for the five T-300/PR520 T-joint flexure specimens is shown in Figure 6.1-4. Loading is shown to be nearly linear up to the point of initial failure. Three distinct regions may be observed on the load displacement plot. The first region up to point "a" is the linear elastic region. The second region from point "b" up to point "c" is the initial damage zone and the third region up to point "d" is the continuation of damage leading to T-joint catastrophic failure.

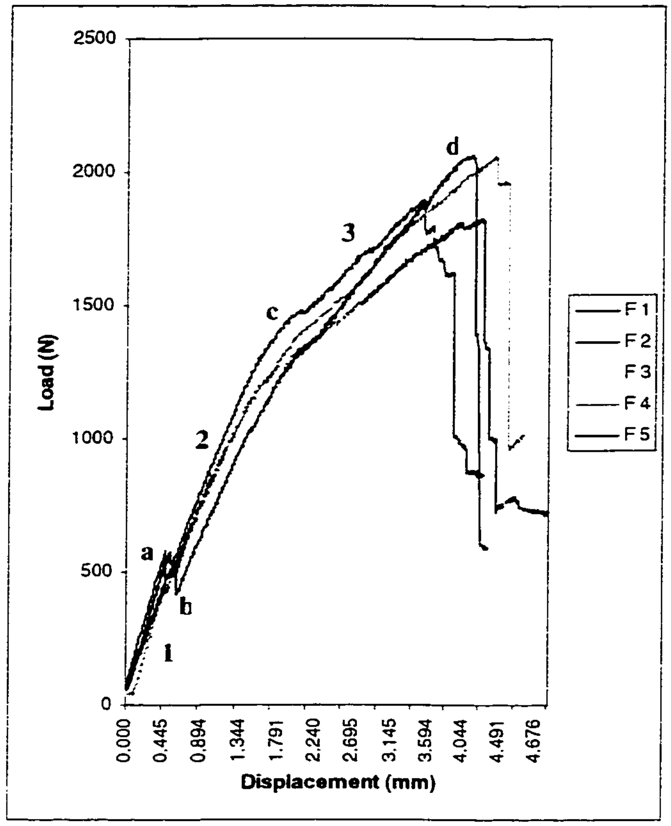

Figure 6.1-4. Load-Displacement of T-Joint Subject to Flexure Loading.

A typical strain-load plot for a flexure specimen F1 is shown in Figure 6.1-5. The initial drop in strain coincides with the initial drop in load at point "a" as shown in Figure 6.1-4. This drop in strain is indicative of initial T-joint failure. A distinctive drop in strain occurs at point "d" where peak recorded strains coinciding with T-joint catastrophic failure. At ultimate failure, the load dropped to 724 N and correspondingly the strain dropped to approximately 1000 uε.

A maximum web laminate surface tensile strain of 3204 με was recorded at strain gage location 9. Strain gage number designations are provided in Chapter 3. The experimentally determined laminate tensile failure strain of 13934 με was not exceeding indicating no web failure occurred during static flexural loading. A maximum web laminate surface compressive strain of 3132 με was recorded at strain gage location 12. The experimentally determined laminate compressive failure strain of 12449 με was not exceeded during static flexural loading indicating that the web laminate did not fail in compression. Failures instead occurred locally at the web-to-flange interface. Additional load-displacement and strain-load plots are provided in Appendix E.

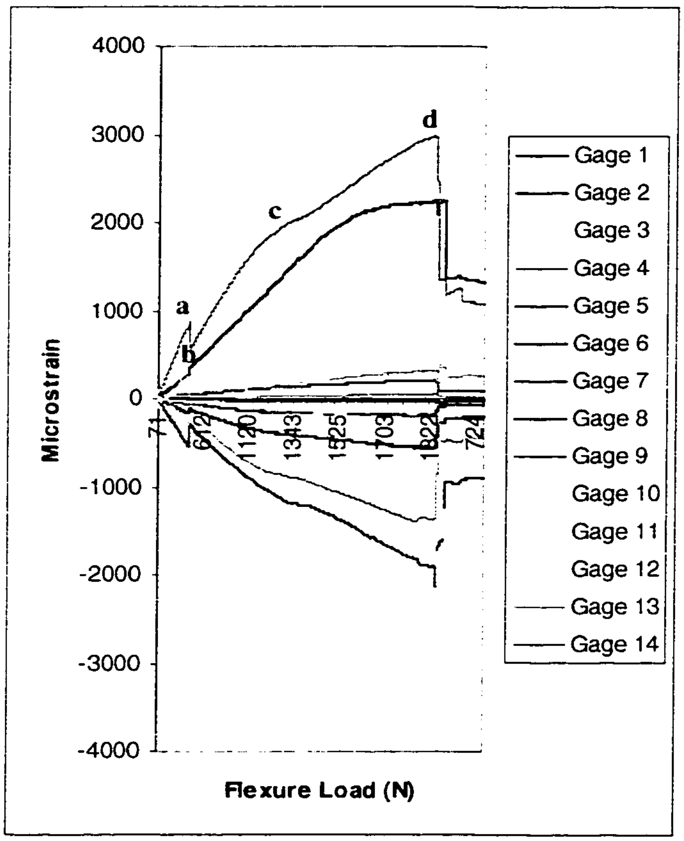

Figure 6.1-5. Typical Strain-Load Plot for T-300/PR520 Flexure Specimen F1.

The damage initiation load and ultimate damage load for the five flexure experiments are summarizes in Table 6.1-1. The average initial damage load was determined to be 566 N and the average ultimate damage load is 1961 N. The coefficient of variations (CoV) at initial failure load is 7.7% and 5.4% at ultimate failure indicating good data consistency.

Table 6.1-1. Flexure Initial Damage and Ultimate Load.

Flexure Specimen	Web Thickness (mm)	Flange Thickness (mm)	Specimen Width (mm)	Damage Initiation Load (N)	Ultimate Load (N)
F 1	4.86	4.86	50.87	582	1824
F 2	4.90	4.88	50.89	533	1895
F 3	4.77	4.77	50.90	625	1954
F 4	4.80	4.80	50.88	579	2066
F 5	4.91	4.91	50.88	515	2068
Mean	4.85	4.84	50.88	567	1961
Std. Dev.	0.06	0.06	0.01	43	107
CoV (%)	1.3	1.2	0.0	7.7	5.4

A typical failed T-joint flexure specimen is shown in Figure 6.1-6. A crack is shown in the resin-rich radius zone along the entire width of the specimen at the flange-to-web interface. Also visible, is the aluminum backing plate bonded to the lower surface of the flange.

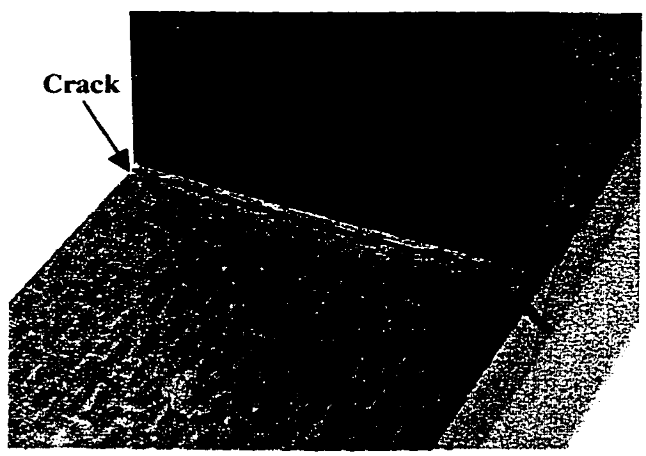

Figure 6.1-6. Typical Failed T-Joint Flexure Specimen.

An optical micrograph for failed flexural specimen F1 is shown in Figure 6.1-7. The web is displaced relative to the flange. Extensive cracking is shown at the interface between the flange and web. The crack initiates from the resin-rich fillet region and propagates to and along the fiber insertions with increasing load. The fiber insertion adjacent to the applied load is deformed in tension and the fiber insertion furthermost from the load is deformed in compression. Ultimate failure occurs due to fiber insertion breakage and pullout.

Figure 6.1-7. Typical Optical Micrograph of Failed Flexure Specimen F1.

6.2 Tension Experiments

Experiments were conducted under tension loading with fixed and simple support boundary conditions. This section discusses the experimental results. Experimental test procedures and specimen instrumentation were discussed previously in Chapter 3.

6.2.1 Fixed Supports

Figure 6.2.1-1 (a) shows the five fixed support tension specimens and Figure 6.2.1-1 (b) shows a typical specimen showing strain gages and aluminum backing plate. Figure

6.2.1-2 (a) shows the experimental setup. Shown is the steel fixture and specimen web prior to gripping. Also shown are the flange aluminum backing plate and strain gage lead wires. Figure 6.2.1-2 (b) shows a side view of the experimental setup.

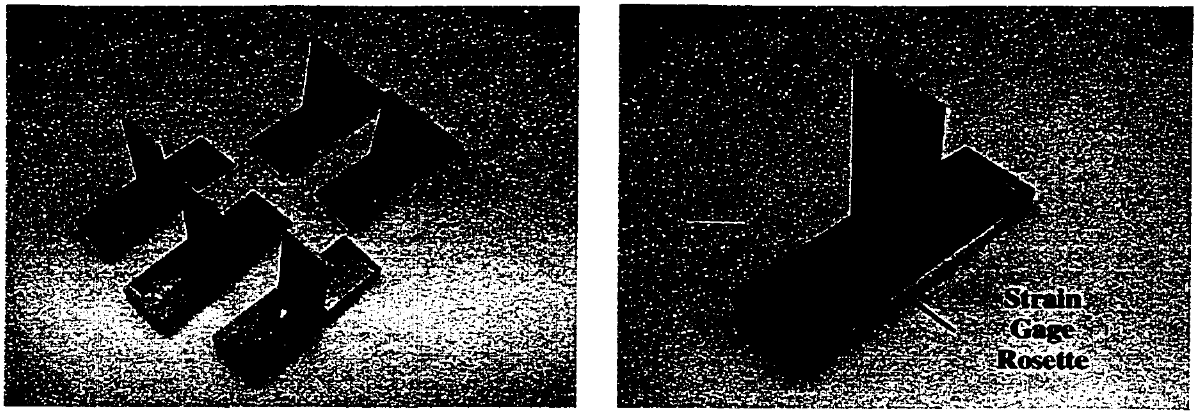

Figure 6.2.1-1. Typical T-300/PR520 T-Joint Fixed Support Tension Specimen: (a) Specimen Set and (b) Typical Specimen Showing Instrumentation.

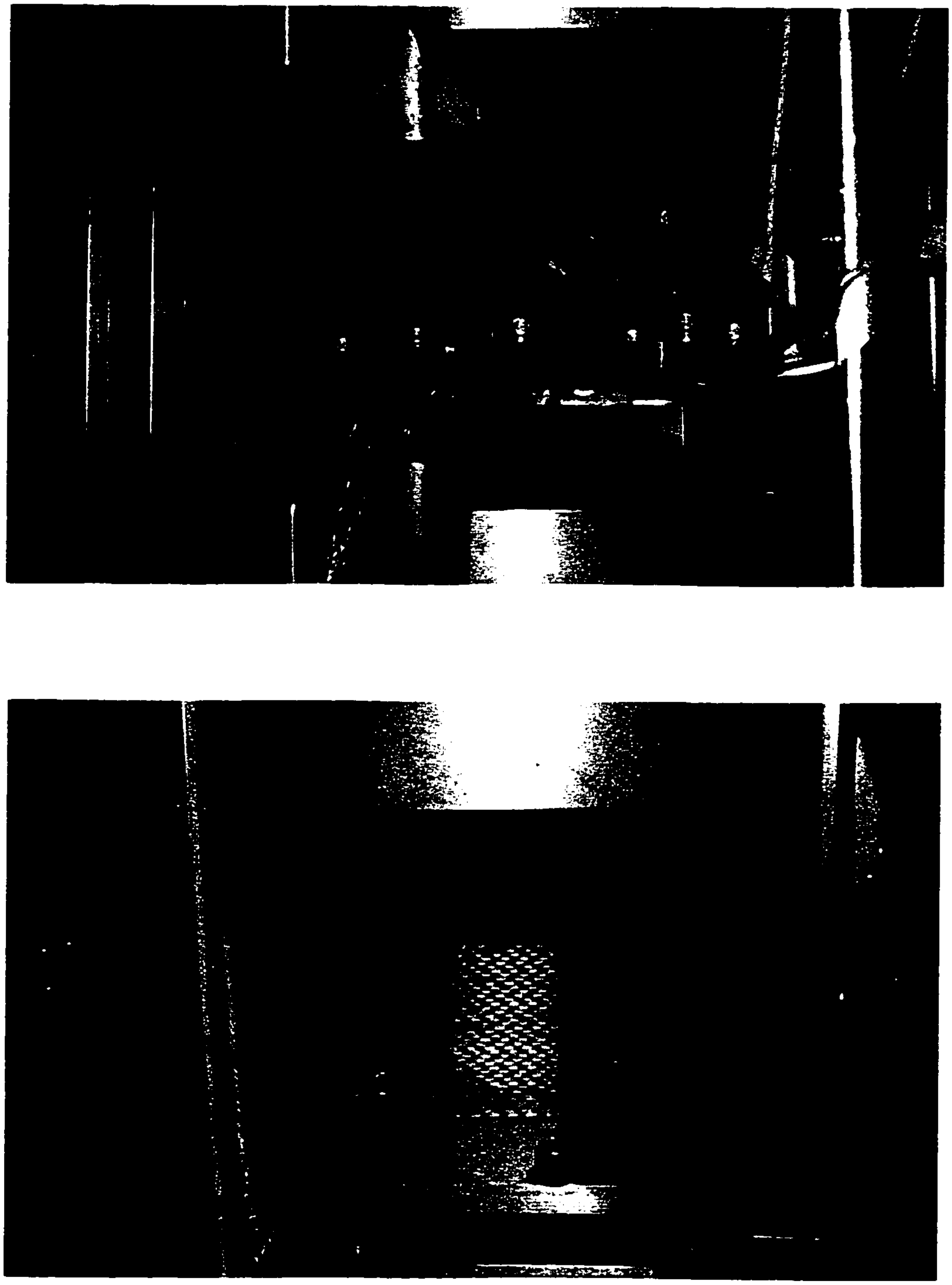

Figure 6.2.1-2. Typical T-300/PR520 T-Joint Fixed Support Tension Specimen: (a) Experimental Setup and (b) Prior to Loading.

Figure 6.2.1-3 shows a load-displacement plot for a typical T-joint tension specimen. The load-displacement plot has two distinct regions. In region 1, load is nearly linear up to initial failure, point "a" on the plot. An additional linear region is observed up to point "b" on the plot. Specimen T3 failed prematurely in the adhesive bondline between the flange and aluminum backing plate.

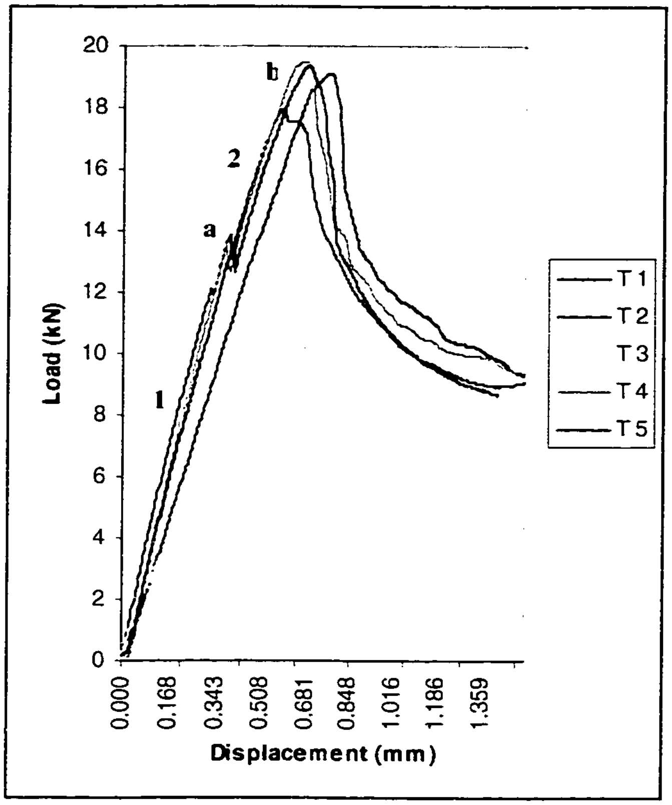

Figure 6.2.1-3. Load-Displacement Plot for Fixed Support Tension Specimens.

Figure 6.2.1-4 shows a typical strain-load plot for a fixed support tension specimens T2. The initial drop in strain at point "a" coincides with the initial drop in load as shown on the load-displacement plot. This drop in strain is indicative of damage initiation. A distinctive drop in strain occurs at peak recorded strains, point "b" coinciding with T-joint ultimate failure. Again, at T-joint ultimate failure the load-strain dropped. Post failure analysis of the fixed support tension specimens indicated that a failure occurred in the adhesive bond line between the specimen and the aluminum backing plate prior to initial joint failure. Based on these results, tension experiments with simple support boundary condition and no aluminum backing plates were performed. No further study of the fixed support tension specimens was conducted.

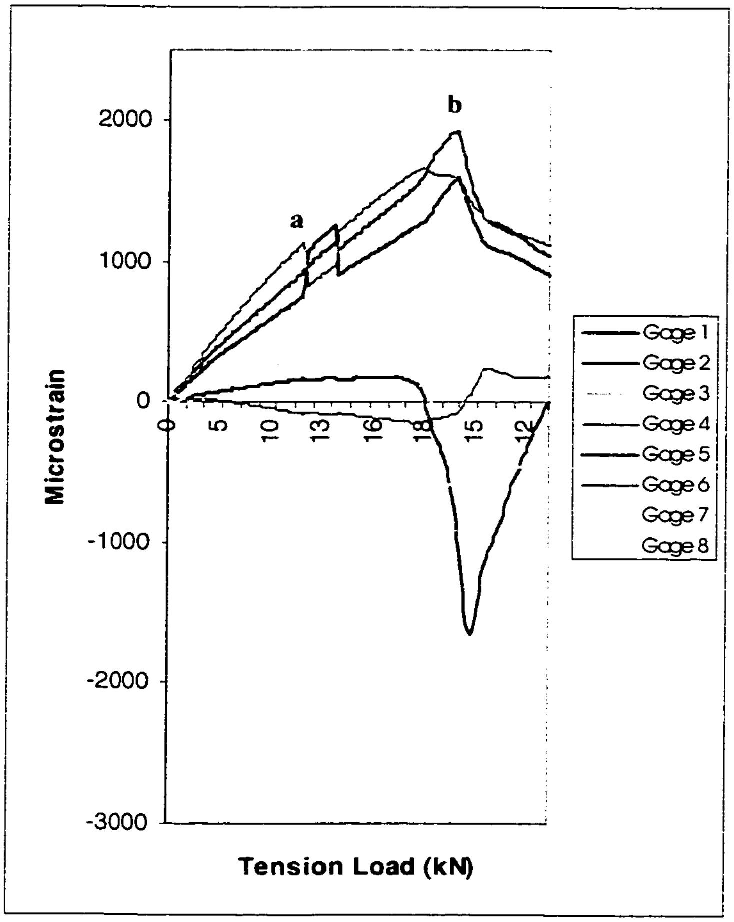

Figure 6.2.1-4 Typical Strain-Load Plot for T-300/PR520 Tension Specimen T2.

Table 6.2.1-1 summarizes the damage initiation load and ultimate damage load for each tension experiment. The average initial and ultimate damage load was determined to be 13.24 kN and 19.02 kN, respectively. The CoV at initial and ultimate failure is very low indicating good data consistency. Due to the premature failure of specimen T3 was discarded from the summary statistics in Table 6.2.1-1.

Table 6.2.1-1. Fixed Support Tension Initial Damage and Ultimate Load.

Tension Specimen	Web Thickness (mm)	Flange Thickness (mm)	Specimen Width (mm)	Damage Initiation Load (kN)	Ultimate Load (kN)
1	4.84	4.85	50.91	13.85	19.12
2	4.87	4.83	50.88	11.96	17.93
3*	4.83	4.81	50.90	6.43	10.22
4	4.78	4.73	50.84	13.57	19.48
5	4.83	4.84	50.91	13.58	19.53
Mean	4.83	4.81	50.89	13.24	19.02
Std. Dev.	0.04	0.06	0.03	0.86	0.75
CoV (%)	0.8	1.2	0.1	6.5	3.9

* *Data not Included in Summary Calculations*

6.2.2 Simple Supports

Figure 6.2.2-1 (a) shows the five simple support tension specimens and Figure 6.2.2-1 (b) shows a typical specimen showing strain gages. Figure 6.2.2-2 shows a typical tension specimen during tension loading. The fixture and flange edge are clearly visible.

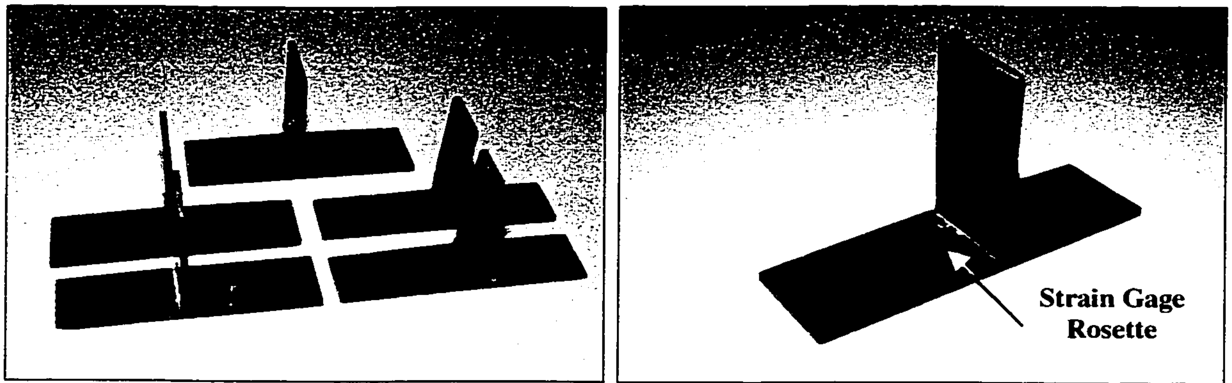

Figure 6.2.2-1. Typical T-300/PR520 T-Joint Simple Support Tension Specimen: (a) Specimen Set and (b) Typical Specimen Showing Instrumentation.

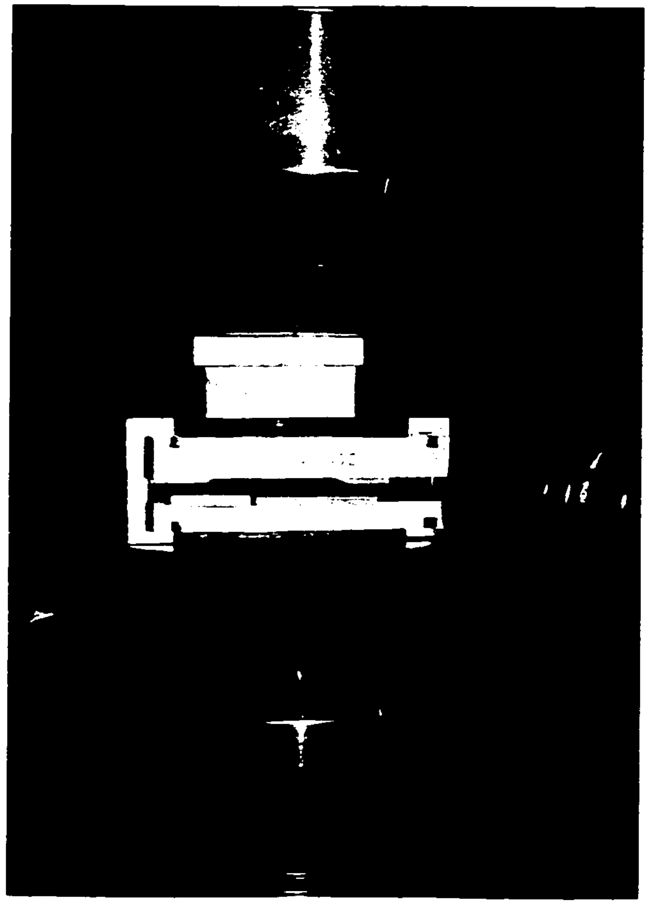

Figure 6.2.2-2. Typical T-300/PR520 T-Joint Simple Support Tension Specimen During Loading.

Figure 6.2.2-3 shows a combined load-displacement plot for the T-joints under tensile loading. The T-joints behave nearly linearly up to initial failure with nonlinearity occurring at the onset of matrix failure as indicated by a drop in the load-displacement curve at point "a" and ultimate failure occurring at point "b". During loading, audible matrix cracking was noted at the onset of initial failure for each specimen The initial nonlinearity noted in the load-displacement plot is indicative of specimen fixture seating. An initial preload of 50 N was applied to the specimens as noted above. The load-displacement for specimens T2 and T4 matched very well. Specimens T1 and T3 had a slope within 5% of that of specimens T2 and T4, but experienced additional seating. Specimen T5 had a low initial failure.

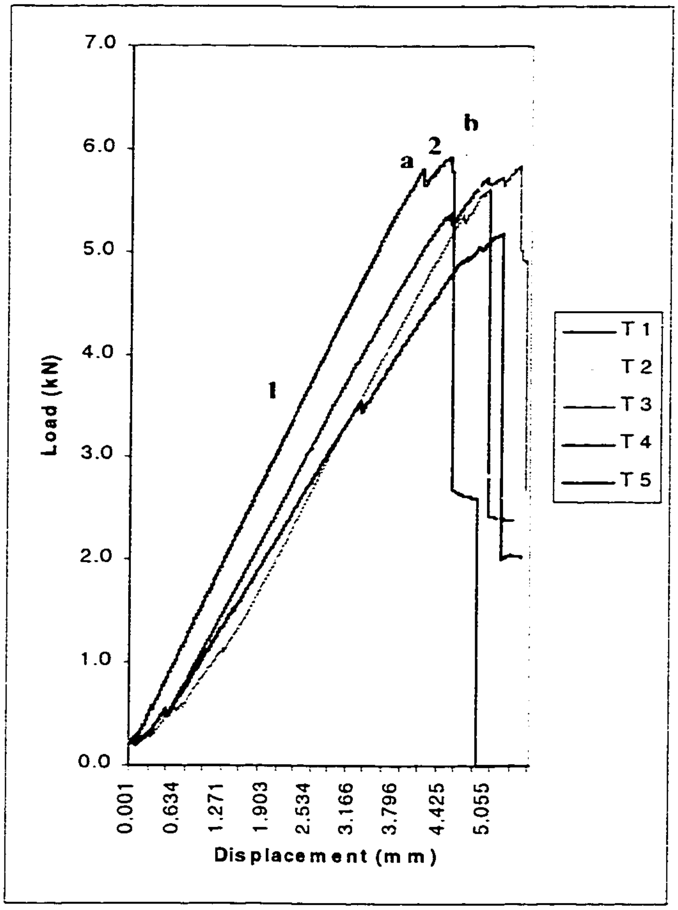

Figure 6.2.2-3. Load-Displacement Record for Simple Support Tension Specimen.

Figure 6.2.2-4 shows the far field strain-load plots for specimen T1. Peak tensile and compressive strains are recorded in the 45° gage locations for each 3-element rosette. Peek tensile strains of 9620 $\mu\varepsilon$ are recorded in strain gage 3 and does not exceed the laminate tensile failure strain of 13934 $\mu\varepsilon$ indicating no web failure occurred during static flexural loading. Peek compressive strains of –980 $\mu\varepsilon$ are recorded in strain gage 4. The experimentally determined laminate compressive failure strain of 12449 $\mu\varepsilon$ was not exceeded during static tensile loading indicating that the web laminate did not fail in compression. A discrete jump in strain is noted in direct correspondence to initial matrix cracking as indicated at point "a" on the load-displacement plots. This may be attributed to load redistribution within the web and flange after initial matrix interface cracking. Failures occurred locally at the web-to-flange interface. The load dropped to 2.4 kN at ultimate failure.

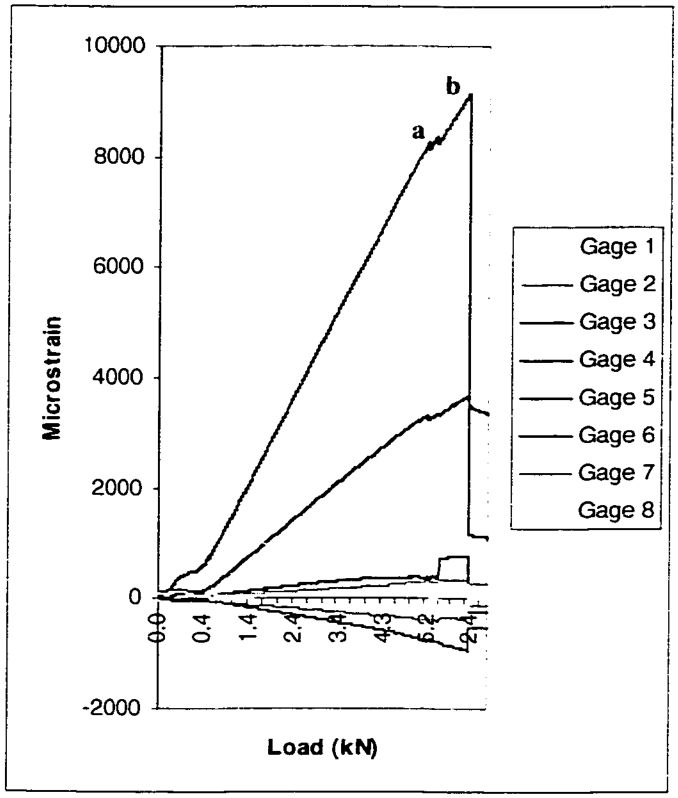

Figure 6.2.2-4. Typical Strain-Load Plot for T-300/PR520 Simple Support Tension Specimen T1.

Table 6.2.2-1 summarizes the damage initiation load and ultimate damage load for each tension experiment. The average initial damage load was determined to be 5.1 kN and the average ultimate damage load is 5.74 kN. The CoV at initial damage and ultimate failure load is 17.4% and 6.0%, respectively. It was noted that specimen T5 failed prematurely. All specimens exhibit a slight amount of additional load carrying capability beyond initial failure.

Table 6.2.2-1. Simple Support Tension Initial Damage and Ultimate Load.

Tension Specimen	Web Thickness (mm)	Flange Thickness (mm)	Specimen Width (mm)	Damage Initiation Load (kN)	Ultimate Load (kN)
T 1	4.78	4.80	50.85	5.37	5.74
T 2	4.80	4.80	50.80	5.38	6.05
T 3	4.83	4.78	50.83	5.38	5.83
T 4	4.83	5.26	50.75	5.81	5.92
T 5	4.78	4.85	50.62	3.55	5.16
Mean	4.80	4.90	50.77	5.10	5.74
Std Dev.	0.03	0.20	0.09	0.89	0.34
CoV (%)	0.5	4.2	0.2	17.4	6.0

A detailed post failure analysis was performed on the T-joint tension specimens. Figure 6.2.2-5 shows a typical optical micrographs of a failed tension specimen. Again, the optical micrographs. Cracking is shown to occur uniformly across the web-to-flange interface. In this case both fiber insertions are loaded in tension. Initial matrix cracking is indicative of initial joint failure. Catastrophic failure occur due to fiber insertion breakage and pullout.

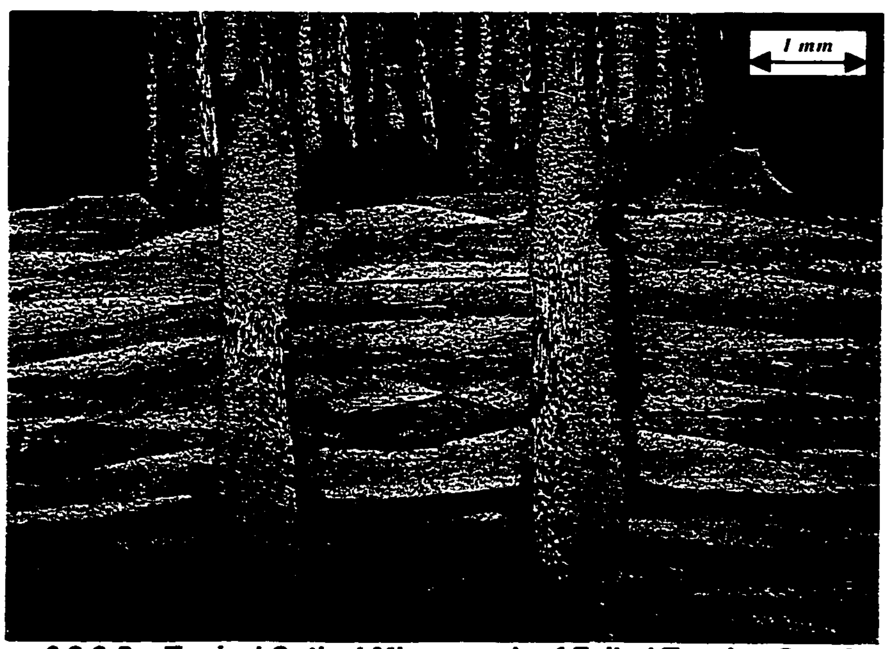

Figure 6.2.2-5. Typical Optical Micrograph of Failed Tension Specimen T3.

6.3 Rail Shear Experiments

Experiments were conducted under rail shear loading with fixed boundary conditions. The rail shear specimen set is shown in Figure 6.3-1 (a). Figure 6.3-1 (b) shows a typical specimen showing web tabs, strain gages, and fixture fastener holes in the web and flange. Figure 6.3-2 shows a typical rail shear specimen during tension loading. The fixture and web are clearly visible. Also shown are the fixture bolts and flange strain gage lead wires. The fixture flange plate is attached to the lower hydraulic grip and the web fixture is attached to the upper hydraulic grip.

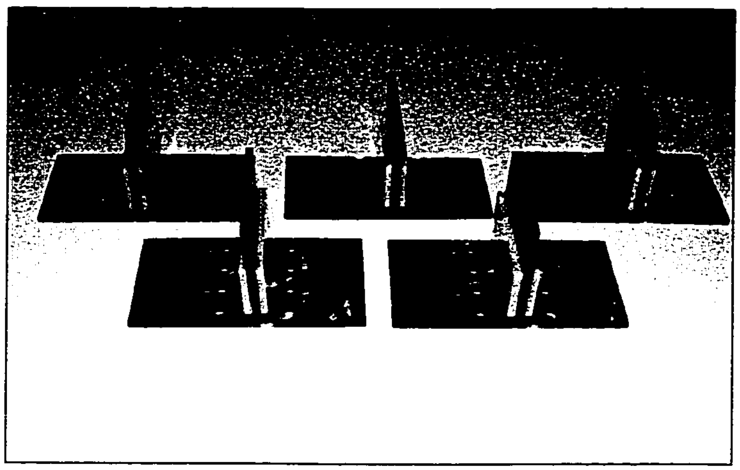

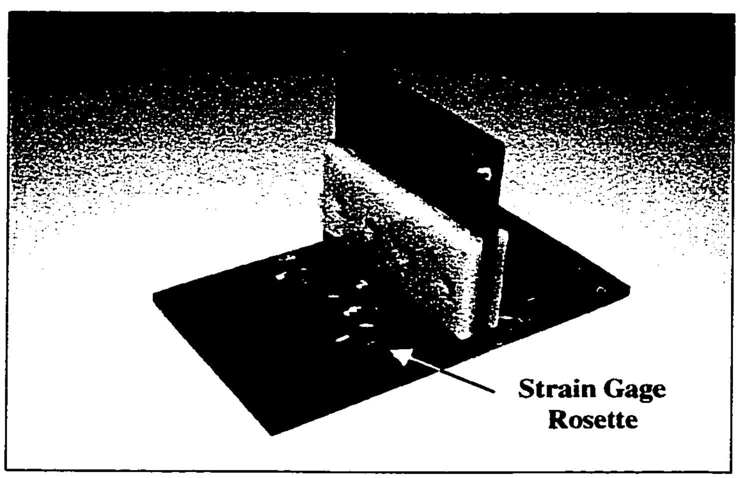

Figure 6.3-1. Typical T-300/PR520 T-Joint Rail Shear Specimen: (a) Specimen Set and (b) Typical Specimen Showing Instrumentation.

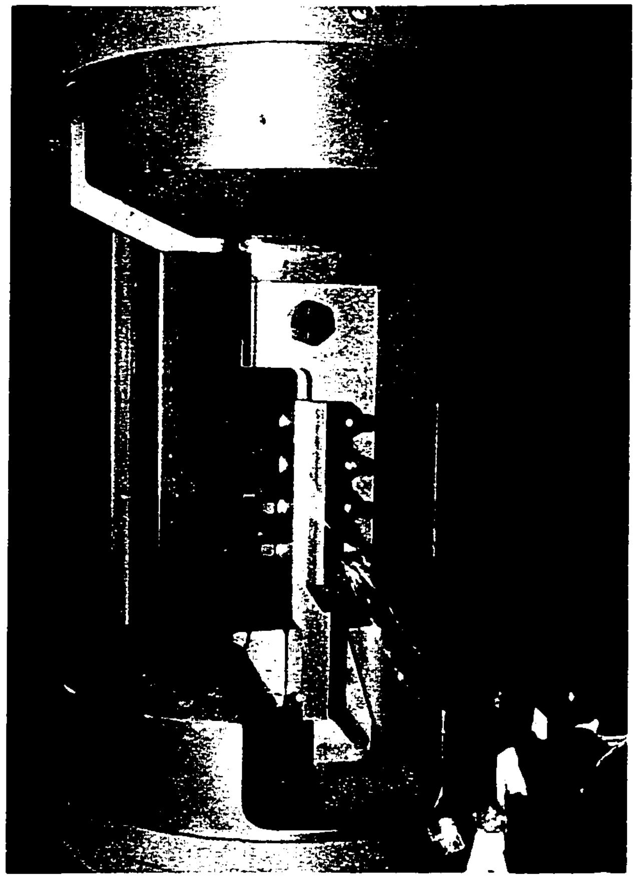

Figure 6.3-2. Typical T-300/PR520 T-Joint Rail Shear Specimen Experimental Setup.

Figure 6.3-3 shows a combined load-displacement plot for the T-joints under rail shear loading. The T-joints behave nearly linearly up to initial failure with nonlinearity occurring at the onset of matrix failure as indicated a leveling off of the load-displacement curve just prior to ultimate failure. During loading, audible matrix cracking was noted at the onset of initial failure for each specimen. A complete separation of the web and flange is indicated by the large drop in load-displacement at the end of experiment. The initial nonlinearity noted in the load-displacement plot is likely specimen fixture seating. An initial preload of 400 N was applied to the specimens as noted above. The specimen seating may be attributed to small misalignments in fastener hole location and/or deviations in fabricated specimen geometric tolerances. The fixture seating indicates that an increased preload to 5 kN may be warranted in future experiments. Post failure examination of failed specimens did not show any appreciable fastener hole bearing damage.

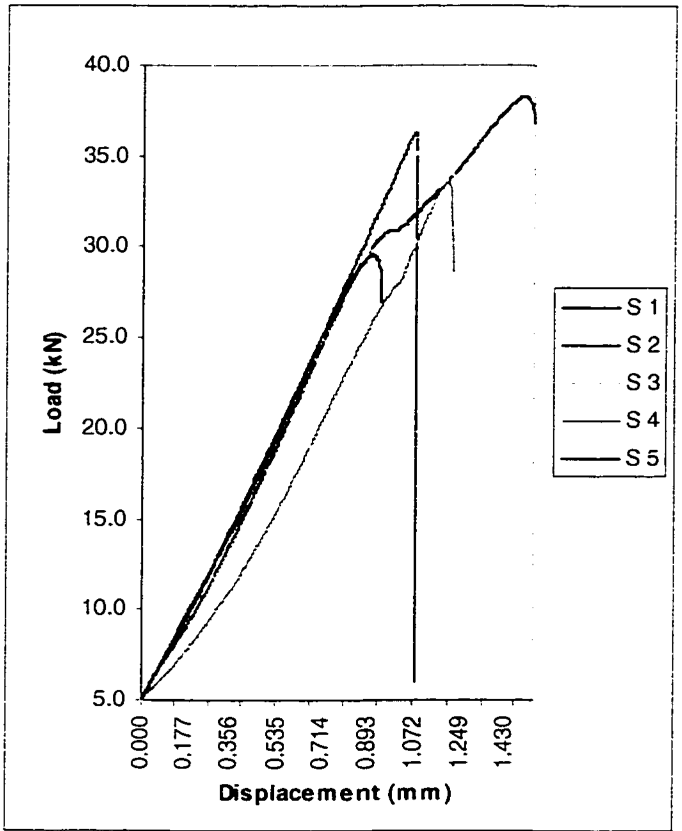

Figure 6.3-3. Load-Displacement for T-300/PR520 Rail Shear Specimens.

Figure 6.3-4 shows the far field strain-load plot for specimen S3. Peak tensile and compressive strains are recorded in the 45° gage locations for each 3-element rosette. A peek surface tensile strains of 2106 $\mu\varepsilon$ was recorded at strain gage location 6. A peek surface compressive strain of −1696 $\mu\varepsilon$ was recorded at gage location 12. A discrete jump in strain is noted in direct correspondence to initial matrix cracking as indicated on the load-displacement plots. This may be attributed to load redistribution within the web and flange after initial matrix interface cracking. Average peak measured far field laminate strains are well below the T-300/PR520 laminate failure strains as indicated in Chapter 5 of this evaluation. Load dropped to 6.1 kN at T-joint ultimate load.

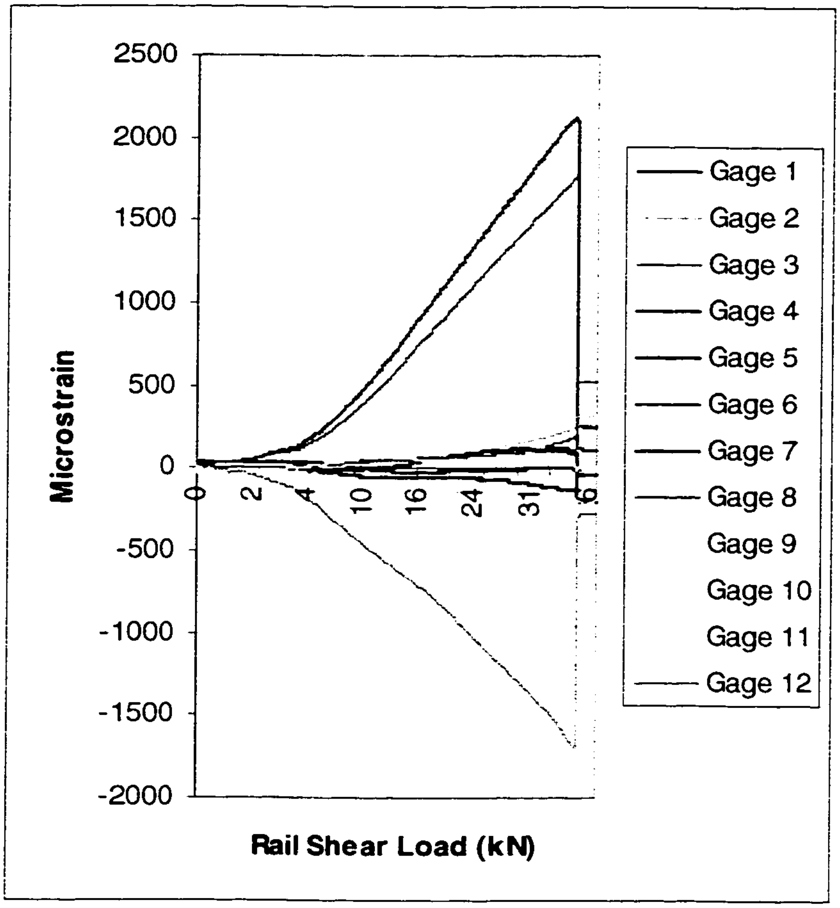

Figure 6.3-4. Typical Strain-Load Plot for T-300/PR520 Rail Shear Specimen S3.

Table 6.3-1 summarizes the damage initiation load and ultimate damage load for each rail shear experiment. The average initial damage load was determined to be 32.30 kN and the average ultimate damage load is 34.81 kN. A moderate amount of scatter was noted in the load data. The CoV at initial failure and ultimate load is 11.6% and 9.7%, respectively. It was noted that specimens S2, S3, and S5 failed catastrophically at the damage initiation load. Specimens S1 and S4 exhibit additional load caring capability beyond initial failure.

Table 6.3-1. Rail Shear Initial Damage and Final Load.

Rail Shear Specimen	Web Thickness (mm)	Flange Thickness (mm)	Specimen Width (mm)	Damage Initiation Load (kN)	Ultimate Load (kN)
S 1	4.95	4.72	101.40	30.93	38.30
S 2	5.21	4.88	101.47	36.30	36.30
S 3	5.16	4.83	101.83	36.25	36.25
S 4	5.26	4.83	101.78	28.43	33.63
S 5	5.18	4.83	101.37	29.58	29.58
Mean	5.15	4.82	101.57	32.30	34.81
Std. Dev.	0.12	0.06	0.22	3.74	3.36
CoV (%)	2.3	1.2	0.2	11.6	9.7

Figure 6.3-5 shows a typical failed T-joint rail shear specimen after catastrophic failure. The web has been completely separated from the flange. Also shown is a detailed view of the flange and web interface. Visible are broken fiber insertion tows and recesses from fiber pullout zones.

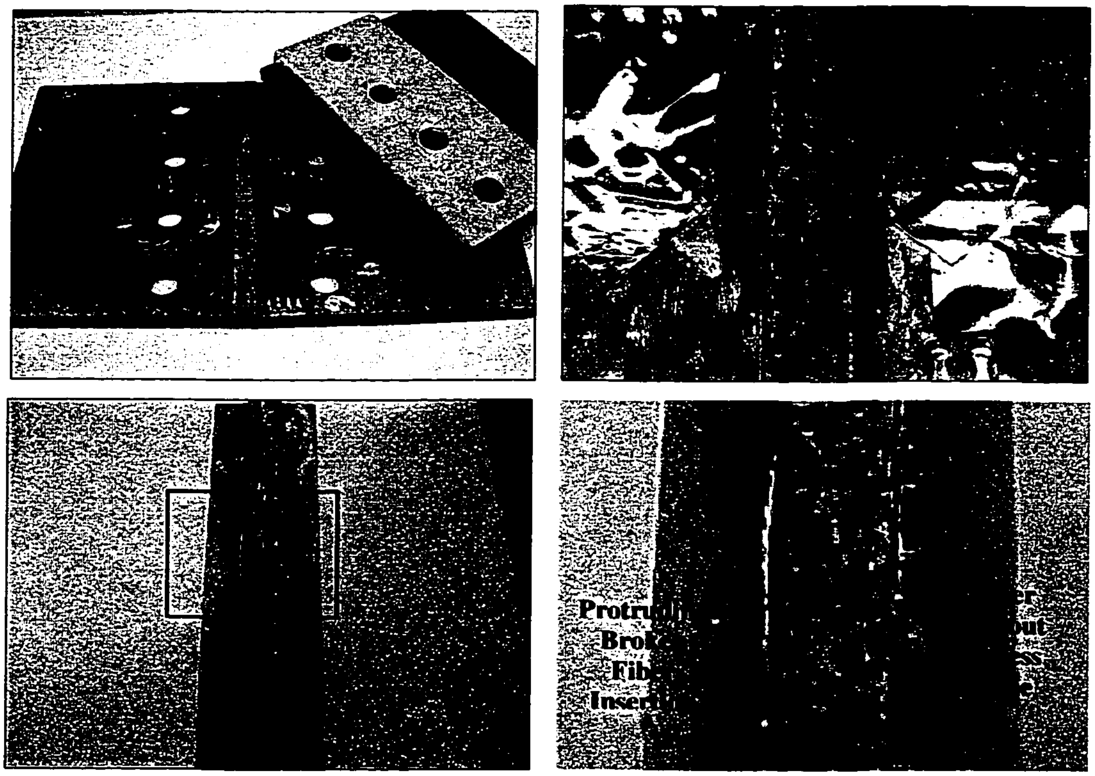

Figure 6.3-5. Typical Failed T-Joint Rail Shear Specimen S2.

A detailed post failure analysis was performed on the T-joint rail shear specimens. Figure 6.3-6 and Figure 6.3-7 show typical optical micrographs of failed rail shear specimens S3 and S5. Matrix cracks are visible at the web-to-flange interface.

Figure 6.3-6. Optical Micrograph of Failed Rail Shear Specimens S3.

Figure 6.3-7. Optical Micrograph of Failed Rail Shear Specimens S5.

CHAPTER 7

T-300/PR520 T-JOINT NUMERICAL RESULTS

7.1 T-Joint Numerical Modeling

T-joint predictive finite element analyses were conducted using ANSYS version 5.6[66] finite element software. Table 7.1-1 shows a summary of the T-joint numerical models for each load condition. Linear elastic, nonlinear elastic, and damage progression two-dimensional models were developed for T-joint flexure. Linear elastic and damage progression two-dimensional models were developed for the case of simple support tension. A linear elastic three-dimensional model was developed for the rail shear analysis. The nonlinear flexure analysis used nonlinear material properties and large displacement. For the two-dimensional analysis, a plane strain assumption was made. Plane strain was assumed because the specimen width is significantly greater than the flange or web thickness.

Table 7.1-1. T-Joint Numerical Model Attributes.

Attribute	Flexure	Tension	Rail Shear
Model Type	2D Linear Elastic, Nonlinear Elastic, and Damage Progression Plane Strain	2D Linear Elastic and Damage Progression Plane Strain	3D Linear Elastic -
ANSYS Element	LINK1 – 2D Spar PLANE2 – 2D 6-Node Triangular Structural Solid PLANE183 – 2D 8-Node Structural Solid	LINK1 – 2D Spar PLANE2 – 2D 6-Node Triangular Structural Solid PLANE183 – 2D 8-Node Structural Solid	LINK8 – 3D Spar SOLID187 – 3D 10-Node Tetrahedral Structural Solid SOLID185 – 3D 8-Node Structural Solid
Boundary Conditions	Fixed Support Flange	Simple Support Flange	Fixed Support Flange

Table 7.1-2 shows the material properties used for this analysis. The previously shown vendor properties were used for the IM7 fiber insertions and PR520 resin. The experimentally determined elastic laminate properties, as presented in Chapter 5, were used for the T-300/PR520 quasi-isotropic web and flange.

Table 7.1-2. Finite Element Analysis Material Properties.

Property	Region 1 (IM7 Fiber Insertion)	Region 2 (PR520 Resin)	Region 3 (T-300/PR520 Web)	Region 4 (T-300/PR520 Flange)
E_x (GPa)	276	3.54	44.24	9.73
E_y (GPa)	276	3.54	9.73	44.24
E_z (GPa)	276	3.54	44.24	44.24
ν_{xy}	0.30	0.38	0.37	0.37
ν_{yz}	0.30	0.38	0.37	0.31
ν_{xz}	0.30	0.38	0.31	0.37
G_{xy} (GPa)	106	1.28	2.98	2.98
G_{yz} (GPa)	106	1.28	2.98	16.53
G_{xz} (GPa)	106	1.28	16.53	2.98

The nonlinear analysis was performed using both nonlinear elastic material properties for the resin-rich region and large displacement for the entire model. Nonlinear material properties were incorporated using the ANSYS multilinear kinematic hardening (KINH) function. Table 7.1-3 shows the PR520 stress-strain data input for the PR520 neat resin. A maximum of five data points are possible for the KINH function within ANSYS. The trues-stress and true-strain data were inputted directly into the KINH function table.

Table 7.1-3. PR520 KINH Stress-Strain Properties.

Stress (MPa)	Strain (%)	Strain	E (GPa)	True Stress (MPa)	True Strain
0.00	0.000	0.0000	0.000	0.00	0.0000
20.68	0.590	0.0059	3.506	20.81	0.0059
41.37	1.300	0.0130	3.182	41.91	0.0129
62.05	2.200	0.0220	2.821	63.42	0.0218
82.74	3.500	0.0350	2.364	85.63	0.0344
91.01	6.020	0.0602	1.512	96.49	0.0585

Figure 7.1-1 shows the T-joint fiber insertion geometry. As indicated symbolically, **p** is the fiber pitch, $\mathbf{t_w}$ is the web thickness, and **S** is the fiber insertion spacing. The fiber insertions were modeled using spar elements that required a cross-sectional area input.

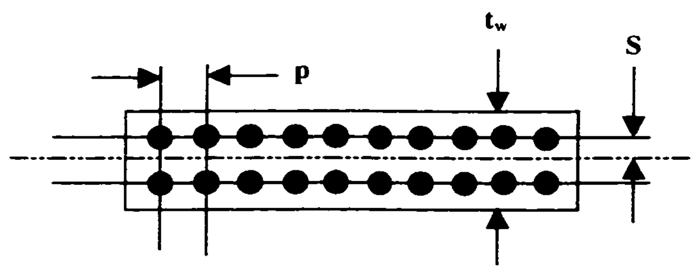

Figure 7.1-1. T-Joint Fiber Insertion Geometry.

The IM7 6k fiber tow cross-sectional area, $\mathbf{A_{tow}}$ was determined using the following expression:

$$A_{Tow} = \left(\frac{\pi d_f^{\,2}}{4}\right) * (\#\, filaments)$$

where $\mathbf{d_f}$ is the filament diameter. There are 6000 filaments per 6k tow and 2 tows per fiber insertion. The IM7 fibers have a filament diameter of 5 μm and a fiber tow area of 0.15 mm.[84] The nominal circular tow diameter was determined to be 0.50 mm assuming a packing fraction of 0.75, where the packing factor is the area of fibers divided by the area of a circle. The fiber insertion tow area and diameter were used as input to the finite element model element attributes.

In order to numerically model the T-joint, the resin-rich interface zone thickness needed to be determined. Using the optical micrograph shown in Figure 7.1-2, the average resin-rich interface zone thickness was determined to be approximately 1.25 mm. This region was modeled using isotropic PR520 neat resin properties. The variation and magnitude of the interface thickness may be attributed to preform edge roughness and fiber preform misalignment during T-joint fabrication. An analytical sensitivity analysis was performed in order to characterize the effective of variations in interfacial thickness on T-joint mechanical behavior and to ensure confidence in the numerical modeling approach. The analysis indicates that the interface thickness has only marginal effect on T-joint displacement ensuring accuracy in the finite element approach. Results of this analysis are provided in Appendix F.

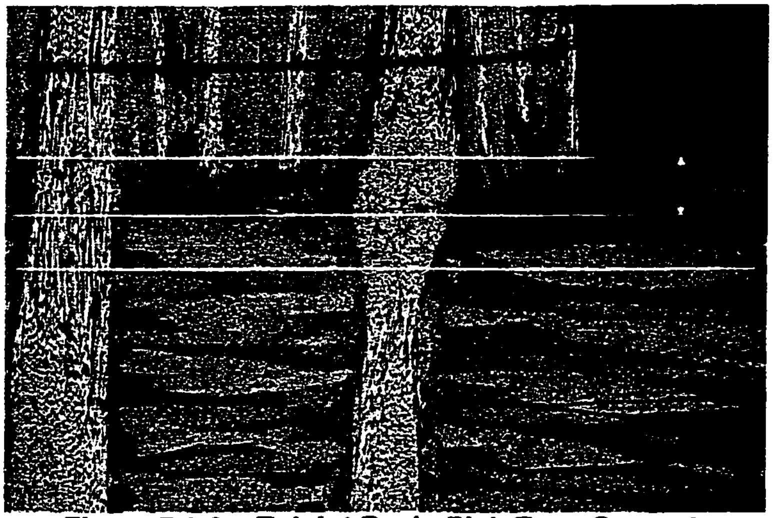

Figure 7.1-2. T-Joint Resin-Rich Zone Geometry.

7.2 Flexure Numerical Results

The flexure analysis finite element model contained 2960 PLANE183 8-node quadrilateral elements, 32 PLANE2 6-node triangular elements, and 156 LINK1 spar elements. The finite element mesh is shown in Figure 7.2-1. Quasi-isotropic material properties were used for the composite web and flange and isotropic material properties were used for the resin-rich fillet and web-to-flange interface. The two rows of fiber insertions were modeled using IM7 6k fiber tow properties. A nodal force of 445 N was applied normal to the web 2.54 cm from the web-to-flange interface. Fixed boundary conditions (zero displacement) were assumed at the flange interface to represent the bonded flange-to-fixture attachment constraint. The nonlinear FEA results include large displacement and nonlinear material properties for the PR520 resin-rich zone. A Newton-Raphson iterative procedure was used to solve each incremental load step.

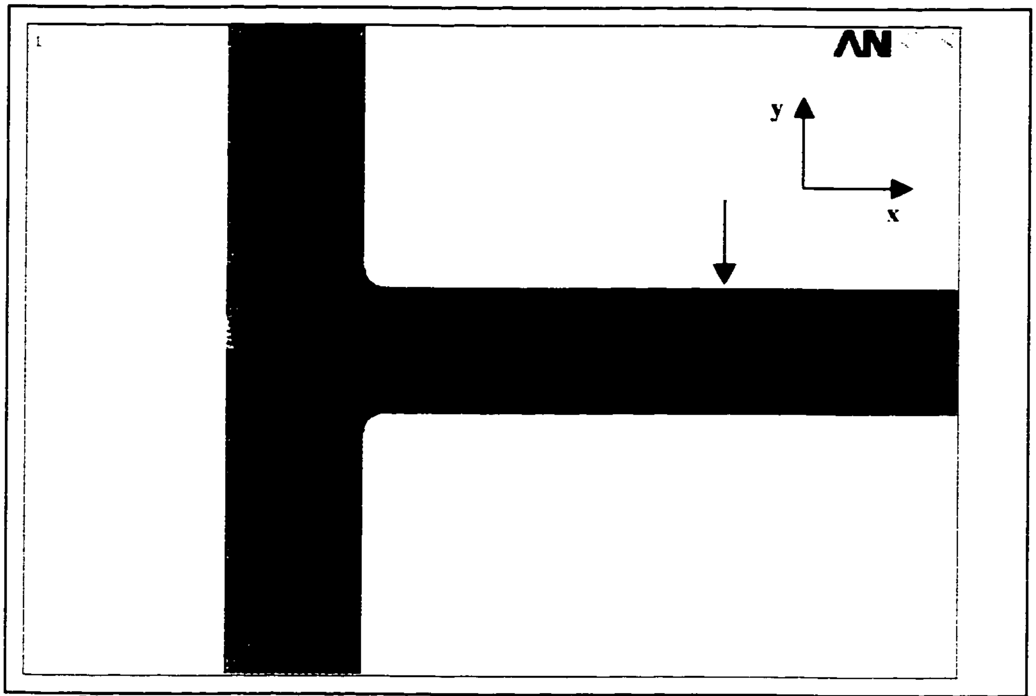

Figure 7.2-1. Linear and Nonlinear Flexure Finite Element Mesh.

Figure 7.2-2 shows the linear and nonlinear predicted and experimental load-displacement response of the T-joint under flexure loading. The experimental load-displacement plot indicates a slight amount of nonlinearity. As shown, the nonlinear predicted response more closely matches the experimental results.

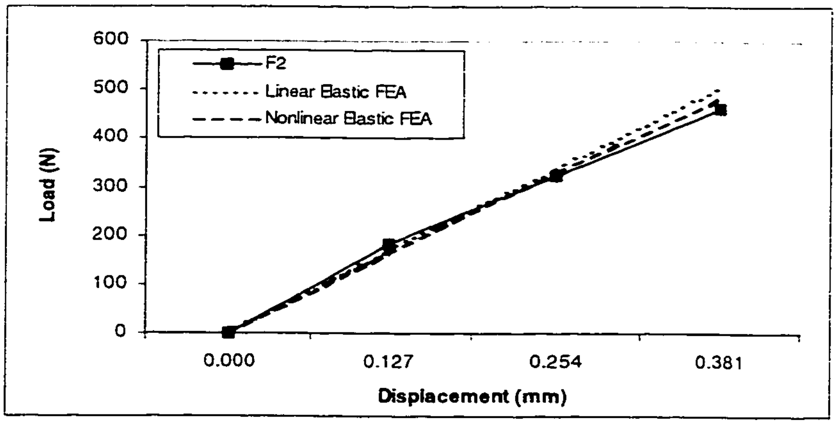

Figure 7.2-2. Linear and Nonlinear Predicted and Actual Load-Displacement Plot for Flexure Specimen F2.

The numerically determined stress contour plot for the linear elastic analysis is shown in Figure 7.2-3. Shown are the normal stress in the x-direction, σ_x and in the y-direction, σ_y, the in-plane shear stress, τ_{xy} and the maximum principal stress, σ_1. Figure 7.2-4, shows the linear elastic effective stress. A peak effective stress of 91.2 MPa is predicted in the linear elastic analysis. Figure 7.2-5 shows the nonlinear stress contour plots and Figure 7.2-6 shows the nonlinear elastic effective stress contour plot. The nonlinear analysis predicts a slightly higher effective stress of 94.5 MPa at the initial damage load. The first principal stress for the linear and nonlinear analysis is 95.0 MPa and 92.9 MPa, respectively.

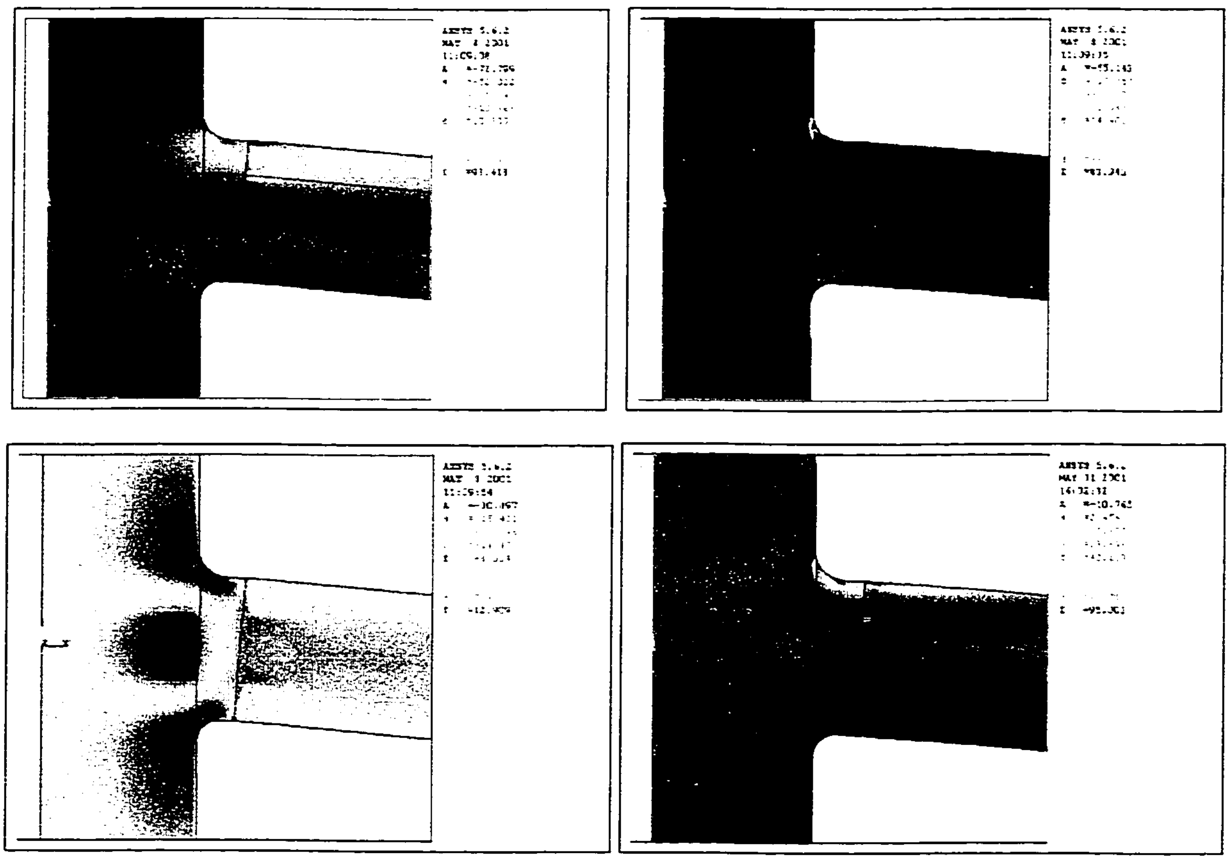

Figure 7.2-3. T-Joint Linear Elastic Flexure Stress Contours (MPa): (a) Normal Stress, σ_x, (b) Normal Stress, σ_y, (c) In-Plane Shear Stress, τ_{xy}, and (d) Maximum Principal Stress, σ_1.

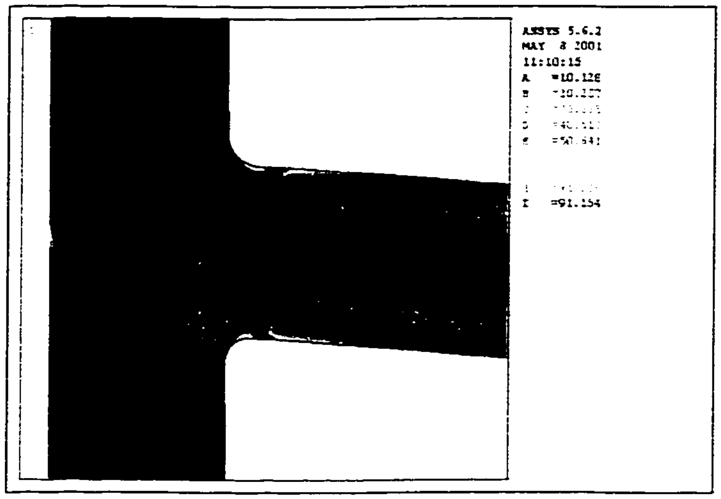

Figure 7.2-4. T-Joint Linear Elastic Flexure Effective Stress Contour, σ_{eff} (MPa).

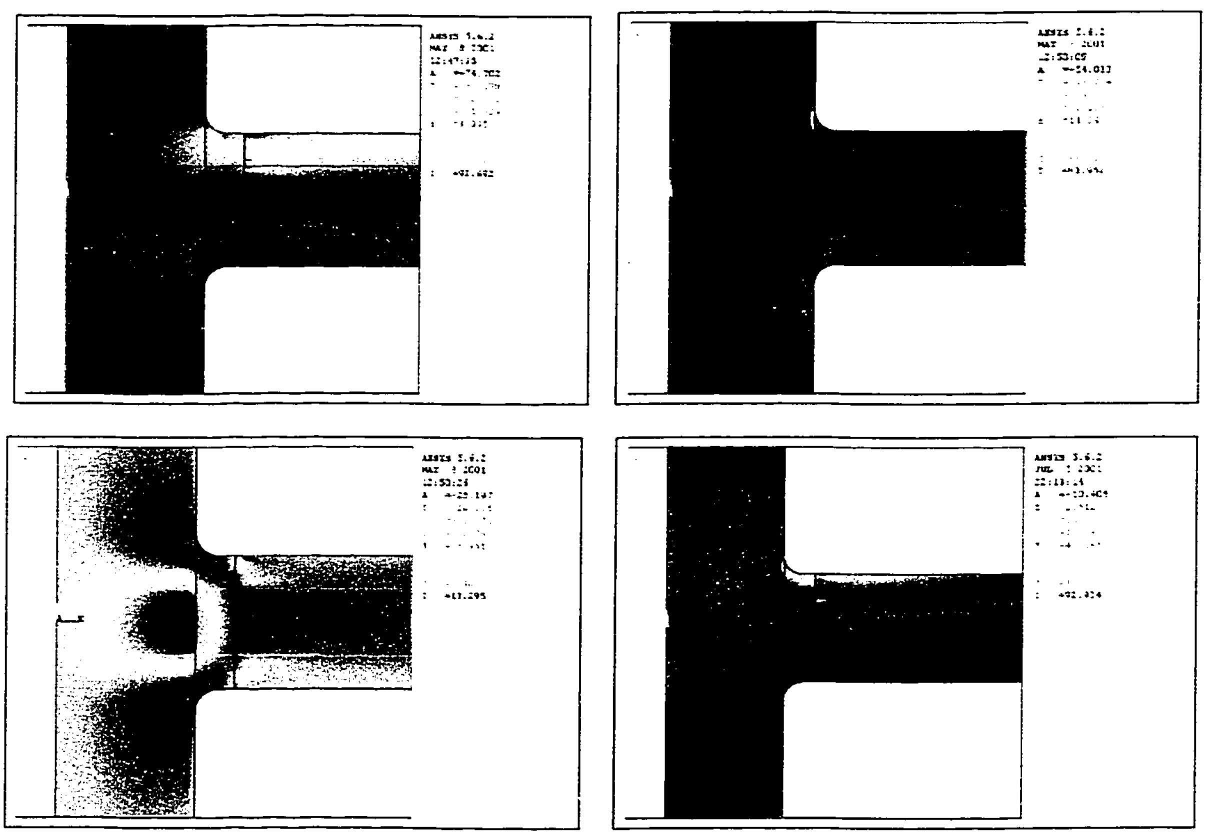

Figure 7.2-5. T-Joint Nonlinear Elastic Flexure Stress Contours (MPa): (a) Normal Stress, σ_x, (b) Normal Stress, σ_y, (c) In-Plane Shear Stress, τ_{xy}, and (d) Maximum Principal Stress, σ_1.

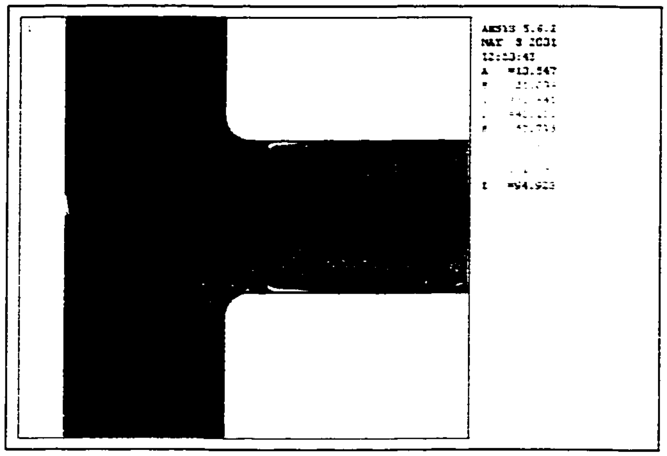

Figure 7.2-6. T-Joint Nonlinear Elastic Flexure Effective Stress Contour, σ_{eff} (MPa).

Experimental observations of the optical micrographs of failed flexure specimens, as shown in Figure 6.1-7, demonstrated that a crack initiates from the resin-rich fillet region and propagates across the web-to-flange interface. Based on these observations, a damage progression finite element analysis was performed. A series of six steps representing an accumulation of damage with increased load were created to model the mechanical behavior under flexure loading. The extent of damage accumulation in the models was defined by the experimental load-displacement record of Figure 6.1-4.

Figure 7.2-7 (a) through (f) show the finite element mesh for the damage progression model. In Figure 7.2-7 (a) no damage is present. This represents the elastic region of the load-displacement plot up to initial failure. Figure 7.2-7 (b) shows an incipient crack in the resin-rich fillet region at the web-to-flange interface. This represents the initial drop in load-displacement. The magnitude of the drop is indicative of the extent of damage to the T-joint. Figure 7.2-7 (c) shows continued fillet crack propagation, (d) shows the crack traversing the web-to-flange interface, (e) shows the crack extending to the 1st fiber insertion, and (f) shows the crack reaching the 2nd fiber insertion.

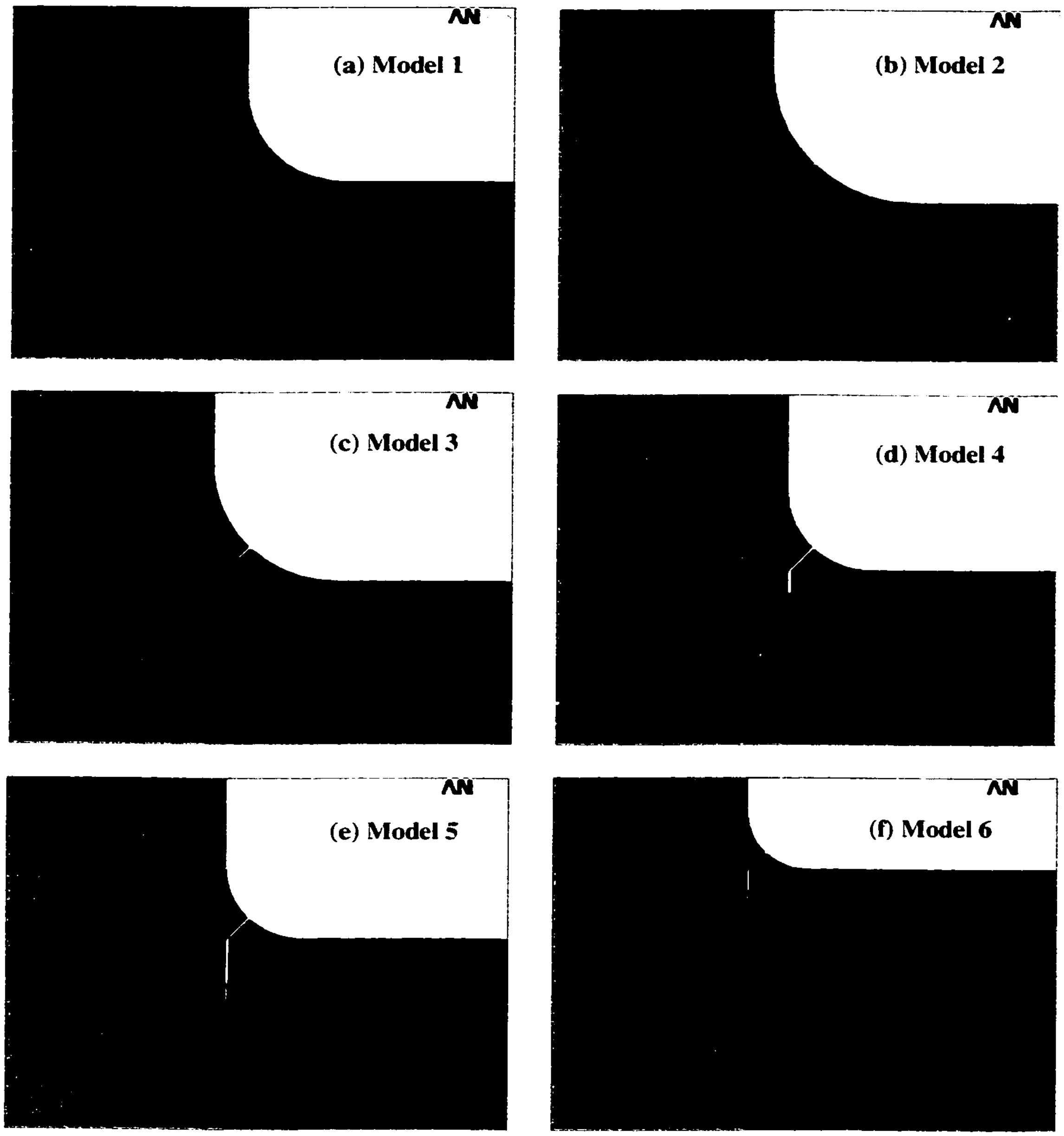

Figure 7.2-7. Flexure Damage Progression Finite Element Analysis Mesh for Models 1-6.

An analysis was performed on the T-joint to model the fiber insertion tow under progressive damage. T-joint deflection is measured as a function of fiber insertion tow area under constant flexural loading and crack length. Results of this analysis are shown in Figure 7.2-8. The T-joint displacement increases as the IM7 tow area decreases under progressive fiber insertion damage.

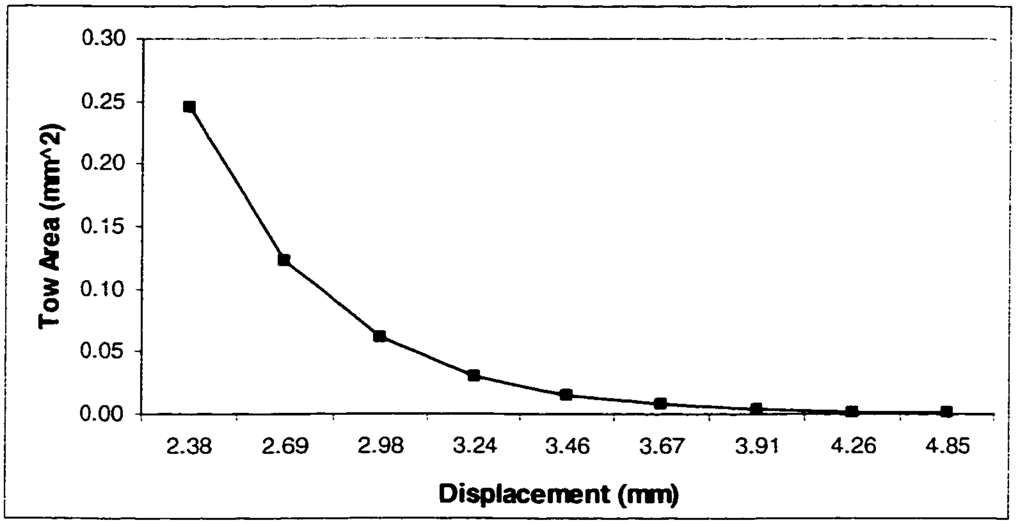

Figure 7.2-8. IM7 Fiber Insertion Damage Progression under Flexure Loading.

Figure 7.2-9 shows the predicted load-displacement plot under flexural load for specimen F1. The initial nearly linear region is modeled with no damage as shown in Figure 7.2-7 (a). The initial crack at point "a" coincides with a matrix cracking forming in the fillet region at the web-to-flange interface and propagating to the fiber insertion adjacent to the applied load or first fiber insertion. As shown, the load-displacement plot is again nearly linear from point "b" up to point "c". In this region, as indicated by the analysis, the damage is propagating to the second fiber insertion and increasing the load on the first fiber insertion. The first fiber insertion is degrading as represented by Figure 7.2-8. Further loading to point "d" results in fiber tow filament breakage and insertion/matrix interface degradation.

Figure 7.2-10 shows the predicted and actual strain-load data for gage location 9 and 12. The trend of the predicted response is in agreement with the experimental data. The predicted tensile strain at gage location 9 is approximately 26% higher at initial failure and 19% higher at ultimate failure. The predicted compressive strain at gage location 12 is approximately 13% lower at initial failure and 22% lower at ultimate failure. The difference in magnitude may potentially be attributed to T-joint web-to-flange perpendicularity tolerances during part manufacture.

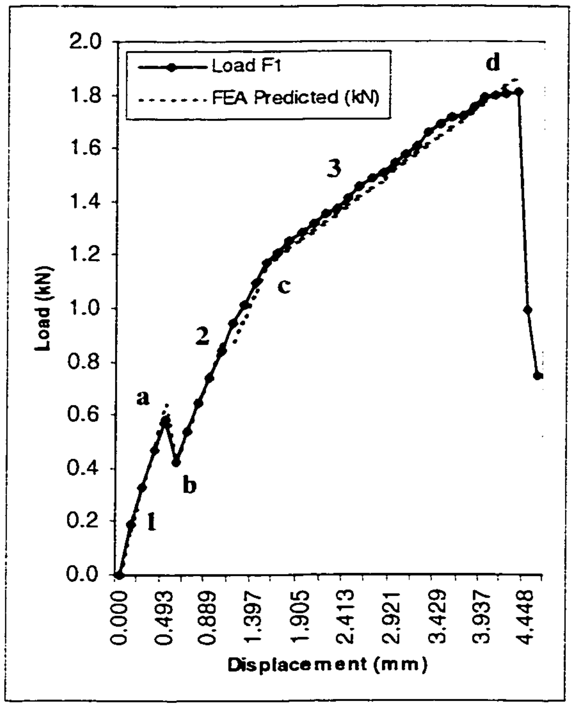

Figure 7.2-9. Predicted and Actual Load-Displacement Damage Progression Under Flexure Loading.

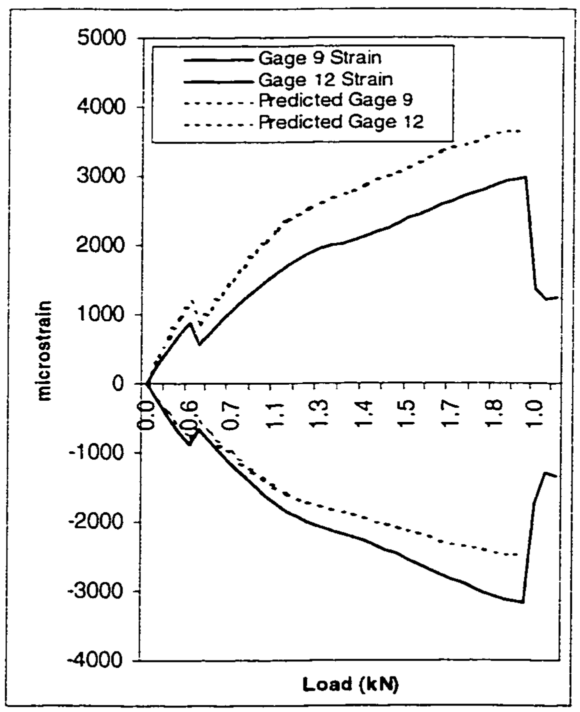

Figure 7.2-10. Predicted and Actual Strain-Load Plot of Damage Progression Under Flexure Loading.

Figure 7.2-11 shows the effective stress contours for damage progression models 1 through 6. Damage progresses at the point the peak stress exceeds the local matrix tensile stress in the radius fillet and web-to-flange interface. Additional contour plots representing the entire stress field are contained in Appendix H.

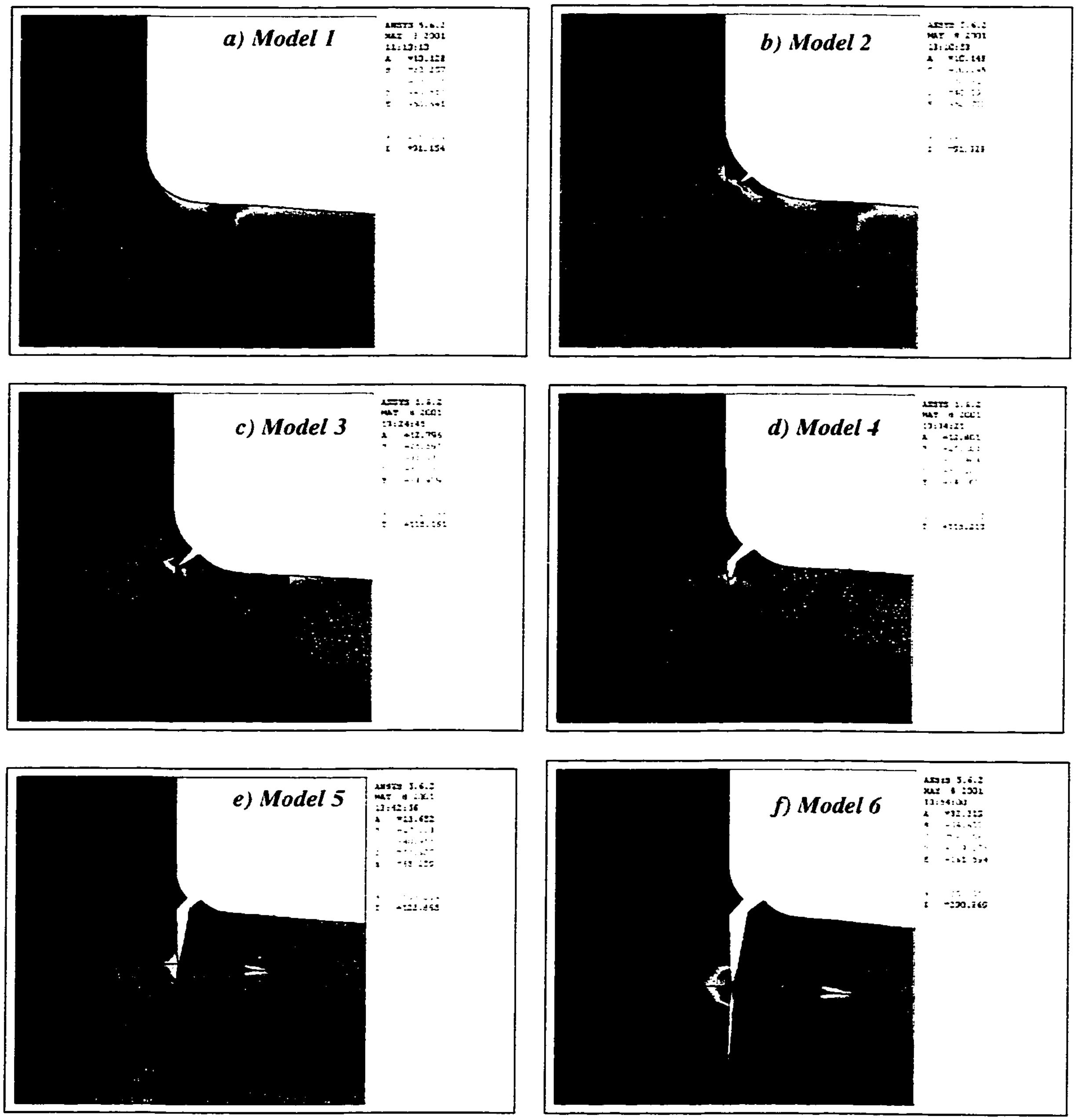

Figure 7.2-11. Flexure Damage Progression Effective Stress (MPa), σ_{eff}.

7.3 Tension Numerical Results

Simple support tension specimens were modeled using linear elastic and progressive damage finite element analyses. Figure 7.3-1 shows the direction of load application and boundary conditions for the symmetric simple support tension analysis. The finite element model used for this analysis contained 1260 PLANE183 8-node quadrilateral elements, 32 PLANE2 6-node triangular elements, and 38 LINK1 2-node spar elements. The finite element mesh is shown in Figure 7.3-2. Quasi-isotropic material properties were used for the composite web and flange and isotropic material properties were used for the resin-rich fillet and web-to-flange interface. The two rows of fiber insertions were modeled using IM7 6k fiber tow properties. Simple support boundary conditions (zero displacement) were assumed at the flange interface to represent the flange constraint.

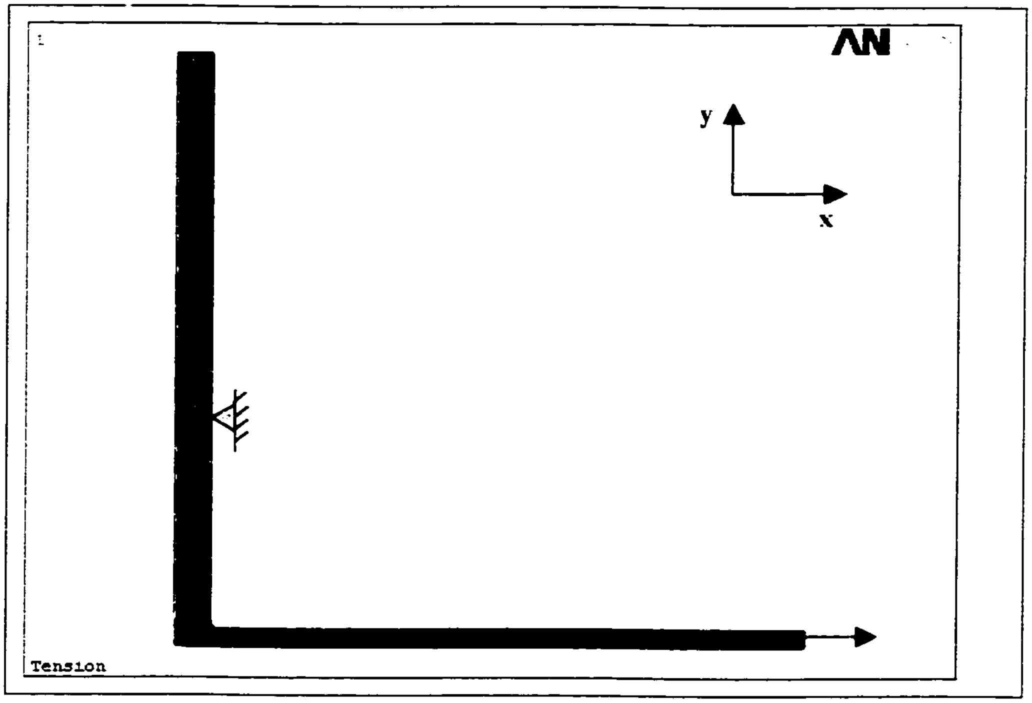

Figure 7.3-1. Tension Finite Element Boundary Conditions.

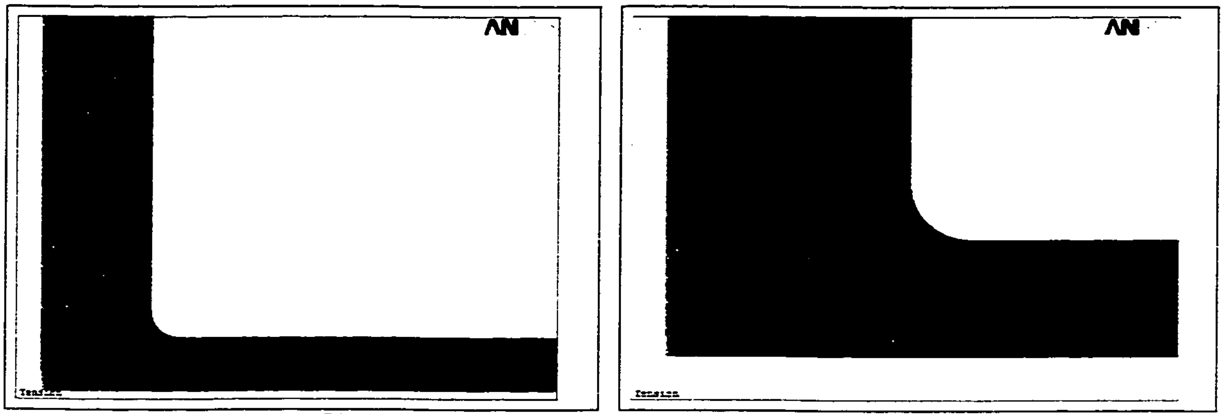

Figure 7.3-2. Tension Finite Element Mesh.

Figure 7.3-3 shows the predicted and actual load-displacement response of the T-joint under tension loading. Good agreement is shown between the experimental and predicted results. The stress contour plots are shown in Figure 7.2-4. Shown are the local normal stress in the x-direction, σ_x and in the y-direction, σ_y. Also shown are the in-plane shear stress, τ_{xy} and the maximum principal stress, σ_1. Figure 7.3-5 shows the effective stress plot for the T-joint under tensile loading. Peak stresses are shown at the radius fillet and at the fiber insertion transition zone in the upper portion of the web-to-flange interface.

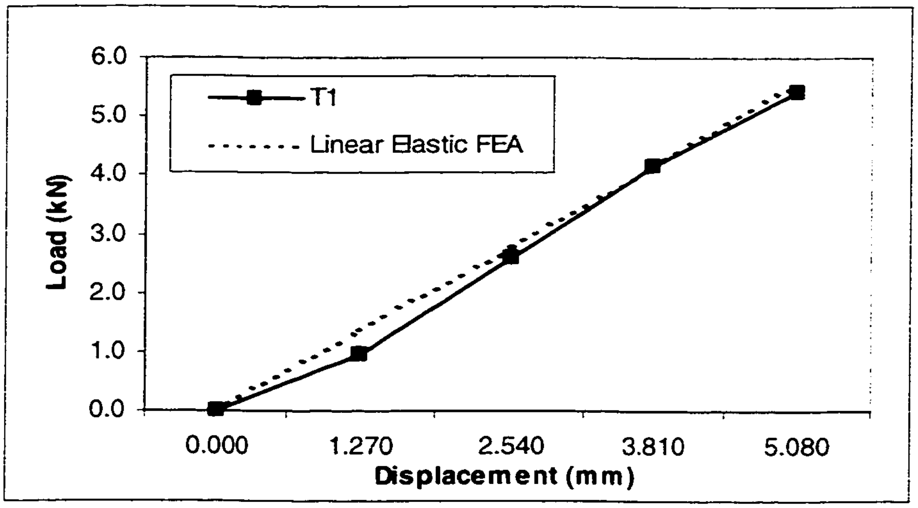

Figure 7.3-3. Predicted and Actual Load-Displacement Plot: Tension Specimen T1

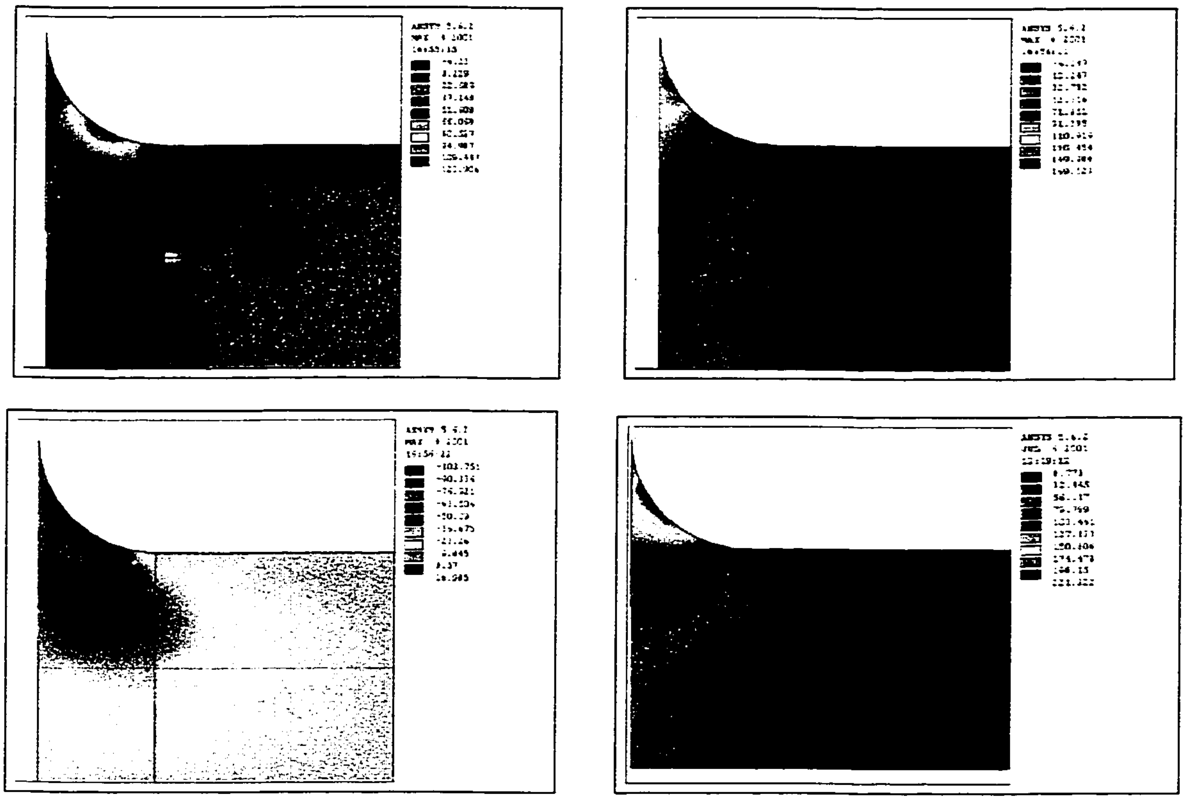

Figure 7.3-4. Linear Elastic Tension Effective Stress (MPa): (a) Normal Stress, σ_x, (b) Normal Stress, σ_y, (c) In-Plane Shear Stress, τ_{xy}, and (d) Maximum Principal Stress, σ_1.

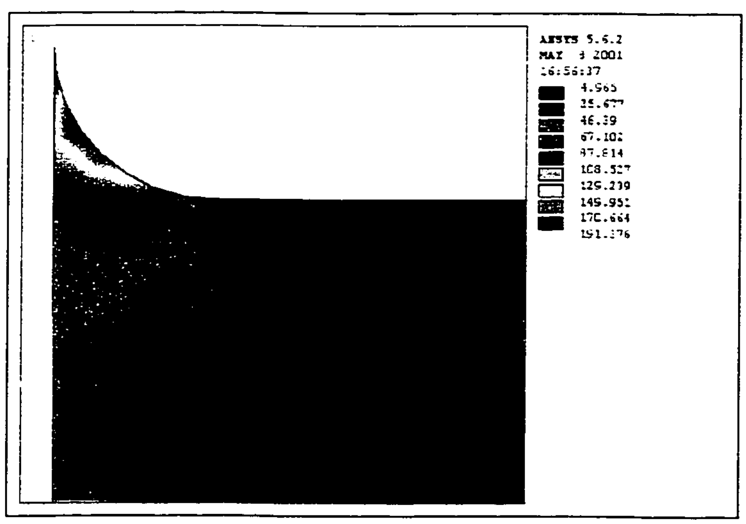

Figure 7.3-5. Linear Elastic Tension Effective Stress, σ_{eff} (MPa).

A damage progression analysis was performed on the T-joint under tension loading. As in the case of the flexure numerical analysis, experimental observation of failed specimens were used in determining the extend and direction of the accumulative damage under increased load. Figure 7.3-6 (a) through (d) shows the finite element mesh for the damage progression analysis. Model 1 shows the FEA mesh for the T-joint with no crack present. Model 2 represents a crack that emanates from the resin-rich radius filler. Model 3 contains a crack at the web-to-flange interface and model 4 shows the crack extending to the first IM7 fiber tow insertion.

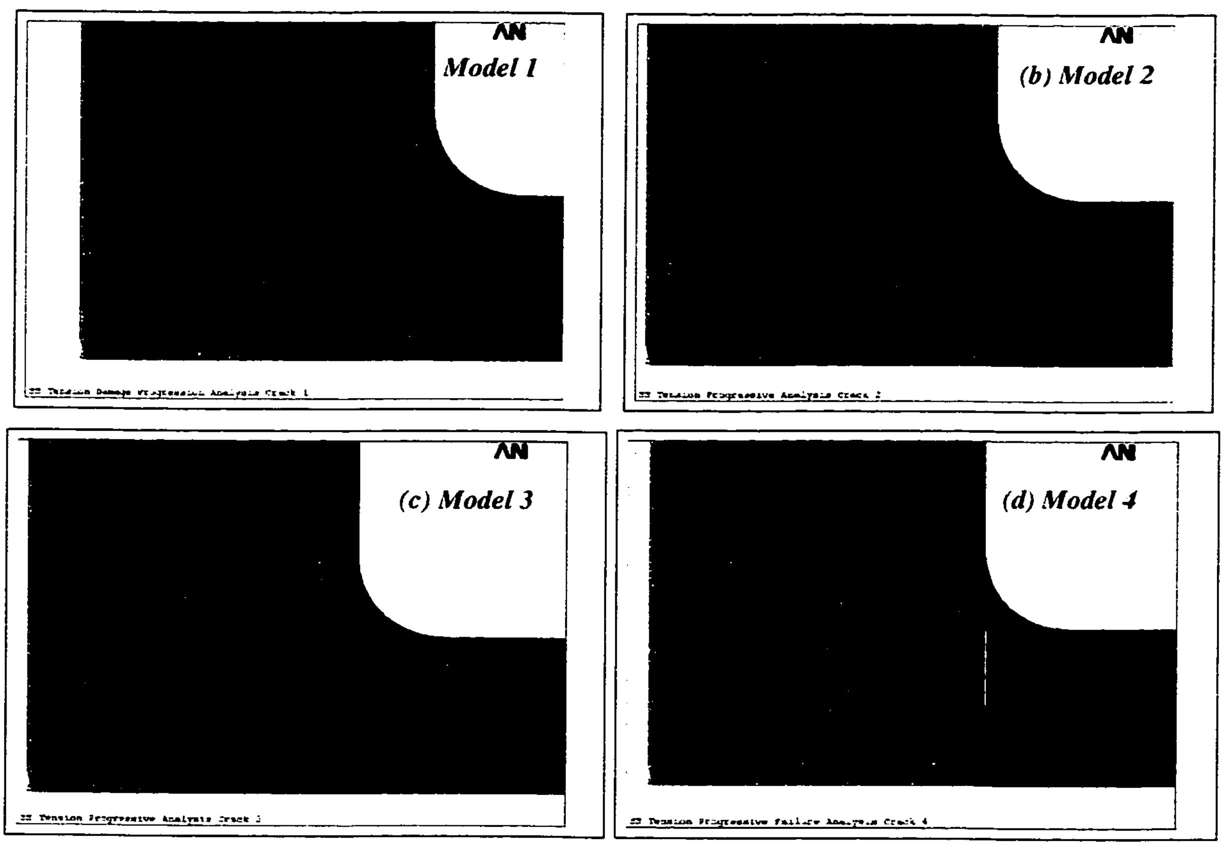

Figure 7.3-6. Tension Damage Progression Finite Element Analysis Mesh for Models 1-4.

Figure 7.3-7 shows the predicted and experimental load-displacement plot through ultimate failure. At initial failure, a drop is observed in the load-displacement plot. This is indicative of initial crack formation as shown in Figure 7.3-6 (b). The predicted response matches the experimental behavior. Figure 7.3-8 shows the predicted and actual strain-load response for strain gage locations 3 and 6. Close agreement is shown for predicted and experimentally determined strain at gage location 6 at T-joint ultimate failure. At gage location 3, a similar trend is shown for the predicted and actual strain response. However, strain is over predicted by approximately 25% at ultimate failure. Variations in part manufacture including web-to-flange perpendicularity, fiber insertion spacing and pitch, and preform thickness may attribute in part to the differences in predicted and actual load-strain response.

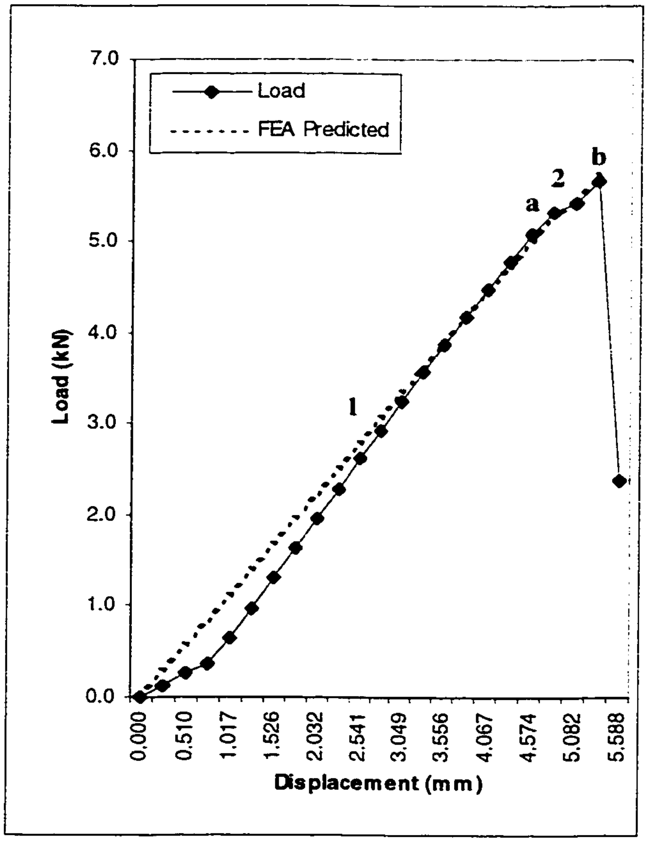

Figure 7.3-7. T-Joint Tension Damage Progression Predicted and Experimental Load-Displacement Plot.

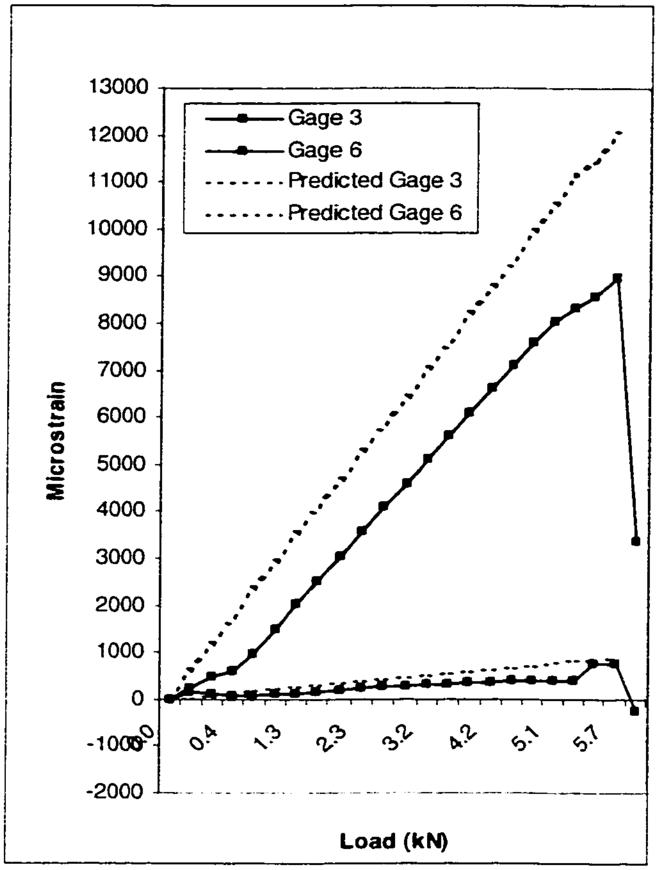

Figure 7.3-8. T-Joint Damage Progression Predicted and Actual Strain-Load Results.

Figure 7.3-9 shows the normal stress contours, σ_x for the damage progression analysis under simple support tension loading. In model 1, the applied load is equal to the average initial damage load. Damage progression models correspond to that of the mesh geometry shown in Figure 7.3-6. The peak stresses in models 2 through 4 far exceeds that of the matrix tensile stress indicating crack propagation. Again, additional contour plots representing the entire stress field are contained in Appendix H.

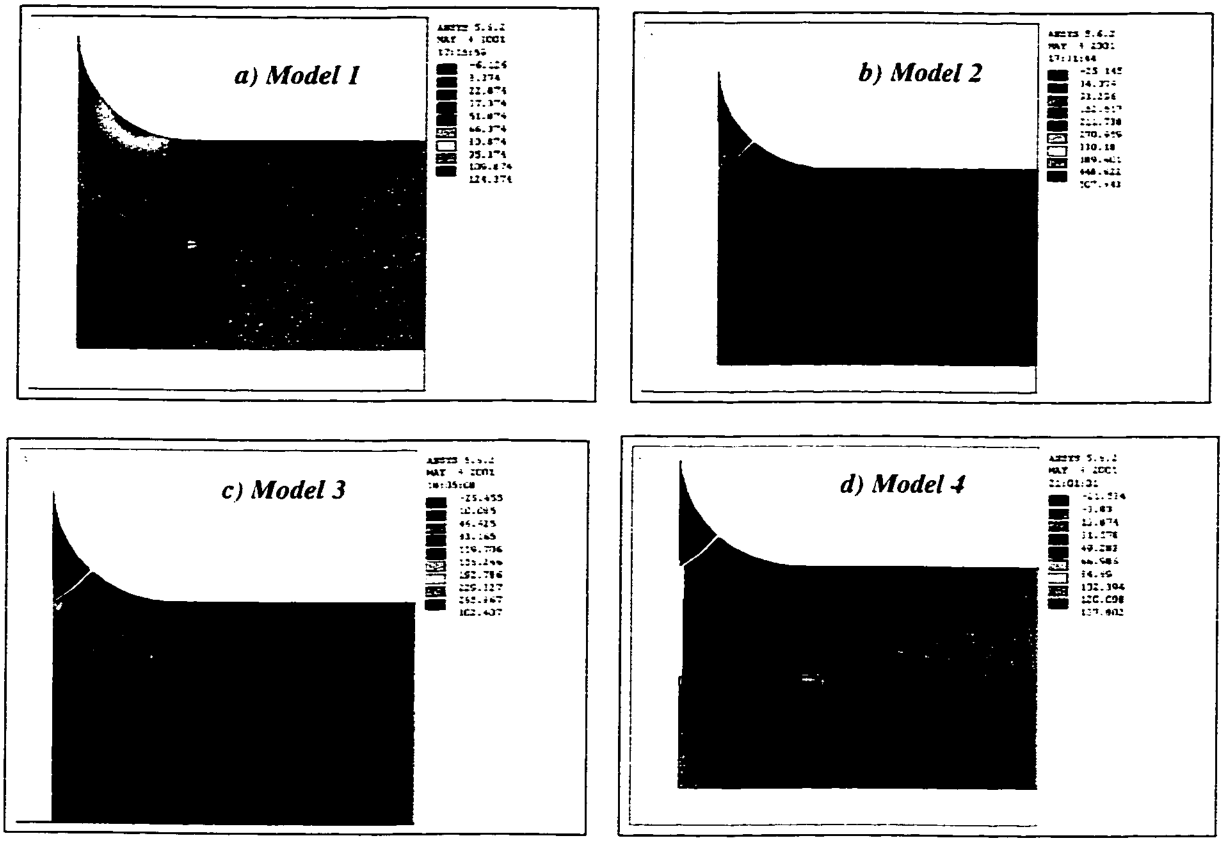

Figure 7.3-9. Tension Damage Progression Normal Stress (MPa), σ_x.

7.4 Rail Shear Numerical Results

A three-dimensional rail shear linear elastic finite element analysis was performed using ANSYS software. For this analysis, a half symmetric model was created including 1/8 of the specimen depth. The finite element model used for this analysis contained 9000 SOLID185 three-dimensional 8-node structural solid elements, 1007 SOLID187 three-dimensional 10-node tetrahedral solid elements, and 250 LINK8 three-dimensional 2-node spar elements. The model has 36023 degrees of freedom. The finite element boundary conditions for the rail shear model is shown in Figure 7.4-1. The finite element mesh is shown in Figure 7.4-2. Quasi-isotropic material properties were used for the composite web and flange and isotropic material properties were used for the resin-rich fillet and web-to-flange interface. The two rows of fiber insertions were modeled using

IM7 6k fiber tow properties. A 0.125 mm nodal displacement was applied to the web in the z-direction. Fixed boundary conditions (zero displacement) were assumed at the flange interface to represent the bolted flange-to-fixture attachment constraint. The reaction load at the fastener boundary condition was then compared to the actual load-displacement data.

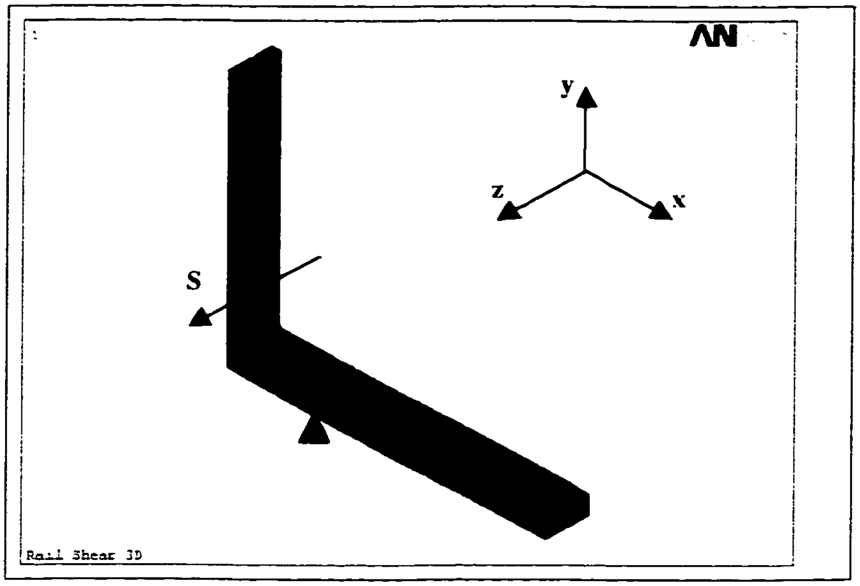

Figure 7.4-1. Rail Shear Finite Element Boundary Conditions.

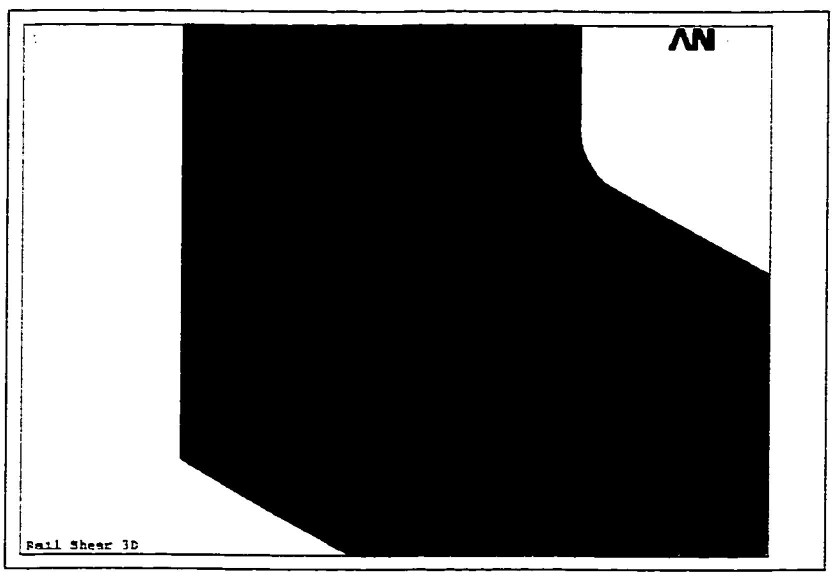

Figure 7.4-2. Rail Shear Finite Element Mesh.

Results of the linear elastic finite element analysis are shown in Figure 7.4-3. The predicted and average actual load-displacement are shown to be in close agreement through T-joint ultimate failure. The initial nonlinearity in the load-displacement curve is indicative of specimen fixture seating.

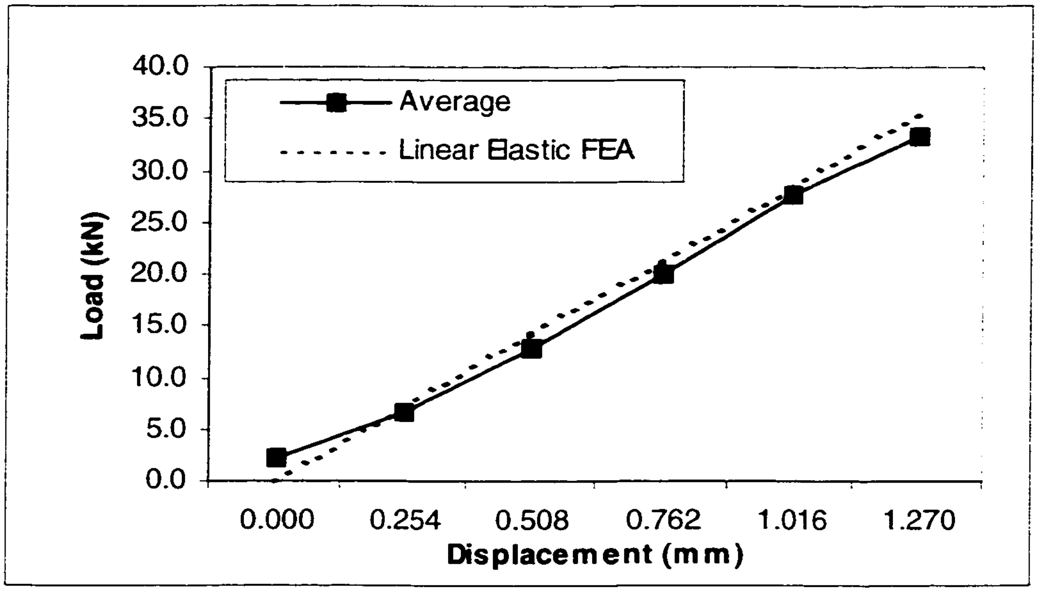

Figure 7.4-3. Predicted and Actual Load-Displacement Plot: Rail Shear Average.

Figure 7.4-4 shows the effective stress contours for the T-joint under rail shear loading. Peak stresses are shown to occur at the fiber insertion and in the web-to-flange interface region. The peak matrix interface effective stress is 101.3 MPa and the maximum model effective stress is 129.0 MPa. Appendix H contains the remaining stress contour plots under shear loading. Since the T-joint behavior under rail shear loading was linear up to ultimate failure, a damage progression finite element analysis was not performed.

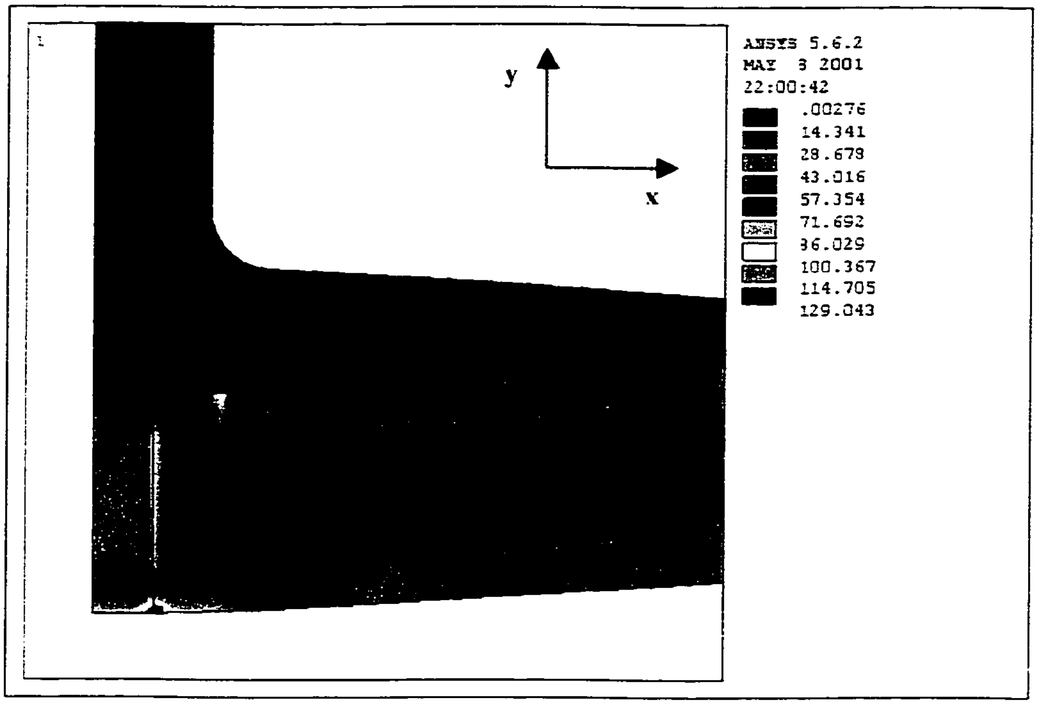

Figure 7.4-4. Linear Elastic Rail Shear Effective Stress (MPa), σ_{eff}.

CHAPTER 8
DISCUSSION

This chapter provides a detailed discussion of T-joint failure analysis, mechanical behavior, and parametric analysis. The T-joint failure analysis and mechanical behavior are established from experimental and numerical results. Numerical models, developed in Chapter 7, are used to establish parametric design curves to discern the effects of fiber insertion tow modulus and filament count, fiber insertion depth, and resin-rich interface thickness under flexure, tension, and shear loading.

8.1 T-Joint Failure Analysis

A Failure analysis was performed on the T-joints under flexure, tension, and rail shear loading. Table 8.1-1 shows a comparison of experimentally determined allowable laminate strains as presented in Chapter 5 and measured peak T-joint strains as presented in Chapter 6. Peak laminate outer ply shear strains were determined using the 3-element rectangular stacked rosette relations given by equation 8.1-1:[87]

$$\varepsilon_A = \varepsilon_{xx} \qquad \varepsilon_B = \frac{\varepsilon_{xx} + \varepsilon_{yy} + \gamma_{xy}}{2} \qquad \varepsilon_C = \varepsilon_{yy} \qquad 8.1\text{-}1$$

where the shear strain γ_{xy}, is given by equation 8.1-2:

$$\gamma_{xy} = 2\varepsilon_B - \varepsilon_A - \varepsilon_C \qquad 8.1\text{-}2$$

The laminate failure margin of safety, MS[85] was then determined using the maximum strain failure criteria as provided in Appendix B and is given by equation 8.1-3:

$$MS = \frac{e_f}{\varepsilon_f} - 1 \qquad 8.1\text{-}3$$

Table 8.1-1. T-Joint Laminate Maximum Strain Failure Analysis.

T-joint	Critical Measurement	Gage Numbers	Average Measured Peak Laminate Outer Ply Strain (microstrain)	Laminate Failure Strain (microstrain)	Margin of Safety (MS)
Flexure					
Web	Tensile Strain (ε_x)	9	2984	13934	3.65
Web	Compressive Strain (ε_x)	12	3192	12449	2.90
Web	Shear Strain (γ_{xy})	9, 10, 11	5296	12166	1.30
Tension					
Flange	Tensile Strain (ε_x)	3	9620	13934	0.45
Flange	Shear Strain (γ_{xy})	3, 4, 5	2020	12166	5.03
Rail Shear					
Flange	Shear Strain (γ_{xy})	10, 11, 12	4240	12166	1.87

As shown in Table 8.1-1, the positive margins of safety indicate no web or flange laminate failure occurred during the T-joint experiments. Instead, the failures occurred locally at the web-to-flange interface. This is supported by experimental observation and numerical analysis. Initial T-joint failure may be predicted by close examination of the local stresses at the web-to-flange interface. Assuming isotropic matrix properties, initial T-joint failure may be defined as the point when the effective stress in the resin-rich interface fillet region exceeds that of the neat resin tensile failure strength. The effective stress relation in terms of principal stresses for the three-dimensional case is given by equation 8.1-4:[88]

$$\sigma_{eff}^2 \geq \frac{1}{2}\left[(\sigma_1 - \sigma_2)^2 + (\sigma_2 - \sigma_3)^2 + (\sigma_3 - \sigma_1)^2\right] \geq \sigma_{fm} \qquad 8.1\text{-}4$$

where σ_{fm} is the uniaxial failure stress of the neat resin. For the case of two-dimensional plane strain the effective stress is then given by equation 8.1-5:

$$\sigma_{eff}^2 \geq \left[\left(\sigma_1^2+\sigma_2^2\right)\left(v^2-v+1\right)-\sigma_1\sigma_2\left(2v^2-2v-1\right)\right] \geq \sigma_{fm} \qquad 8.1\text{-}5$$

Table 8.1-2 provides a summary of the T-joint initial damage analysis based on the effective stress failure criteria. Comparisons are made under flexure, tension, and rail shear loading. The linear and nonlinear elastic finite element analysis models, as presented in Chapter 7, were used to determine the effective stress. The effective matrix strength was determined at the point of the experimentally determined average initial damage load. Good agreement is shown between the predicted effective matrix strength and the PR520 allowable matrix tensile strength. For the case of linear elastic and nonlinear elastic flexure, the difference in predicted and actual failure stress is 2% and 3%, respectively. For the tension analysis the difference in predicted and actual failure stress is 9% and for the case of rail shear 11% .

Table 8.1-2. T-Joint Initial Damage Failure Analysis.

T-joint Load Case	Finite Element Analysis Type	PR520 Tensile Failure Strength (MPa)	Average Initial Damage Load (kN)	Predicted Effective Matrix Strength at Initial Damage Load (MPa)
Flexure	2D Linear Elastic	91.0	0.567	89.1
	2D Nonlinear Elastic	91.0	0.567	93.3
Tension	2D Linear Elastic	91.0	5.095	99.5
Rail Shear	3D Linear Elastic	91.0	32.29	101.3

8.2 Mechanical Behavior

The mechanical behavior of the T-300/PR520 transverse stitched composite T-joints under flexure loading may be characterized in three distinct regions as indicated on the load-displacement plot of Figure 6.1-4. In region 1, the behavior is nearly linear elastic up to the initial damage load, showing only a slight amount of nonlinearity near the proportional limit. In region 2, with increased load, the behavior is again nearly linear. Region 3 is marked by a change in slope of the load-displacement plot leading to catastrophic failure. The three regions of behavior are discussed in greater detail below and a damage progression schematic is presented based on experimental and numerical results.

Under initial flexure load, as represented by region 1 of the load-displacement plot of Figure 6.1-4, the T-joint web deflects under increased load. This has the effect of loading the fiber insertion adjacent to the applied load in tension and the furthermost fiber insertion in compression. As the fillet matrix stress exceeds the PR520 neat resin tensile strength, as predicted in Table 8.1-2, a crack initiates at the outer surface of the radius filler. The linear and nonlinear elastic finite element analysis contour plots of Figure 7.2-4 and Figure 7.2-6 predict that the effective stress in the fillet region will just exceed the matrix tensile stress at the experimentally determined damage initiation load. The predicted linear and nonlinear elastic effective stresses are 89.1 MPa and 93.3 MPa, respectively.

Initial T-joint failure may be observed as a discrete drop in the load-displacement record as shown from point "a" to "b" in Figure 6.1-4. A 25% drop in load-displacement at initial damage is typical under flexure loading. The strain-load plot of Figure 6.1-5 shows increased surface strains up to the initial damage load. At the initial damage load, the surface strain-load measurements have a discrete drop in recorded strain indicating a loss in stiffness of the T-joint under the initial damage.

The extent of initial damage may be characterized by a damage progression finite element analysis. Based on the damage progression models of Figure 7.2-7, it can be shown that in order to match the appropriate response of the T-joint under flexure loading, as shown at points "a" and "b" on the load-displacement plot of Figure 6.1-4, the crack must be extended through the resin-rich fillet region and along the interface to the first fiber insertion. This damage accumulation is represented by the damage progression finite element model 5 of Figure 7.2-7 (e). The direction of the crack used in this analysis may be intimated from the optical micrograph of the failed specimen shown in Figure 6.1-7. Based on experimental observations and numerical analysis, the extent of the initial damage under flexure loading may then be represented in a damage progression schematic. Figure 8.2-1 (a) and (b) show the extent of the damage accumulation at the initial damage load. Again, this is substantiated by the progressive failure analysis load-displacement response.

Region 2 of Figure 6.1-4 is marked by nearly linear load-displacement and strain-load behavior. The initial damage has the effect of redistributing additional load to the first fiber insertion. Increased loading beyond the initial damage load, as represented by region 2 of the load-displacement plot of Figure 6.1-4 point "b" causes fiber bridging and crack propagation to the neighboring fiber insertion. The fiber bridging behavior gives rise to an increased damage tolerance or an ability to carry additional load beyond initial failure.

The extent of damage represented by point "c" of Figure 6.1-4 may be represented by model 6 of the damage progression finite element analysis shown in Figure 7.2-7. The predicted and actual load-displacement behavior for region 2 is given in Figure 7.2-9. Good agreement is shown between experimental and predicted results based on the extent of damage represented by model 6. Based on the damage progression analysis and optical micrographs of failed specimens, the damage accumulation is then shown in the damage progression schematic Figure 8.2-1 (c).

Region 3 of the load-displacement plot from point "c" to "d" is marked by a change in slope and subsequent loss of T-joint stiffness. Under increased load, the fiber insertion adjacent to the applied load continuously degrades. This behavior is represented in the finite element analysis model 6 of Figure 7.2-7 by a change in fiber insertion area. Figure 7.2-8 shows the effect of fiber insertion area on T-joint deflection under flexural loading.

As the area decreases the T-joint deflection increases. Based on the fiber degradation model, good agreement is shown between the experimental and predicted load-displacement behavior of Figure 7.2-9 from point (c) to (d). With the extent of damage determined, the damage progression schematic may be further developed. Figure 8.2-1 (d) and (e) show the damage progression under increased load. Similar observations of fillet matrix cracking and subsequent damage progression was observed by Phillips and Shenoi[41] in T-joints without transverse stitching.

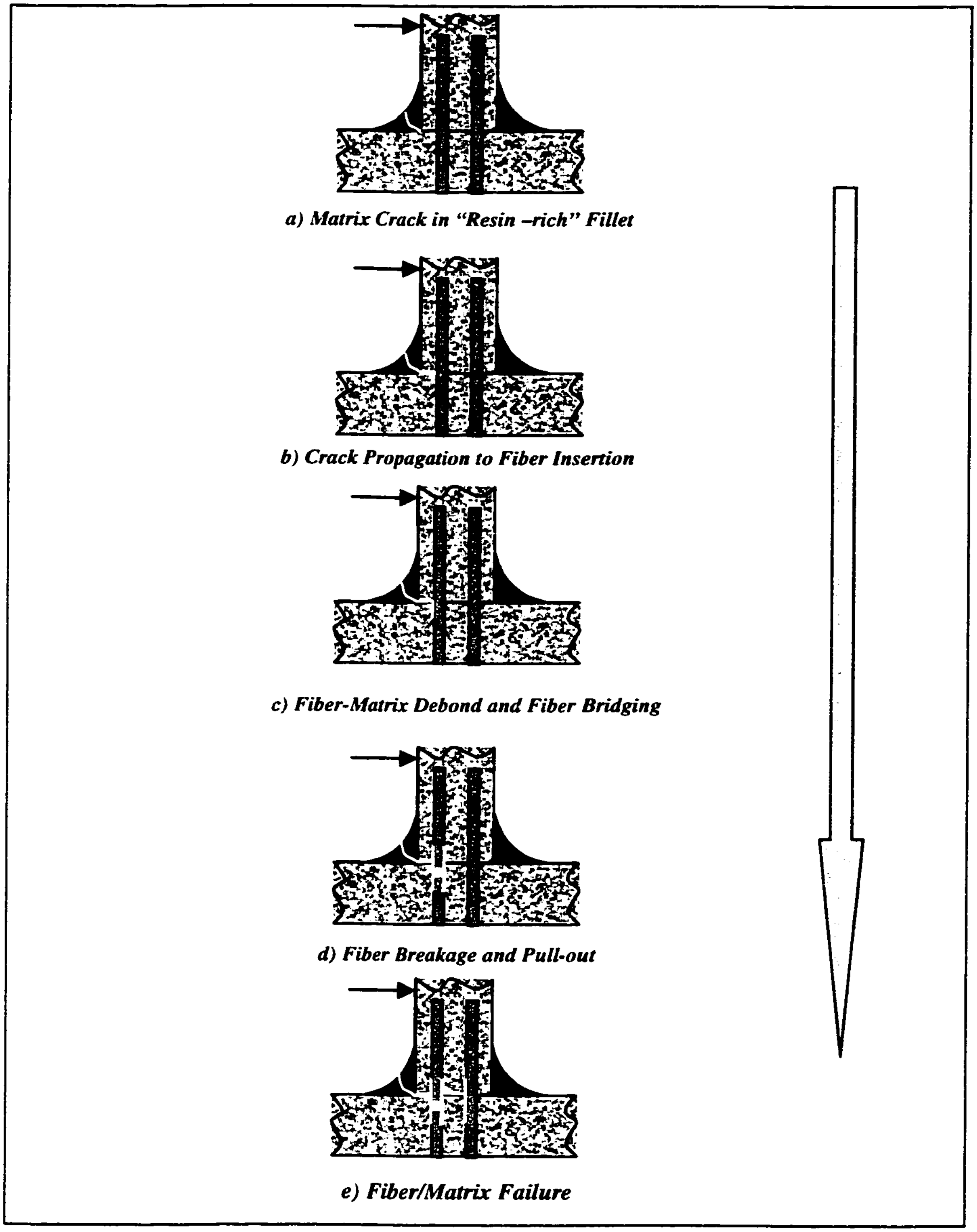

Figure 8.2-1. T-Joint Damage Progression Under Flexure Loading.

Figure 8.2-2 (a) below, shows the strain-load record for strain gage 1 under flexural loading. Gage 1, as shown in Figure 8.2-2 (b), is located on the edge of the flexure specimen near the fiber insertion, 0.624 cm from the web-to-flange interface. At initial T-joint failure, a marked jump in strain is shown that may be indicative of load transfer to the fiber insertion after fillet and flange-to-web interface matrix cracking. Also observed, is a small jump, followed by a leveling off of the strain in Region 3. This is likely due to fiber insertion degradation. The marked reduction in strain at the onset of ultimate failure is likely caused by fiber insertion failure and pullout as shown on the optical micrograph of Figure 8.2-2 (c). This experimental evidence supports the mechanical behavior presented above.

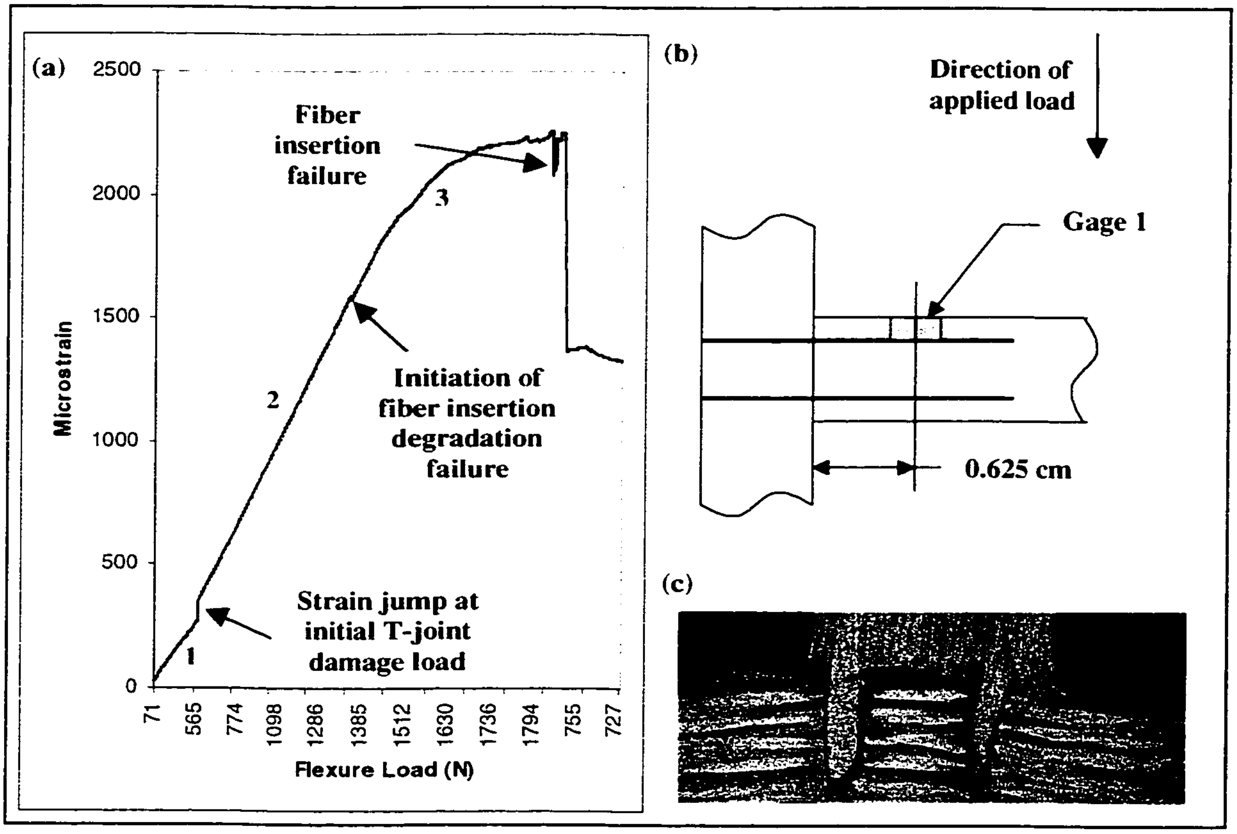

Figure 8.2-2. Strain-Load Record for Flexure Specimen F1 Gage 1: (a) Showing Damage Accumulation Events, (b) Local Instrumentation Layout, and (c) Optical Micrograph of Failed Specimen.

A comparison of the mechanical behavior of the stitched T-joints using PR520 and Shell 862 resin systems can be made. Both material systems have similar damage progression under flexure loading with three distinct load-displacement regions. In both cases the failure initiates in the resin-rich radius region and ultimate failure occurs by fiber breakage and fiber pullout.

The mechanical behavior of the T-300/PR520 transverse stitched T-joint under simple support tensile loading is marked by linear elastic behavior up to initial failure and ultimate failure occurring by fiber insertion breakage and pullout. In this case, the fiber insertions are loaded symmetrically in tension. This symmetric loading of the fiber insertions gives the tensile specimens a far greater load carrying capability than that of flexure loading. The initial damage load under simple support tension is approximately ten times greater than that of flexure. The ultimate load carrying capability under tension is approximately three times greater than that of flexure.

The mechanical behavior under tensile loading may be divided into two distinct regions as shown in Figure 6.2.2-3. In region 1, the flange deflects elastically under increased load up to point "a" on the load displacement plot. Region 2 is marked by additional linear behavior up to point "b" or ultimate load. The linear elastic finite element analysis of Figure 7.3-3 predicts the behavior in region 1. Good agreement is shown between the experimental and predicted load-displacement. Near the initial damage load, the fillet region at the web-to-flange interface exceeds that of the PR520 neat resin tensile strength. This is predicted in the failure analysis of Table 8.1-2. This is also shown in the stress contour plots of Figure 7.3-5. At the damage initiation load, a crack initiates in the fillet region and propagates to the fiber insertions. This causes a marked drop in the load-displacement as shown at point "a" of Figure 6.2.2-3. A 3-5% drop in load was noted at initial T-joint failure. A similar response is recorded in the strain-load plot as shown in Figure 6.2.2-4.

Based on the optical micrographs of the failed tension specimens, the direction and extent of damage may be determined. In the damage progression finite element model, the crack is initiated when the effective stress exceeds the tensile strength of the matrix. Based on the predicted and actual load-displacement response at initial failure as shown in Figure 7.3-7, the extent of T-joint damage may be determined. The extent of damage that provides a similar response as the experimental load-displacement is represented by Figure 7.3-6 (c) model 3, where the crack is shown starting at the radius fillet and continuing along the web-to-flange interface to the fiber insertions. The damage progression finite element model 3 shows good agreement with the experimental results at point "a" in Figure 7.3-7. Based on the ability of model 3 to predict the load-displacement response and the optical micrographs of failed specimens, the damage progression at initial failure may be developed schematically as shown in Figure 8.2-3 (a) and Figure 8.2-3 (b).

Increased loading beyond the initial damage as defined as region 2 of the load-displacement plot of Figure 6.2.2-3 than causes fiber bridging. This fiber bridging gives the T-joint an increased damage tolerance or an ability to carry additional load after first failure occurs. Region 2 of the experimental load-displacement is represented by model 4 in the damage progression finite element analysis. Again, good agreement is shown between predicted and actual load-displacement in region 2. Based on observations of optical micrographs of failed specimens, Figure 8.2-3 (c) and (d) show the accumulated damage. Fiber elongation is shown, followed by fiber breakage and fiber pullout. Loading beyond this point leads to catastrophic failure of the T-joint as shown in Figure 6.2.2-3 point "b."

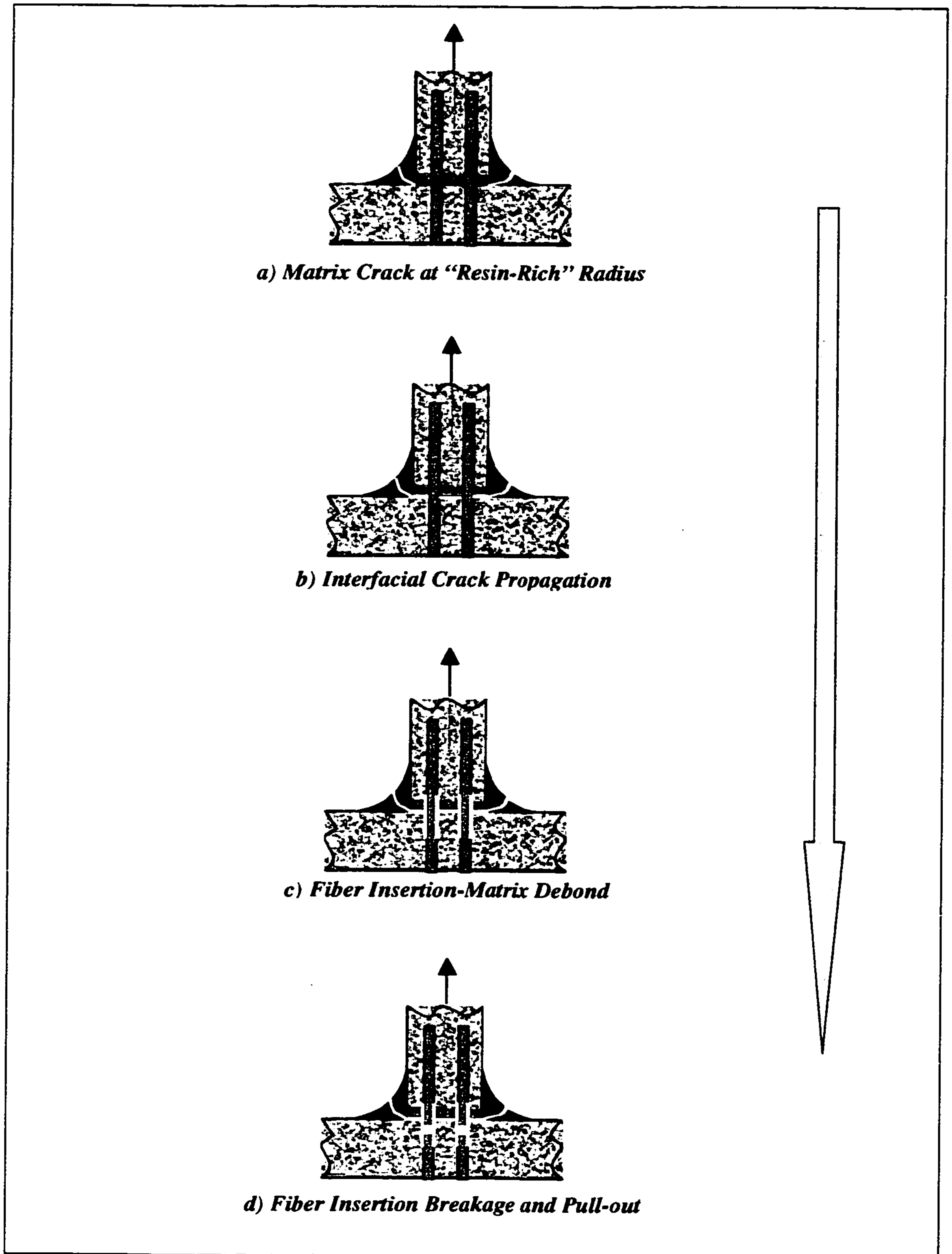

a) Matrix Crack at "Resin-Rich" Radius

b) Interfacial Crack Propagation

c) Fiber Insertion-Matrix Debond

d) Fiber Insertion Breakage and Pull-out

Figure 8.2-3. T-Joint Damage Progression under Tension Loading.

Figure 8.2-4 (a) shows the strain-strain load plot for simple support tension strain gage location 2. This gage is located on the edge of the specimen at the maximum depth of the fiber insertion as shown in Figure 8.2-4 (b). Just prior to the initial damage load, a jump in strain is noted. This jump may be due to increased load transfer to the fiber insertion at the onset of matrix cracking at the web-to-flange interface. Also shown is a discrete drop in strain at T-joint ultimate load that is likely due to fiber insertion failure. Several other discrete events are observed at various stages of damage accumulation.

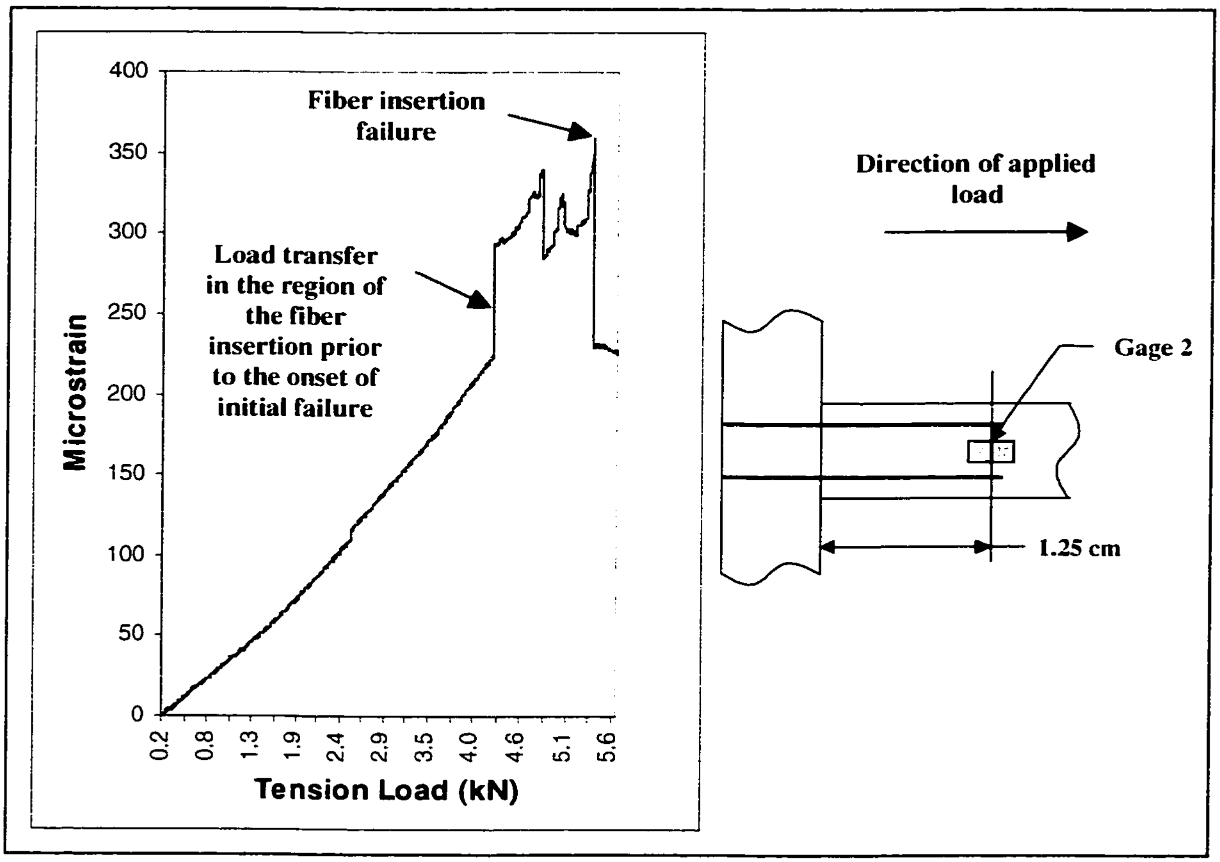

Figure 8.2-4. Strain-Load Record for Simple Support Tension Specimen T2 Gage 2: (a) Showing Damage Accumulation Events and (b) Local Instrumentation Layout.

The mechanical behavior of the T-300/PR520 rail shear T-joint specimens is marked by linear elastic behavior, with a sudden onset of damage leading to ultimate failure. This linear behavior is shown in the load-displacement plot of Figure 6.3-3 and is predicted using linear elastic finite element analysis as shown in Figure 7.4-3.

Figure 8.2-5 shows a damage progression schematic for the T-joint subjected to rail shear loading based on extensive experimental, numerical, and post failure analysis of the failed specimens. In this schematic of damage evolution, as shear load is applied to the joint, the matrix deforms elastically, placing the fiber insertions in shear and tension (a). Just prior to T-joint ultimate load, the allowable matrix stress is exceeded and an interfacial matrix crack forms at the web-to-flange interface (b) and quickly propagates across the entire surface (c). The initial matrix crack may be predicted assuming isotropic resin properties using the effective stress failure criteria as shown in Table 8.3-2. This matrix crack is also observed in the optical micrograph of Figure 6.3-6 and Figure 6.3-7.

The onset of damage is very sudden, as indicated by the smooth load-displacement and strain-load plots shown in Figure 6.3-3 and Figure 6.3-4, respectively. As in the case of flexure and tensile loading, as the load is transferred to the fiber insertions, fiber breakage and fiber pull-out occur. In the case of rail shear loading, fiber breakage and pull-out leads to catastrophic failure of the T-joint, resulting in complete separation of the web and flange (d). Figure 6.3-5 shows a catastrophically failed rail shear specimen. Failed fiber insertion tows are clearly shown protruding from the web and recesses are visible where the fiber insertion tows pulled out of the web.

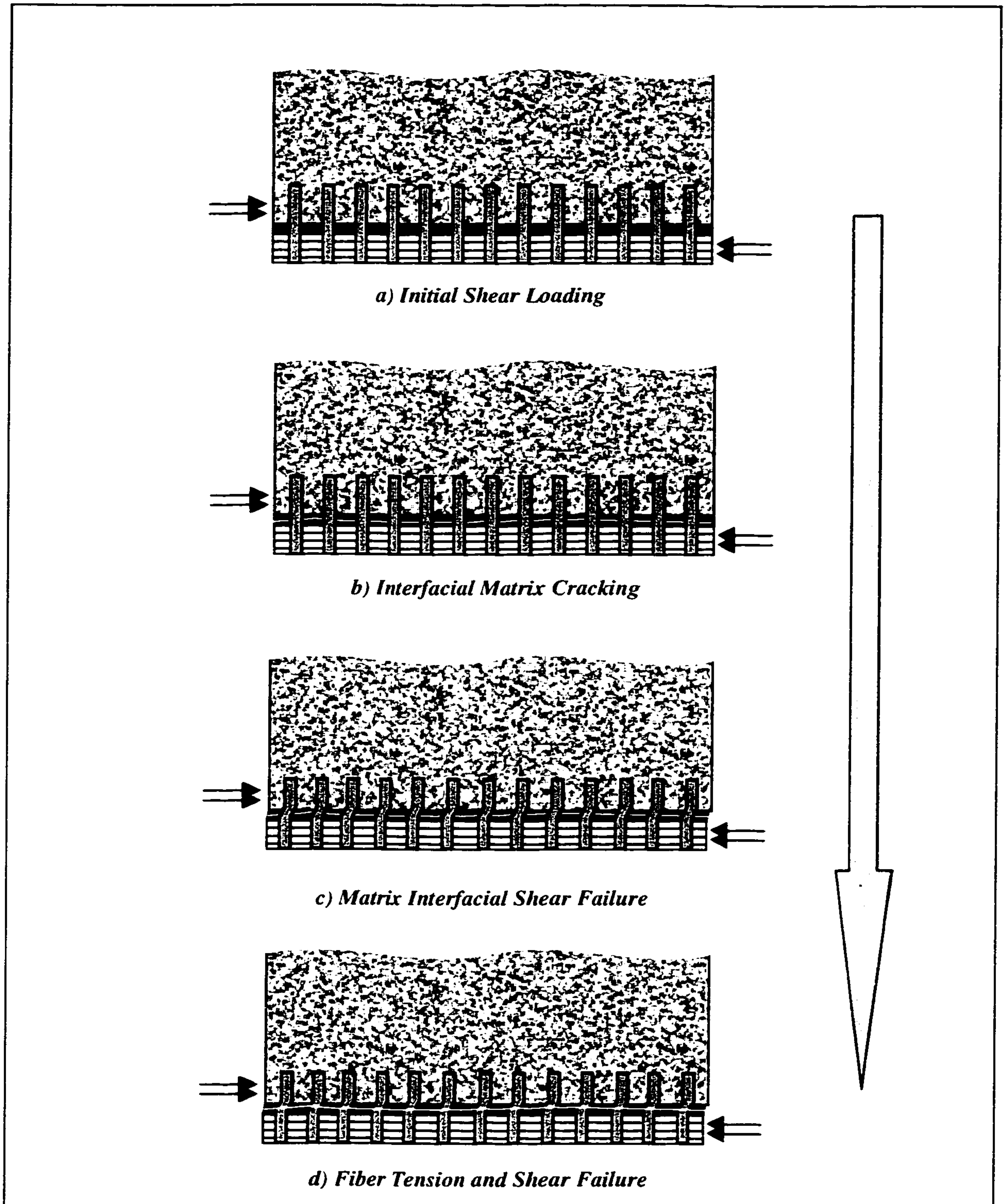

Figure 8.2-5. T-Joint Damage Progression Under Rail Shear Loading.

Based on the above discussion, a comparison of mechanical behavior of the T-joints under each load condition is provided in Table 8.2.1. It may be observed that the flexural specimens failed in part due to asymmetric loading of the fiber insertions and in part due to high stress concentration in the resin-rich fillet region. Flexure specimens exhibit additional load caring capability beyond initial failure indicating a significant damage tolerance. However, the initial and ultimate damage load under flexure is significantly lower than that of tension. Tensile specimens have symmetric loading of both sets of fiber insertions and fail due to matrix cracking at the web-to-flange interface. Tension specimens exhibit additional load carrying capability beyond initial failure indicating a moderate amount of damage tolerance. Mechanical response under rail shear is marked by nearly linear behavior up to initial interfacial crack formation. Specimens initially fail by interfacial matrix cracking at the web-to-flange interface and onset of T-joint catastrophic failure occurs through fiber insertion breakage and pullout with complete separation of the web and flange. Rail shear specimens exhibit very little load carrying capability, more often than not failing catastrophically.

Table 8.2.1. Summary of T-Joint Mechanical Behavior

Characteristic	**Flexure Loading**	**Simple Support Tension Loading**	**Rail Shear Loading**
Load Response	Three distinct regions: 1) Elastic to crack initiation 2) Fiber insertion loading 3) Fiber insertion degradation	Two distinct regions: 1) Elastic to crack initiation 2) Fiber insertion loading	One distant region: 1) Linear elastic to Failure
Failure Initiation	Stress concentration at resin-rich fillet crack	Stress concentration at resin-rich fillet crack	Web-to-flange interfacial matrix crack
Onset of Ultimate Failure	Fiber breakage and pullout	Fiber breakage and pullout	Fiber breakage and pullout
Fiber Insertion Loading	Asymmetric loading of fiber insertions (tension and compression)	Symmetric loading of fiber insertions (tension)	Symmetric loading of fiber insertions (tension and shear)
Ratio of Ultimate/Initial Failure Load	3.46	1.13	1.08

8.3 Parametric Analysis

A parametric finite element analysis was performed on the composite T-joints under flexure, tension, and rail shear loading.[86] The design parameters used in this analysis were fiber insertion tow modulus and filament count, fiber insertion depth, and resin-rich interface thickness. These parameters were varied to evaluate their effect on T-joint displacement and initial damage load. Table 8.3-1 shows the fiber insertion tow moduli and tow filament counts used in the analysis. The baseline experimental T-joint and finite element analysis models included an IM7 fiber insertion tow with a modulus of 276 GPa and filament count of 6k. All other T-joint geometric parameters and material parameters were held constant during this analysis. The fiber insertion tow depth was varied from 1.25 mm to 12.7 mm with the a nominal experimental depth of 12.7 mm. The resin zone interface thickness was varied from 0.8 mm to 1.8 mm with a nominal experimental value of 1.25 mm.

Table 8-3.1. T-Joint Design Study Parameters.[84]

Fiber Insertion Tow Modulus (GPa)	Fiber Insertion Tow Filament Count (K)	Fiber Insertion Tow Area (mm^2)
207	3	0.07
276*	6*	0.15
345	12	0.29
414	30	0.74
483	75	1.84
552	-	-
621	-	-
689	-	-

** Experimental baseline tow modulus and tow filament count*

Initial T-joint damage was defined as the point when the effective stress of the constrained matrix at the web-to-flange interface exceeds the neat resin failure stress:

$$\sigma_{eff} > \sigma_{fin}$$

where the as published failure stress of the PR520 toughened epoxy is 91.0 MPa.[63]

8.3.1 Flexure Parametric Analysis

An evaluation of the effect of fiber insertion tow modulus and filament count, fiber insertion depth, and resin-rich interface thickness on the T-joint displacement and initial damage load under flexural loading was performed. For the initial failure load parametric analysis, varying loads were applied as a nodal load to the T-joint linear elastic finite element model 2.54 cm from the web-to-flange interface.

Figure 8.3.1-1 shows the initial damage load as a function of tow modulus for a constant 6k tow fiber insertion. As expected, as the tow modulus increases the initial damage load providing additional load caring capability prior to T-joint initial failure. Figure 8.3.1-2 shows the T-joint flexural initial damage load as a function of tow filament count. Similarly, the initial damage load increases with increased tow filament count.

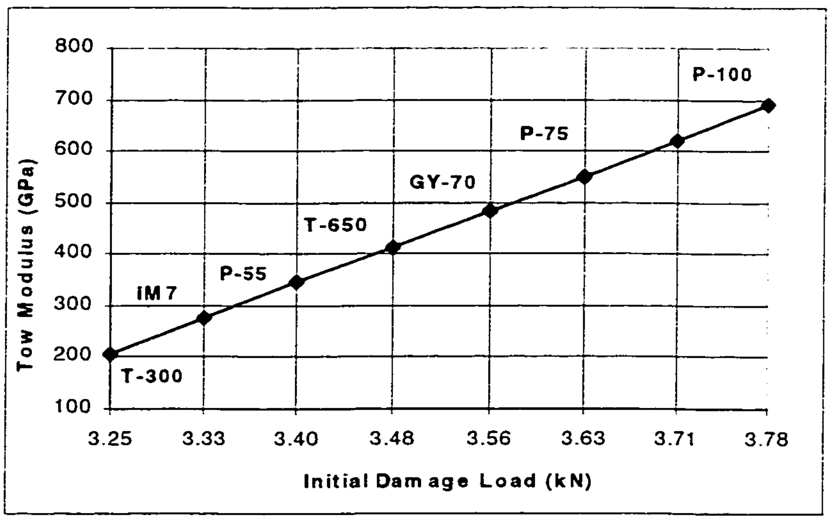

Figure 8.3.1-1. Effect of Fiber Insertion Tow Modulus on Initial Damage Load Under Flexural Loading: Constant 6k Tow Filament Count.

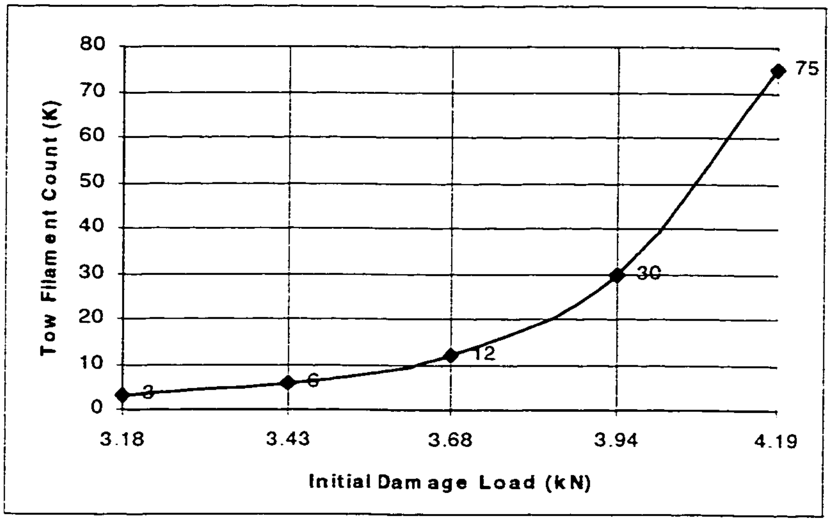

Figure 8.3.1-2. Effect of Fiber Insertion Tow Filament Count on Initial Damage Load Under Flexural Loading: Constant IM7 Fiber Insertion Modulus.

Figure 8.3.1-3 shows the initial flexural damage load for various tow moduli and filament counts. As shown, the tow filament count has a greater effect on initial damage load than that of tow modulus.

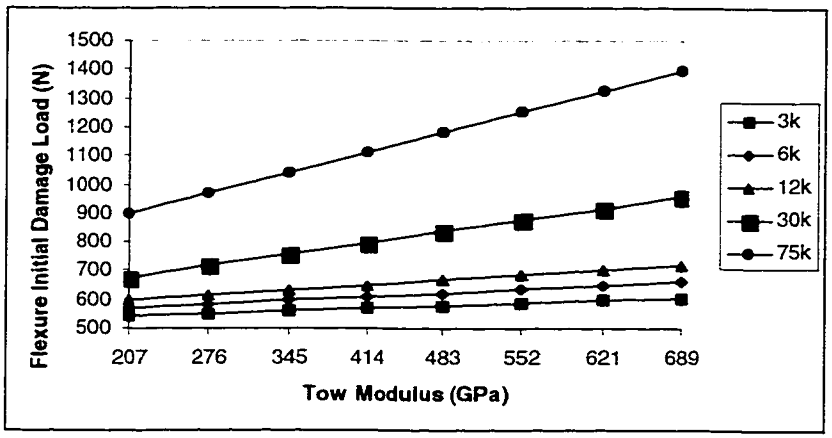

Figure 8.3.1-3. Initial Flexural Damage Load for Various Tow Moduli and Tow Filament Count.

The effect of fiber insertion depth on T-joint displacement at the initial damage load is shown in Figure 8.3.1-4. As shown, the T-joint displacement decreases with increase fiber insertion depth. As the fiber insertion extends into the flange the insertions reaches a depth where the effect on T-joint displacement is diminished. Figure 8.3.1-5 shows the effective of fiber insertions depth on initial damage load under flexure. An increased insertion depth increases the damage initiation load with diminishing effectiveness beyond the flange depth.

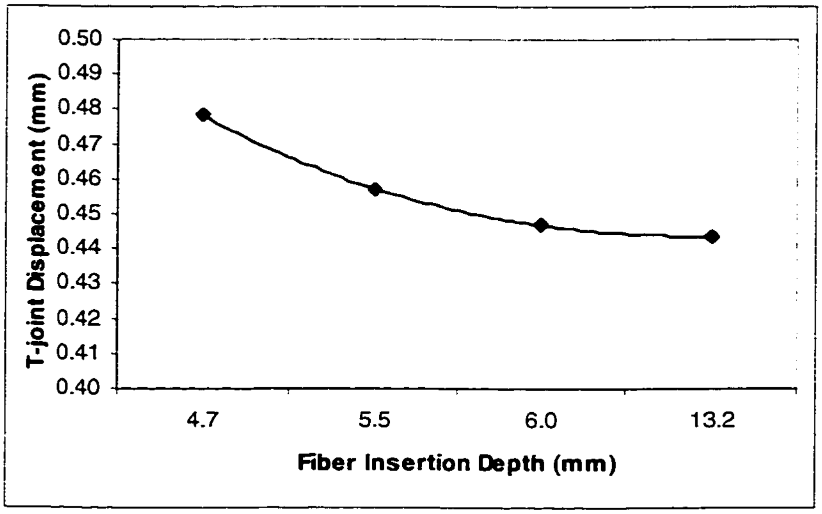

Figure 8.3.1-4. Effect of T-Joint Fiber Insertion Depth on Displacement Under Flexural Loading: Constant IM7 Fiber Insertion Tow Modulus and 6k Tow Filament Count.

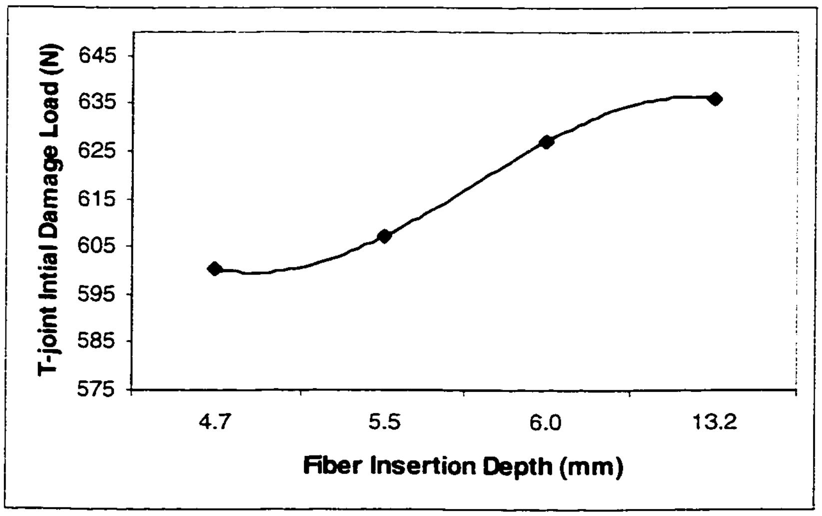

Figure 8.3.1-5. Effect of T-Joint Fiber Insertion Depth on Initial Damage Load Under Flexural Loading: Constant IM7 Fiber Insertion Tow Modulus and 6k Tow Filament Count.

A parametric finite analysis was performed to determine the effect of resin-rich interface thickness on T-joint displacement and initial damage load under flexure loading. The interface zone is nominally 1.25 mm thick as provided previously in Figure 7.1-2. As shown in Figure 8.3.1-6, a lower limit of 0.8 mm and an upper limit of 1.8 mm were considered in this analysis. Based on this analysis, it may be inferred that as the resin zone thickness increases, the T-joint deflection increases. This is due to the lower modulus resin-rich zone having a greater area with an increased thickness.

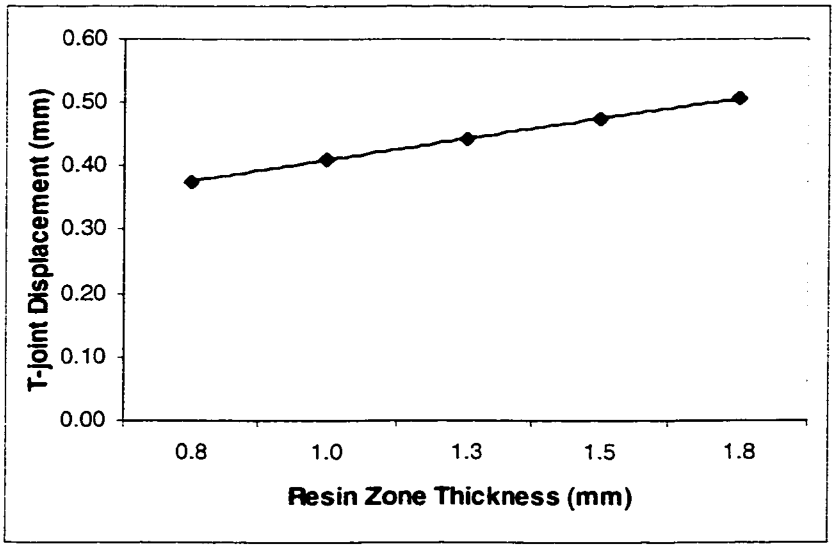

Figure 8.3.1-6. Effect of T-Joint Interface Resin Zone Thickness on Displacement Under Flexural Loading: Constant IM7 Fiber Insertion Tow Modulus and 6k Tow Filament Count.

A similar analysis was performed to determine the effect of resin-rich interface thickness on T-joint initial damage load under flexure. Again, as shown in Figure 8.3.1-7, a lower limit of 0.8 mm and an upper limit of 1.8 mm were considered in the analysis. As indicated, the T-joint initial damage load increase with increased thickness up to 1.0 mm thickness and decreases gradually. The initial increase is due to a reduction in stress concentration at the radius fillet with in increased thickness. However, with greater thicknesses the T-joint experience substantial stiffness losses that increase the local stress concentration at the interface.

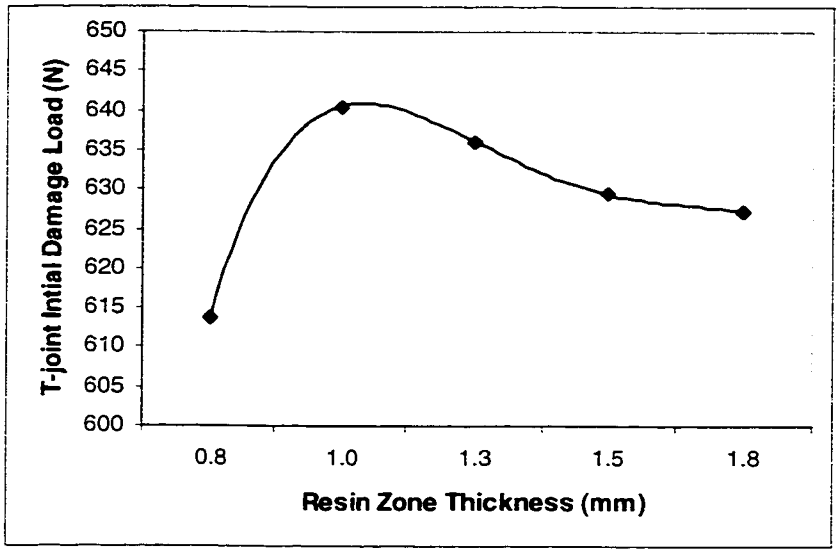

Figure 8.3.1-7. Effect of T-Joint Interface Resin Zone Thickness on Initial Damage Load Under Flexural Loading: Constant IM7 Fiber Insertion Tow Modulus and 6k Tow Filament Count.

8.3.2 Tension Parametric Analysis

A parametric analysis was performed to evaluate the effect of fiber insertion tow modulus and tow filament count on the T-joint displacement under tensile loading. A constant load of 5.4 kN was applied to the T-joint linear elastic finite element model. Figure 8.3.2-1 shows the tension displacement as a function of tow modulus for a 6k tow filament count. The tow modulus has little effect on the T-joint tensile displacement. An increase in the tow modulus only slightly decreases the T-joint displacement. Figure 8.3.2-2 shows the T-joint flexural displacement as a function of tow filament count. Similarly, the tensile displacement decreases only slightly with increased tow count.

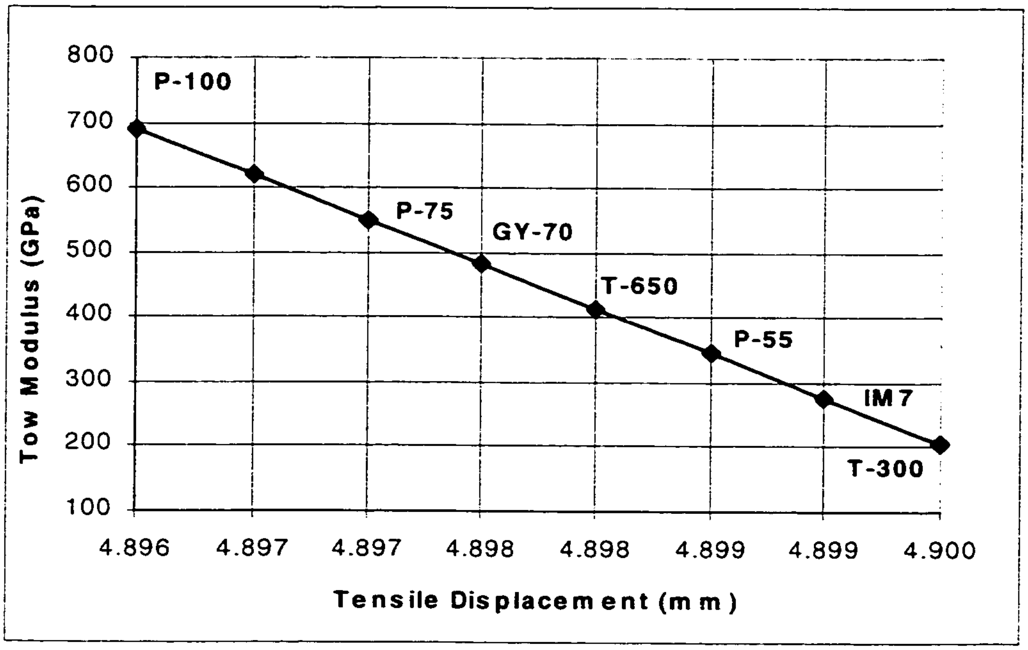

Figure 8.3.2-1. Effect of Fiber Insertion Tow Modulus on Displacement Under Tension Loading: Constant 6k Tow Filament Count.

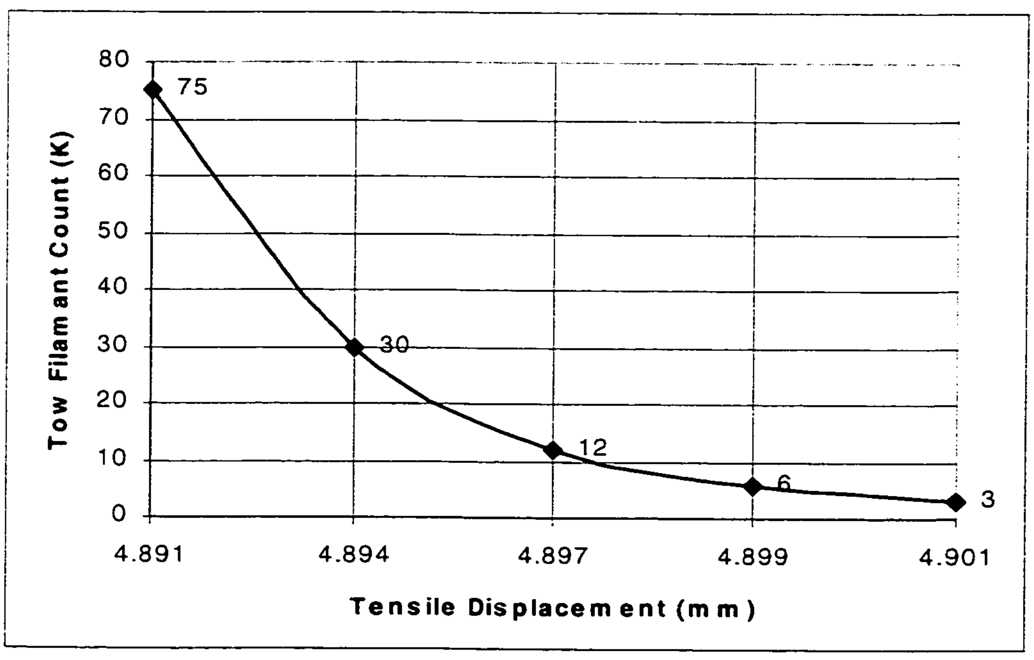

Figure 8.3.2-2. ***Effect of Fiber Insertion Tow Filament Count on Displacement Under Tensile Loading: Constant IM7 Fiber Insertion Modulus.***

8.3.3 Rail Shear Parametric Analysis

A parametric finite element analysis was performed to evaluate the effect of tow modulus and tow filament count on initial damage load. An initial displacement of 1.25 mm was applied to the web in the out-of-plane (z-direction). Figure 8.3.3-1 shows the initial damage load as a function of tow modulus for a constant 6k tow fiber insertion. Figure 8.3.3-2 shows the T-joint flexural initial damage load as a function of tow filament count. The tow modulus and tow filament count had only marginal effect on the initial damage load.

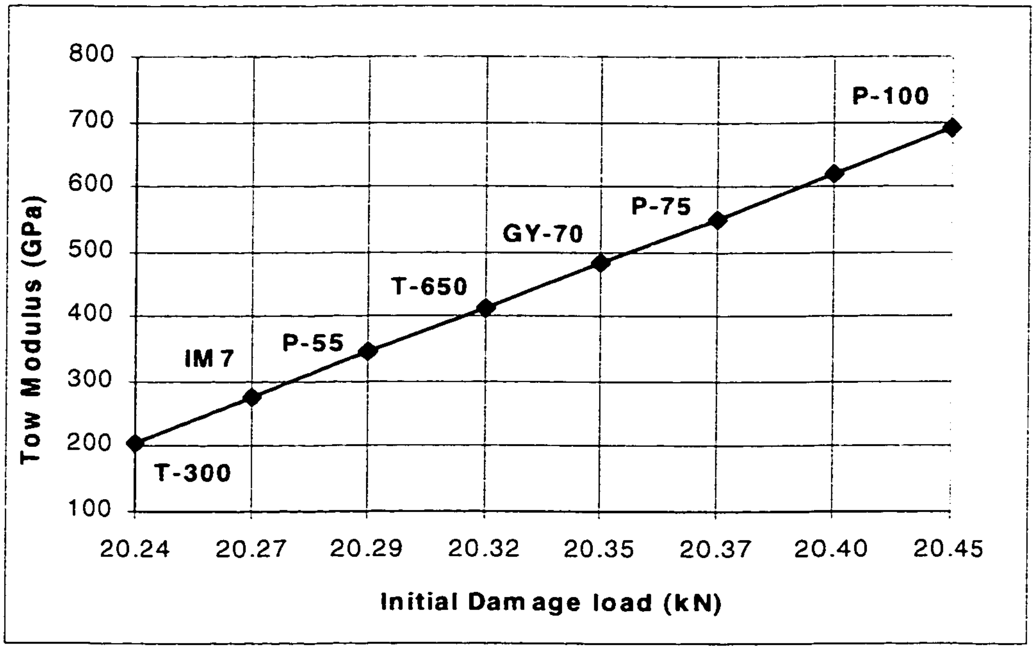

Figure 8.3.3-1. Effect of Fiber Insertion Tow Modulus on Initial Damage Load Under Rail Shear Loading: Constant 6k Tow Filament Count.

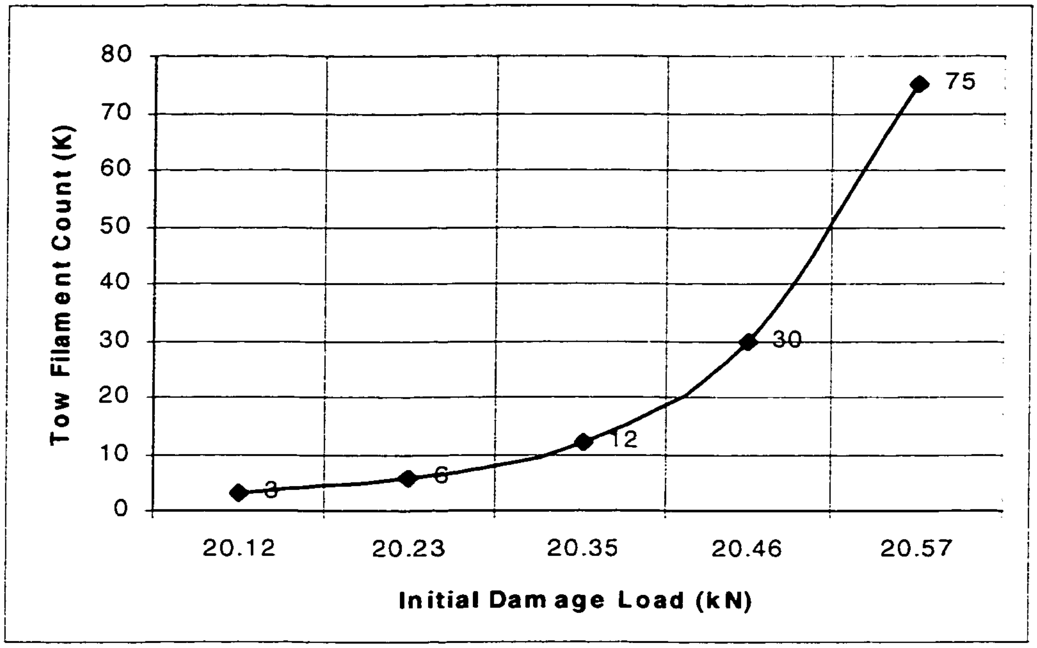

Figure 8.3.3-2. Effect of Fiber Insertion Tow Filament Count on Initial Damage Load Under Rail Shear Loading: Constant IM7 Fiber Insertion Modulus.

8.3.4 Summary

Parametric design studies were performed to characterize the effects of fiber insertion tow modulus and filament count, fiber insertion depth, and resin-rich interface thickness on T-joint initial damage load and displacement. Results of this research will assist designers in the application of composite T-joint with transverse stitching to future products and will reduce the amount of testing required to validate these designs. Under an applied T-joint load and known constraints, a combination of fiber insertion modulus and filament count may be select to ensure adequate load carrying capability or to minimize deflection. Additional design curves may be developed for other T-joint parameters using the finite element models developed herein.

CHAPTER 9

CONCLUSIONS AND RECOMMENDATIONS

9.1 Conclusions

A new low cost damage tolerant method of joining polymer matrix composites using two-dimensional dry fabric preforms with transverse stitching and a novel fiber insertion process with resin transfer molding has recently been developed. Prior to this research, the mechanical behavior and failure mechanisms of this type of joint were not well understood. This investigation developed fundamental knowledge of strength prediction and failure mechanisms under flexure, tension, and rail shear load conditions through detailed experimental, numerical, and post failure analyses. Experimental data and post failure results were used to assist in the development of predictive linear elastic, nonlinear, and damage progression finite element models. Using the finite element models developed herein, parametric design studies were performed to characterize the effects of resin-rich interface thickness, fiber insertion tow modulus and filament count, and fiber insertion depth on T-joint initial damage load and displacement. Results of this research will assist designers in the application of composite T-joint with transverse stitching to future products and will reduce the amount of testing required to validate these designs.

The main accomplishments of this research include:

- The mechanical behavior of a new type of T-joint with transverse stitching was characterized for the first time.
- Experimental procedures were established including fixture development and instrumentation layout.
- Linear elastic, nonlinear, and damage progression finite element models were developed to predict the load carrying capability through ultimate failure.

- Stitched T-joint failure mechanisms were identified and a damage progression model was developed under each load condition.

Specific conclusions of this research under flexure, tension, and rail shear load include:

T-Joint Mechanical Behavior and Failure Mechanisms Under Flexure Loading

- Flexural specimens fail in part due to asymmetric loading of the fiber insertions and in part due to high stress concentration in the resin-rich fillet region.
- Flexure specimen elastic and nonlinear finite element predictions of load-displacement show good agreement with experimental results.
- Progressive failure numerical modeling shows good agreement through ultimate failure under flexural loading.
- Initial flexural damage load increases with increased fiber insertion tow modulus and tow filament count.

T-Joint Mechanical Behavior and Failure Mechanisms Under Tensile Loading

- Tensile specimens have symmetric loading of both sets of fiber insertions and fail due to matrix cracking at the web-to-flange interface.
- Tension specimen linear elastic finite element predictions of load-displacement show good agreement with experimental results.
- Progressive failure numerical modeling shows good agreement through ultimate load.
- Fiber insertion tow modulus and filament count have little effect on initial tensile damage load and T-joint displacement.

T-Joint Mechanical Behavior and Failure Mechanisms Under Rail Shear Loading

- Specimens initially fail by interfacial matrix cracking at the web-to-flange interface.
- Onset of T-joint catastrophic failure occurs through fiber insertion breakage and pullout with complete separation of the web and flange.
- Rail shear specimen linear elastic finite element predictions of load-displacement show good agreement with experimental results.
- Fiber insertion tow modulus and filament count have little effect on initial tensile damage load and T-joint displacement

9.2 Recommendations

Specific research and development areas have been identified to gain further understanding of the mechanical behavior and failure mechanisms of composite T-joints with transverse stitching and to facilitate the adoption of this technology to primary structural applications.

- T-joint experimental and numerical evaluation of mechanical behavior under fatigue loading.
- Further evaluation of T-joint interface matrix failure. Evaluate applicability of matrix failure criteria including the strain invariant failure criteria.[89-90] The critical value of first invariant for matrix failure for PR520 resin needs to be established.
- Experimental and numerical investigation of T-joint damage tolerance to discern the effects of impact damage on static and fatigue behavior
- Development of a comprehensive T-joint design tool through further optimization studies to discern the effects of additional T-joint variables including number of

insertions rows, insertion pitch, insertion angle, local web thickness, and local flange thickness.

- Improved T-joint processing including fiber insertion positional tolerance, reduced preform misalignment and edge trimming prior to RTM consolidation, and reduced interfacial matrix cracking.

Bibliography

1. Mallick, P.K., ***Fiber-Reinforced Composites: Materials, Manufacturing, and Design***, Marcel Dekker, Inc., (1993).

2. Chawla, Krichan K., ***Composites Materials: Science and Engineering, 2nd Edition***, Springer, (1998).

3. Johns, Robert M., ***Mechanics of Composite Materials***, Taylor and Frances, (1975).

4. Tsai, Stephen W. and H. Thomas Hahn, ***Introduction to Composite Materials***, Technomic Publishing, (1980).

5. Halpin, John C., ***Primer on Composite Materials Analysis, 2nd Edition***, Revised Technomic Publishing, (1992).

6. Eckold, Geoff, ***Design and Manufacturing of Composite Structures***, McGraw-Hill, Inc., (1994).

7. Baker, A., "Joining and Repair of Aircraft Composite Structures." In: ***Composite Materials Handbook***, Edited by P.K. Mallick, Marcel Decker, NY, (1997).

8. Adams, Robert D. and William C. Wake, ***Structural Adhesive Joints in Engineering***, Elsevier Applied Science Publisher LTD, (1984).

9. Hart-Smith, L. J., "Joints." In: ***Engineered Materials Handbook: Composites,*** Volume 1, ASM International, (1986).

10. Kretsis, G. and Matthews, F.L., "The Strength of Bolted Joints in Glass Fibre/Epoxy Laminates." Composite, Vol. 16, No. 2, (1985), pp. 92-102.

11. Eisenmann, J.R. and Leonhardt, J.L., "Improving Composite Bolted Joint Efficiency by Laminate Tailoring." In: Edward K.T., Editor, Joining of Composite Materials, ASTM STP-749, American Society for Testing of Materials, (1981), pp. 117-130.

12. Crothers, P.J. Drechsler, K. Feltin, D. Herszberg, I. and Bannister, M., "The Design and Application of Tailored Fiber Placement." Proceedings of ICCM11, Gold Coast, Australia. Vol. 1, 14-18, July (1997), pp. 600-610.

13. Wang, J.T., Lotts C.C., and Davis, D.D., "Analysis of Bolt-loaded Elliptical Holes in Laminated Composite Joints." Journal of Reinforced Plastics and Composites, Vol. 12, (1993), pp. 128-138.

14. Rispler, A.R., Stevens, Grant P., and Tong, Liyong, "Photoelastic Evaluation of Metallic Inserts of Optimized Shape." Composite Science and Technology, Vol. 60, (2000), pp. 95-106.

15. Volkersen, O., "Die Niektraftverteiling in Zugbeansprunchten mit Konstanten Laschenquerscritten." Luftfahrforsch, Vol. 15, (1938), pp. 41-47.

16. Goland, M. and Reissner, E., "The Stresses in Cemented Joints." ASME J. of Adhesion and Adhesives, Vol. 8, (1944), pp. A17-27.

17. Renton, W.J. and Vinson, J.R., "The Analysis and Design of Anisotropic Bonded Joints." Report No. 2, AFOSR Scientific Report, MAE TR 171, August (1974).

18. Hart-Smith, L.J., "Adhesively Bonded Joints for Fibrous Composite Structures." in ***Joining Fiber-Reinforced Plastics***, F. L. Matthews, Ed., Elsevior, (1987), pp. 271-311.

19. Adams, R.D. and Peppiatt, N.A., " Stress analysis of Adhesive-Bonded Lap Joints." Journal of Strain Analysis, Vol. 9, (1974), pp. 185.

20. Tong, L. and Stevens, G.P., ***Analysis and Design of Composite Bonded Joints***, Kluwer Academic Publishers, (1999).

21. Mignery, L.A., Tan, T.M. and Sun, C.T., "The use of Stitching to Suppress Delamination in Laminated Composites." Delamination and Dedonding, ASTM STP 876, (1985), pp. 371-385.

22. Tong, L. and Jain, L.K., "Analysis of Adhesive Bonded Composite Lap Joints with Transverse Stitching." Applied Composite Materials, Vol. 2, No. 6, (1995), pp. 343-365.

23. Tong, L. and Steven, G.P., "A Numerical Study on Stresses in RTM Lap Joints Reinforced with Transverse Stitching." Composite Structures, Vol. 36, No. 1-2 (Sep.-Oct. 1996), pp. 91-100.

24. Tong, L., Jain, L.K., Leong, K.H., Kelly, D. and Hertzberg, I., "Failure of Transversely Stitched RTM Lap Joints." Composite Science & Technology, Vol. 58, No. 2, (1998), pp. 221-227.

25. Tong, L., Cleaves, K., Kruckenberg, T. and Steven, G.P., "Effect of Transverse Stitching on the Fracture Loads of RTM Single Lap Joints." Key Engineering Materials, Vol. 137, (1998), pp. 195-202.

26. Dransfield, K.A., Jain, L.K. and Mai, Y.W., "On the Effects of Stitching in CFRPs – I. Mode I Delimitation Toughness." Composite Science and Technology, Vol. 58, (1998), pp. 815-827.

27. Jain, L.K., Dransfield, K.A. and Mai, Y.W., "On the Effects of Stitching in CFRPs – II. Mode I Delimitation Toughness." Composite Science and Technology, Vol. 58, (1998), pp. 829-837.

28. Barrett, D.J., "The Mechanics of Z-fiber Reinforcement." Composite Structures, Vol. 36, (1996), pp. 23-32.

29. Jain, L.K. and Mai, Y.W., "Determination of Mode II Delimitation Toughness of Stitched Laminated Composites." Composites Science and Technology, Vol. 55, (1995), pp. 241-253.

30. Jain, L.K. and Mai, Y.W., "Analysis of Stitched Laminated ENF Specimens for Interlaminar Mode II Fracture Toughness." International Journal of Fracture Vol. 68, (1994), pp. 219-2443.

31. Jain, L.K., "On the Effect of Stitching on Mode I Delamination Toughness of Laminated Composites." Composites Science and Technology, Vol. 51, (1994), pp. 331-345.

32. Shu, D. and Mai, Y.W., "Effect of Stitching on Interlaminar Delamination Extension in Composite Laminates." Composites Science and Technology, Vol. 49, (1993), pp. 165-171.

33. Dransfield, K.A., Baillie, C. and Mai, Y.W., "Improving the Delimitation Resistance of CFRP by Stitching - A Review." Composite Science and Technology, Vol. 50, (1994), pp. 305-317.

34. Mouritz, A.P., Bannister, M.K., Falzone, P.J., and Leong, K.H. "Review of Applications for Advanced Three-Dimensional Fiber Textile Composites." Composites: Part A, Vol. 30, (1999), pp. 1445-1461,

35. Wehrenberg, R.H. II "Composites Get Stronger with 3-D Reinforcement." Materials Engineering, Vol. 97, (1983), pp. 27-31.

36. Soden, J.A., Weissenbach, G. and Hill, B.J., "The Design and Fabrication of 3D Multi-layer Woven T-Section Reinforcements." Composite Part A: Applied Science and Manufacturing, Vol. 30, (1999), pp. 213-220.

37. Burgess, K. and Paradis, S. "Application of 3-D Woven Preforms to Laminated Composites." 1st AIAA Aircraft Engineering, Technology, and Operations Congress, AIAA 95-3890, September 19-21, (1995).

38. Gillespie, J.W. and Pipes, R.B. "Behavior of Integral Composite Joints – Finite Element and Experimental Evaluation." J. Composite Materials, Vol. 12, (1978), pp.408-421.

39. Shenoi, R.A. and Violette, F.L.M., "A Study of Structural Composite Tee Joints in Small Boats." *Journal of Composite Materials*, Vol. 24, (1990), pp. 644-665.

40. Shenoi, R.A. and Hawkins, G.L., "Influence of Material and Geometry Variations on the Behavior of Bonded Tee Connections in FRP Ships." *Composite*, Vol. 23, Number 5, (1992), pp. 335-345.

41. Phillips, H.J. and Shenoi, R.A., "Damage Tolerance of Laminated Tee Joints in FRP Structures," Composites Part A, Vol. 29, (1998), pp. 465-478.

42. Junhou, P. and Shenoi, R.A., "Examination of Key Aspects Defining the Performance Characteristics of Out-of-plane Joints in FRP Marine Structures." Composite Part A: *Applied Science and Manufacturing*, Vol. 27A, Number 5, (1996), pp. 89-103.

43. Theotokoglou, E.E. and Moan, T. "Experimental and Numerical Study of Composite T-Joint." Journal of Composite Materials, Vol. 30, No. 2, (1996), pp. 190-209.

44. Theotokoglou, E.E. "Study of Numerical Fracture Mechanics Analysis of Composite T-Joints." Journal of Reinforced Plastics and Composites, Vol. 18, No. 3, (1999), pp. 215-223.

45. Theotokoglou, E.E. "Strength of Composite T-Joints under Pull-Out Loads." Journal of Reinforced Plastics and Composites, Vol. 16, No. 6, (1997), pp. 503-518.

46. Dulieu-Smith, J.M., Quinn, S., Shenoi, R.A., Read, P.J.C.L., and Moy, S.S.J. "Thermoelastic Stress Analysis of a GRP Tee Joint." Applied Composite Materials, Vol 4, (1997), pp. 283-303.

47. Holt, D.J. "Future Composite Aircraft Structures may be Sewn Together." Automotive Engineering, Vol. 90, (1982), pp. 46-49.

48. Young, W.B. and Chuang, M.T. "Fabrication of T-shaped Composite through Resin Transfer Molding." Journal of Composite Materials, Vol. 29, No. 16, (1996), pp. 2192-2214.

49. Rispler, A.R., Stevens, G.P. and Tong, L. "Failure Analysis of Composite T-Joints Including Inserts." Journal of Reinforced Plastics and Composites, Vol. 16, No. 18, (1997), pp. 1642-1658.

50. Tada, Y. and Ishikawa, T., "Experimental Evaluation of the Effects of Stitching on CFRP Laminate Specimens with Various Shapes and Loadings." Key Engineering Materials, Vol. 37, (1989), pp. 305-316.

51. Freitas, G., Fusco, T., Campbell, T., Harris, J. and Rosenberg, S., "Z-Fiber Technology and Products for Enhancing Composite Design." AGARD Conference Proceedings 590, Bolted/Bonded Joints in Polymeric Composites, (1997), pp. 17-1 to 17-8.

52. Stickler, P.B., Ramulu, M., and Johnson, P.S., "Experimental and Numerical Analysis of Transverse Stitched T-Joints in Bending." Composite Structures, Vol. 50, No. 1, (2000), pp. 17-27.

53. Stickler, P.B., Ramulu, M., and Van West, B., "Transverse Stitched T-joints in Bending with PR520 Resin." Journal of Reinforced Plastics and Composites, Vol. 20, No 1, (2001), pp. 65-75.

54. Stickler, P.B. and Ramulu, M., "Investigation of Mechanical Behavior of Transverse Stitched T-joints with PR520 Resin in Flexure and Tension." Composite Structures, Vol. 52, No. 3-4, (2001), pp. 307-314.

55. Kermandis, T., Labeas, G., Tserpes, K.I., and Pantelakis, Sp. "Finite Element Modeling of Damage Accumulation in Bolted Composite Joints under Incremental Tensile Loading." ECCOMAS, Barcelona, (11-14 September 2000).

56. Camanho, P.P. and Matthews, F.L. "A Progressive Model for Mechanically Fastened Joints in Composite Laminates." Journal of Composite Materials, Vol. 33, No. 24 (1999), pp. 2248-2280.

57. Chiu, W.K., Galea, S., and Jones, R. "The Role of Material Nonlinearities in Composite Structures." Composite Structures, Vol. 38, No. 1-4, (1997), pp. 71-81.

58. Jones, R. and Alesi, H. "On the Analysis of Composite Structures with Material and Geometric Non-linearities." Composite Structures, Vol. 50 (2000), pp. 417-431.

59. Potter, K.D., Davies, R., Barret, M., Godbehere, A., Bateup, L., Wisnom, M., and Mills, A. "Heavily Loaded Bonded Composite Structure: Design, Manufacture and Test of "I" Beam Specimens." Composite Structures, Vol. 51 (2001), pp. 389-399.

60. Thornel® T-300 PAN-Based Fiber Product Data Sheet, BP Amoco Chemicals, (2000).

61. IM7 Carbon Fiber Product Data Sheet, Hexcel Carbon Fibers, (2001).

62. Epon 862/W Epoxy Resin Product Data Sheet, Shell Corporation, (2000).

63. PR520 Epoxy Resin Product Data Sheet, 3M Corporation, (2000).

64. Micromeasurements Group, Inc. "Interactive guide to Strain Gage Technology," http://www.measurementsgroup.com/guide/, (2000).

65. Tuttle, M.E. and Brinson, H.F., "Resistance-foil Strain-gage Technology as Applied to Composite Materials." Experimental Mechanics, Vol.24, (1984), pp. 54-65.

66. ANSYS, Inc. Version 5.6 Users Manual, Canonsburge, PA, (2000).

67. Stickler, P.B., Ramulu, M., Coguill, S.L. and Tuttle, M.E., "Experimental Investigation of T-300/PR520 Laminate Properties and Failure Analysis," Submitted for Publication, Experimental Mechanics.

68. Hunt, M. "Test Composites with Ultrasound," Materials Engineering, Vol. 108, No. 10, (1991), pp. 30-32.

69. Reynolds, W.N. "Nondestructive Testing (NDT) of Fibre-Reinforced Composite Materials," Materials & Design, Vol. 5, No. 6, (1985), pp. 256-270.

70. Grandia, W.A. and Fortunko, C.M. "NDE Applications of Air-Coupled Ultrasonic Transducers," 1995 IEEE International Ultrasonic Symposium, Seattle, Washington, Proceedings, Vol. 1, (1995), pp. 697-709.

71. ASTM D 3171-99, *Standard Test Method for Constituent Content of Composite Materials*, (1999), Philadelphia, PA: American Society for Testing and Materials.

72. ASTM D 3039-95a, *Standard Test Method for Tensile Properties of Polymer Matrix Composite Materials*, (1995), Philadelphia, PA: American Society for Testing and Materials.

73. ASTM D 3410-95, *Standard Test Method for Compression Properties of Polymer Matrix Composite Materials with Unsupported Gage Section by Shear Loading*, (1995), Philadelphia, PA: American Society for Testing and Materials.

74. Bogetti, T.A., Gellespie, J. W.J., and Pipes, R.B., "Evaluation of the IITRI Compression Test Method for Stiffness and Strength Determination," Composite Science and Technology, Vol. 32, No. 1, (1989), pp.57-76.

75. ASTM D 4255-83, *Standard Guide for Testing Inplane Shear Properties of Composite Laminates*, (1983), Philadelphia, PA: American Society for Testing and Materials.

76. Hussain, A. and Adams, D.F., "The Wyoming-Modified Two-Rail Shear Test Fixture for Composite Materials," Journal of Composites Technology and Research, Vol. 21, No. 4, October, (1999), pp. 215-223.

77. ASTM Draft No. 1, *Out-of-Plane Tension Test for Fiber-Reinforced Polymer Matrix Composites*, (1997), Philadelphia, PA: American Society for Testing and Materials.

78. ASTM D 5379-98, *Standard Test Method for Shear Properties of Composite Materials by the V-Notched Beam Method*, (1998), Philadelphia, PA: American Society for Testing and Materials.

79. Ho, H., Tsai, M.Y., Morton, J., and Farley, G.L., "An Experimental Investigation of Iosipescu Specimen for Composite Materials," Experimental Mechanics, Vol. 31, No. 4, (1991), pp. 328-336.

80. Iosipescu, N., "New Accurate Procedure for Single Shear Testing of Metals," J. Mat., Vol. 2, No. 3, (1967), pp. 537-566.

81. Adams, D.F. and Walrath, D.E., "Further Development of the Iosipescu Shear Test Method," Experimental Mechanics, Vol. 27, No. 2, (1987), pp. 113-119.

82. Hoskin, B.C. and Baker, A.A., ***Composite Materials for Aircraft Structures***, AIAA Education Series, (1986).

83. Naik, N.K. ***Woven Fabric Composites***, Technomic Publishing Co., Inc. (1994).

84. Cox, B.N. and Flanagan, G., ***Handbook of Analytical Methods for Textile Composites***, NASA Contractor Report 4750, March (1997).

85. Gere J.M. and Timoshenko, S.P., ***Mechanics of Materials 4^{th} ed.,*** PWS Publishing Company, (1997).

86. Moaveni, S., ***Finite Element Analysis: Theory and Application with ANSYS***, Prentice Hall, (1999).

87. Kobayashi, A.S., ed., ***Handbook on Experimental Mechanics, 2nd Edition***, SEM, (1993).

88. Dowling, N.E., ***Mechanical Behavior of Materials: Engineering Methods for Deformation, Fracture, and Fatigue, 2nd Edition***, Prentice Hall, (1999).

89. Gosse, J.H. and Christensen, S., "Strain Invariant Failure Criteria for Polymers in Composite Materials," AIAA-2001-1184, (2001).

90. Tsai, H.C., Alper, J., and Barrett, D., "Failure Analysis of Composite Bonded Joints," AIAA-2000-1428, (2000).

APPENDIX A

STRAIN GAGE SPECIFICATIONS

Table A-1. Strain Gage Specifications

Specification	EA-06-062AQ-350	WA-06-120WR-350
Type	Uniaxial	3-element stacked rosette
Carrier Matrix (backing)	Tough flexible polyimide film backing	High temperature glass fiber reinforced epoxy-phenolic resin
Foil Alloy	Constantan	Constantan
Self Temperature Compensation	yes (see Figure A-1a)	yes (see Figure A-1b)
Active Gage Length (mils)	0.062	0.120
Resistance (Ohms) @ 24°C	350±0.15%	350±0.15%
Temperature Range (°C)	-75 to +175	-75 to +205
Strain Range	±3%	±3%
Fatigue Life Strain Level (με)	±1500	±1500
Fatigue Life # Cycles	10^7	10^7
Gage Factor @ 24°C	2.090±0.5%	2.10
Transverse Sensitivity @ 24°C	(+1.1 ±0.2)%	(+0.2 ±0.2)%
Bonding cement	M-Bond 200	M-Bond 200

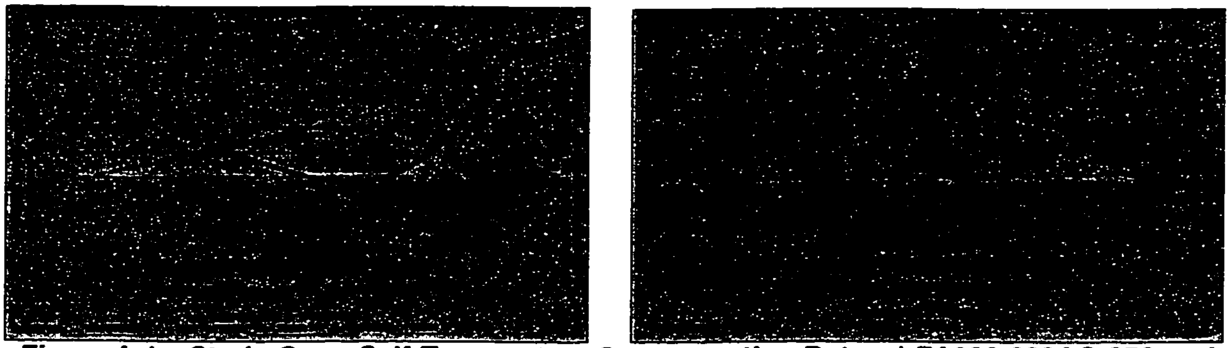

Figure A-1. Strain Gage Self-Temperature Compensation Data: a) EA006-062AQ-350 and b) WA-06-062AQ-350

APPENDIX B

COMPOSITE FAILURE CRITERIA

Table B-1. Composite Laminate Failure Criteria

Failure Criteria	Basic Theory	Governing Equations	Measured Quantities
Maximum Stress	Failure occurs when any stress in the principal material direction is equal to or greater than the corresponding ultimate strength	$-S_{Lc} < \sigma_{11} < S_{Lt}$ $-S_{Tc} < \sigma_{22} < S_{Tt}$ $-S_{LTs} < \tau_{12} < S_{LTs}$	S_{Lc} – ultimate longitudinal compressive strength S_{Lt} – ultimate longitudinal tensile strength S_{Tc} – ultimate transverse compressive strength S_{Tt} – ultimate transverse tensile strength S_{LTs} – ultimate in-plane shear strength
Maximum Strain	Failure occurs when any strain in the principal material direction is equal to or greater than the corresponding ultimate strain	$-\varepsilon_{Lc} < \varepsilon_{11} < \varepsilon_{Lt}$ $-\varepsilon_{Tc} < \varepsilon_{22} < \varepsilon_{Tt}$ $-\gamma_{LTs} < \gamma_{12} < \gamma_{LTs}$	ε_{Lc} – ultimate longitudinal compressive strain ε_{Lt} – ultimate longitudinal tensile strain ε_{Tc} – ultimate transverse compressive strain ε_{Tt} – ultimate transverse tensile strain γ_{LTs} – ultimate in-plane shear strain
Tsai-Hill	Based on Hill's anisotropic yield for metals, the Tsai-Hill failure criteria proposes that failure does not occur in an orthotropic lamina if and when the following inequality is satisfied:	$\frac{\sigma_{11}^2}{S_{Lt}^2} - \frac{\sigma_{11}\sigma_{22}}{S_{Lt}^2} + \frac{\sigma_{22}^2}{S_{Tt}^2} + \frac{\tau_{12}^2}{S_{LTs}^2} < 1$	S_{Lc} – ultimate longitudinal compressive strength S_{Lt} – ultimate longitudinal tensile strength S_{Tc} – ultimate transverse compressive strength S_{Tt} – ultimate transverse tensile strength S_{LTs} – ultimate in-plane shear strength
Tsai-Wu	Under plane stress conditions in the 1-2 plane, the Tsia-Wu failure theory predicts failure does not occur in an orthotropic lamina when the following inequality is satisfied:	$F_1\sigma_{11} + F_2\sigma_{22} + F_6\tau_{12} + F_{11}\sigma_{11}^2$ $+F_{22}\sigma_{22}^2 + 2F_{12}\sigma_{11}\sigma_{22} < 1$ $F_1 = \frac{1}{S_{Lt}} - \frac{1}{S_{Lc}}$ $F_2 = \frac{1}{S_{Tt}} - \frac{1}{S_{Tc}}$ $F_{11} = \frac{1}{S_{Lt}S_{Lc}}$ $F_{22} = \frac{1}{S_{Tt}S_{Tc}}$ $F_{66} = \frac{1}{S_{LTs}^2}$ $F_{12} = \frac{1}{2}\sqrt{F_{11}F_{22}}$	S_{Lc} – ultimate longitudinal compressive strength S_{Lt} – ultimate longitudinal tensile strength S_{Tc} – ultimate transverse compressive strength S_{Tt} – ultimate transverse tensile strength S_{LTs} – ultimate in-plane shear strength

APPENDIX B: COMPOSITE FAILURE CRITERIA

Table B-2. Composite Joint Failure Criteria

Failure Criteria	Basic Theory	Governing Equations	Measured Quantities
Interlaminar Peel	Interlaminar failure of a composite adherend occurs when the normal tensile stress at the interface exceeds its ultimate strength	$\frac{\sigma_z}{Z} = 1$	**Z** – interlaminar tensile strength of the composite adherends σ_z – normal tensile or peel stress at the interface

APPENDIX C

T-300/SHELL 862 MATERIAL PROPERTIES DEVELOPMENT

Experiments were conducted to determine the tensile modulus of the quasi-isotropic flange and web layup. A Satec static load frame was used and strains were measured using an extensometer. Figure C-1 shows the experimental test setup. Tensile modulus was determined using ASTM D3039 "Tensile Properties of Polymer Matrix Composites Materials." A lot quantity of six specimens was used to determine the average tensile modules. Figures C2-C7 show the load-strain plots for each specimen.

Table C-1. T-300/Shell 862 Tensile Modulus Data.

SPECIMEN NO.	THICKNESS		WIDTH		AREA			NOTES
	ORIG. (IN)	TESTED (IN)	ORIG. (IN)	TESTED (IN)	ORIG. (IN^2)	TESTED (IN^2)	R.A. (%)	
T-1	0.0898		0.758		0.0681			
T-2	0.0965		0.760		0.0733			
T-3	0.0994		0.760		0.0755			
Avg	**0.0952**		**0.7593**		**0.0723**			
S-1	0.1400		0.757		0.1060			
S-2	0.1389		0.759		0.1054			
S-3	0.1417		0.758		0.1074			
Avg	**0.1402**		**0.7580**		**0.1063**			

SPECIMEN NO.	FILE NAME	TEMP.		ULTIMATE		YIELD		MODULUS
		REQ. (°F)	ACT. (°F)	LOAD (LBS)	STRESS (PSI)	LOAD (LBS)	STRESS (LBS)	(E) 10^6(PSI)
T-1	2488	70	70	2,245	32,982			7.1
T-2	2489	70	70	1,968	26,834			6.6
T-3	2490	70	70	1,900	25,151			6.2
Avg				**2038**	**28322**			**6.63**
S-1	2492	70	70	3,278	30,930			7.7
S-2	2493	70	70	3,247	30,799			7.6
S-3	2494	70	70	3,316	30,873			7.7
Avg				**3280**	**30867**			**7.67**

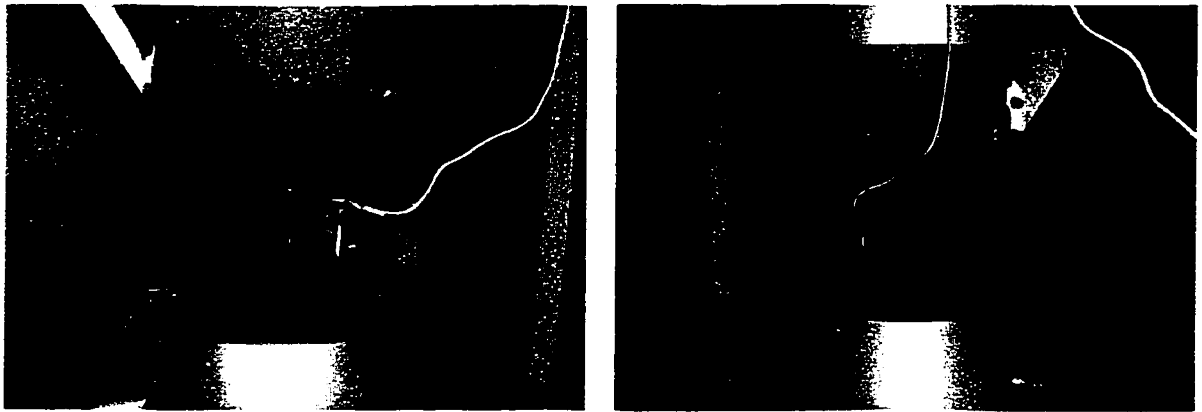

Figure C-1. Experimental Test Setup for T-300/Shell 862 Tensile Modulus Determination.

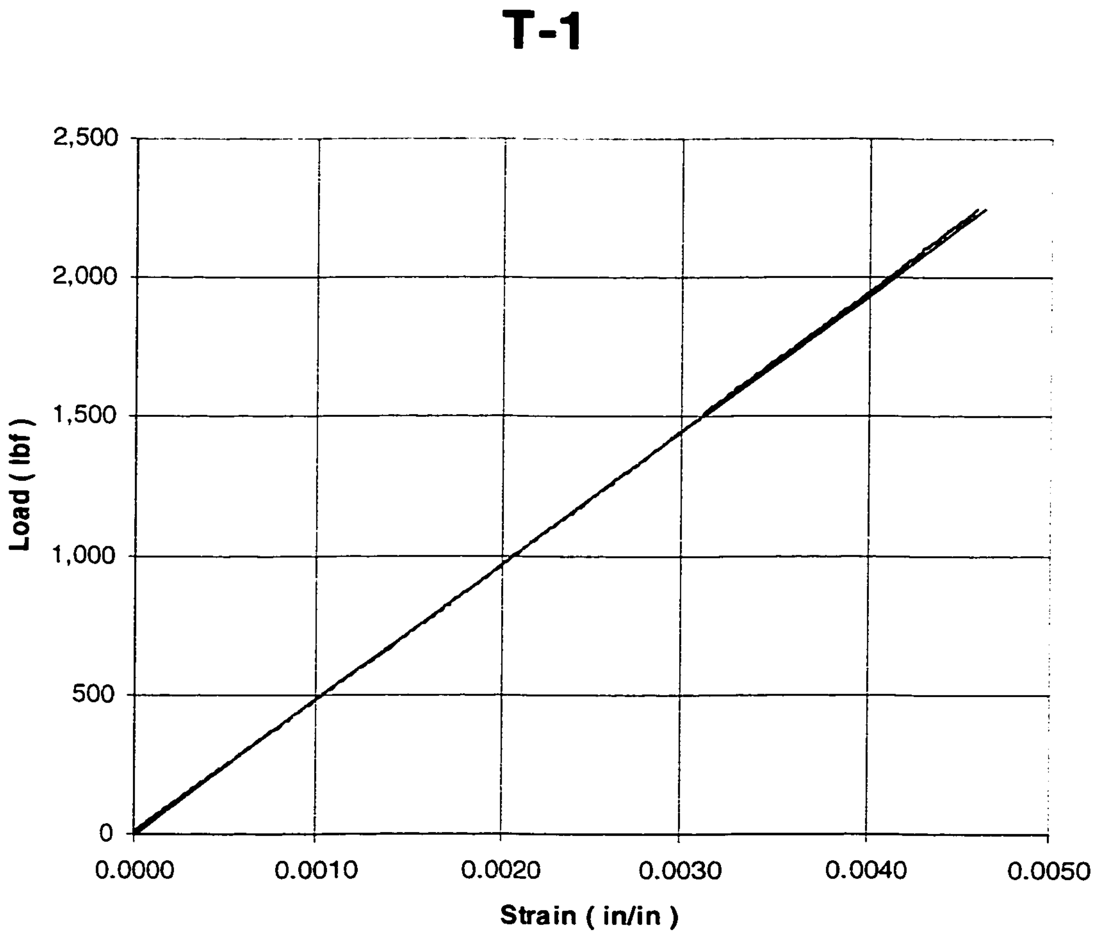

Figure C-2. Load-Strain Plot for T-300/Shell 862 Specimen T-1.

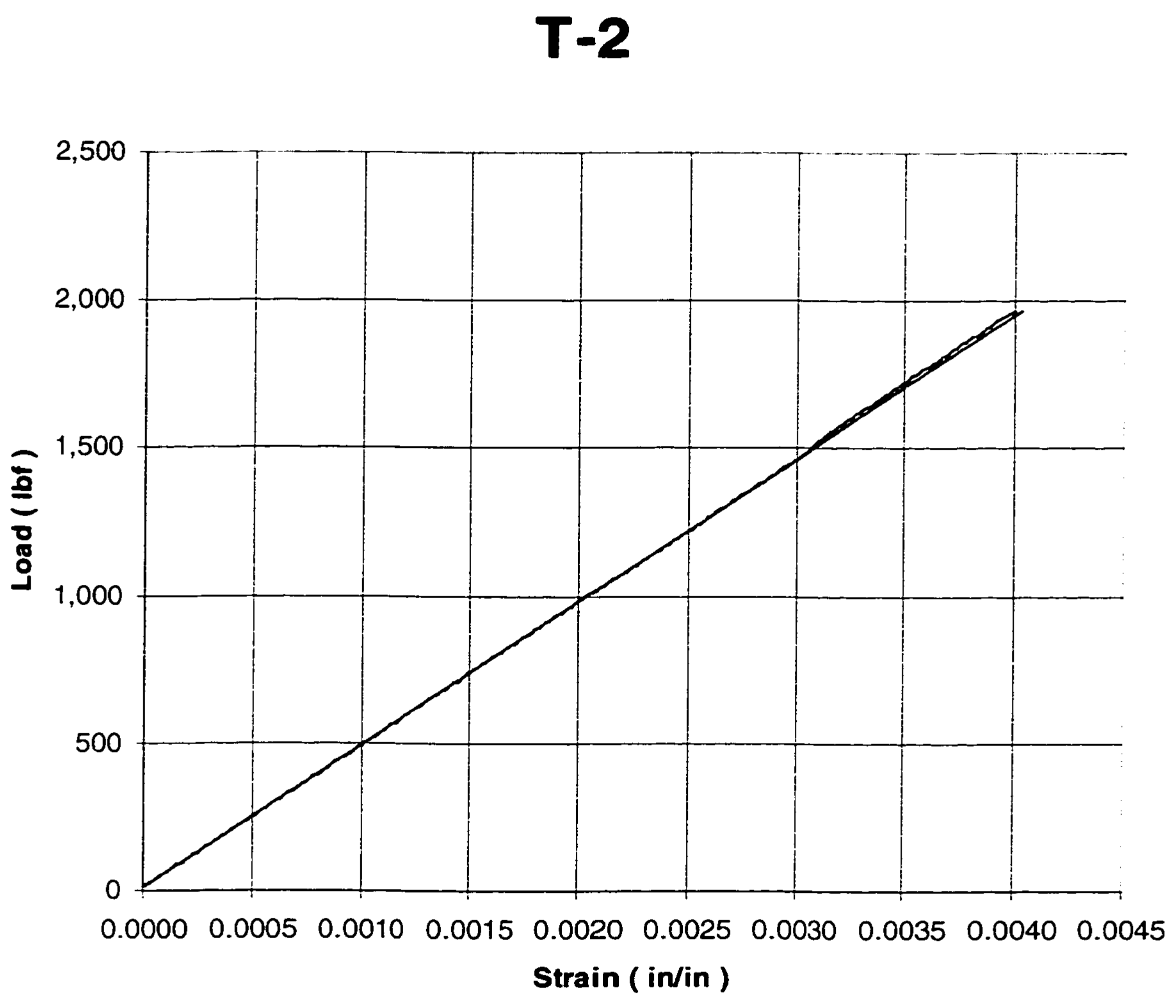

Figure C-3. Load-Strain Plot for T-300/Shell 862 Specimen T-2.

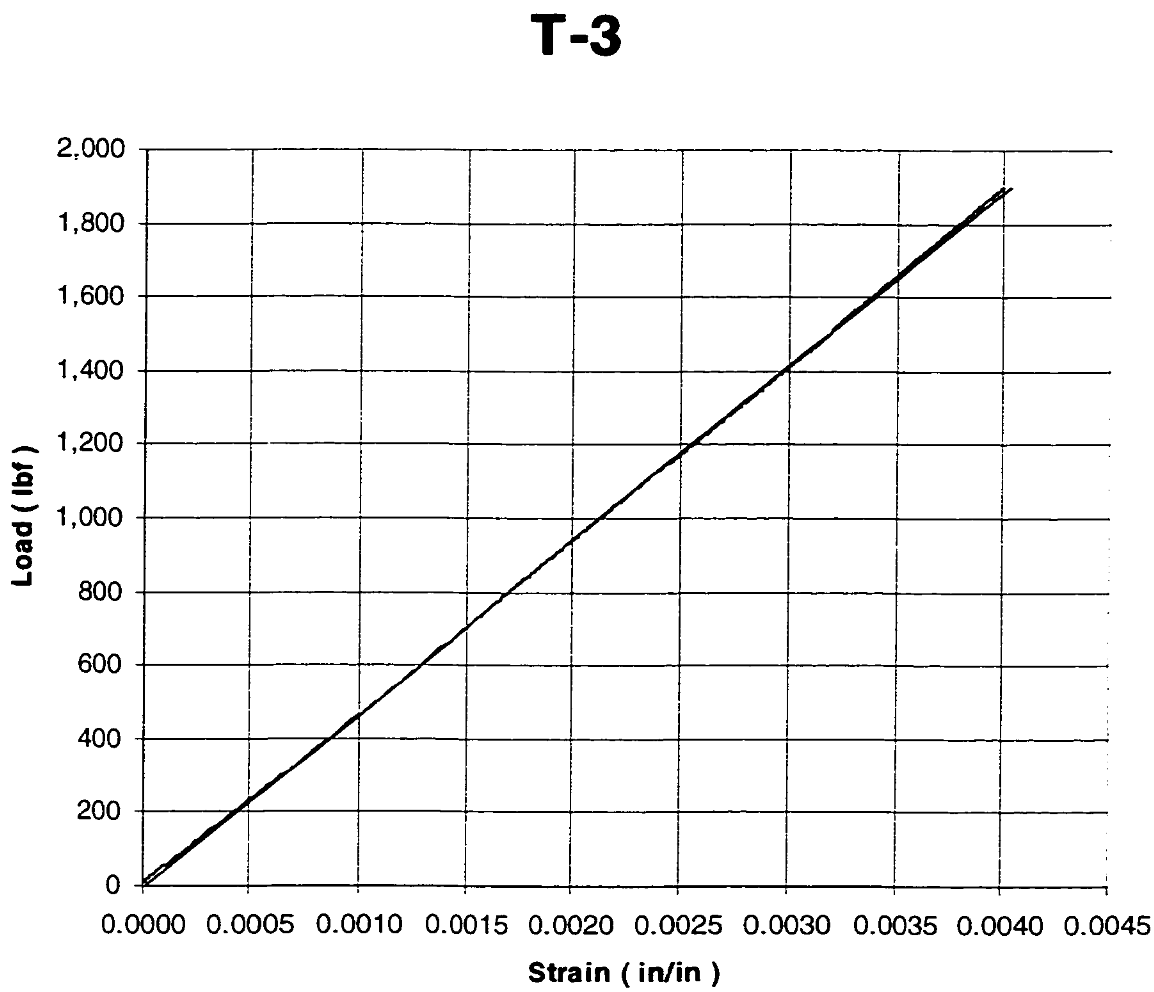

Figure C-4. Load-Strain Plot for T-300/Shell 862 Specimen T-3.

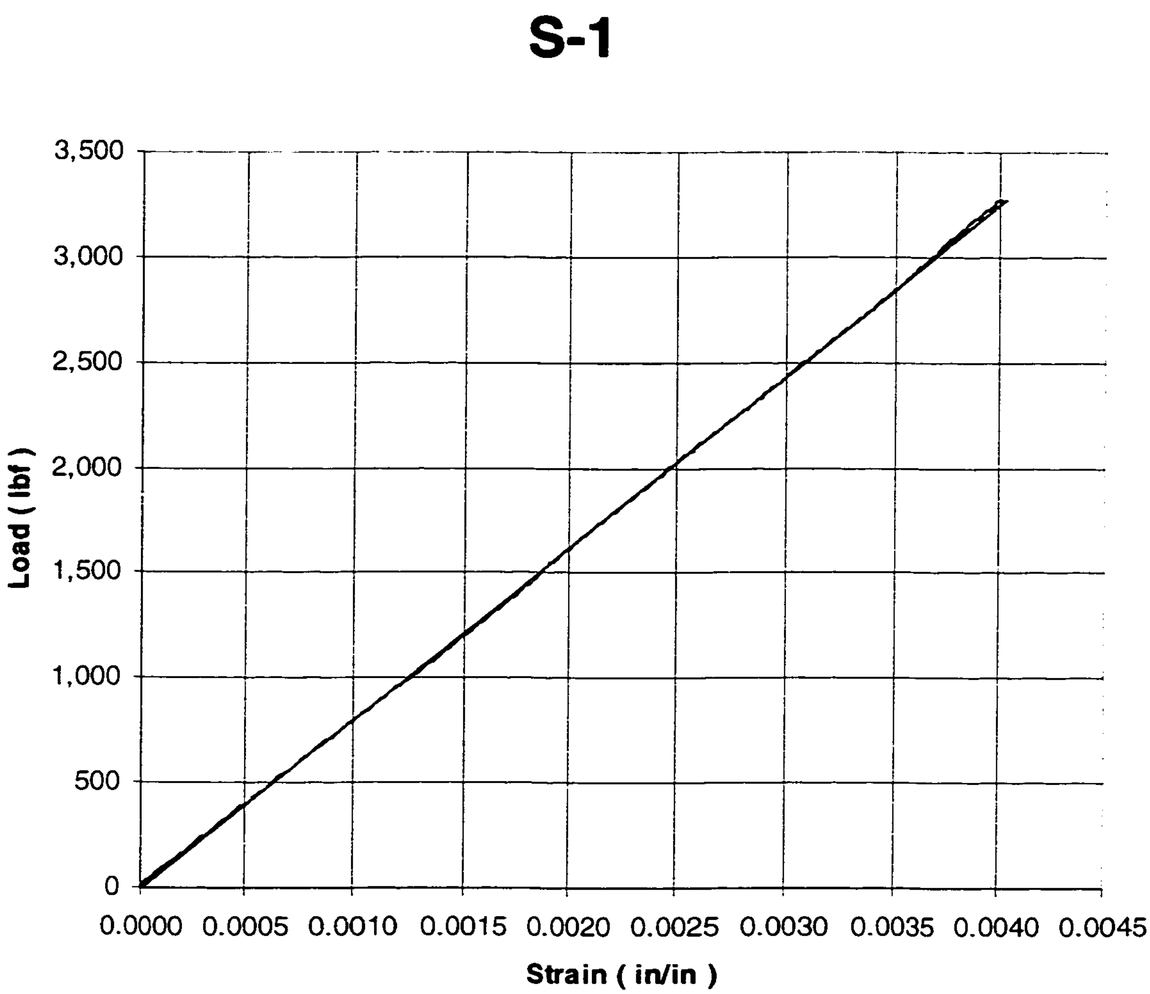

Figure C-5. Load-Strain Plot for T-300/Shell 862 Specimen S-1.

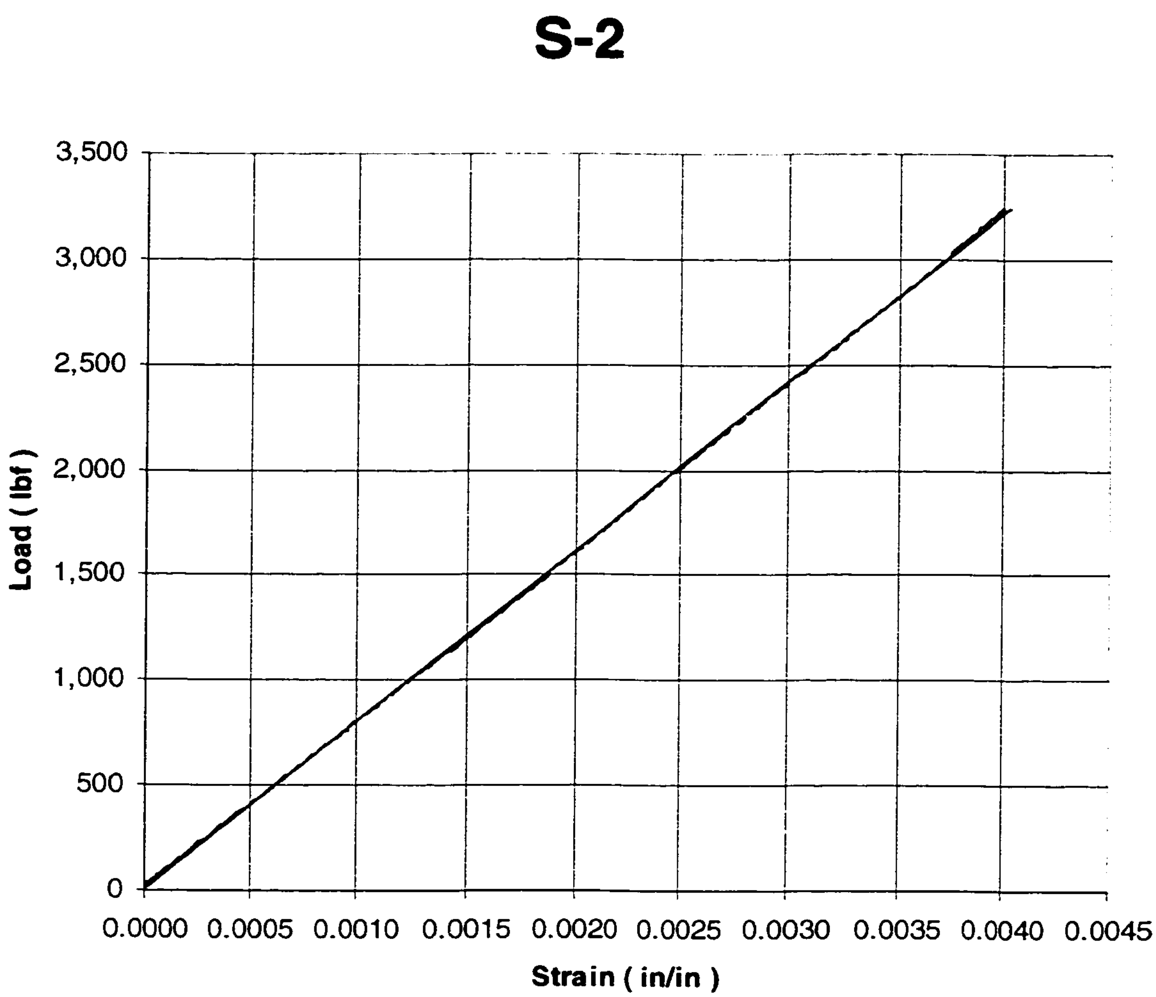

Figure C-6. Load-Strain Plot for T-300/Shell 862 Specimen S-2.

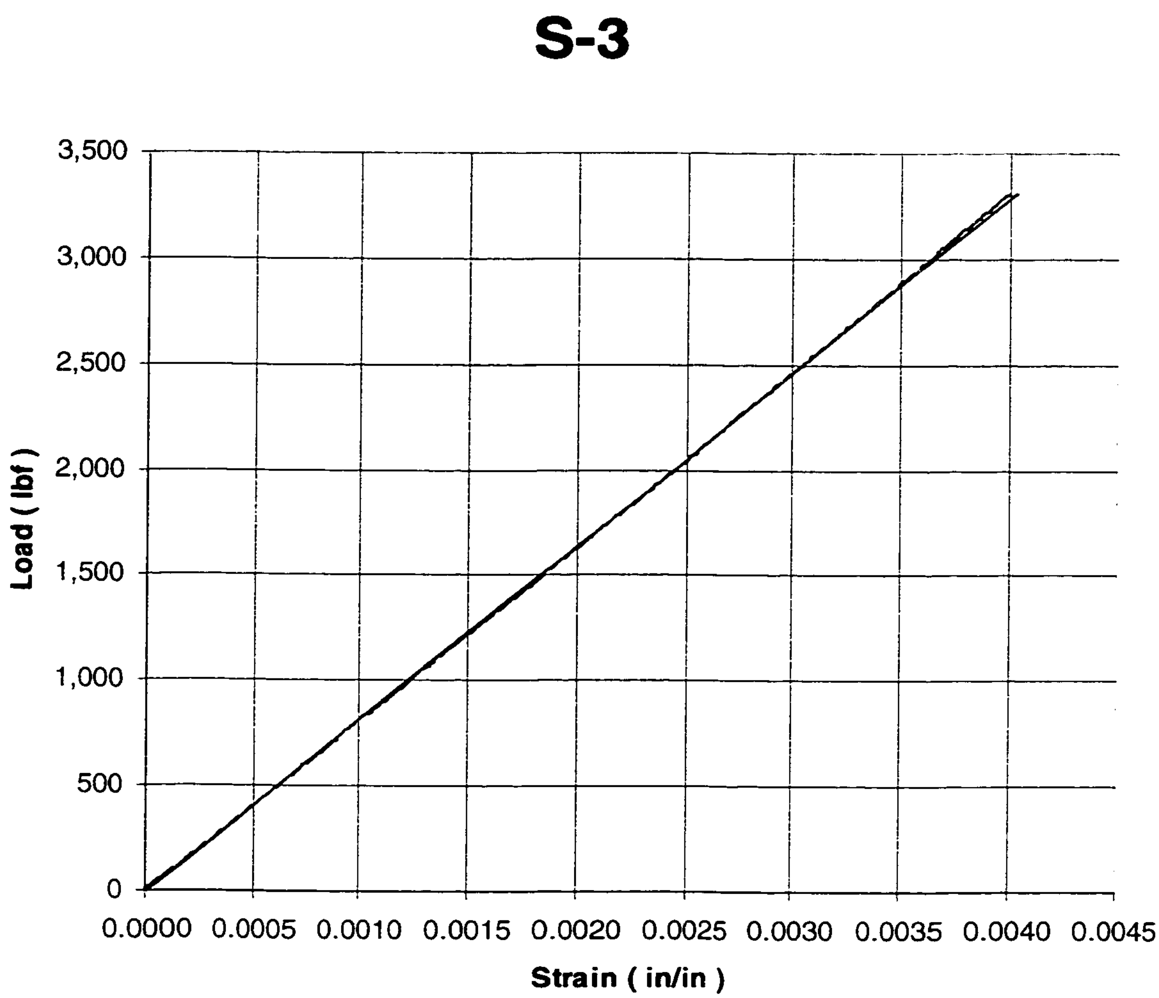

Figure C-7. Load-Strain Plot for T-300/Shell 862 Specimen S-3.

APPENDIX D

T-300/PR520 MATERIAL PROPERTIES DEVELOPMENT

Table D-1. T-300/PR520 Fiber, Matrix, and Void Volume Data.

Material and Layup:	**Panel #5**				**Resin Density =**	**1.2495**			
Water Temp. (deg. C)	**21**				**Fiber Density =**	**1.76**			
Water Density (g/cc)	**0.998**								
Specimen	**Dry Composite Weight (g)**	**Wet Composite Weight (g)**	**Fiber Weight (g)**	**Resin Weight (g)**	**Composite Density (g/cc)**	**Fiber Volume (%)**	**Resin Volume (%)**	**Void Volume (%)**	**Resin Content (%)**
5A	2.4225	0.8244	1.5573	0.8652	1.5128	55.3	44.7	1.5	35.7
5B	2.4156	0.8264	1.5357	0.8799	1.5170	54.8	45.2	1.0	36.4
5C	2.3997	0.8244	1.5233	0.8764	1.5203	54.8	45.2	0.7	36.5
					Average	55.0	45.0	1.1	36.2
					STDEV	0.3	0.3	0.4	0.4
					CV(%)	0.5	0.6	36.7	1.2

*Composite Density = (Dry Weight/(Dry Weight-Wet Weight))*Water Density*
*Fiber Volume = ((Fiber Weight/Fiber Density)/(Dry Weight/Composite Density))*100%*

Material and Layup:	**Panel #4**				**Resin Density =**	**1.2495**			
Water Temp. (deg. C)	**21**				**Fiber Density =**	**1.76**			
Water Density (g/cc)	**0.998**								
Specimen	**Dry Composite Weight (g)**	**Wet Composite Weight (g)**	**Fiber Weight (g)**	**Resin Weight (g)**	**Composite Density (g/cc)**	**Fiber Volume (%)**	**Resin Volume (%)**	**Void Volume (%)**	**Resin Content (%)**
4A	2.2485	0.766	1.4378	0.8107	1.5137	55.0	45.0	1.3	36.1
4B	2.2909	0.7801	1.4463	0.8446	1.5133	54.3	45.7	1.1	36.9
4C	2.3678	0.8062	1.537	0.8308	1.5132	55.8	44.2	1.7	35.1
					Average	55.0	45.0	1.4	36.0
					STDEV	0.8	0.8	0.3	0.9
					CV(%)	1.4	1.7	23.3	2.5

*Composite Density = (Dry Weight/(Dry Weight-Wet Weight))*Water Density*
*Fiber Volume = ((Fiber Weight/Fiber Density)/(Dry Weight/Composite Density))*100%*

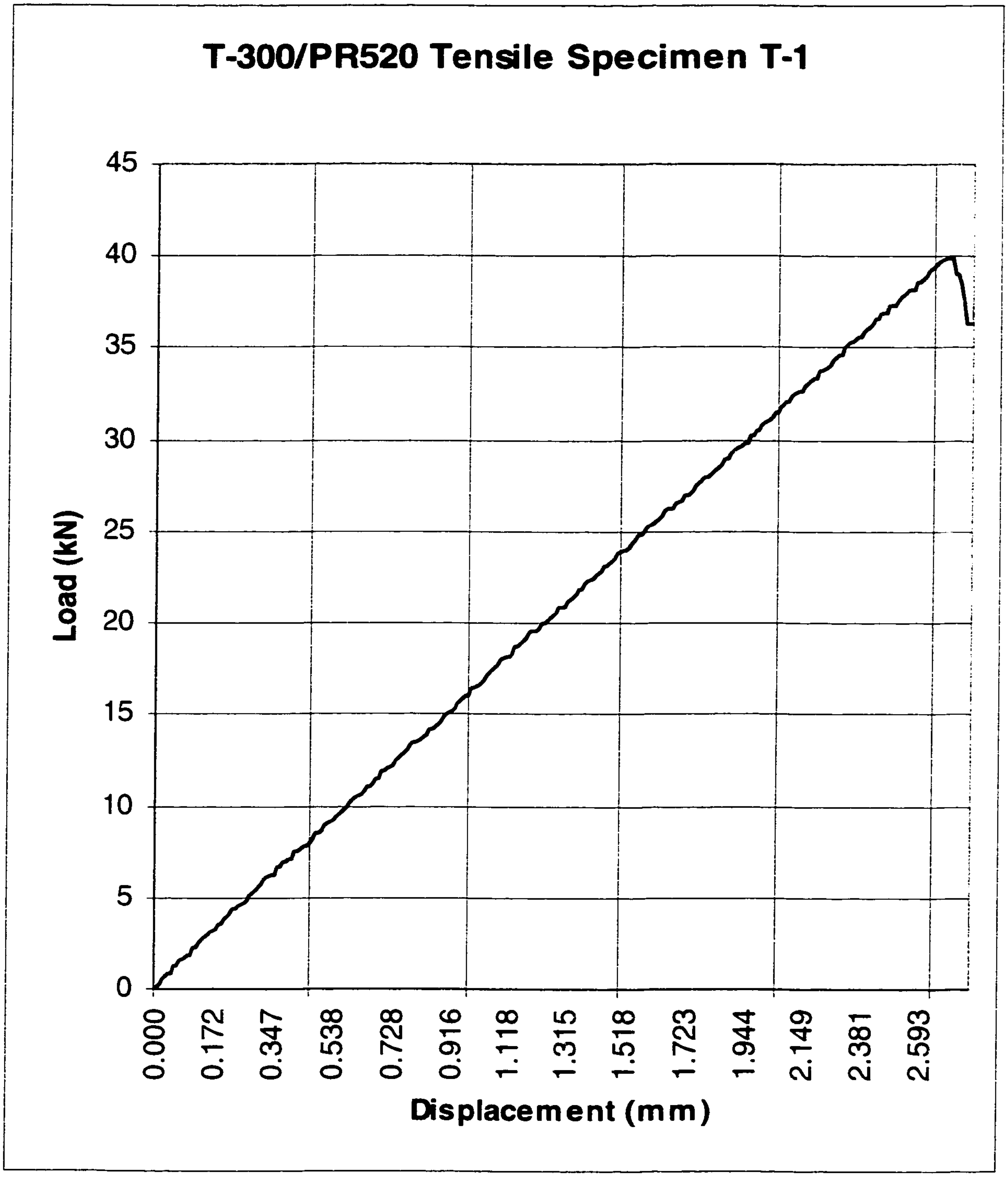

Figure D-1. T-300/PR520 Tensile Load-Displacement Plot: Specimen T-1.

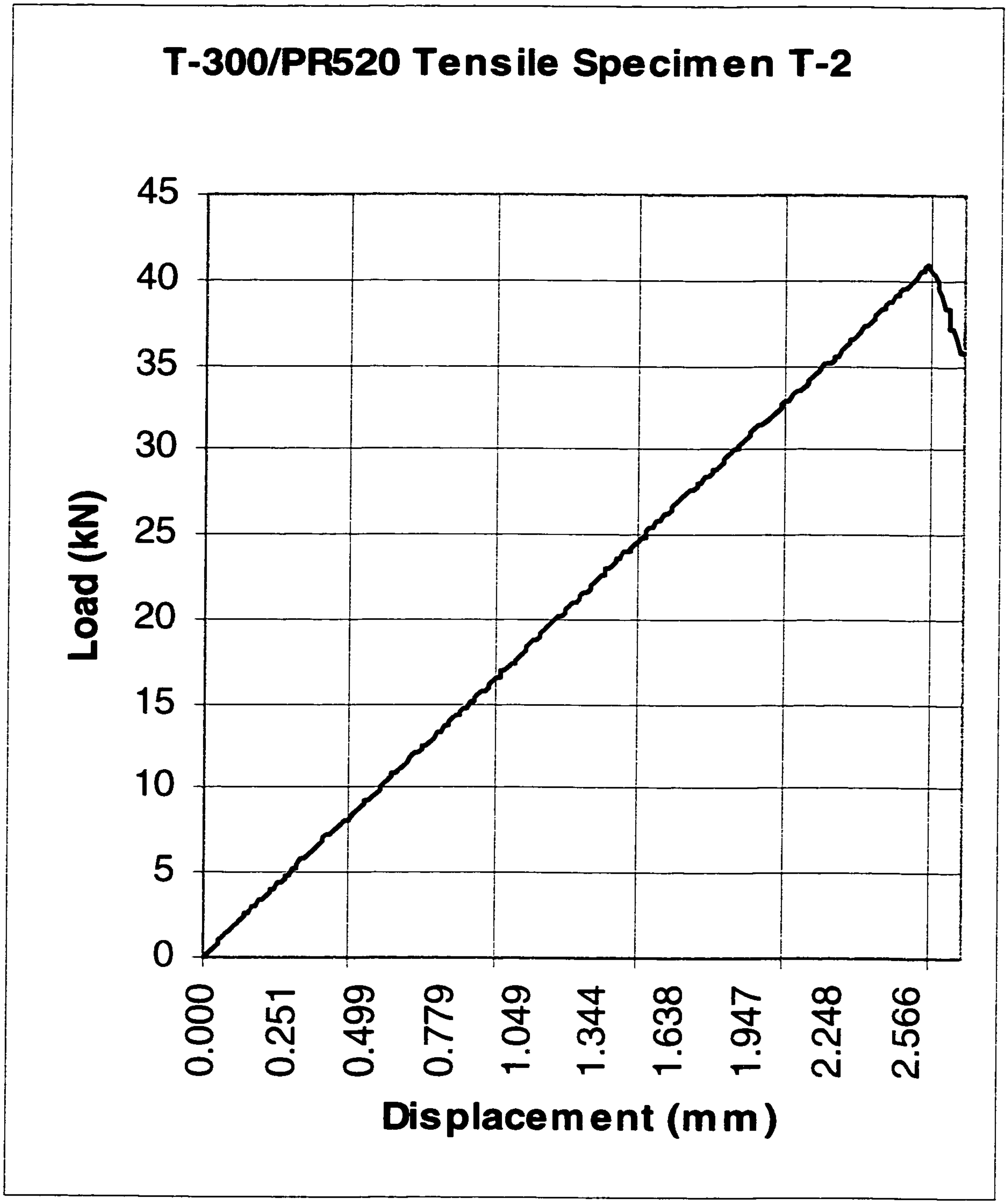

Figure D-2. T-300/PR520 Tensile Load-Displacement Plot: Specimen T-2.

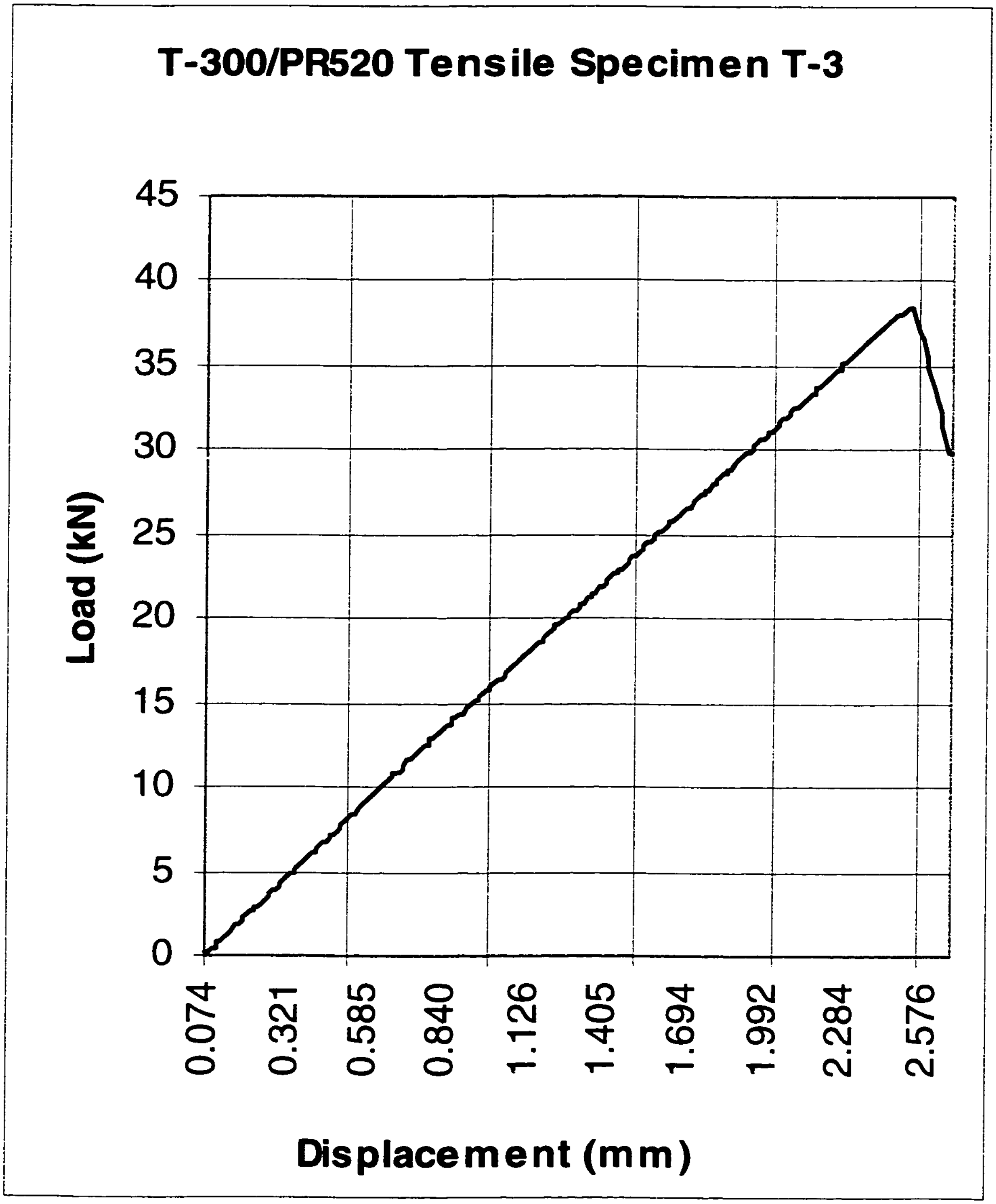

Figure D-3. T-300/PR520 Tensile Load-Displacement Plot: Specimen T-3.

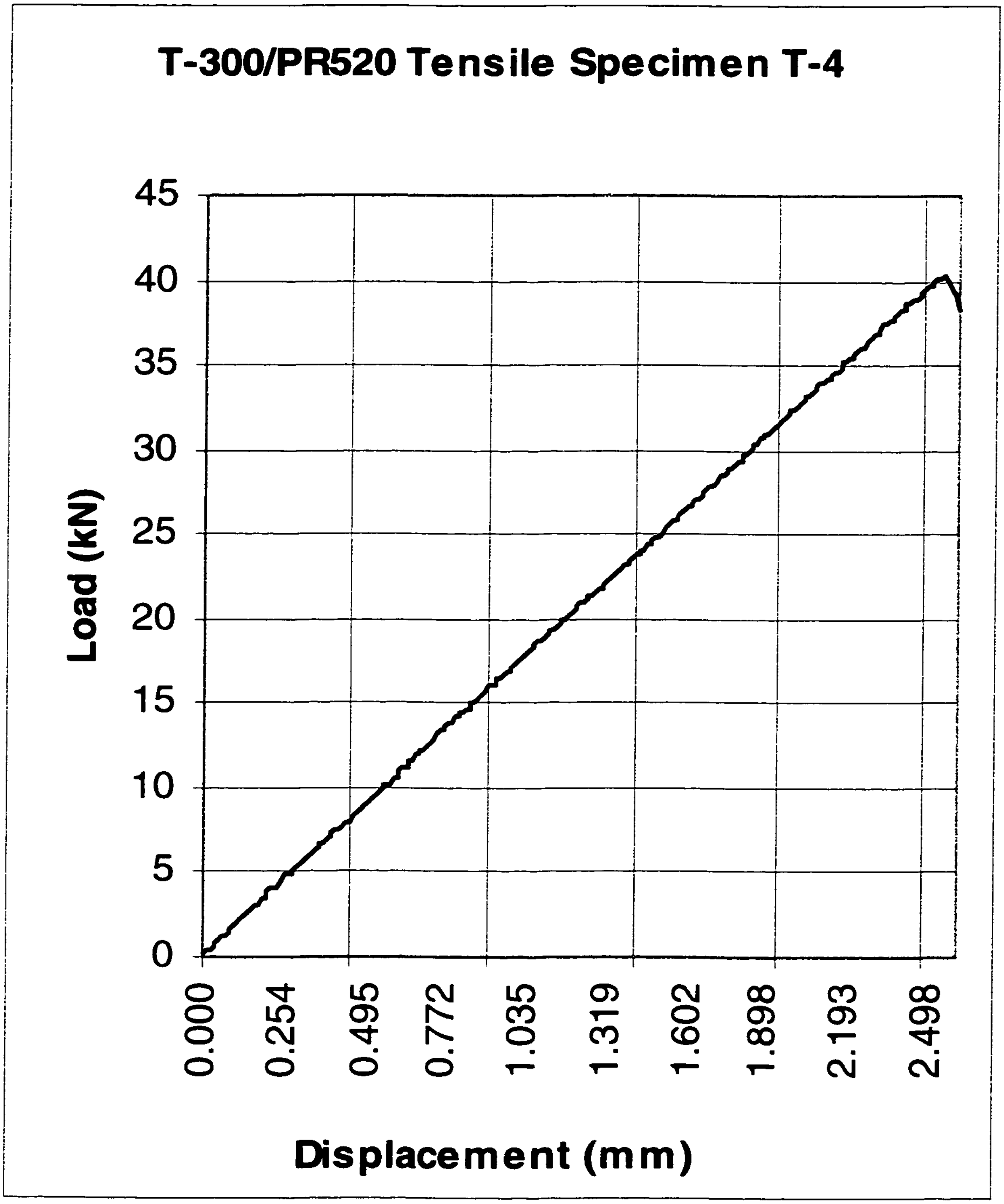

Figure D-4. T-300/PR520 Tensile Load-Displacement Plot: Specimen T-4.

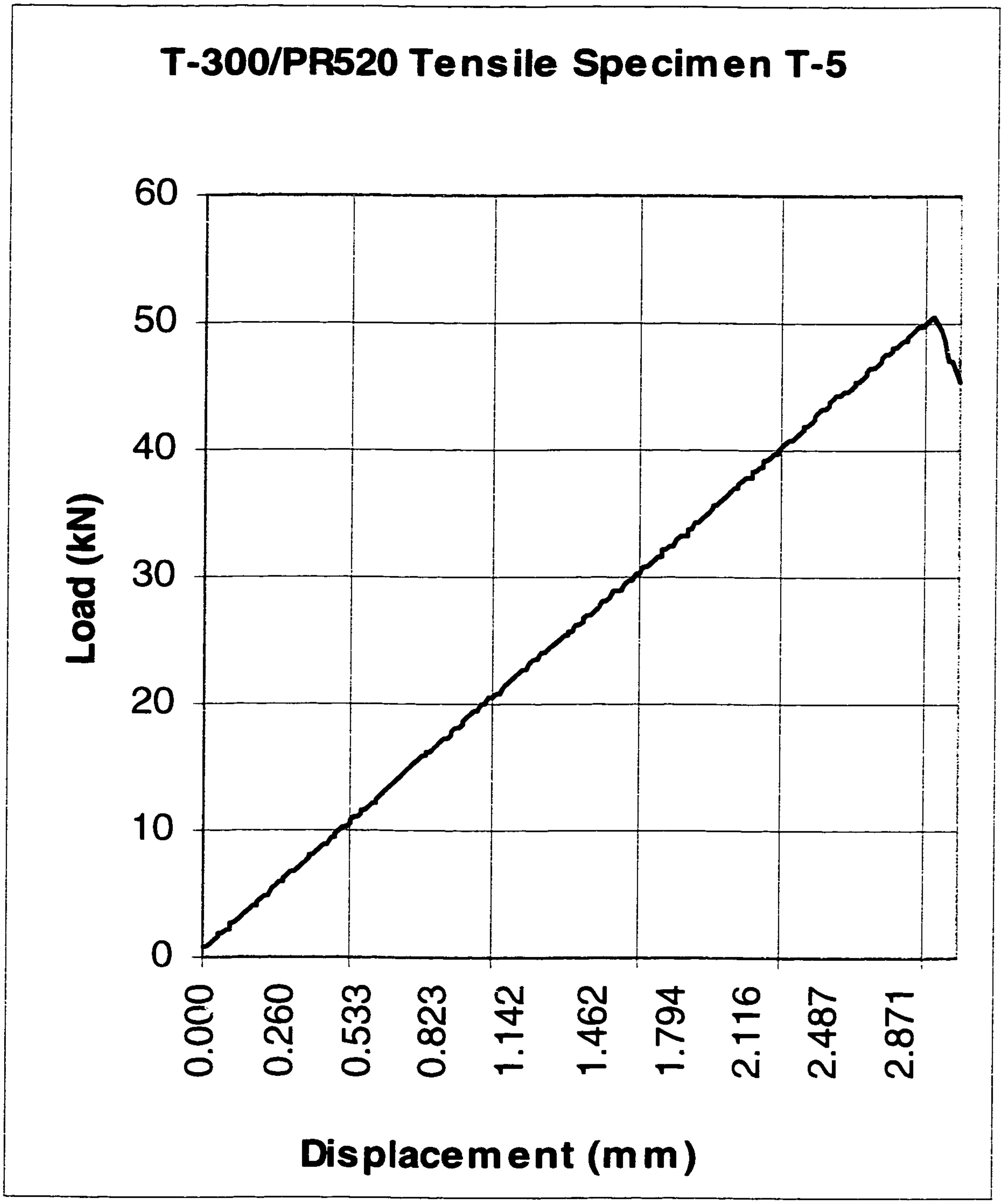

Figure D-5. T-300/PR520 Tensile Load-Displacement Plot: Specimen T-5.

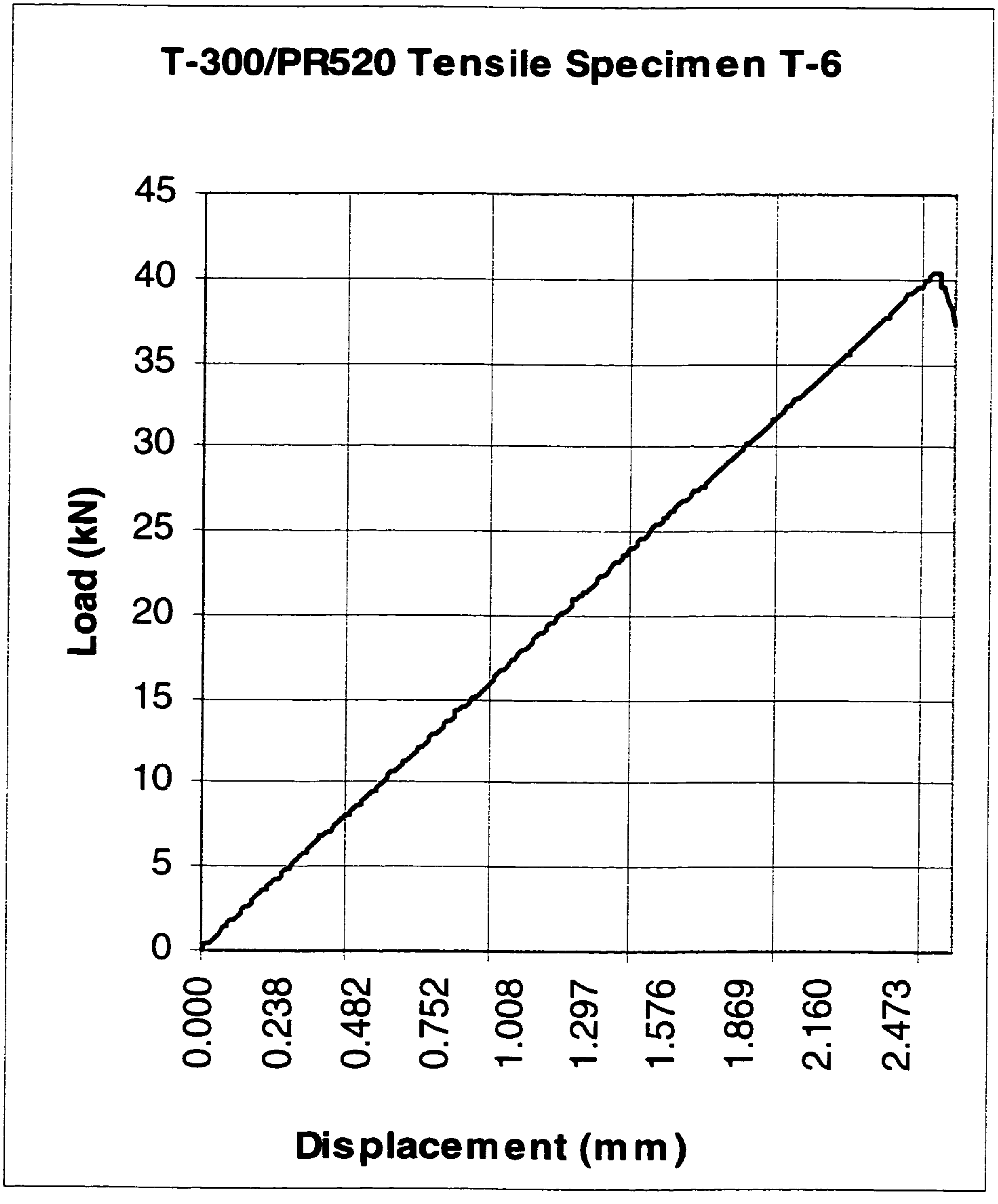

Figure D-6. T-300/PR520 Tensile Load-Displacement Plot: Specimen T-6.

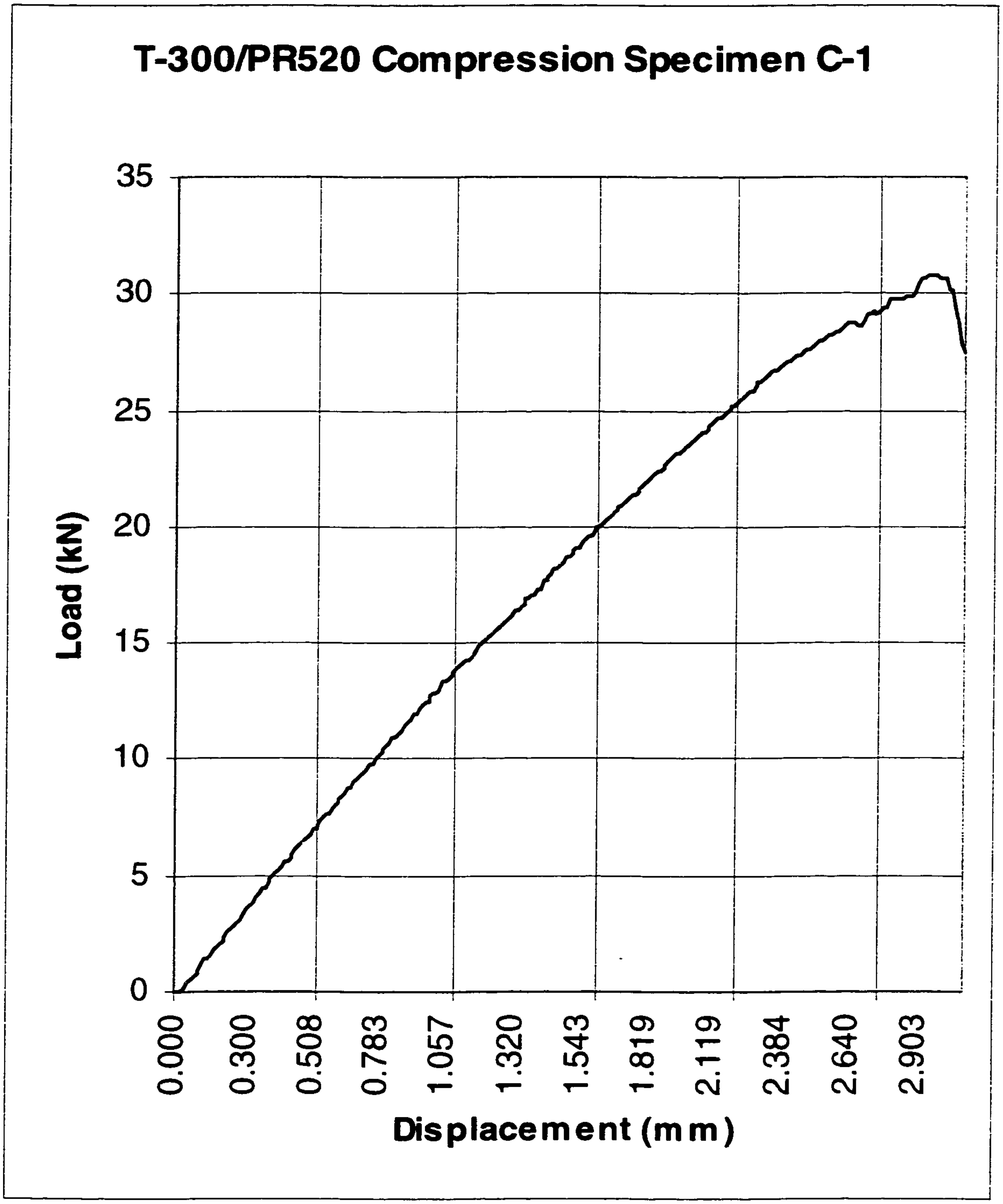

Figure D-7. T-300/PR520 Compression Load-Displacement Plot: Specimen C-1.

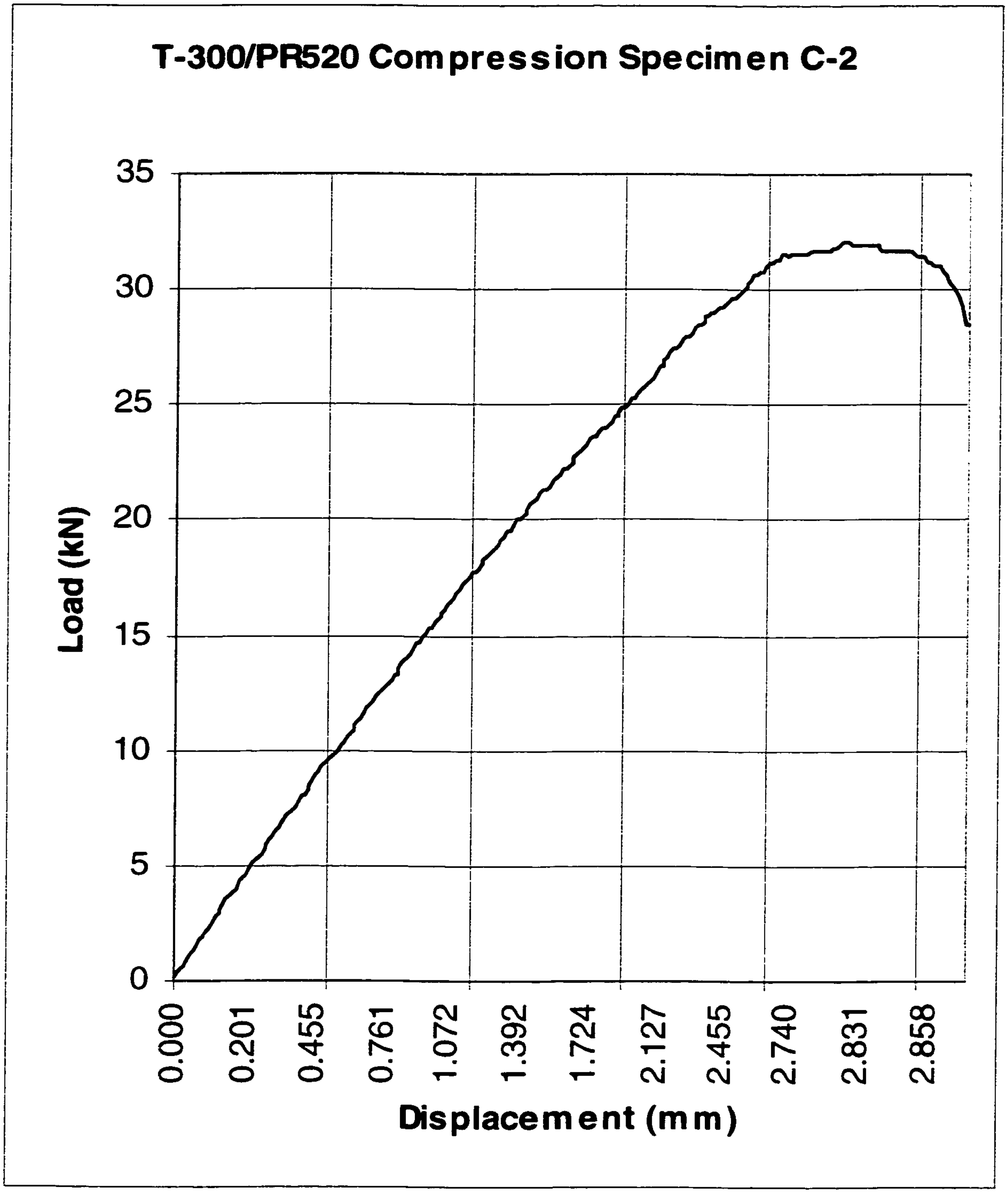

Figure D-8. T-300/PR520 Compression Load-Displacement Plot: Specimen C-2.

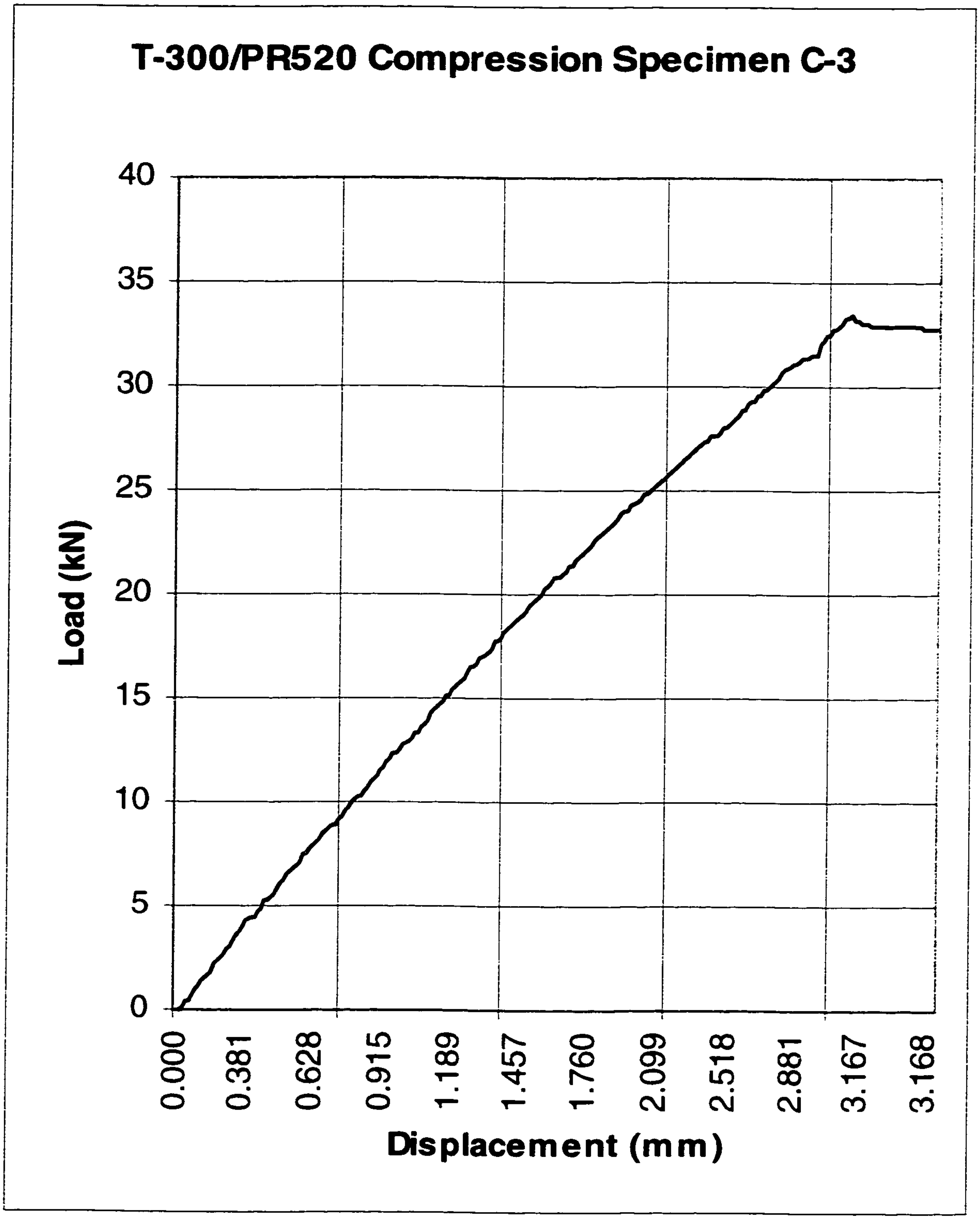

Figure D-9. T-300/PR520 Compression Load-Displacement Plot: Specimen C-3.

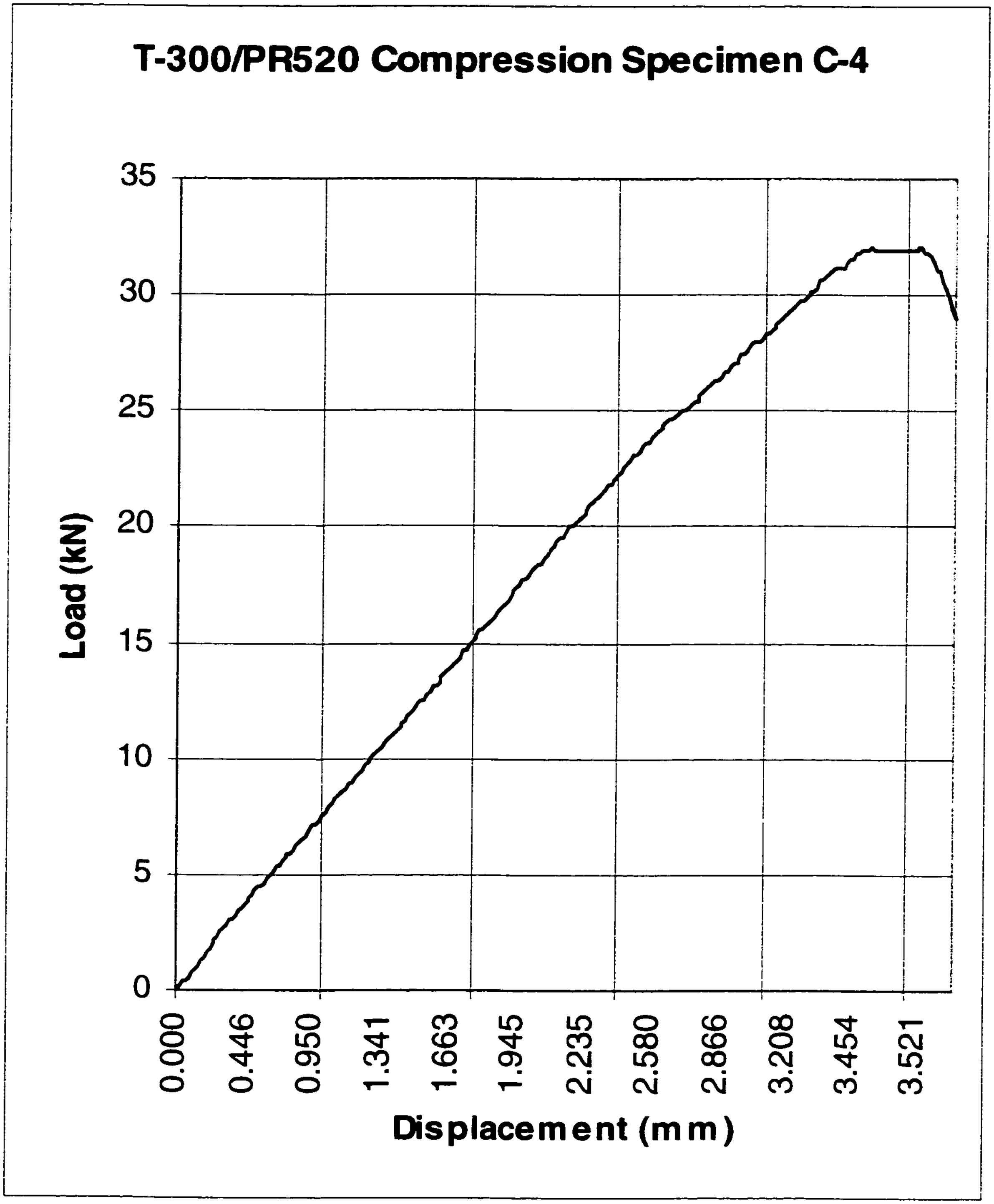

Figure D-10. T-300/PR520 Compression Load-Displacement Plot: Specimen C-4.

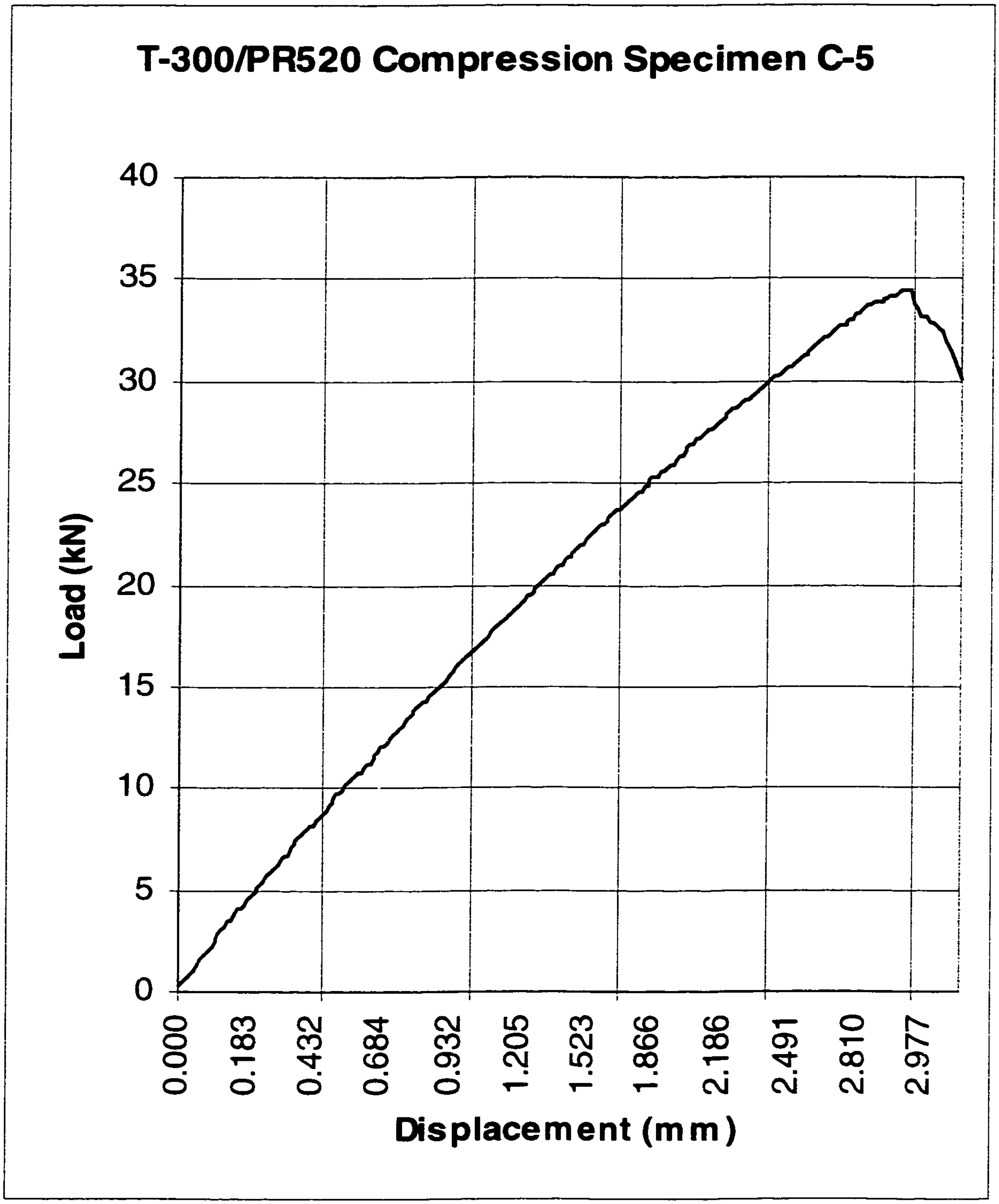

Figure D-11. T-300/PR520 Compression Load-Displacement Plot: Specimen C-5.

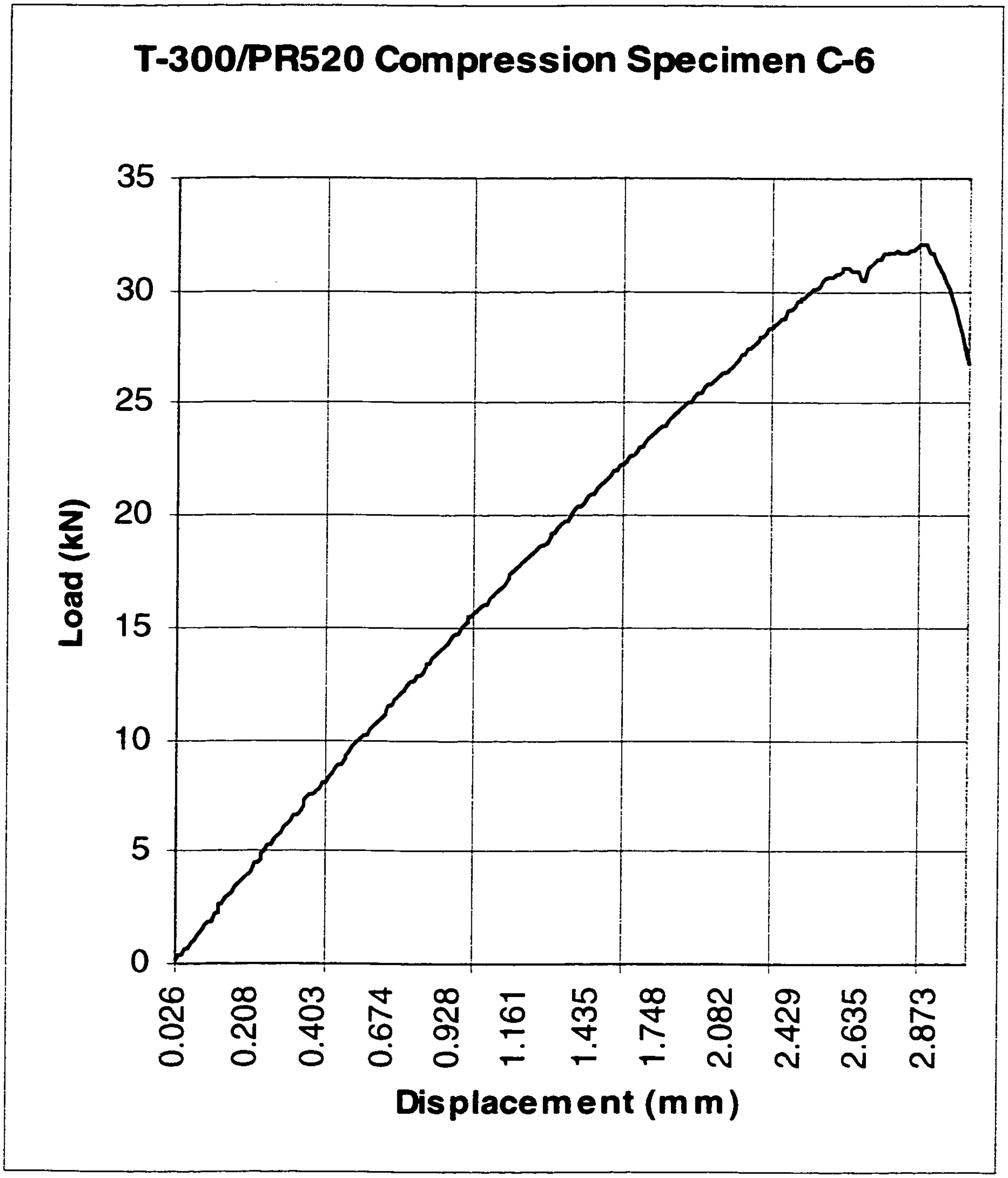

Figure D-12. T-300/PR520 Compression Load-Displacement Plot: Specimen C-6.

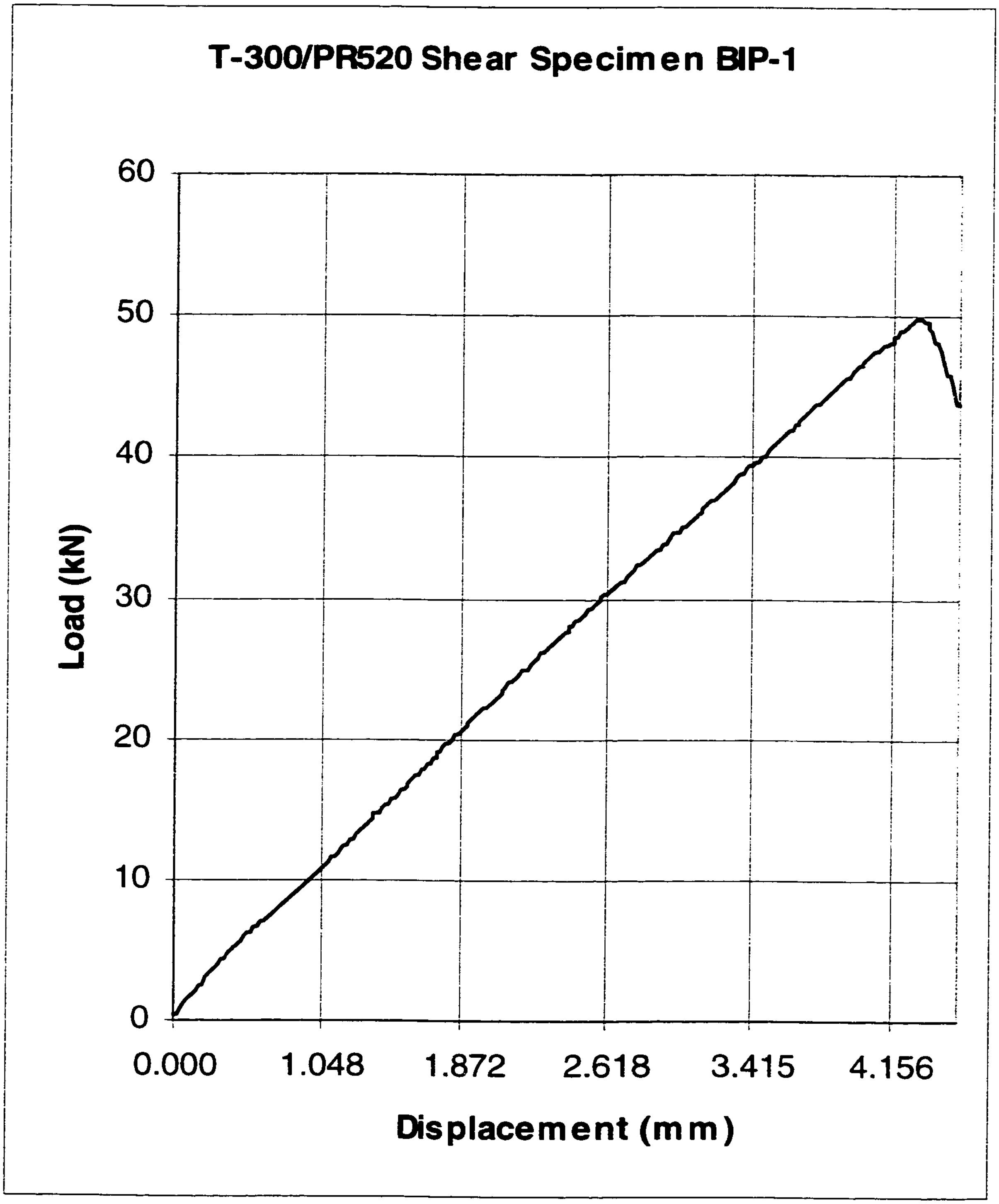

Figure D-13. T-300/PR520 In-Plane Shear Load-Displacement Plot: Specimen BIP-1.

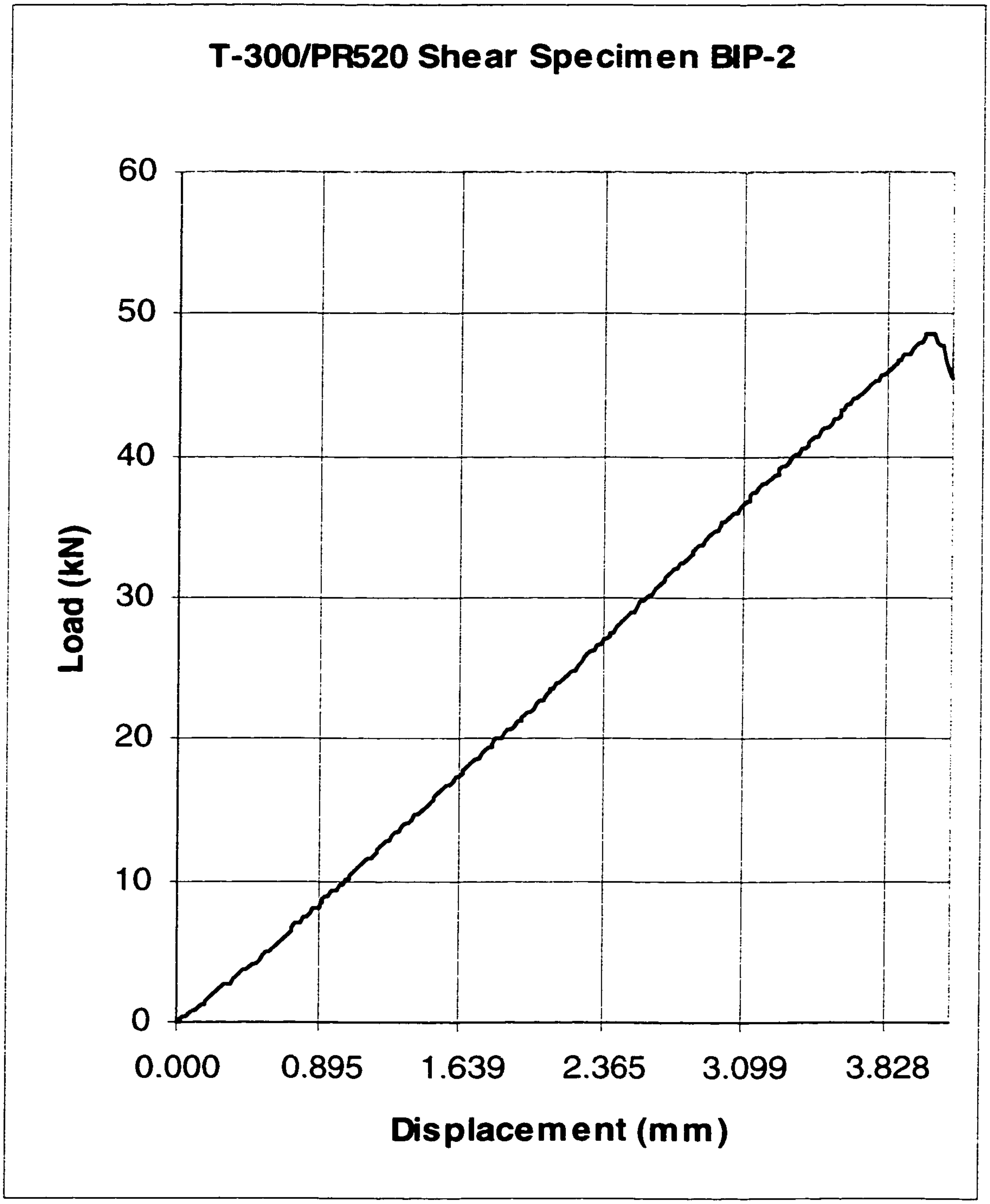

Figure D-14. T-300/PR520 In-Plane Shear Load-Displacement Plot: Specimen BIP-2.

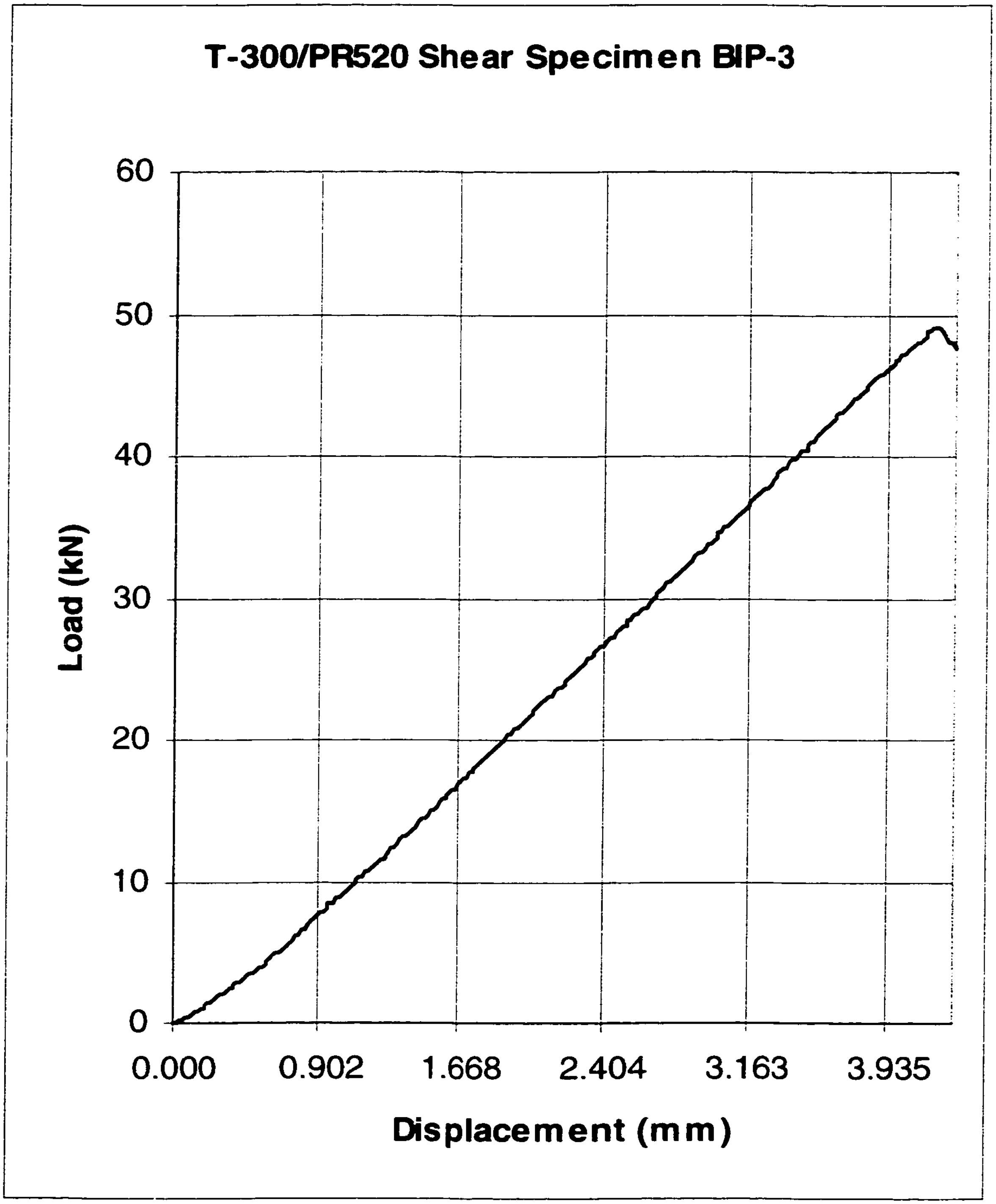

Figure D-15. T-300/PR520 In-Plane Shear Load-Displacement Plot: Specimen BIP-3.

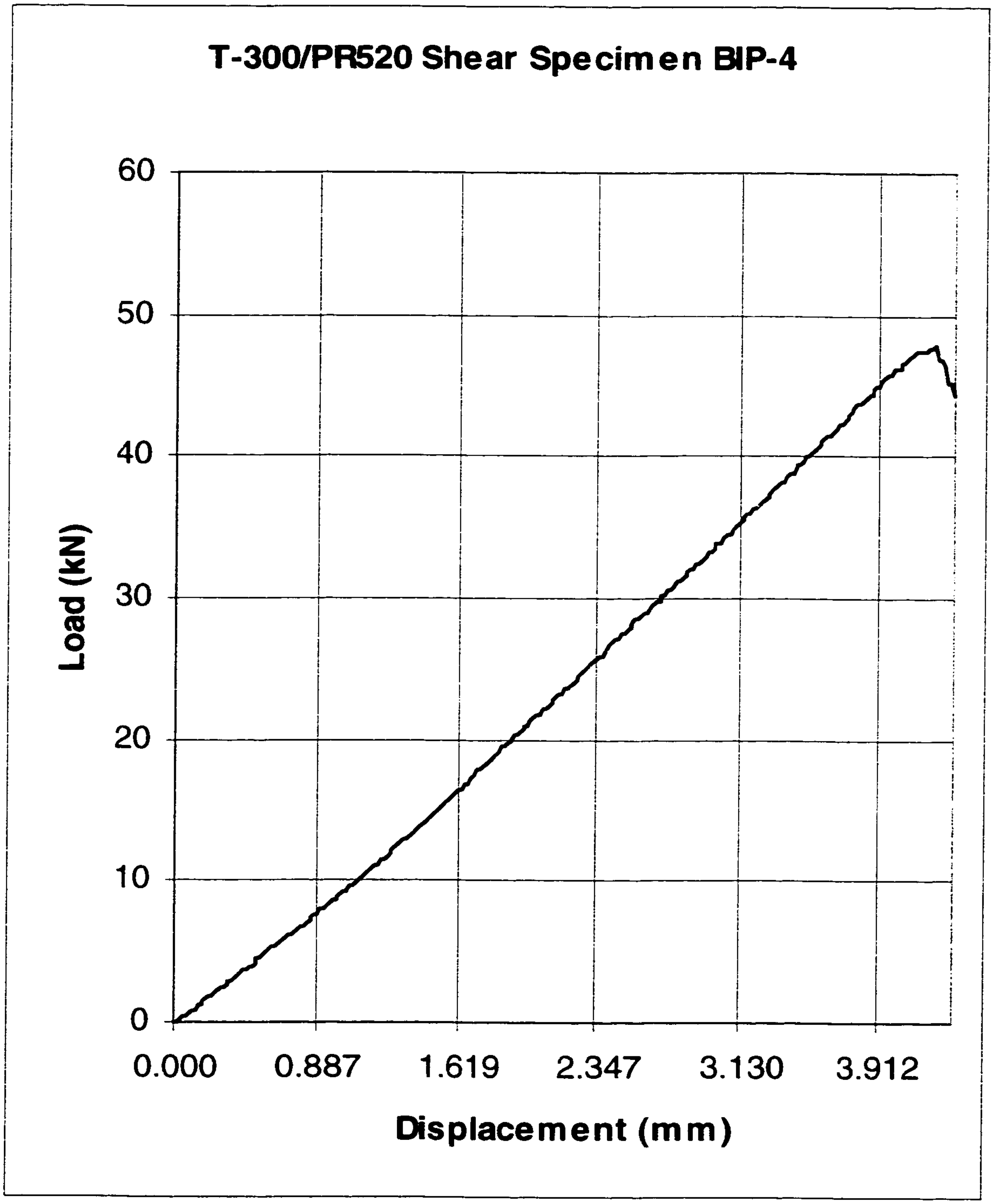

Figure D-16. T-300/PR520 In-Plane Shear Load-Displacement Plot: Specimen BIP-4.

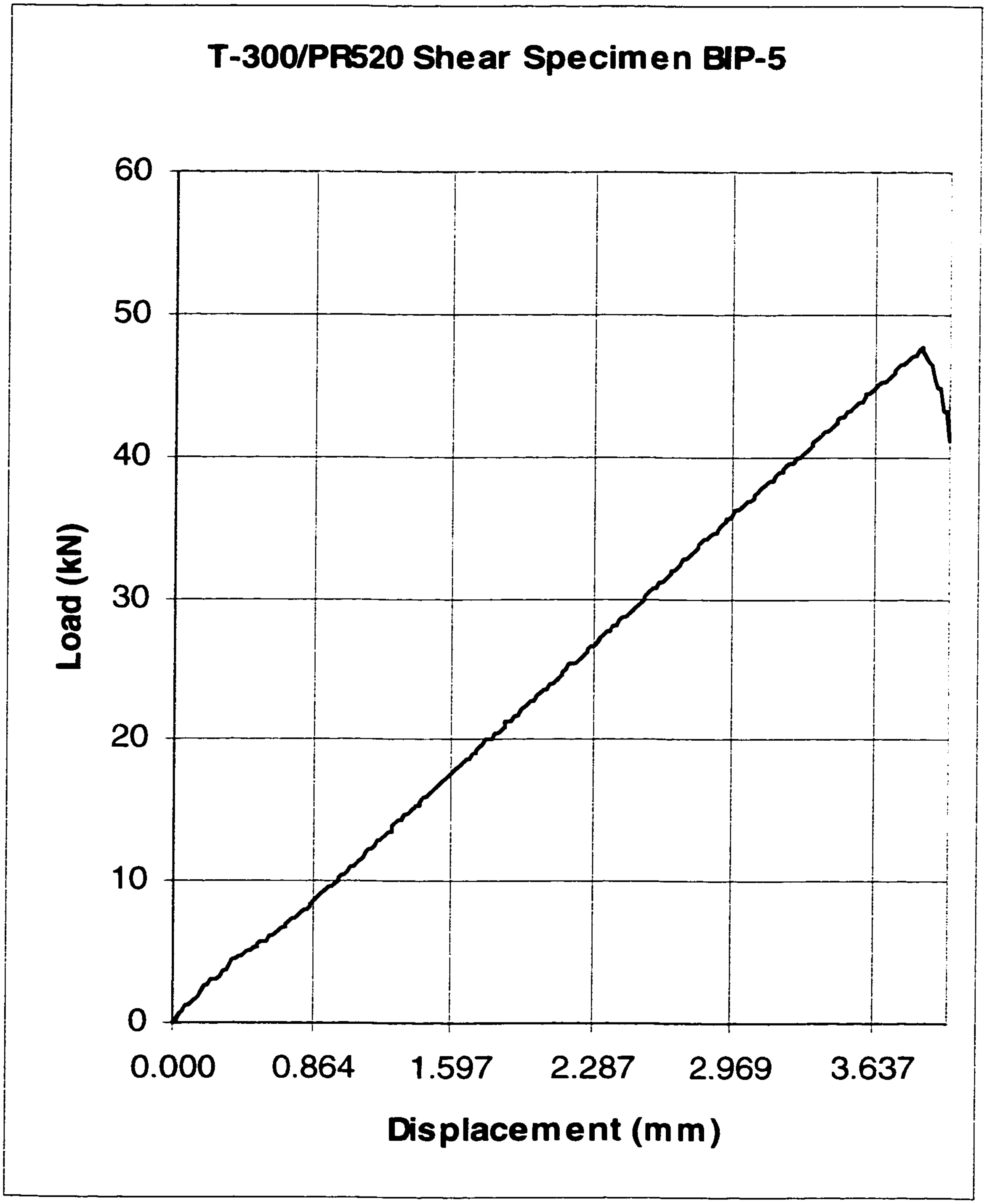

Figure D-17. T-300/PR520 In-Plane Shear Load-Displacement Plot: Specimen BIP-5.

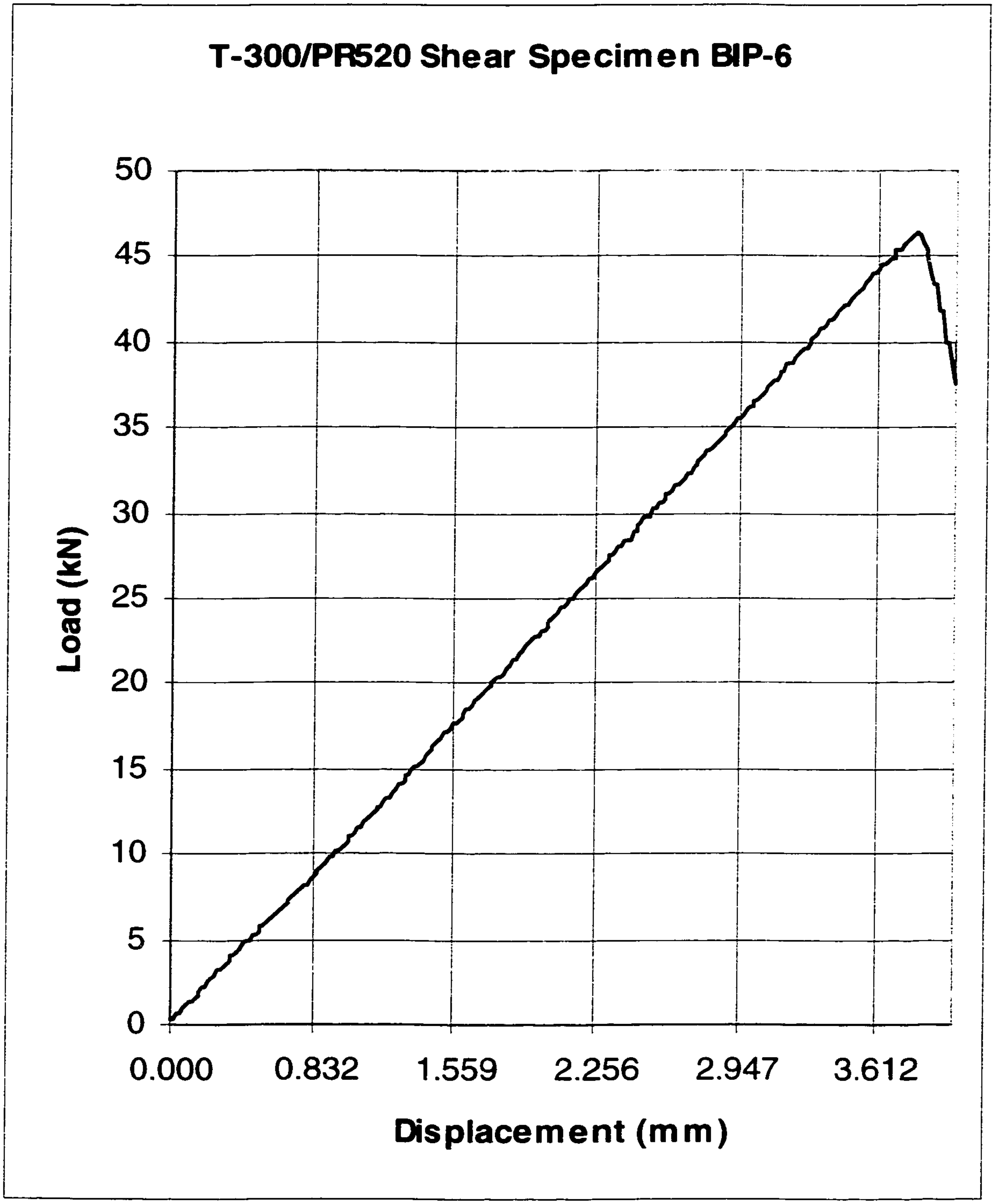

Figure D-18. T-300/PR520 In-plane Shear Load-Displacement Plot: Specimen BIP-6.

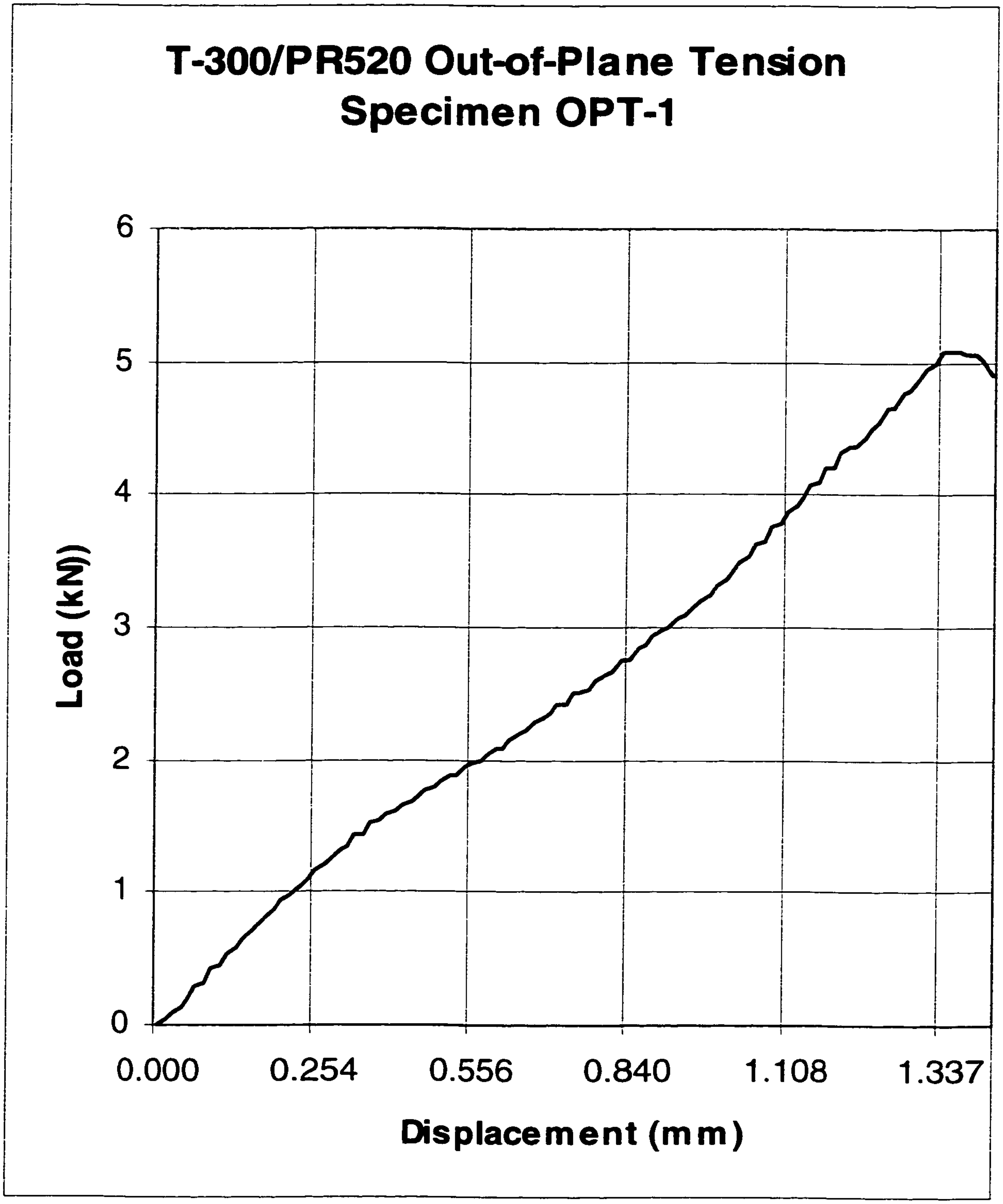

Figure D-19. T-300/PR520 Out-of-Plane Tension Load-Displacement Plot: Specimen OPT-1

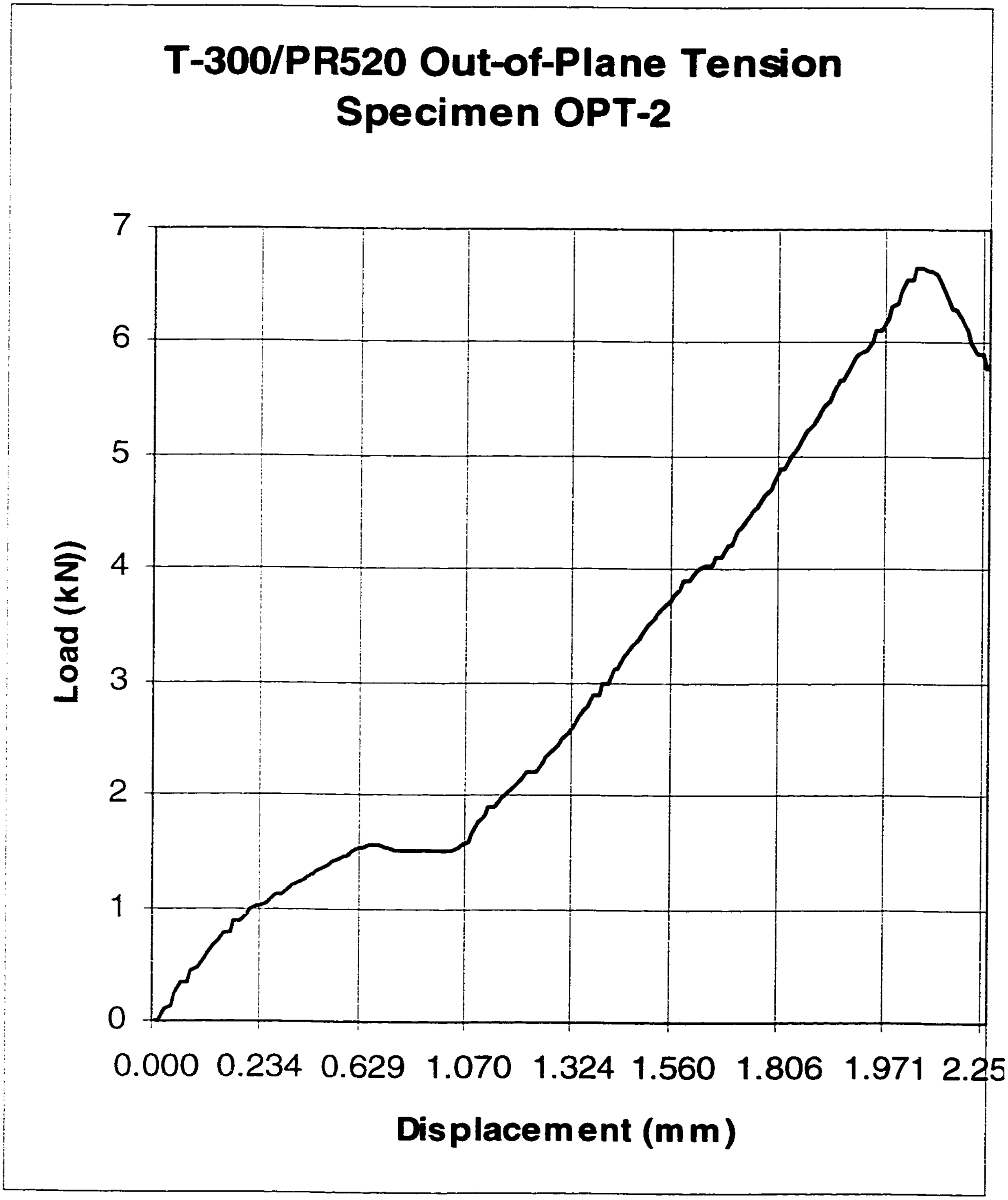

Figure D-20. T-300/PR520 Out-of-Plane Tension Load-Displacement Plot: Specimen OPT-2

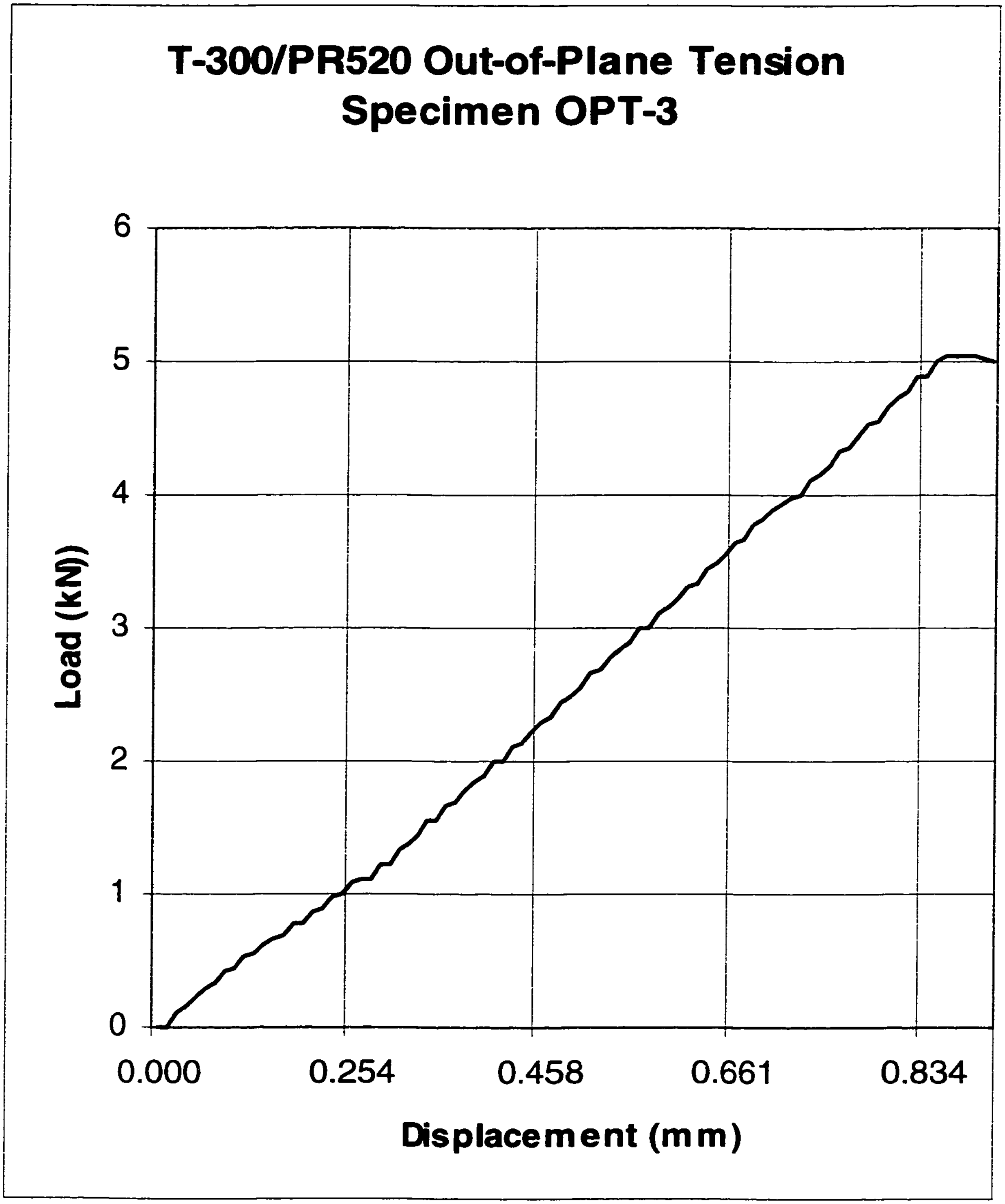

Figure D-21. T-300/PR520 Out-of-Plane Tension Load-Displacement Plot: Specimen OPT-3

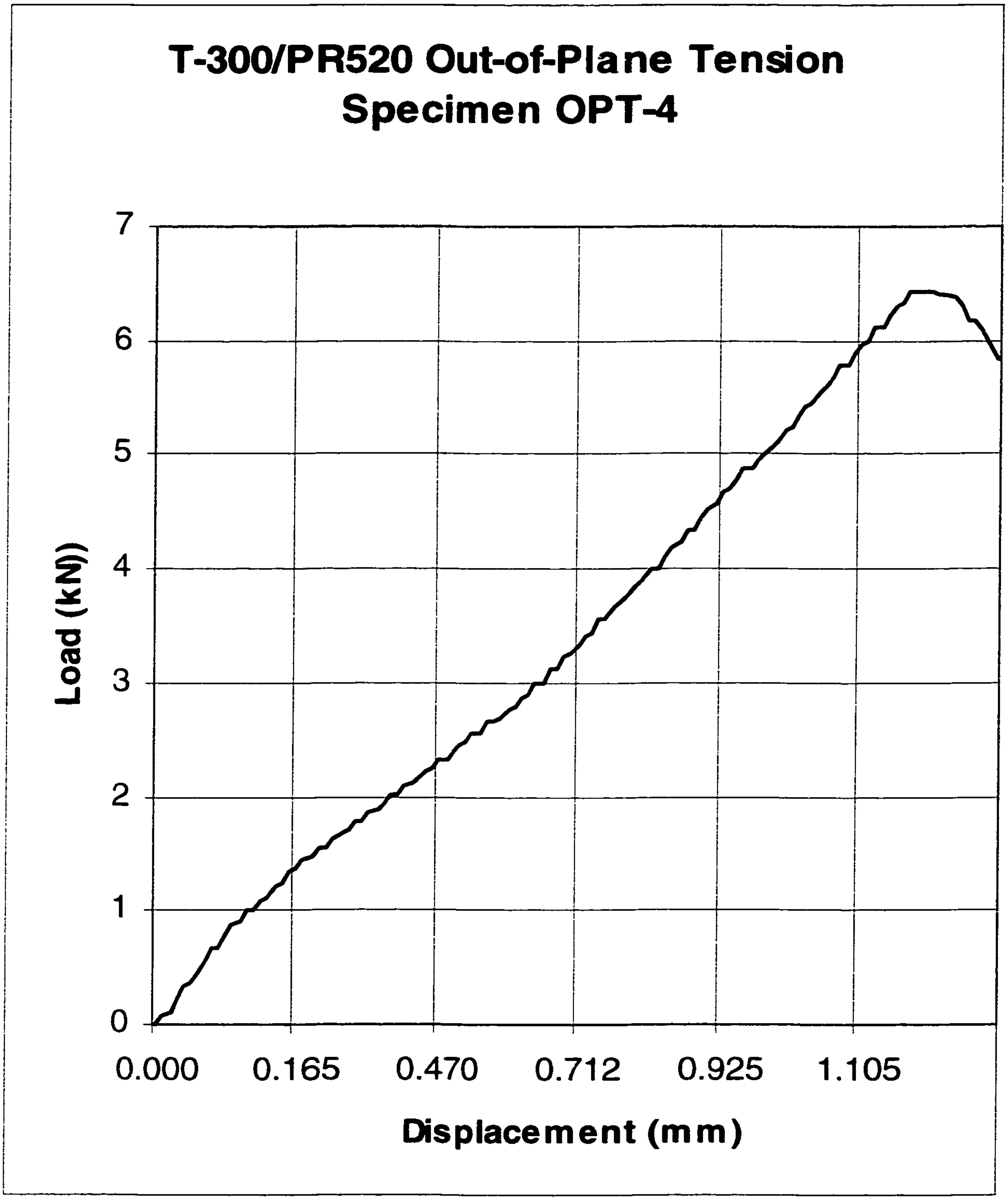

Figure D-22. T-300/PR520 Out-of-Plane Tension Load-Displacement Plot: Specimen OPT-4

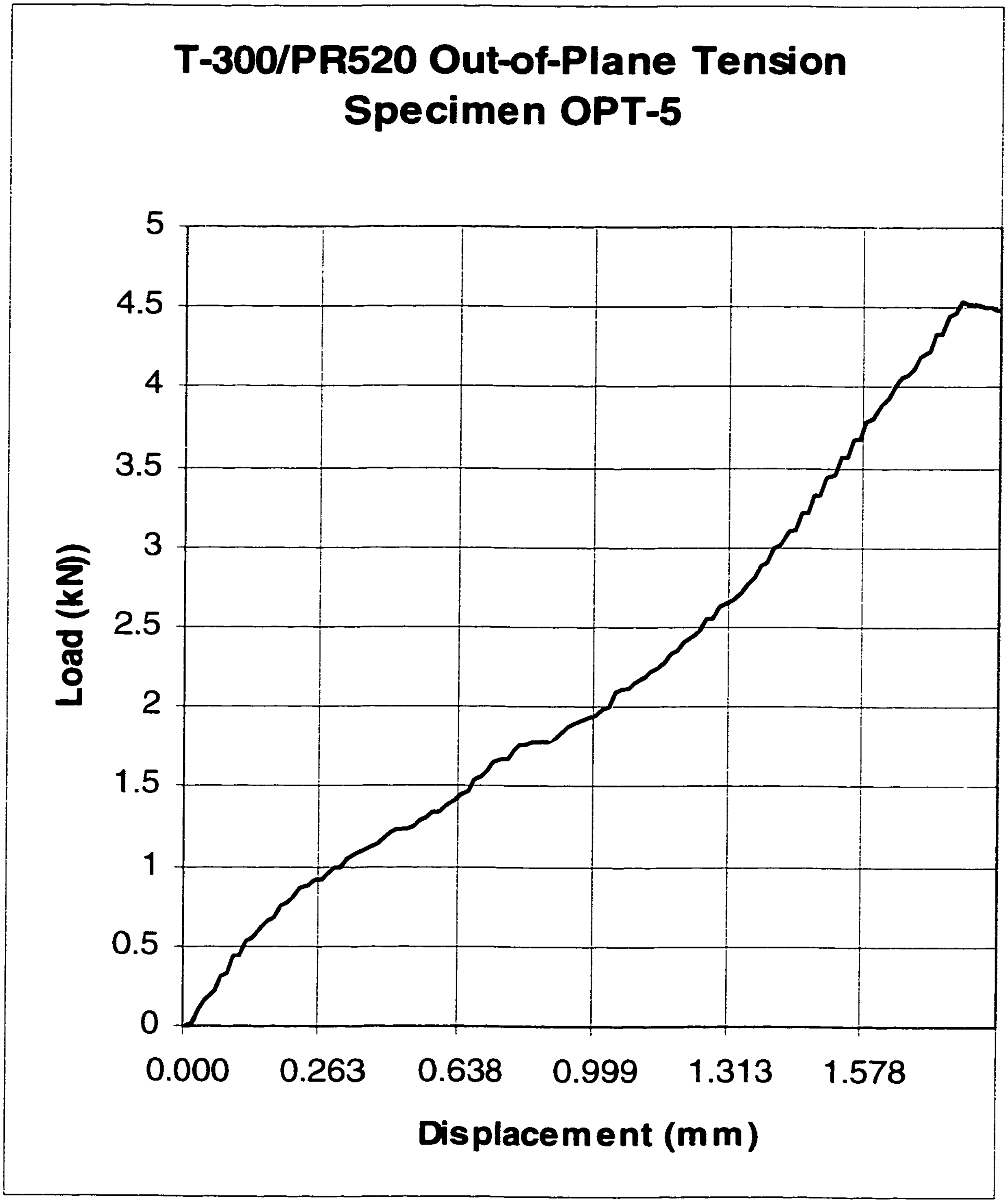

Figure D-23. T-300/PR520 Out-of-Plane Tension Load-Displacement Plot: Specimen OPT-5

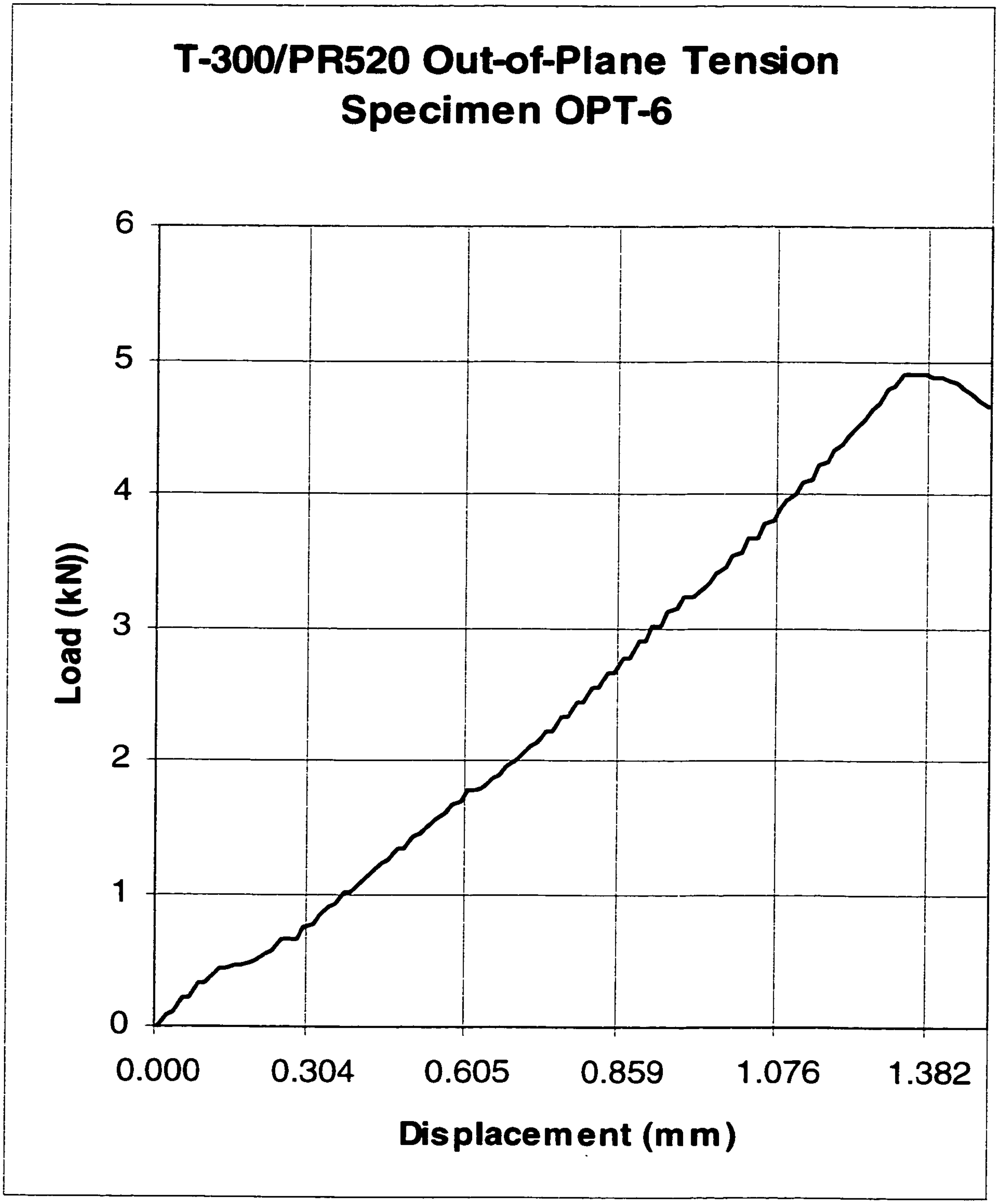

Figure D-24. T-300/PR520 Out-of-Plane Tension Load-Displacement Plot: Specimen OPT-6

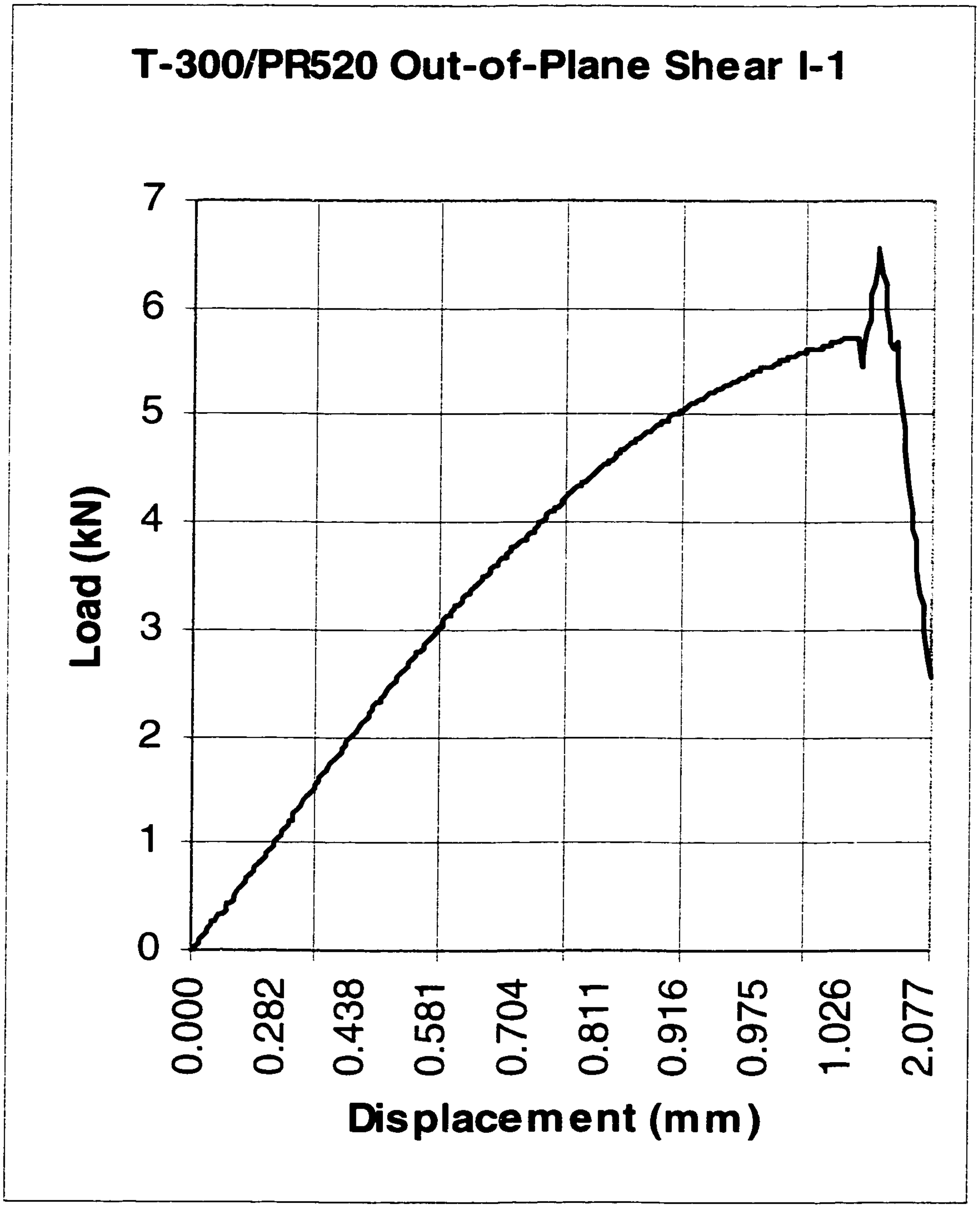

Figure D-25. T-300/PR520 Out-of-Plane Shear Load-Displacement Plot: Specimen I-1

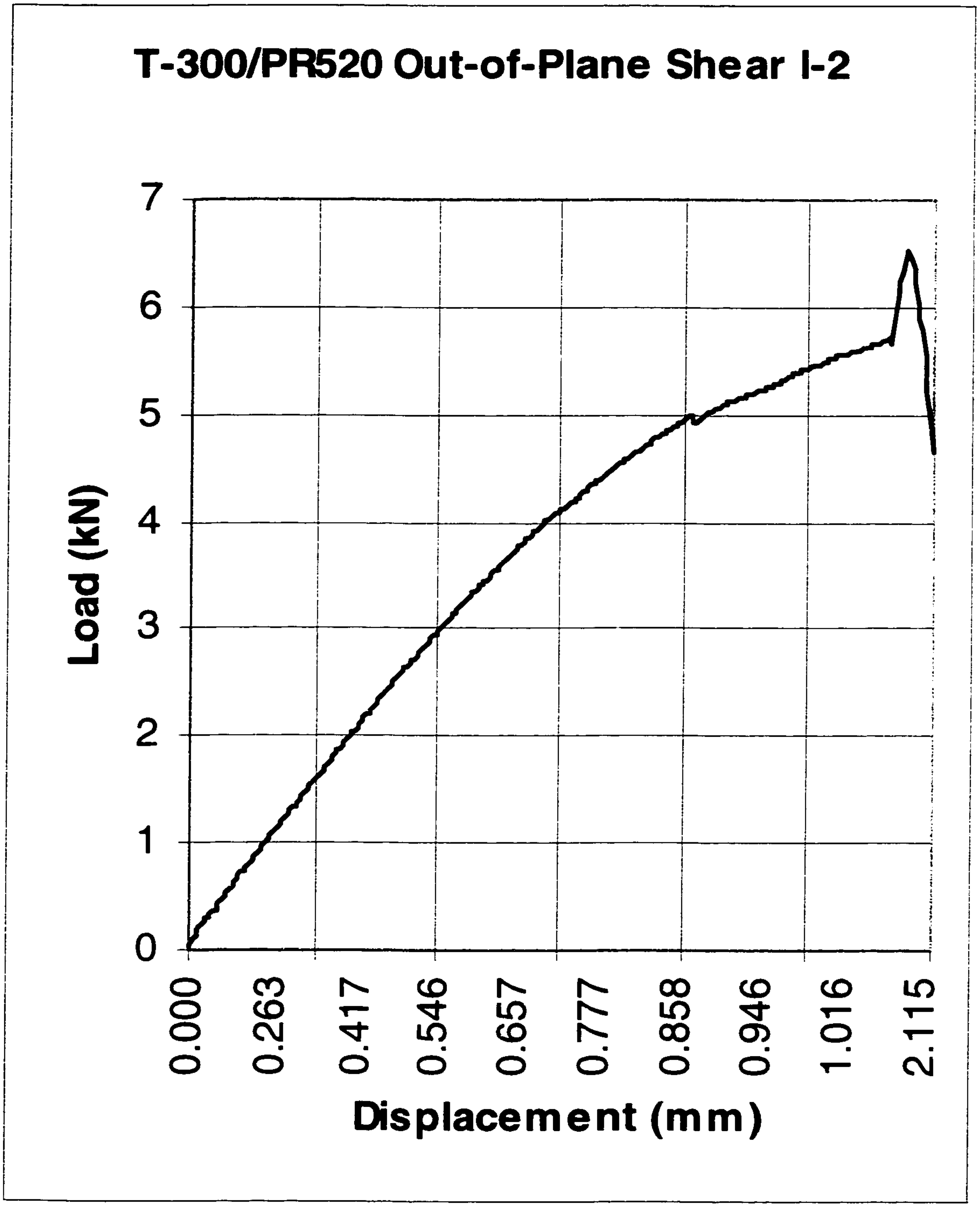

Figure D-26. T-300/PR520 Out-of-Plane Shear Load-Displacement Plot: Specimen I-2

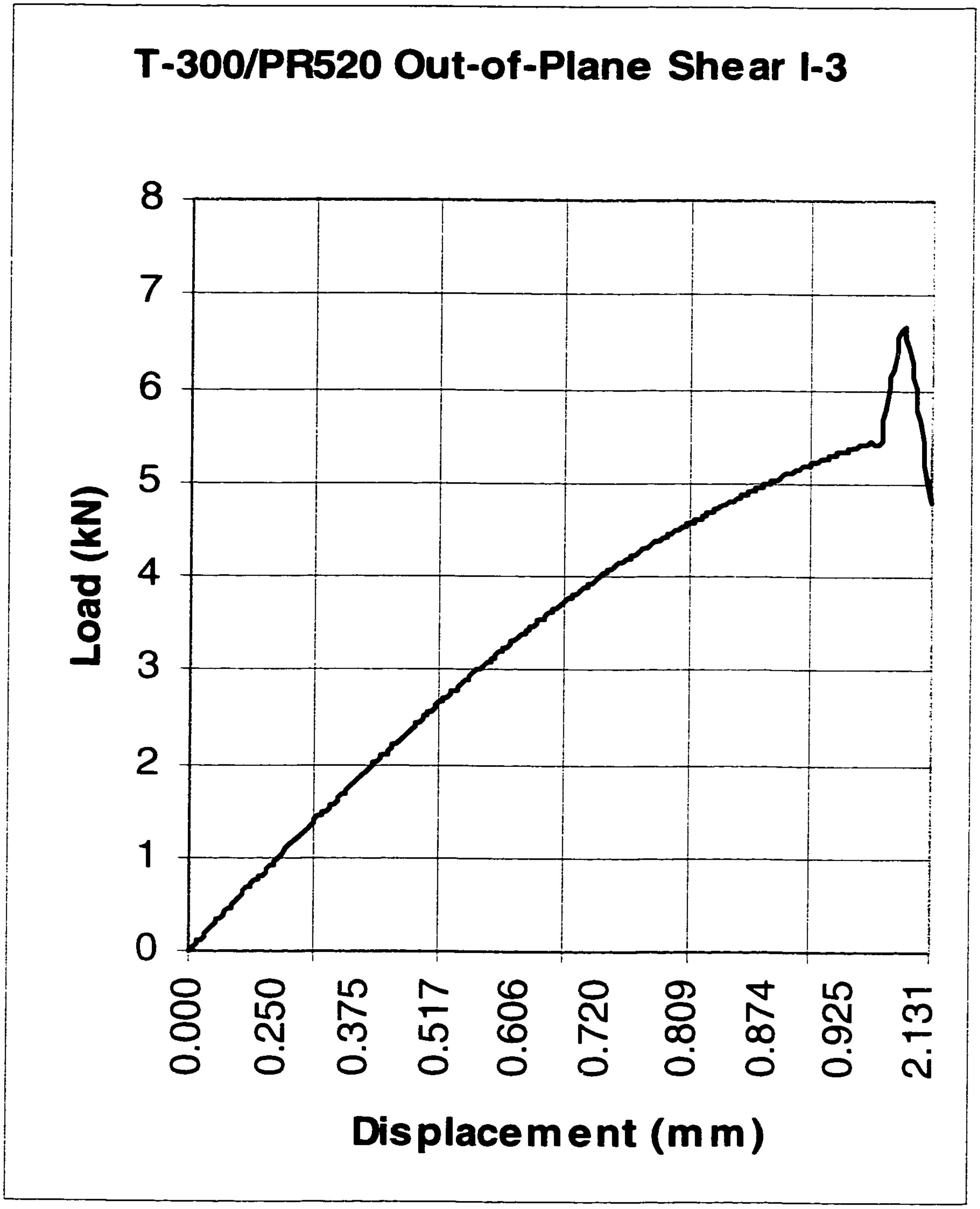

Figure D-27. T-300/PR520 Out-of-Plane Shear Load-Displacement Plot: Specimen I-3

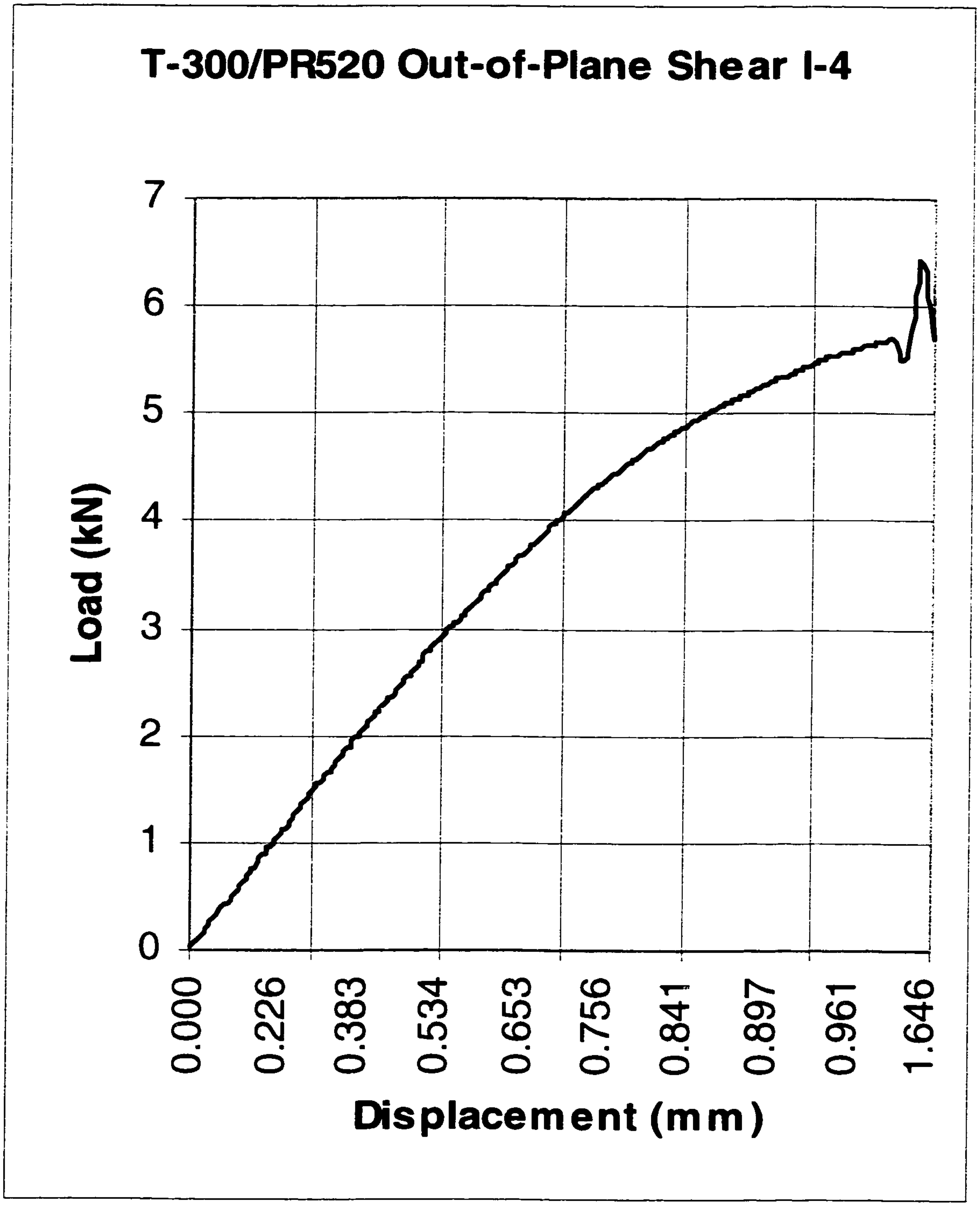

Figure D-28. T-300/PR520 Out-of-Plane Shear Load-Displacement Plot: Specimen I-4

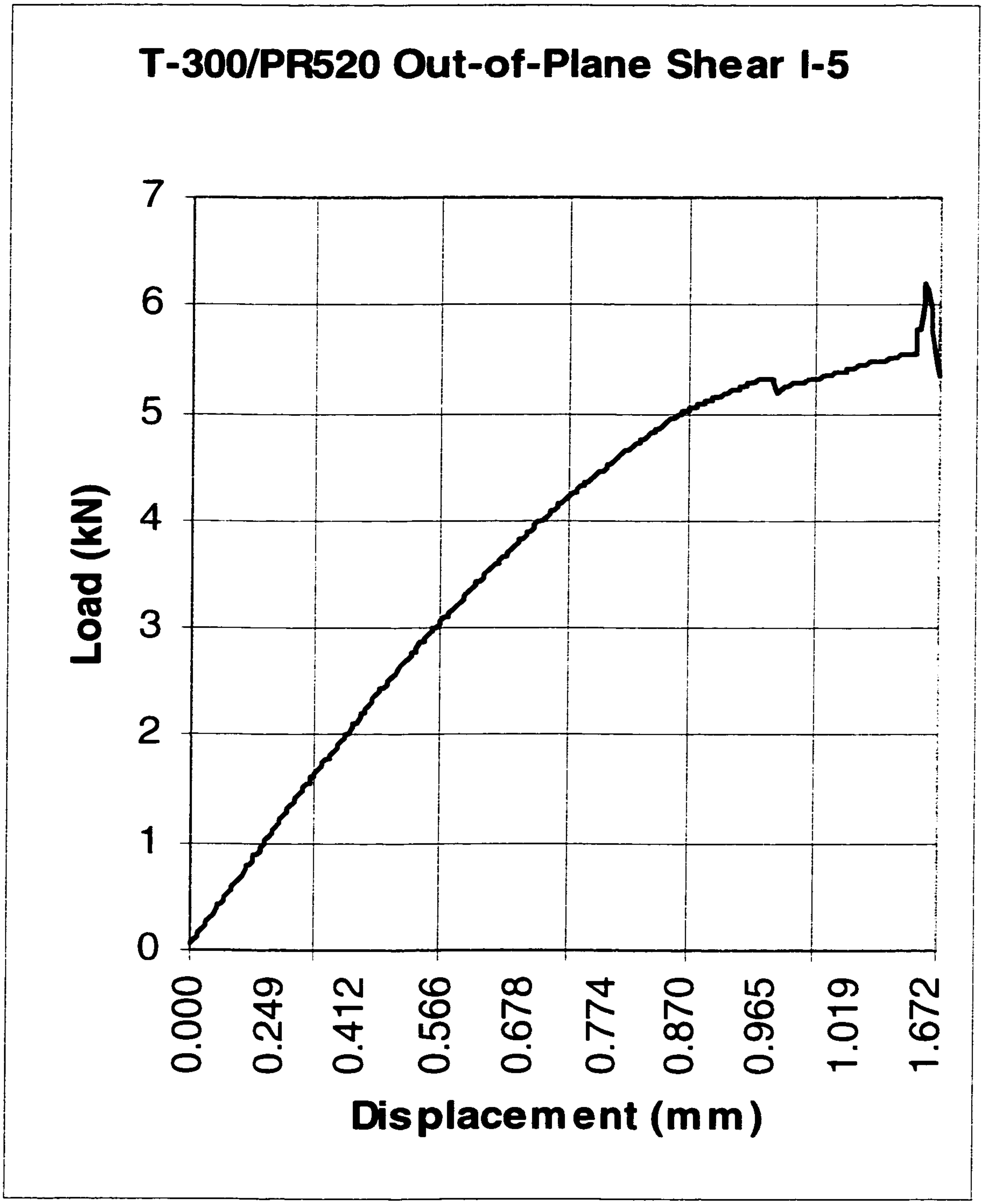

Figure D-29. T-300/PR520 Out-of-Plane Shear Load-Displacement Plot: Specimen I-5

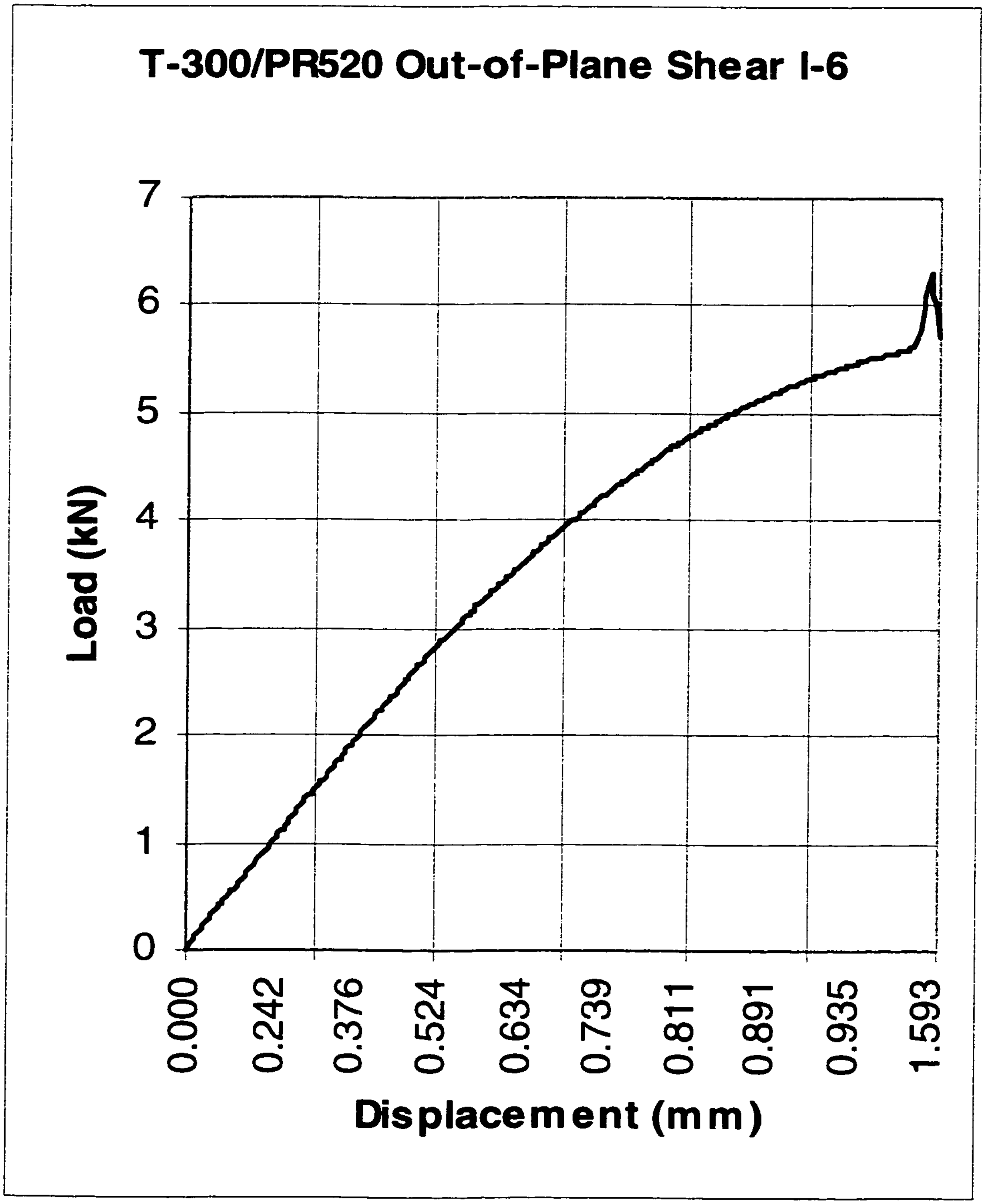

Figure D-30. T-300/PR520 Out-of-Plane Shear Load-Displacement Plot: Specimen I-6

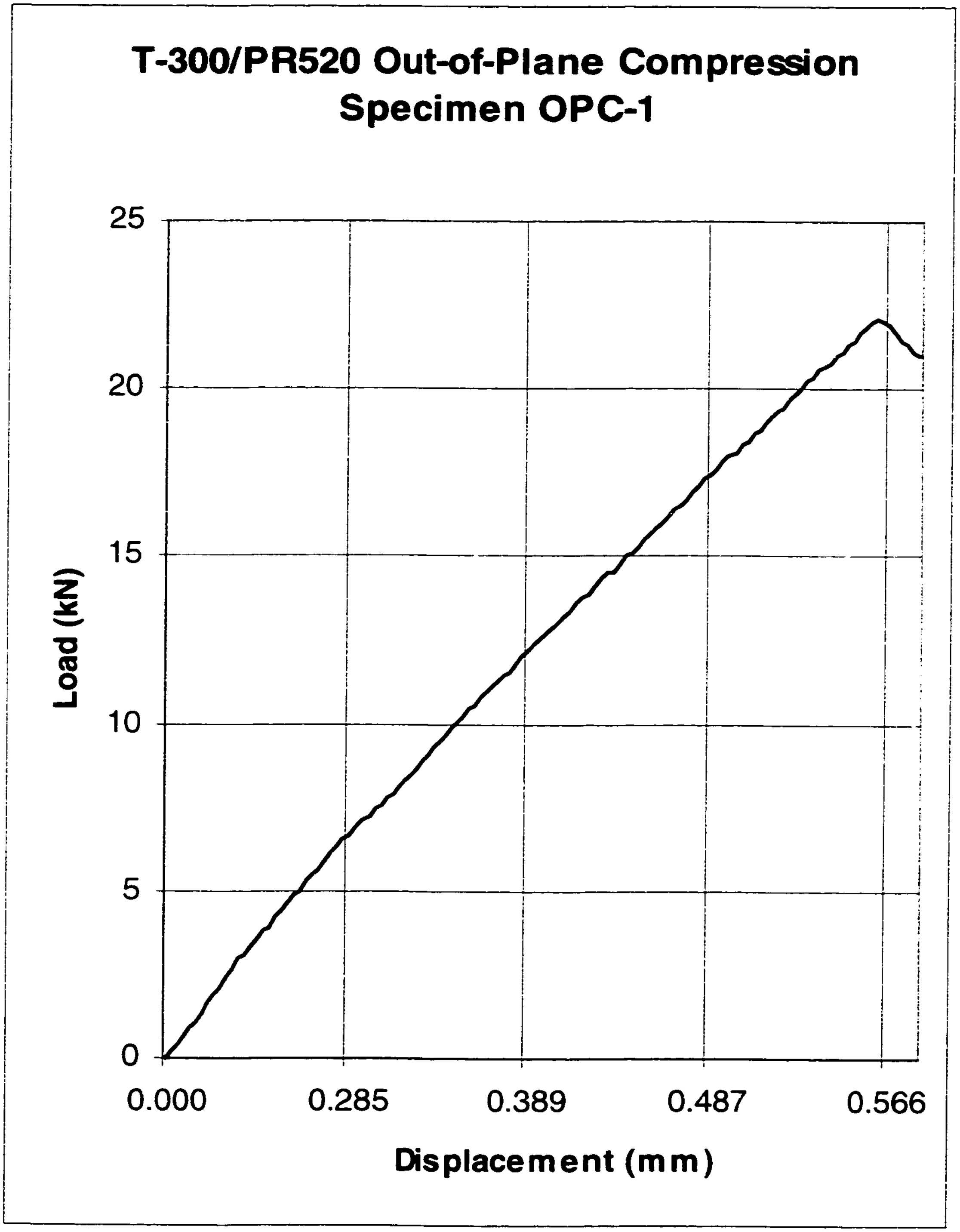

Figure D-31. T-300/PR520 Out-of-Plane Compression Load-Displacement Plot: Specimen OPC-1

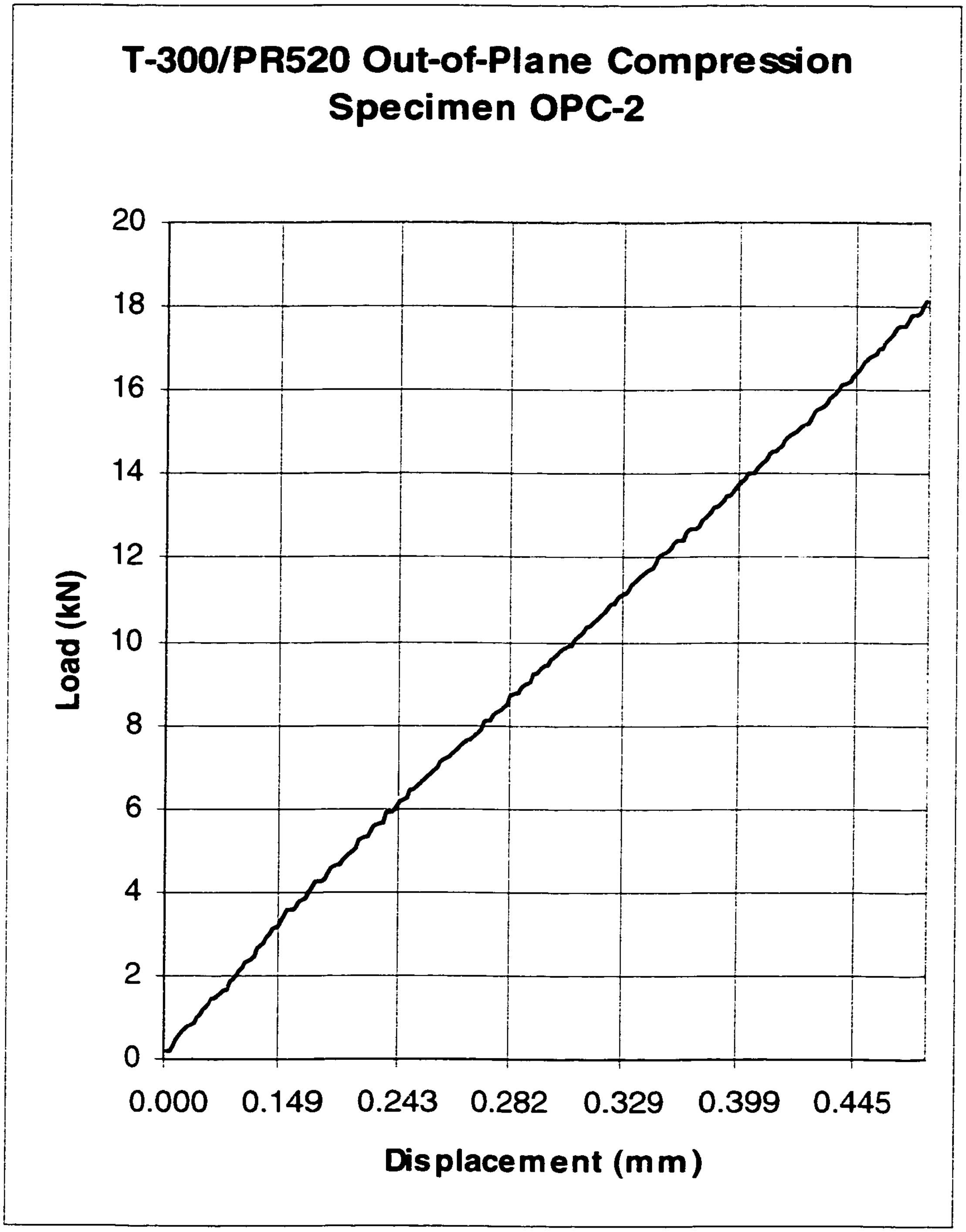

Figure D-32. T-300/PR520 Out-of-Plane Compression Load-Displacement Plot: Specimen OPC-2

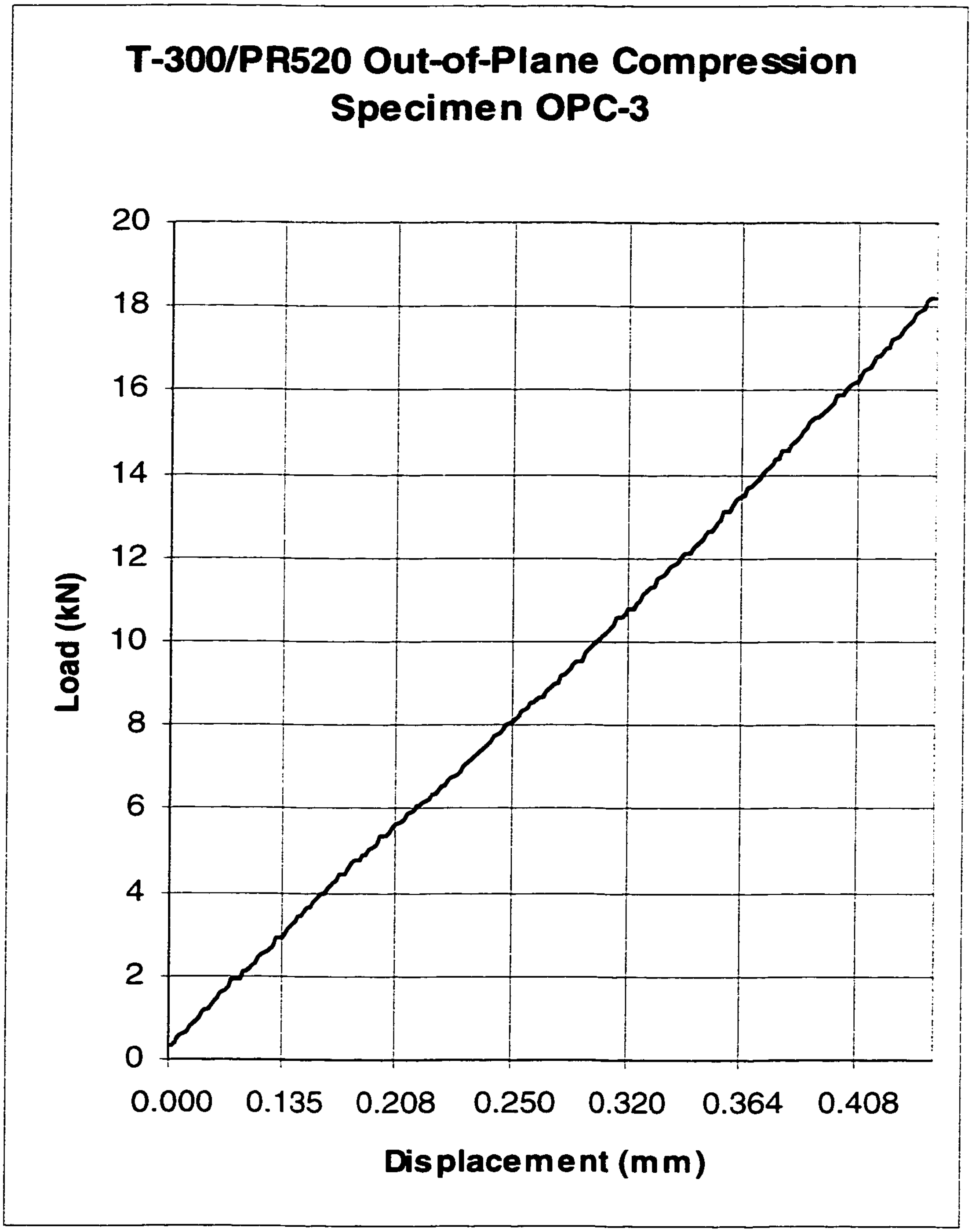

Figure D-33. T-300/PR520 Out-of-Plane Compression Load-Displacement Plot: Specimen OPC-3

APPENDIX E

T-300/PR520 T-JOINT FLEXURE, TENSION, AND RAIL SHEAR DATA

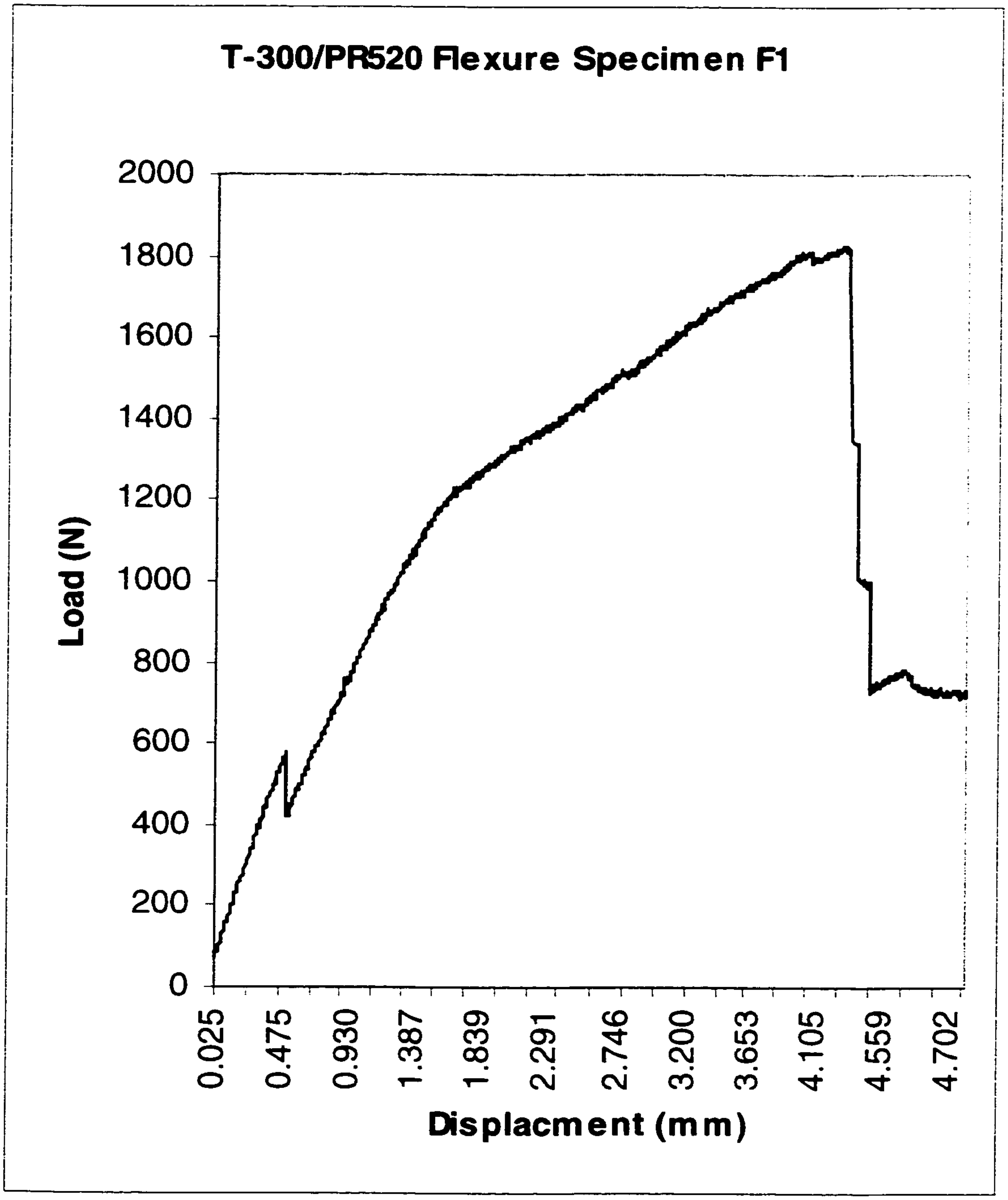

Figure E-1. T-Joint Flexure Load-Displacement Plot Specimen F1.

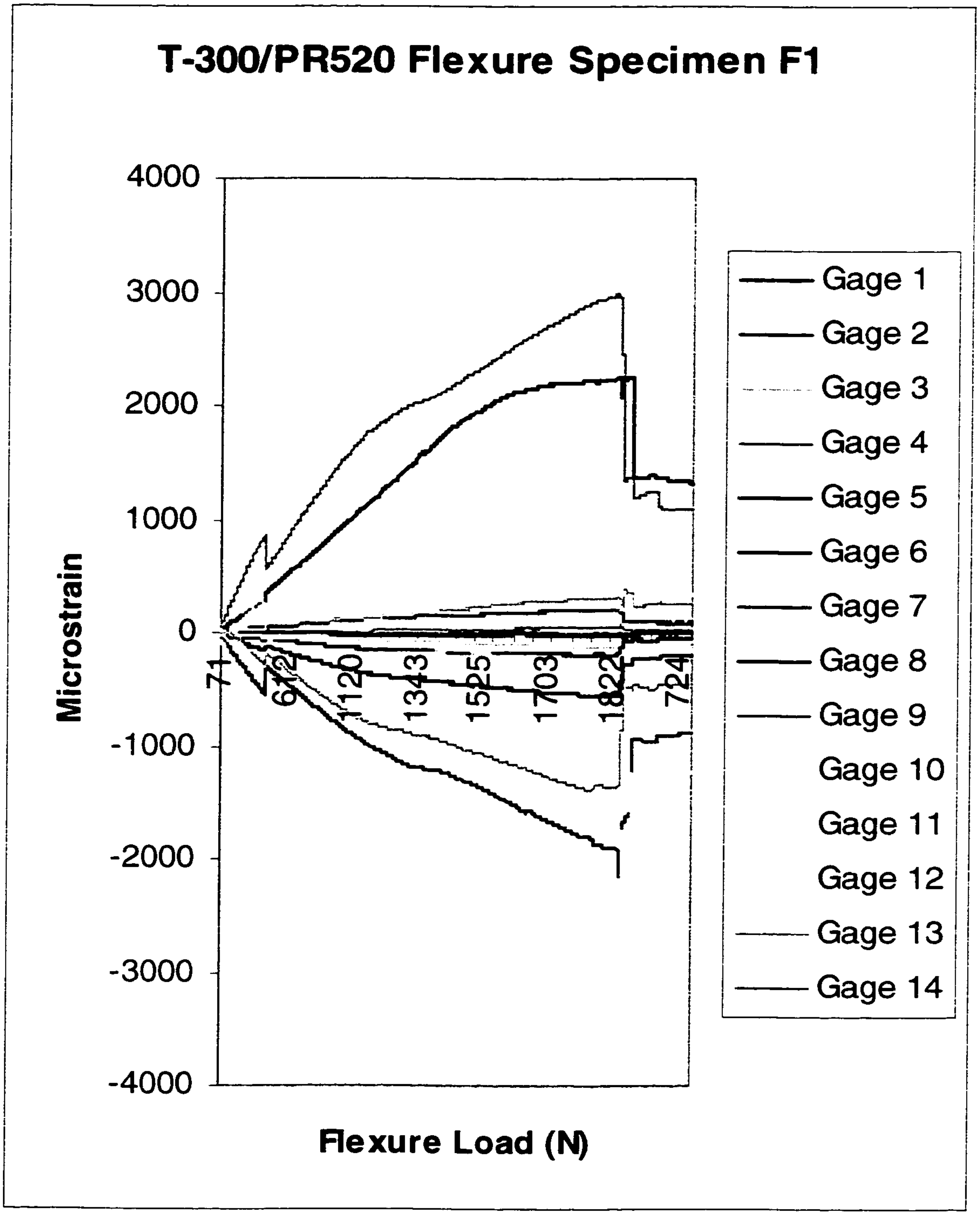

Figure E-2. T-Joint Flexure Strain-Load Plot Specimen F1.

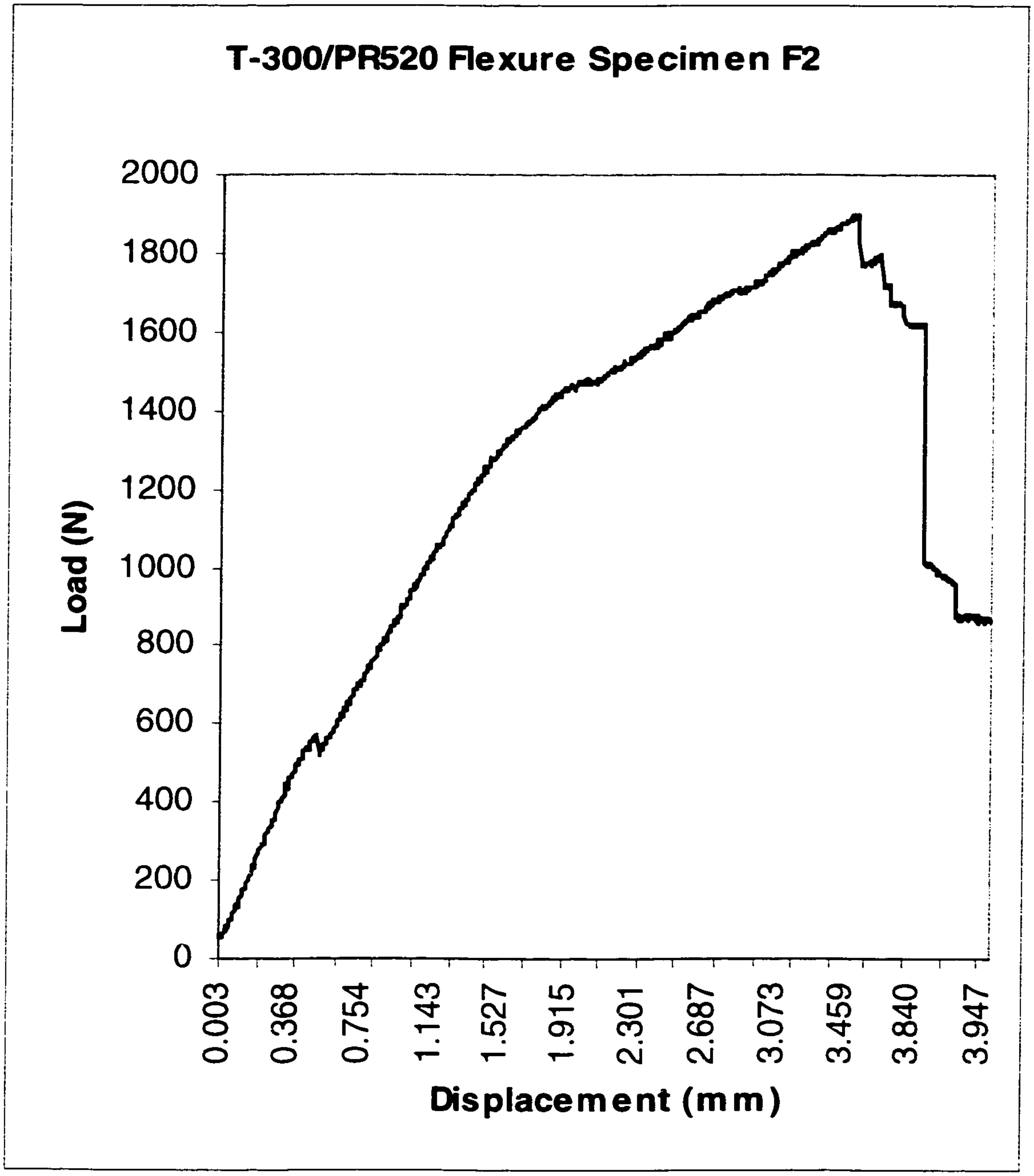

Figure E-3. T-Joint Flexure Load-Displacement Plot Specimen F2.

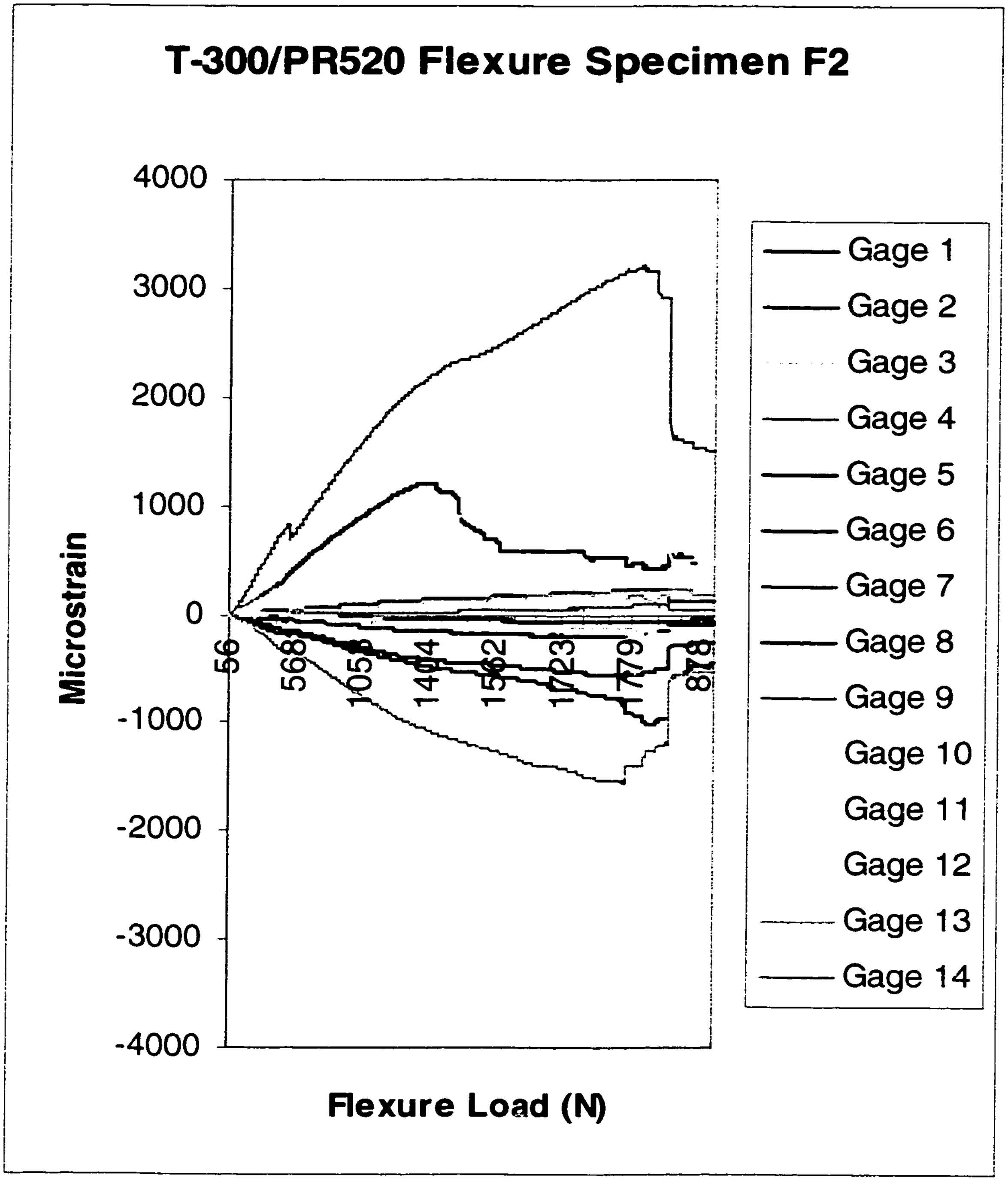

Figure E-4. T-Joint Flexure Strain-Load Plot Specimen F2.

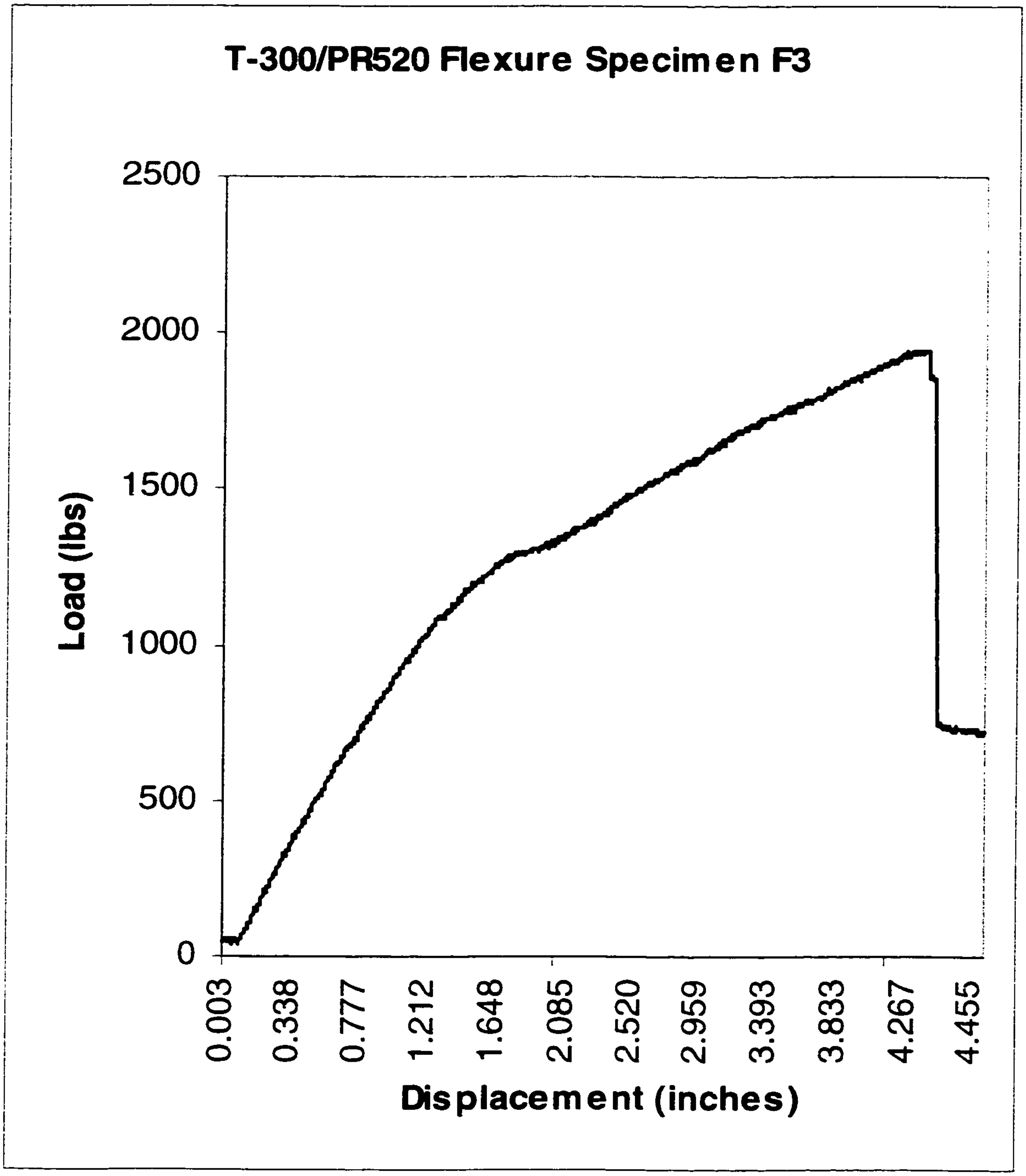

Figure E-5. T-Joint Flexure Load-Displacement Plot Specimen F3.

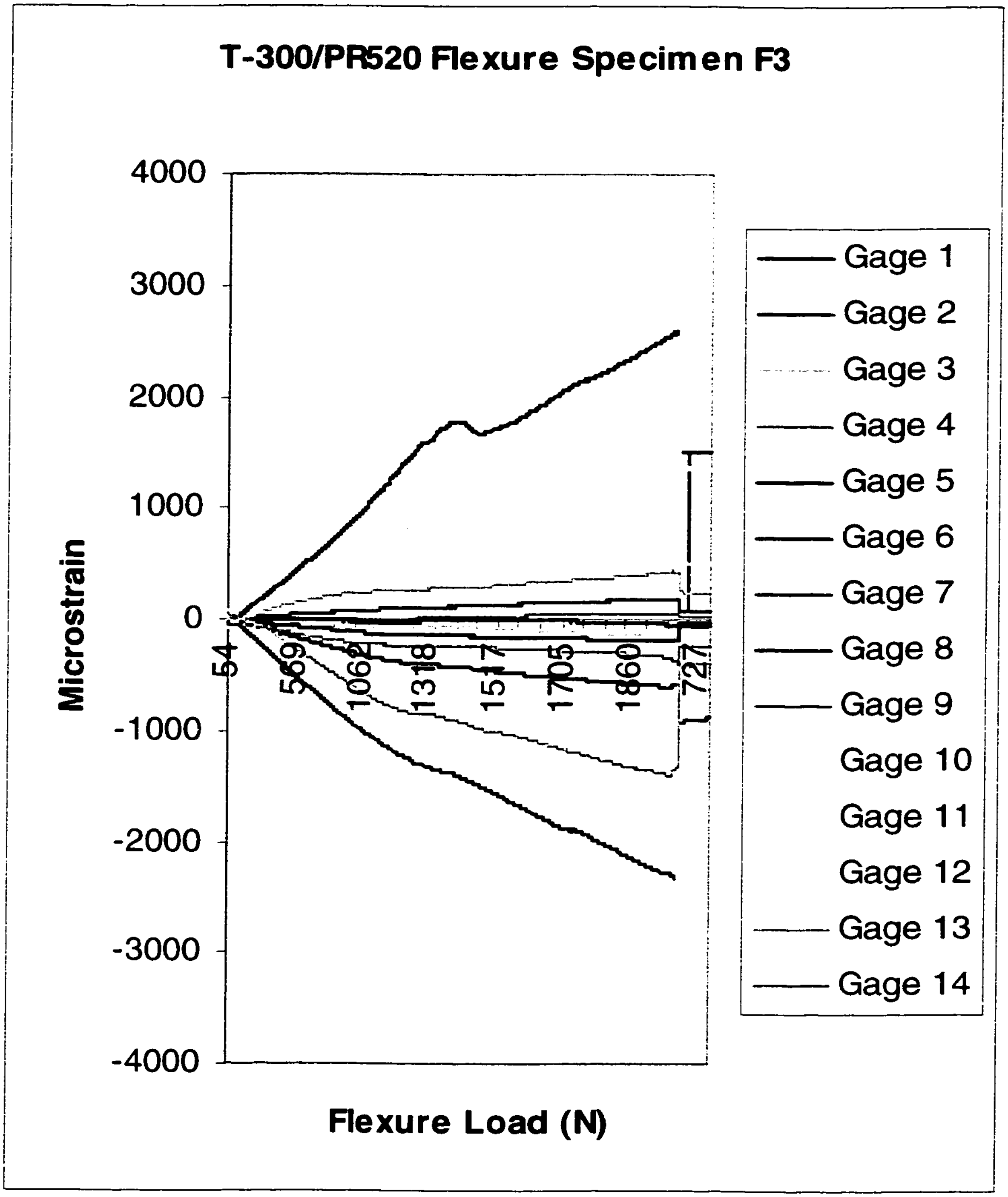

Figure E-6. T-Joint Flexure Strain-Load Plot Specimen F3.

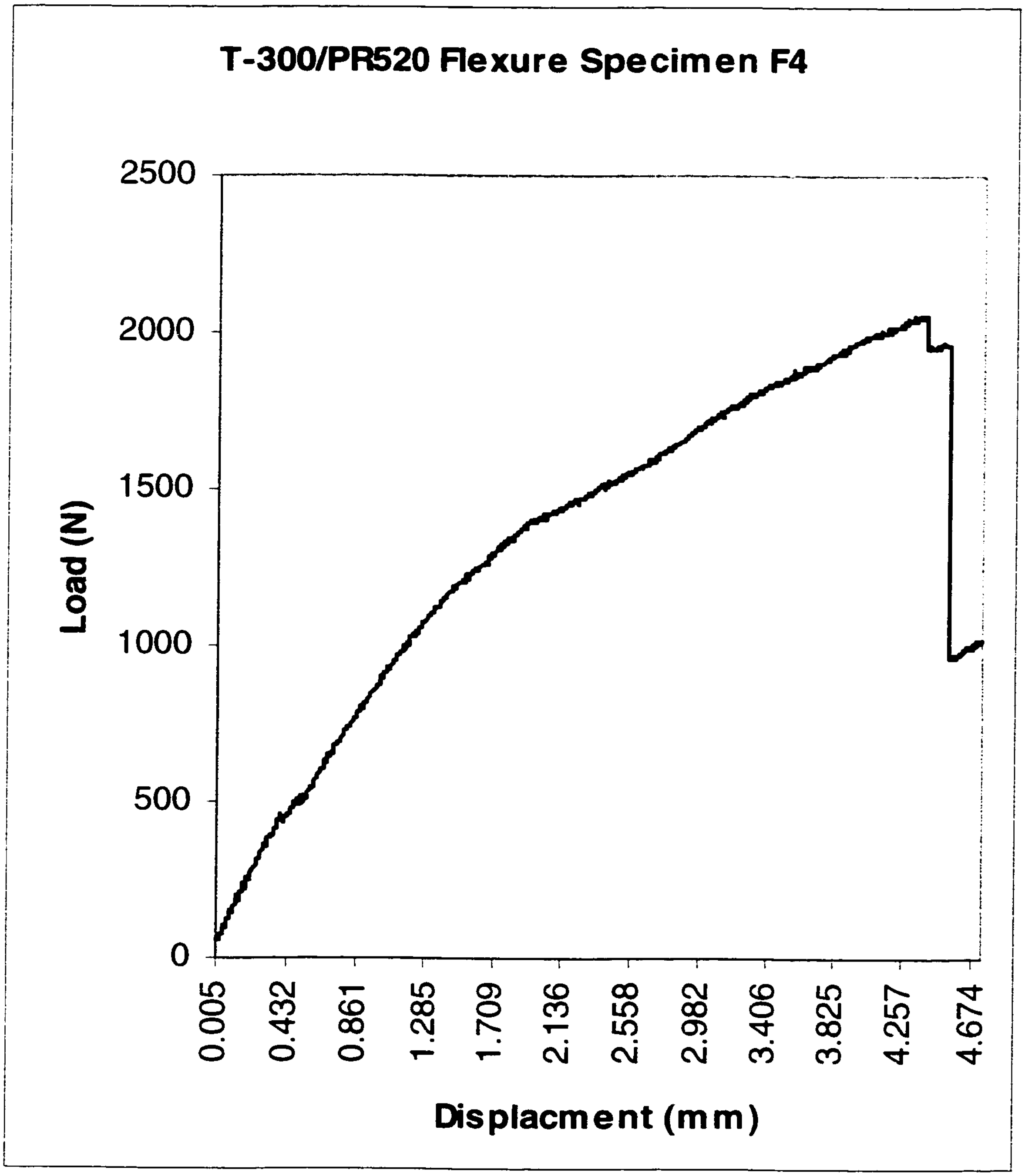

Figure E-7. T-Joint Flexure Load-Displacement Plot Specimen F4.

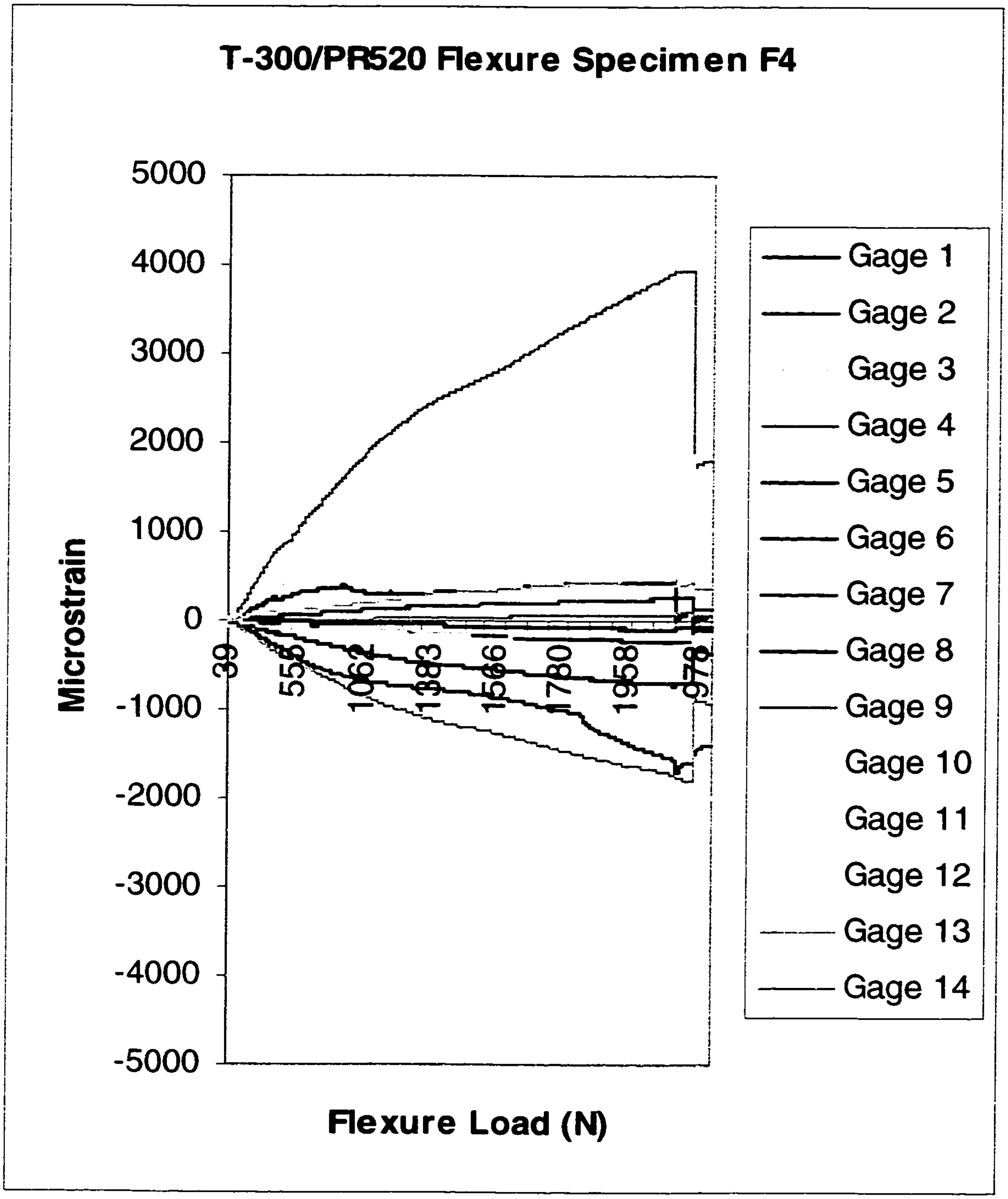

Figure E-8. T-Joint Flexure Strain-Load Plot Specimen F4.

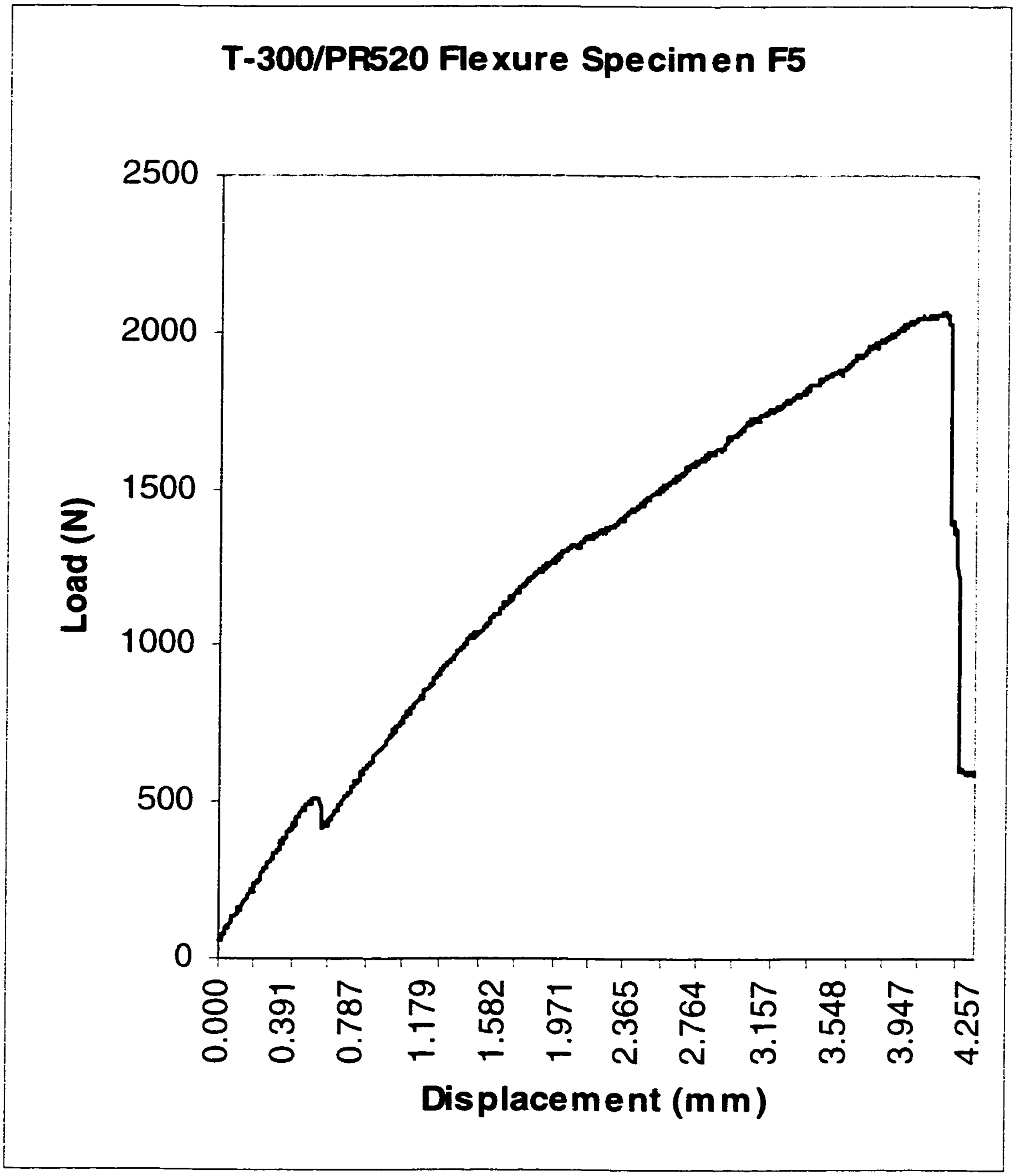

Figure E-9. T-Joint Flexure Load-Displacement Plot Specimen F5.

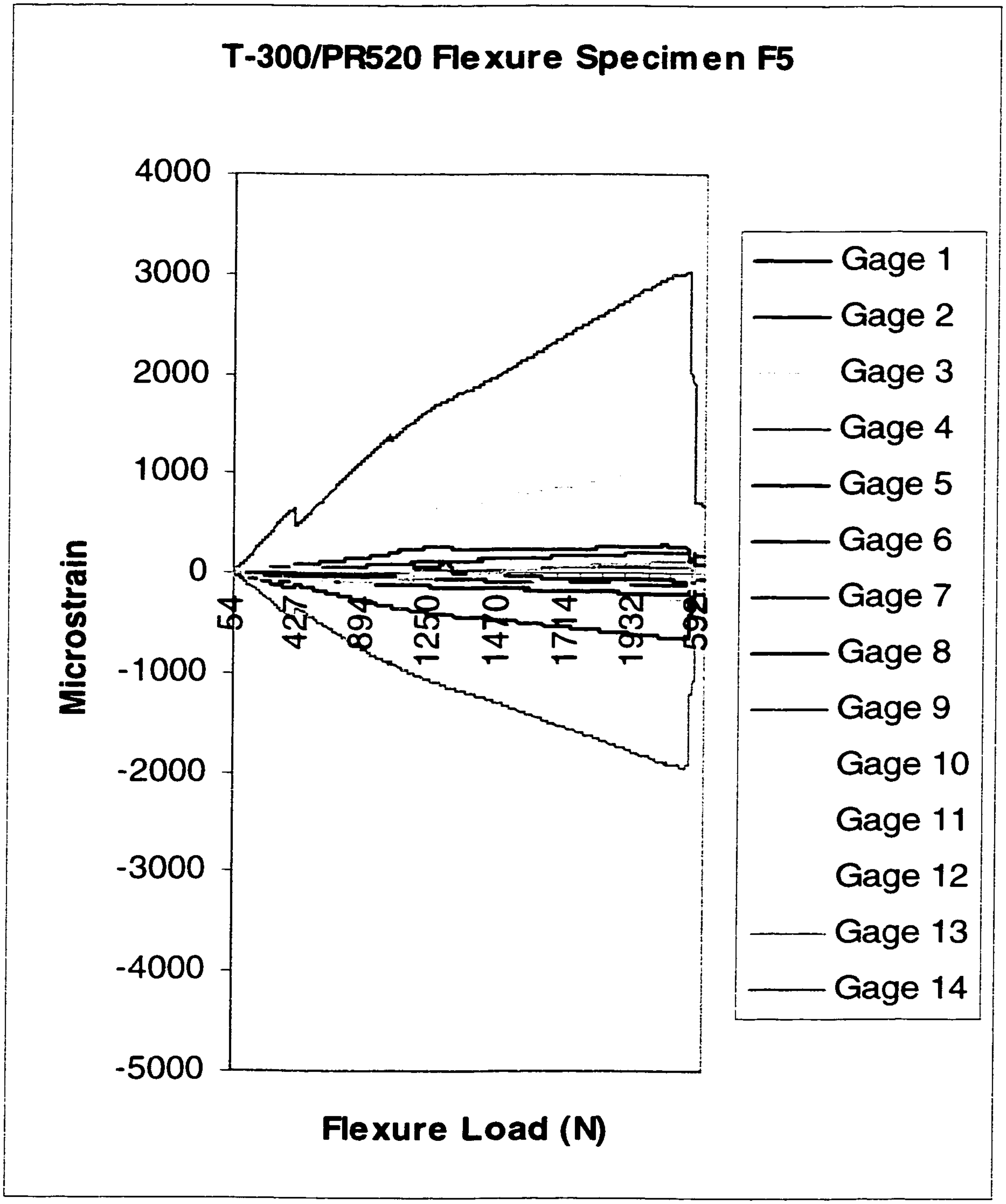

Figure E-10. T-Joint Flexure Strain-Load Plot Specimen F5.

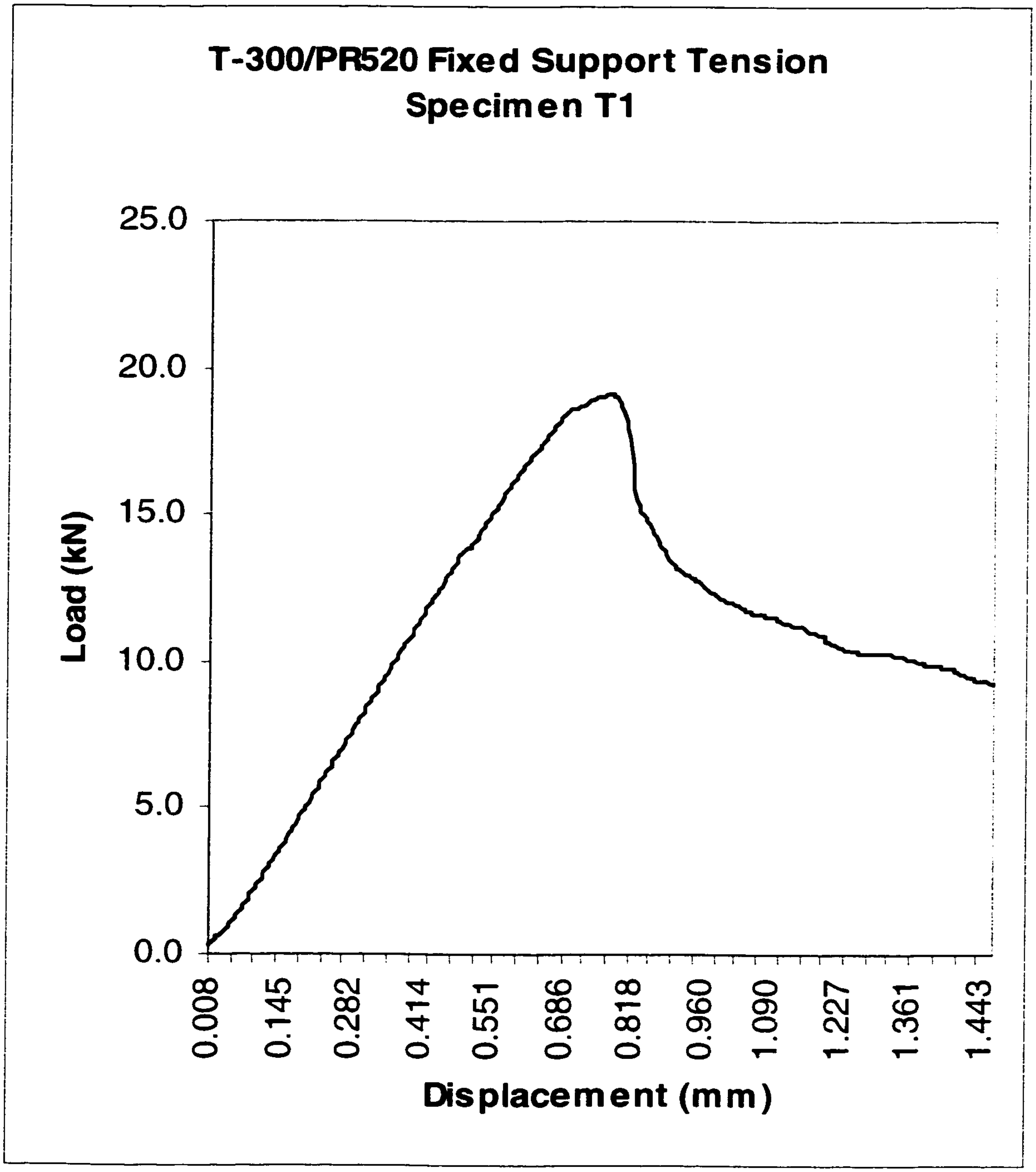

Figure E-11. T-Joint Fixed Support Tension Load-Displacement Plot Specimen T1.

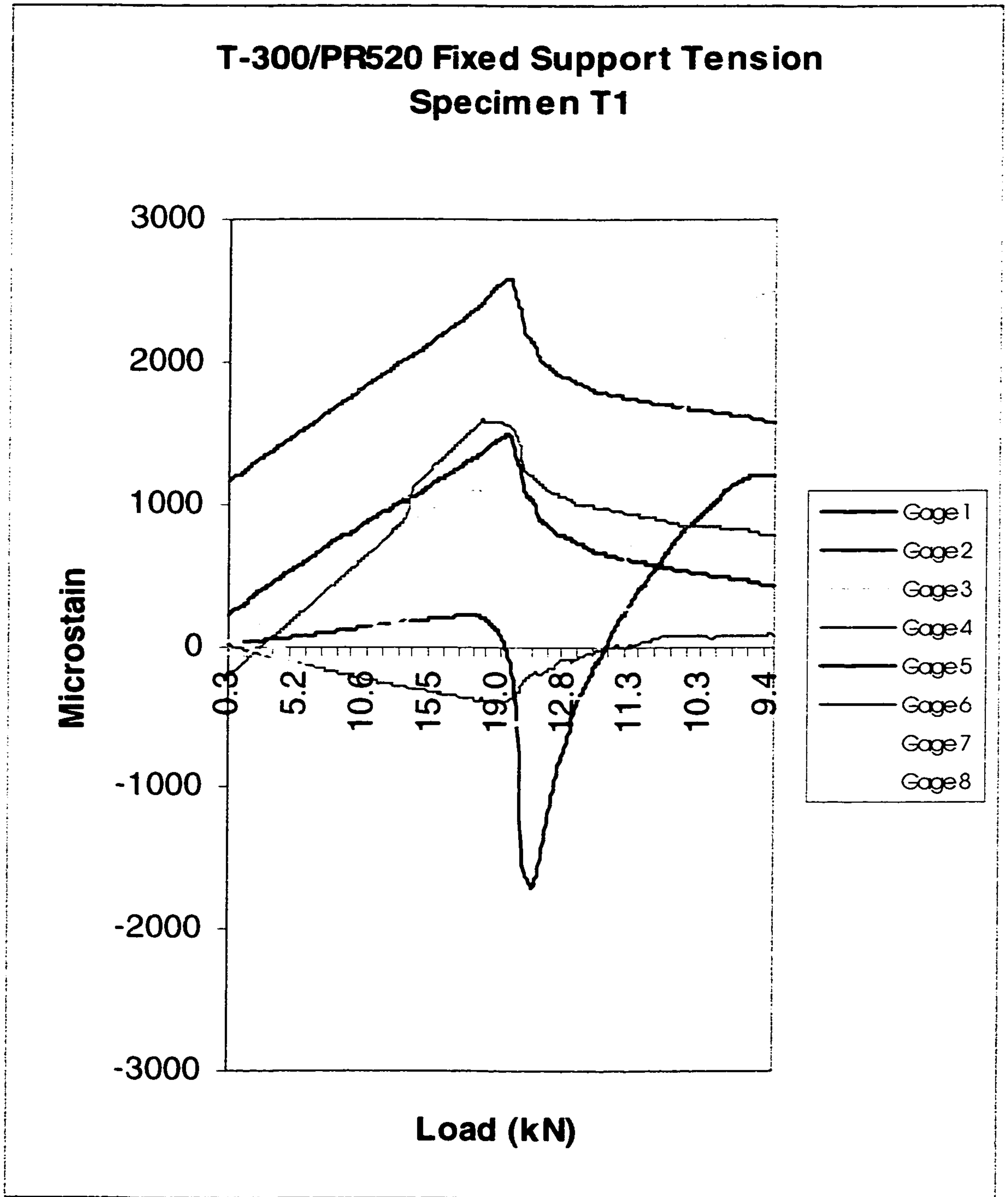

Figure E-12. T-Joint Fixed Support Tension Strain-Load Plot Specimen T1.

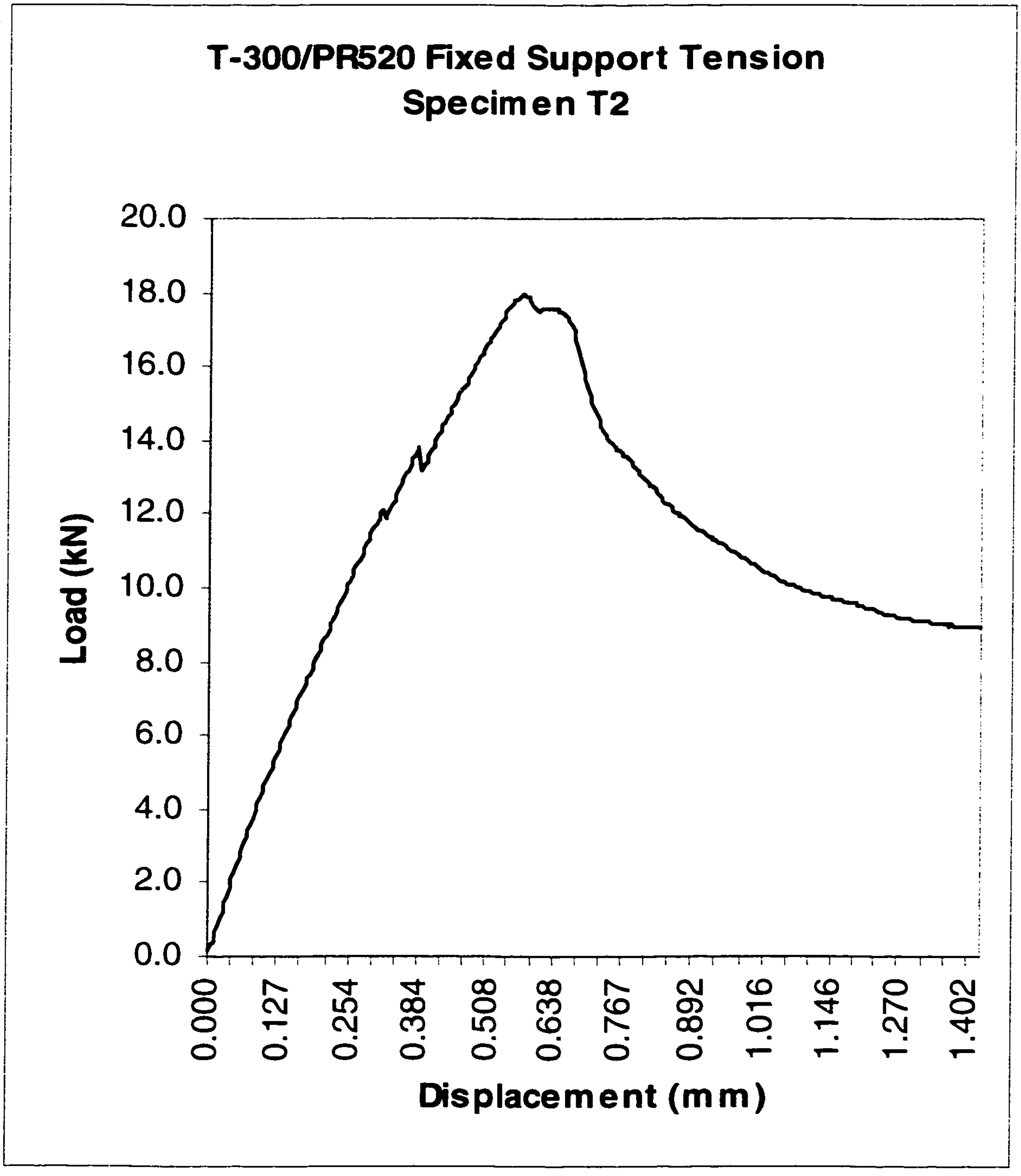

Figure E-13. T-Joint Fixed Support Tension Load-Displacement Plot Specimen T2.

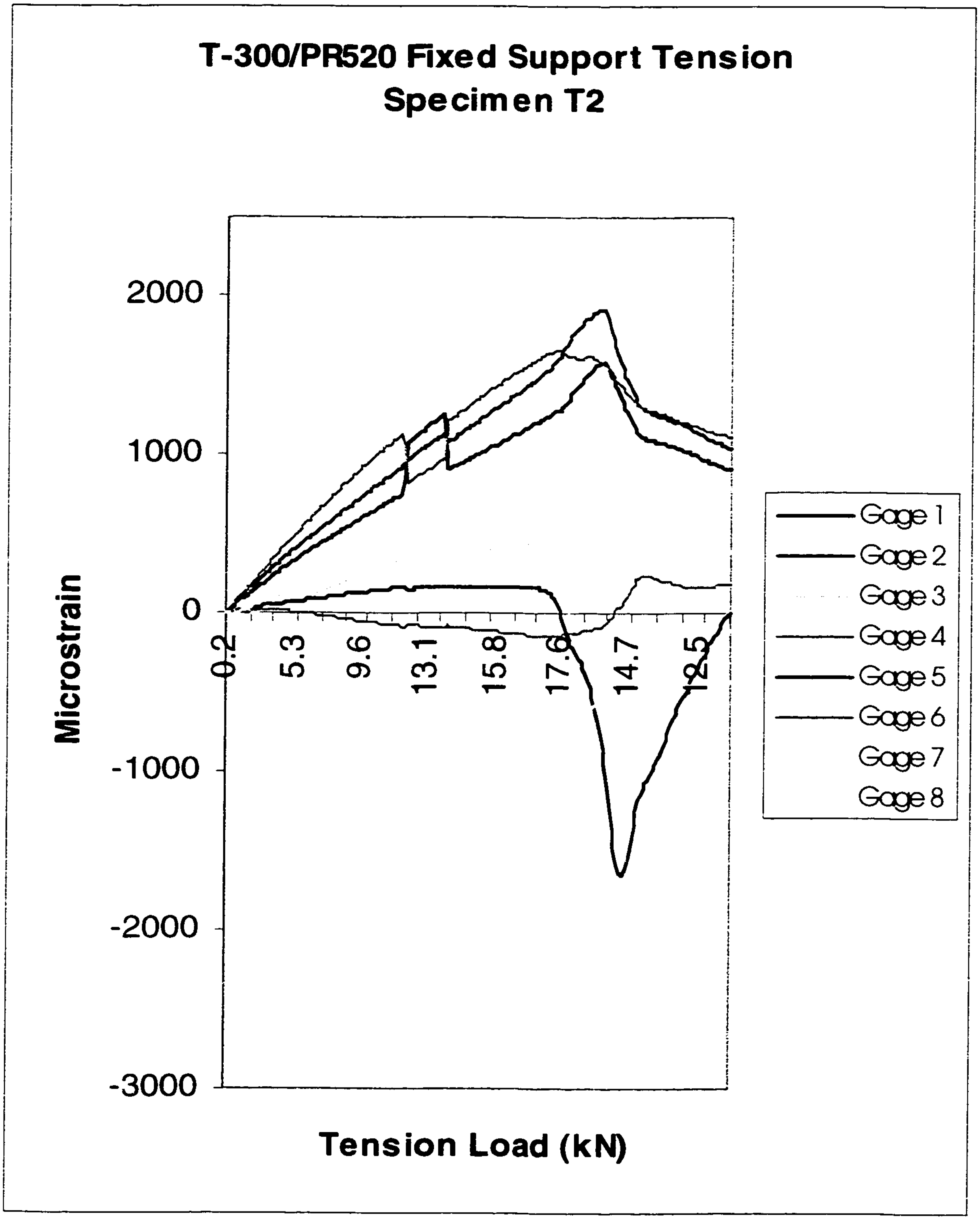

Figure E-14. T-Joint Fixed Support Tension Strain-Load Plot Specimen T2.

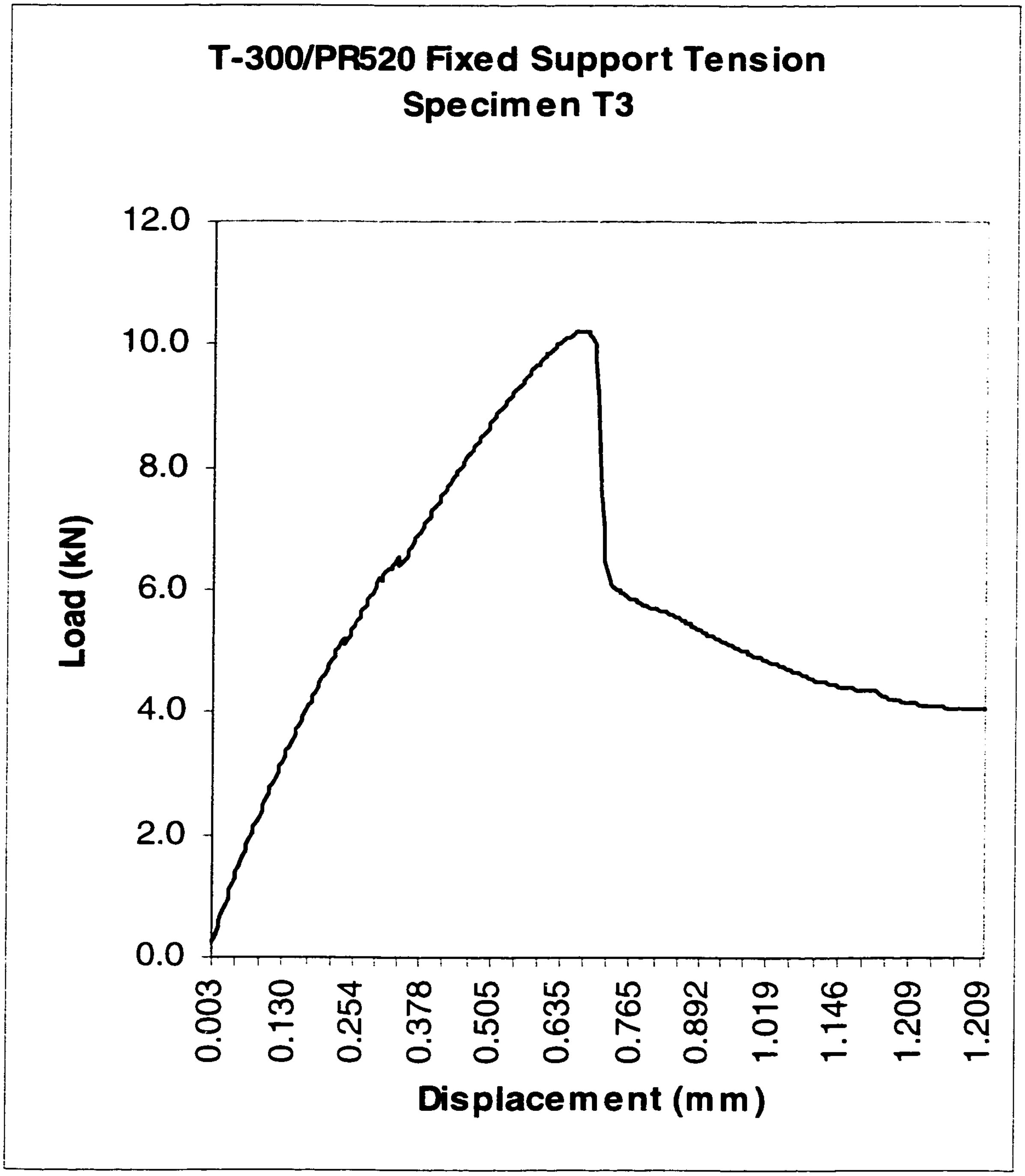

Figure E-15. T-Joint Fixed Support Tension Load-Displacement Plot Specimen T3.

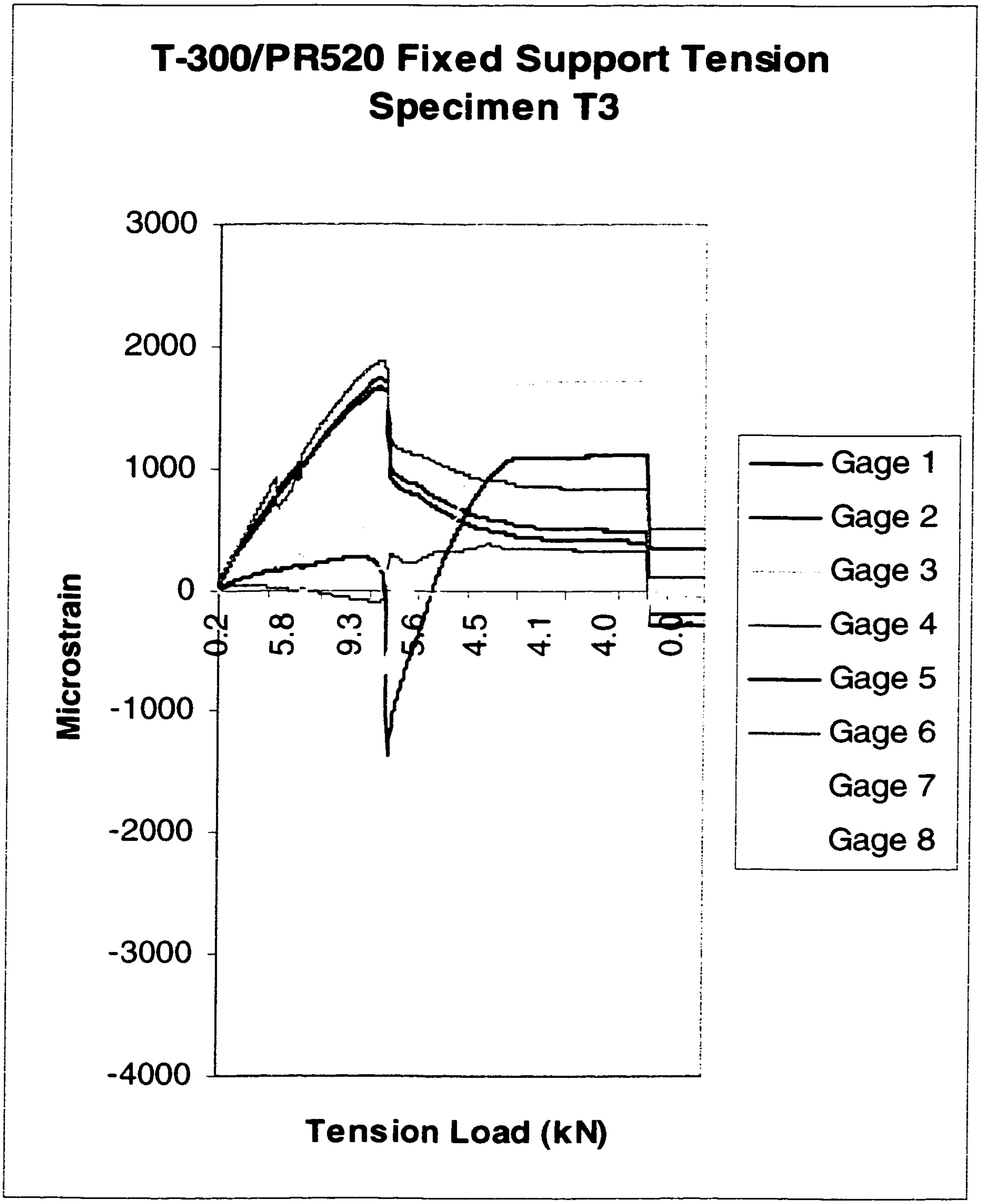

Figure E-16. T-Joint Fixed Support Tension Strain-Load Plot Specimen T3.

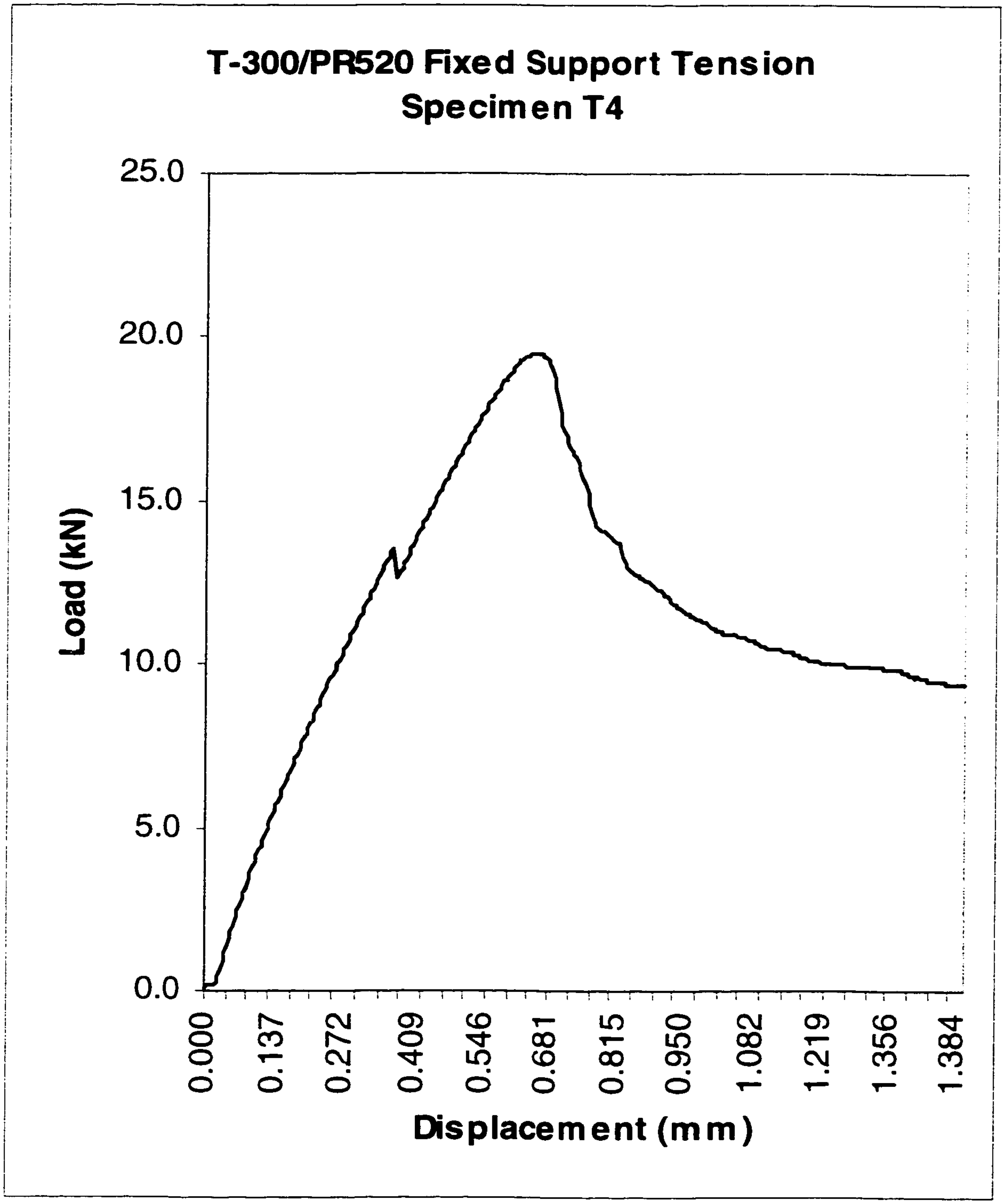

Figure E-17. T-Joint Fixed Support Tension Load-Displacement Plot Specimen T4.

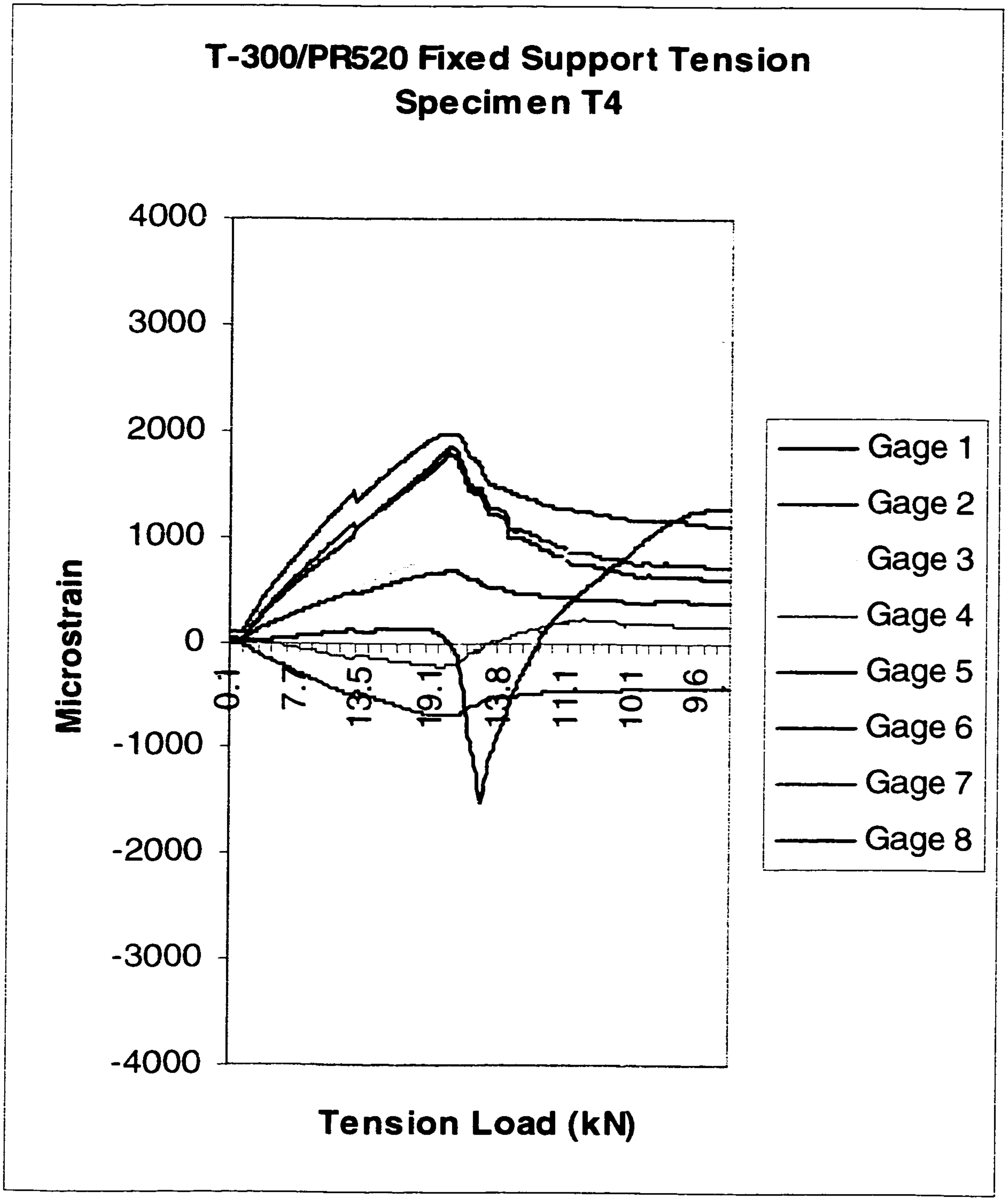

Figure E-18. T-Joint Fixed Support Tension Strain-Load Plot Specimen T4.

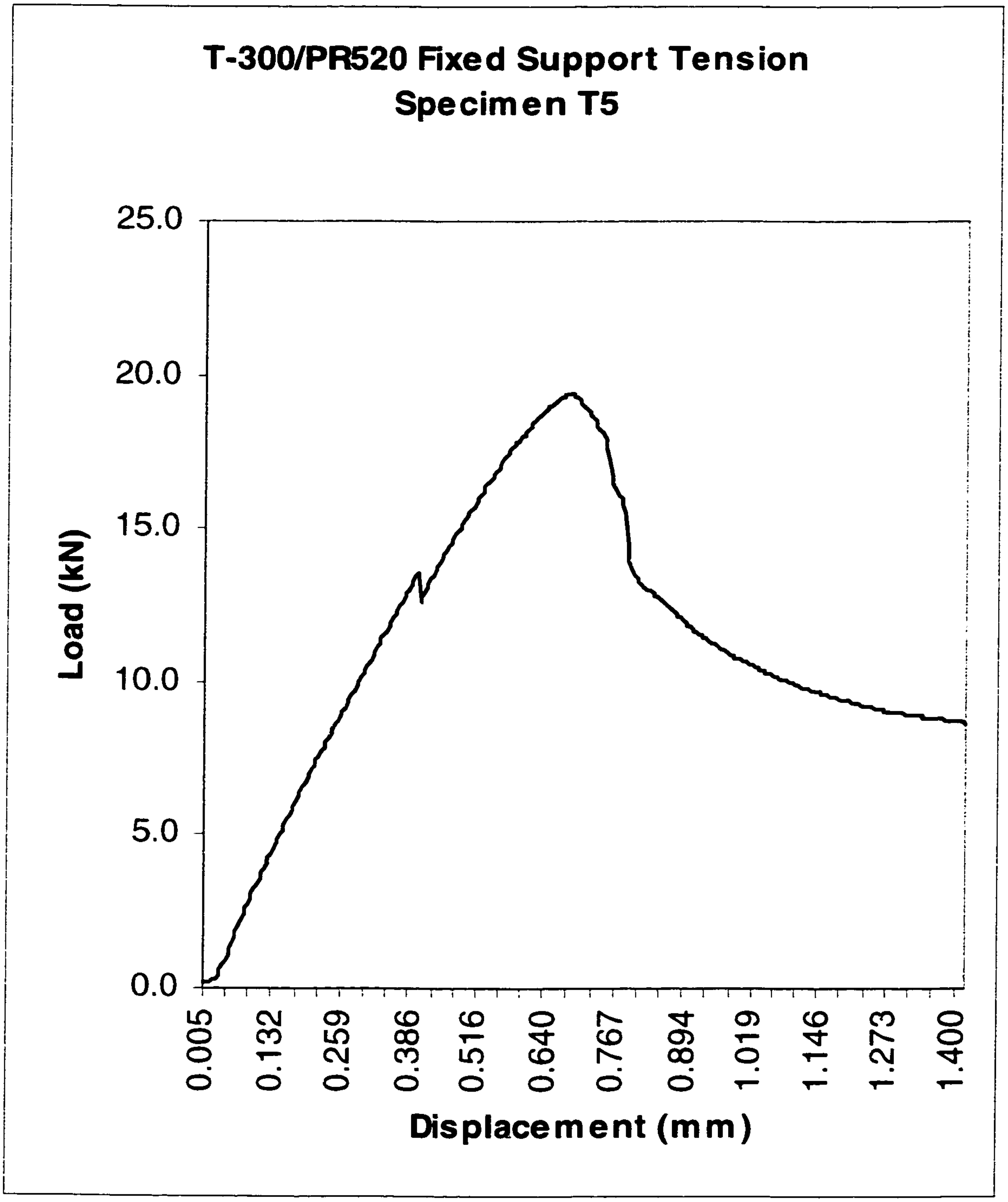

Figure E-19. T-Joint Fixed Support Tension Load-Displacement Plot Specimen T5.

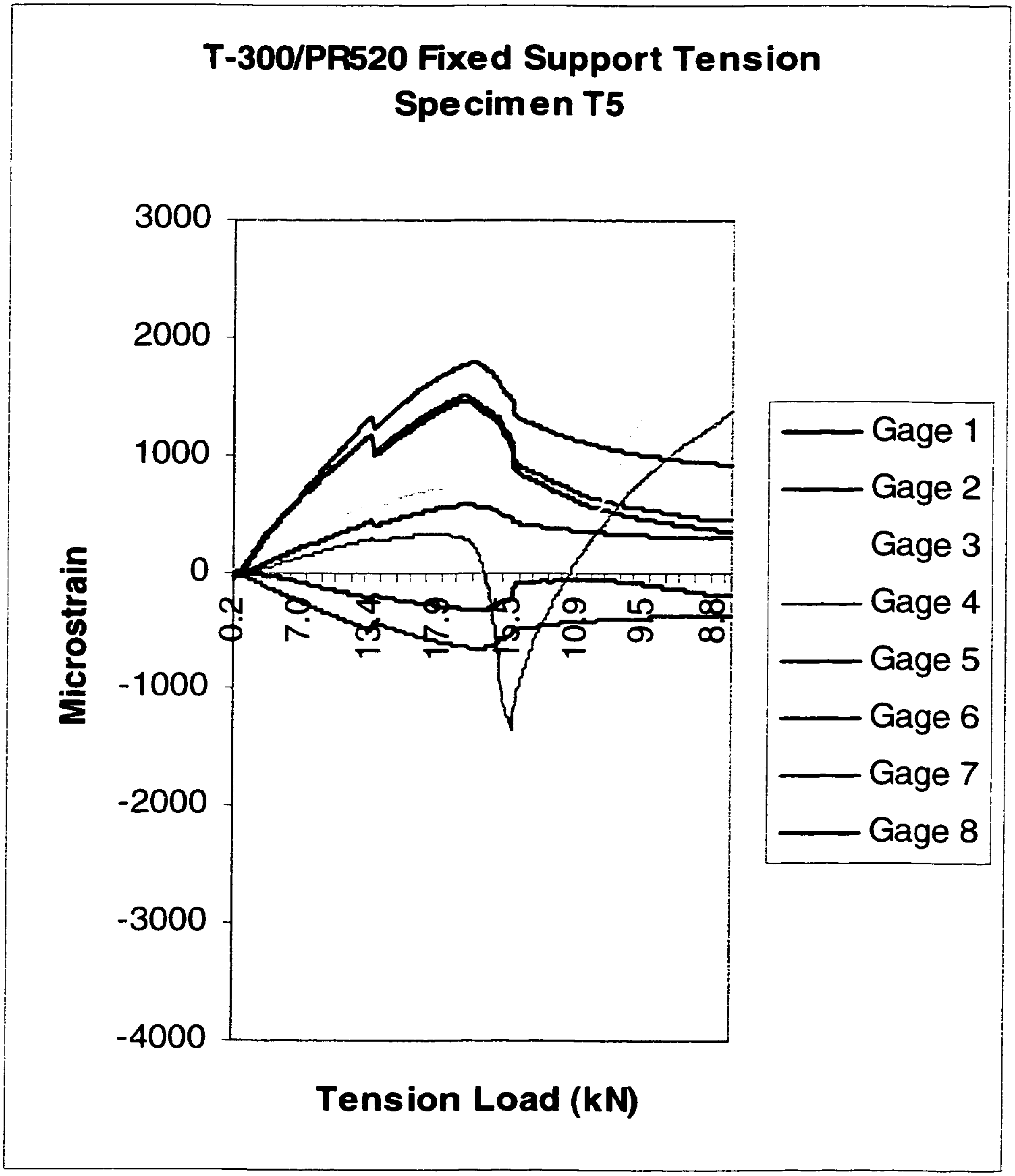

Figure E-20. T-Joint Fixed Support Tension Strain-Load Plot Specimen T5.

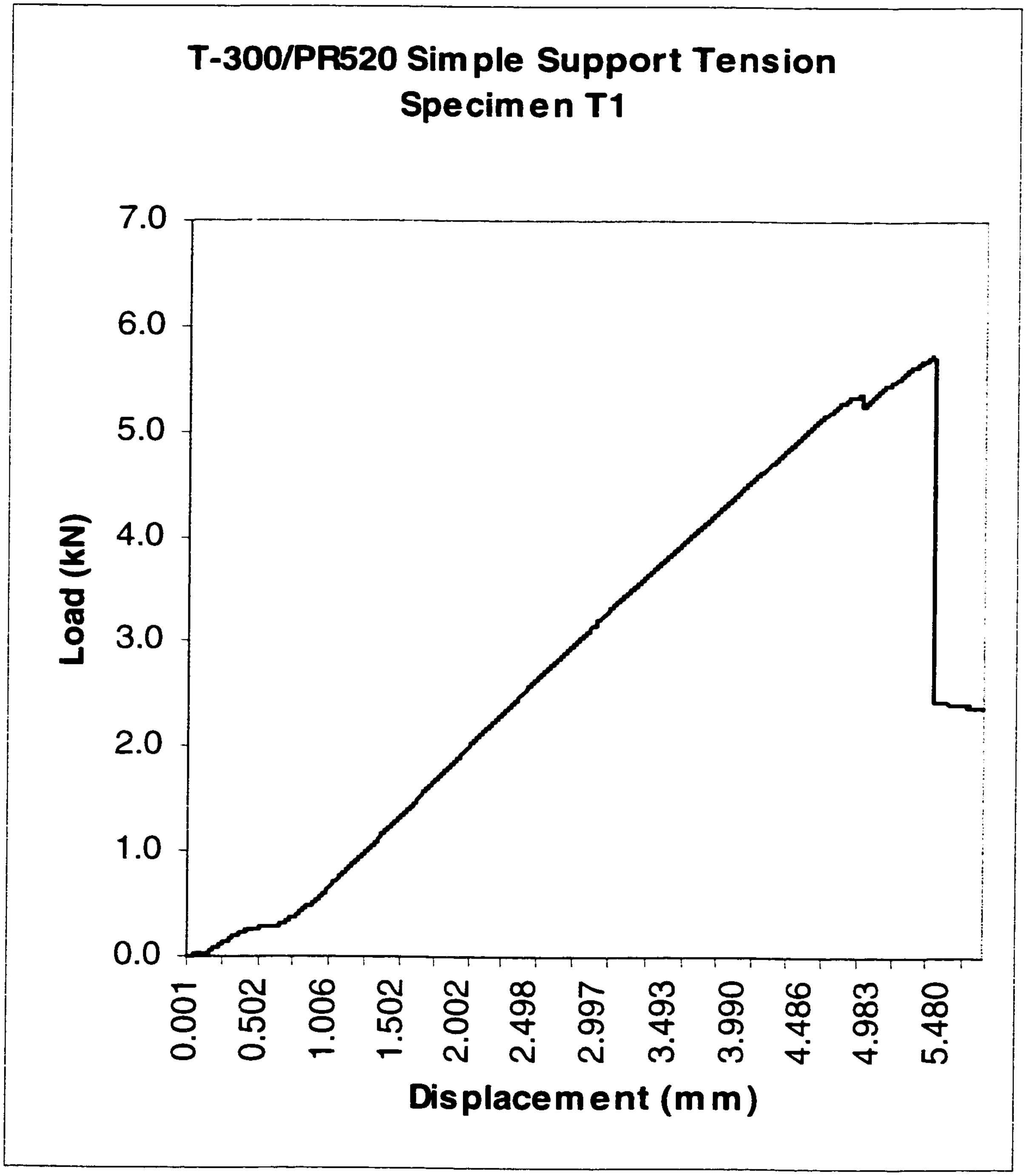

Figure E-21. T-Joint Simple Support Tension Load-Displacement Plot Specimen T1.

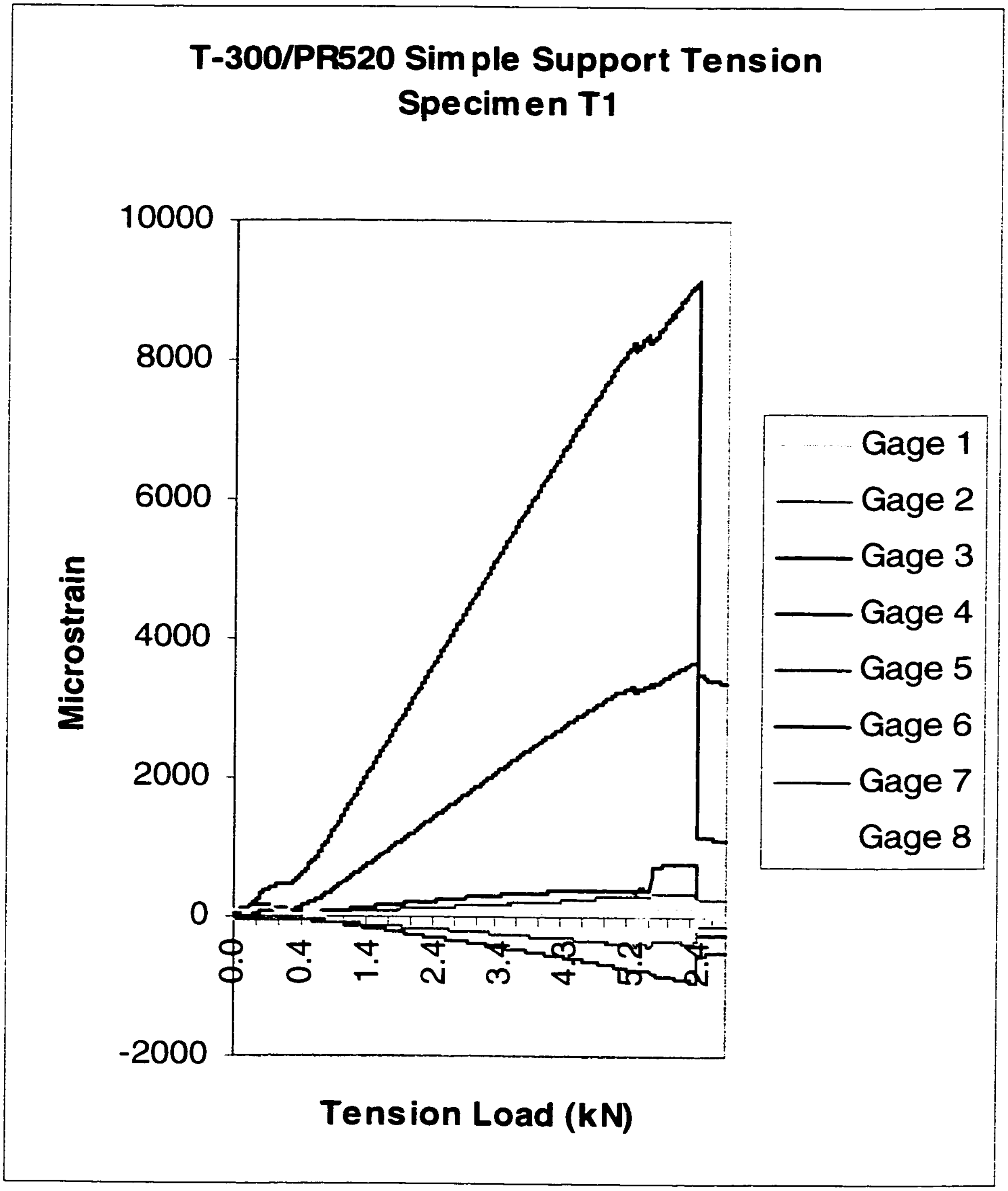

Figure E-22. T-Joint Simple Support Tension Strain-Load Plot Specimen T1.

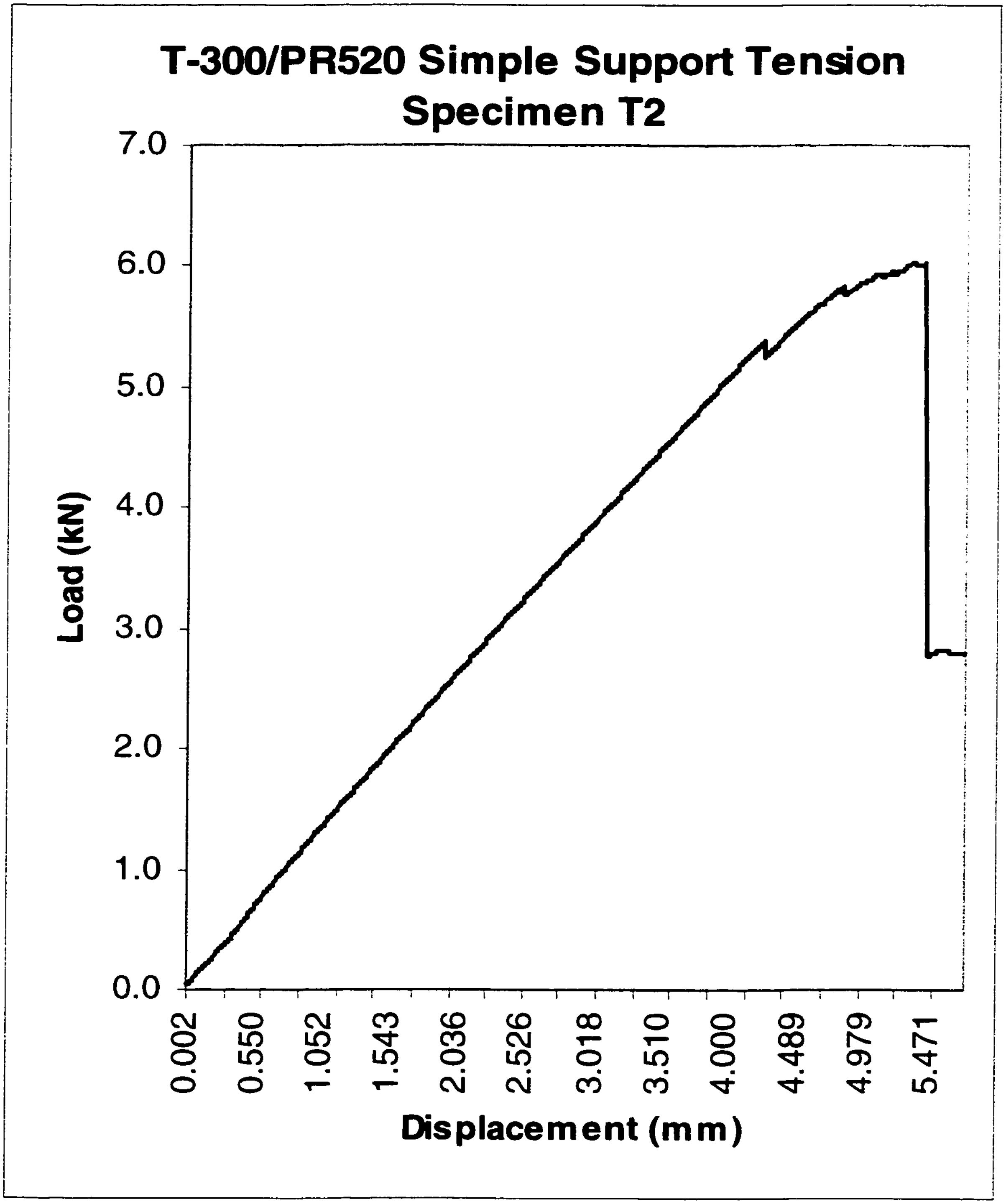

Figure E-23. T-Joint Simple Support Tension Load-Displacement Plot Specimen T2.

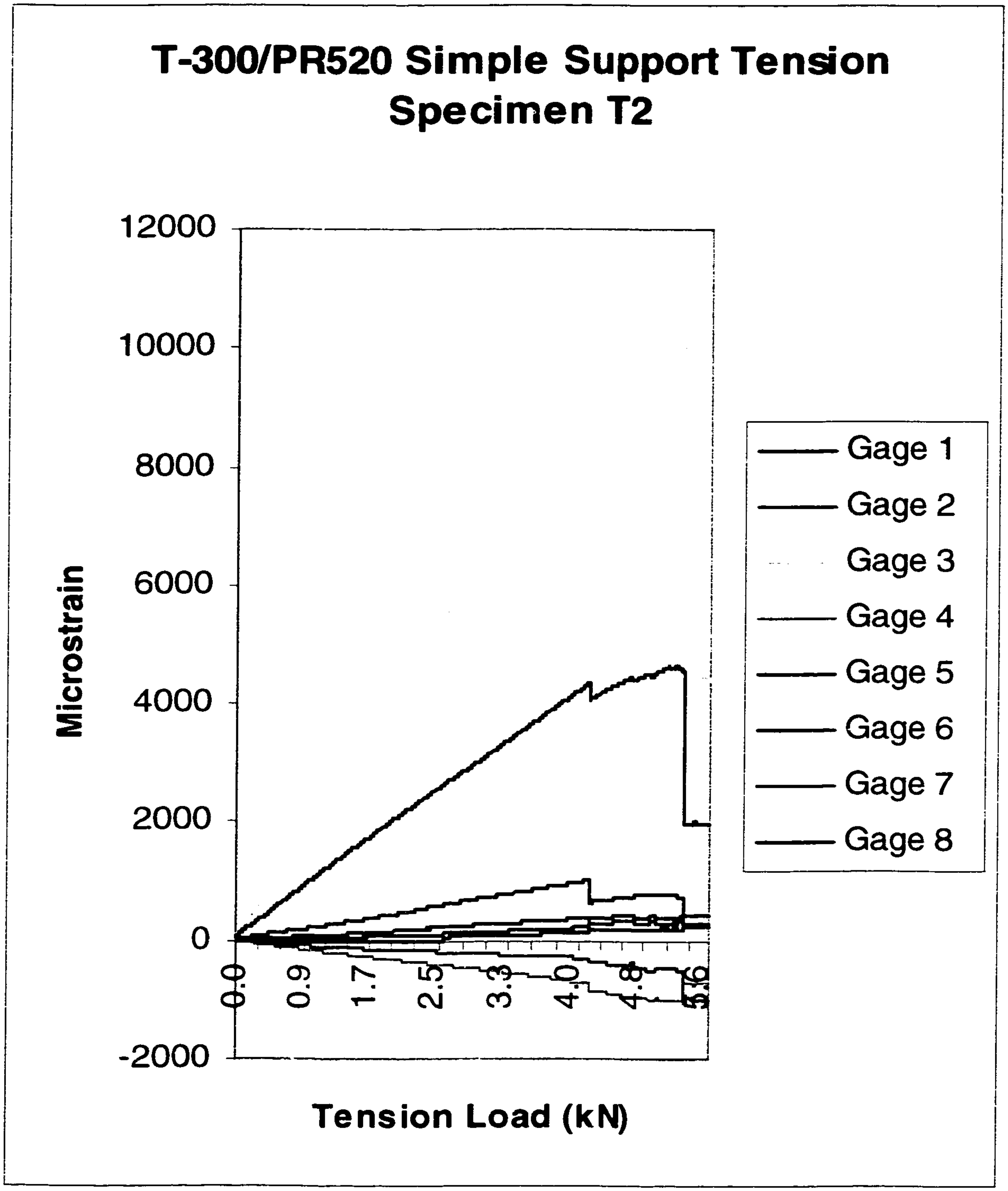

Figure E-24. T-Joint Simple Support Tension Strain-Load Plot Specimen T2.

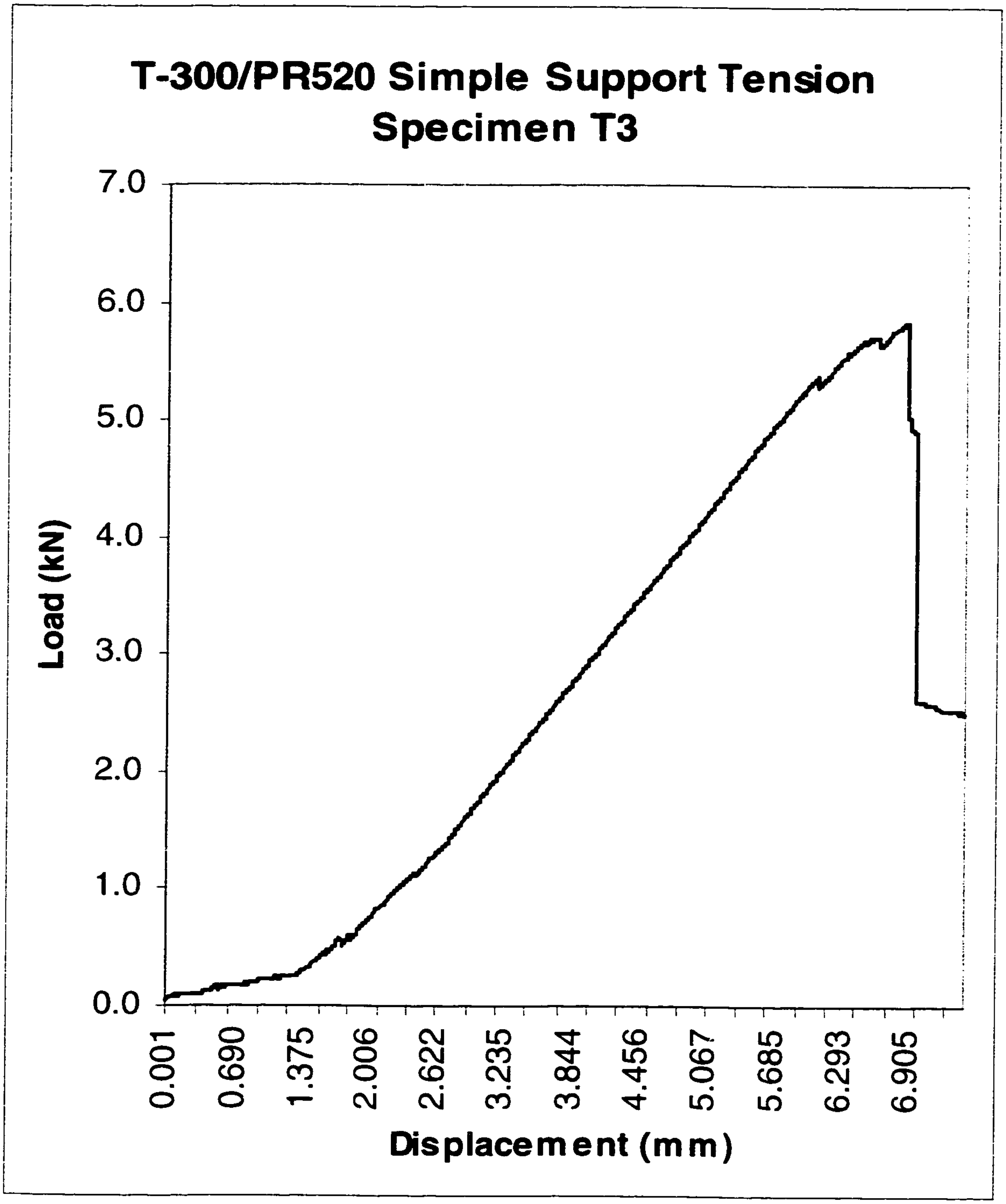

Figure E-25. T-Joint Simple Support Tension Load-Displacement Plot Specimen T3.

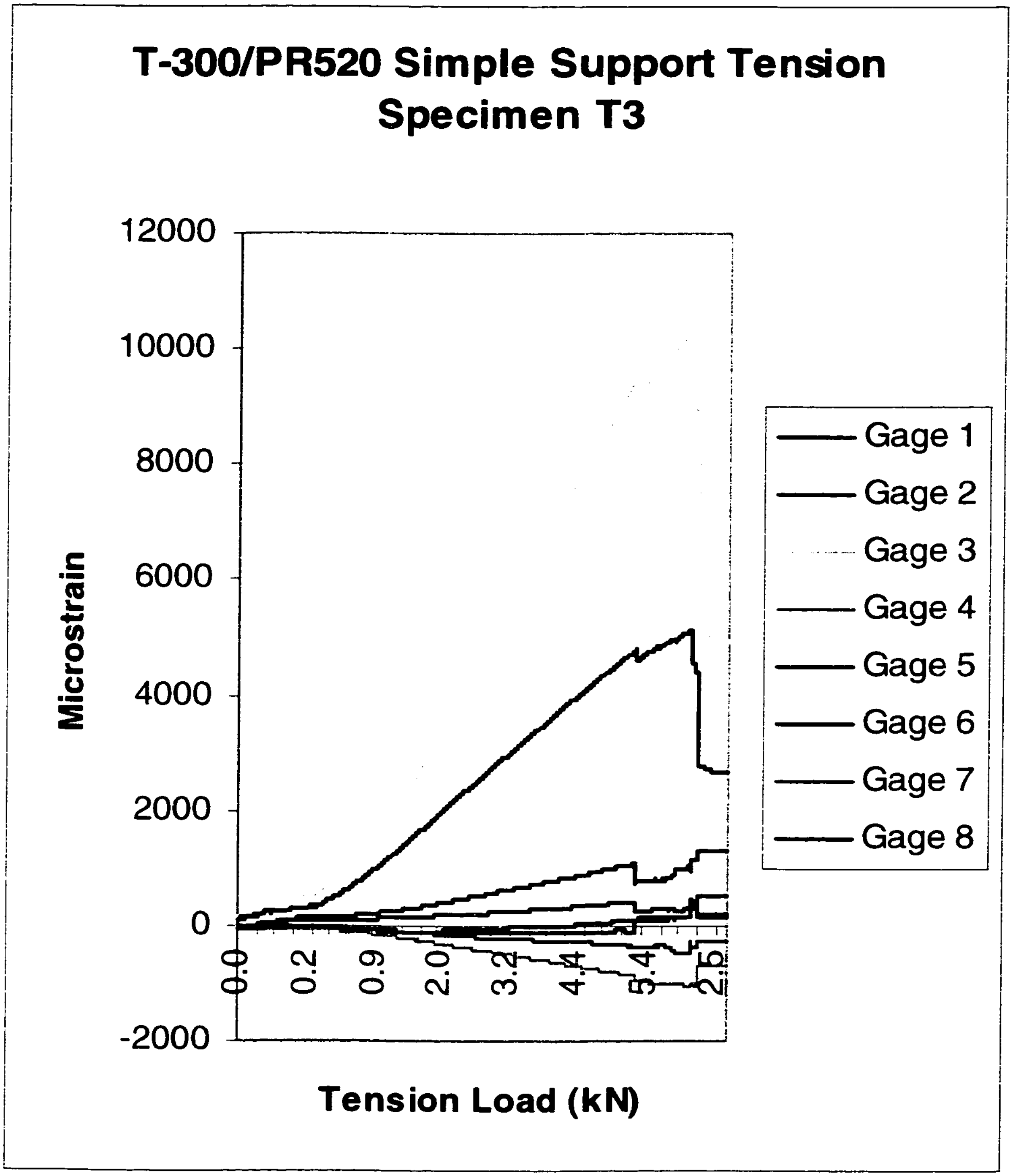

Figure E-26. T-Joint Simple Support Tension Strain-Load Plot Specimen T3.

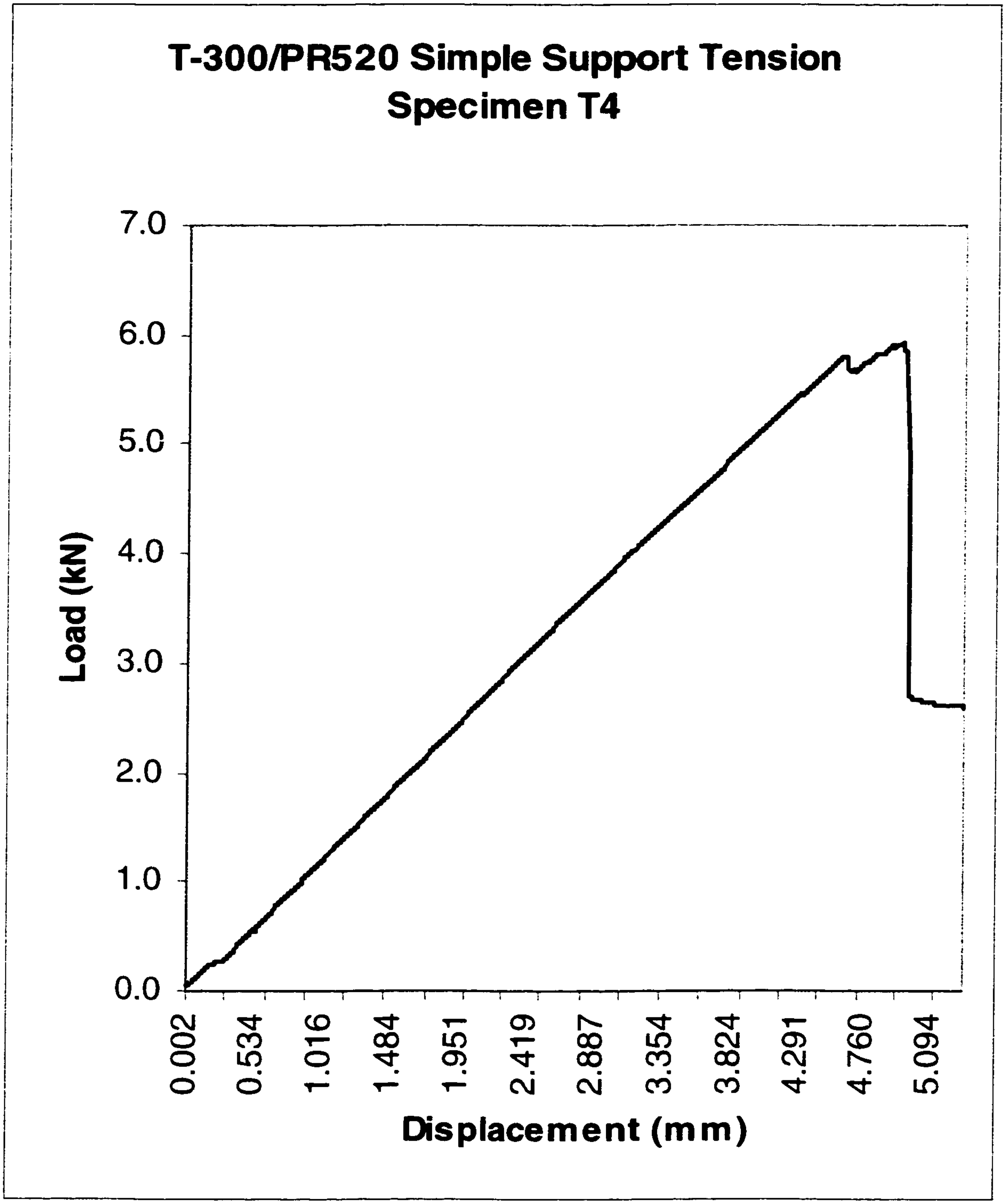

Figure E-27. T-Joint Simple Support Tension Load-Displacement Plot Specimen T4.

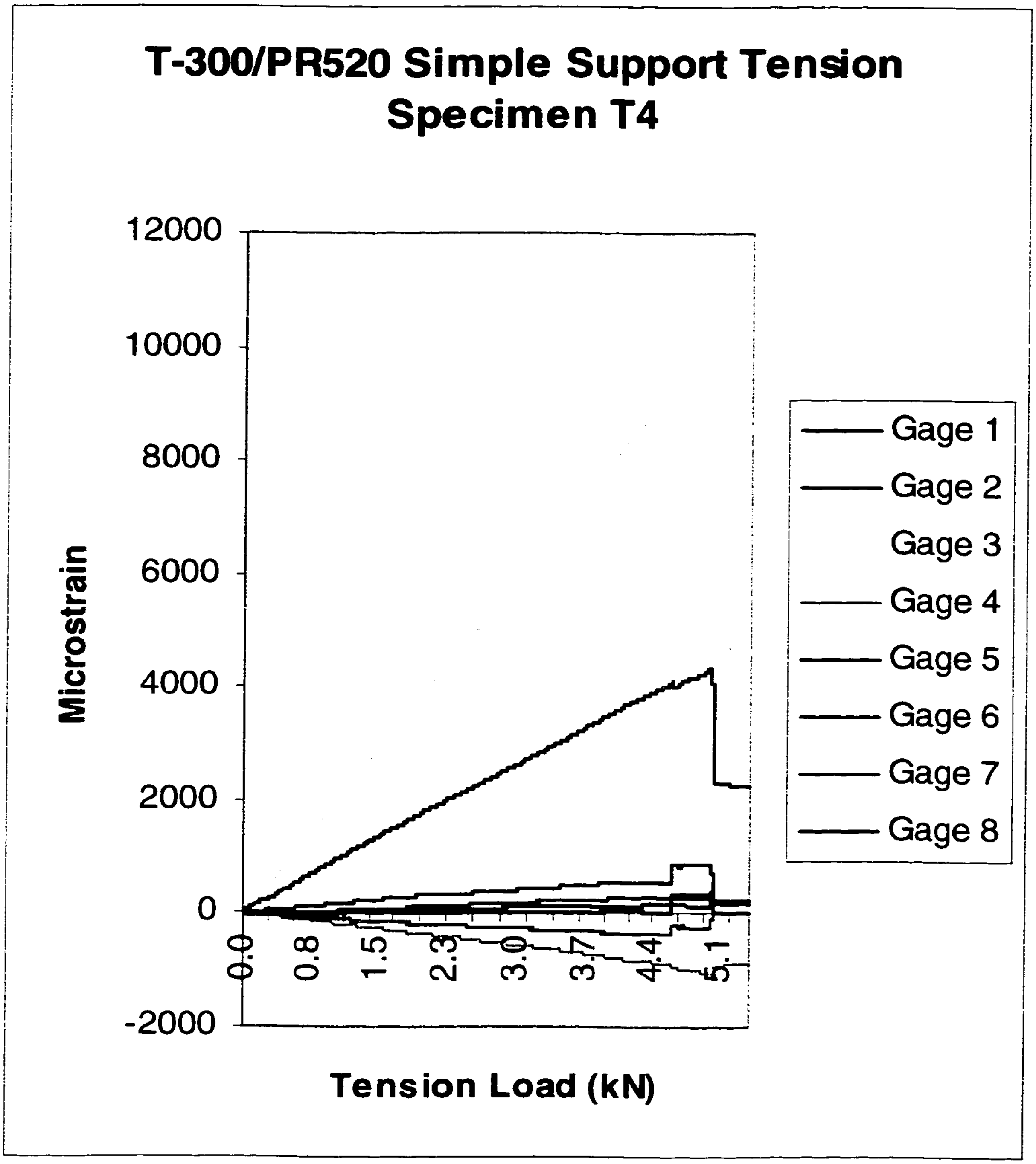

Figure E-28. T-Joint Simple Support Tension Strain-Load Plot Specimen T4.

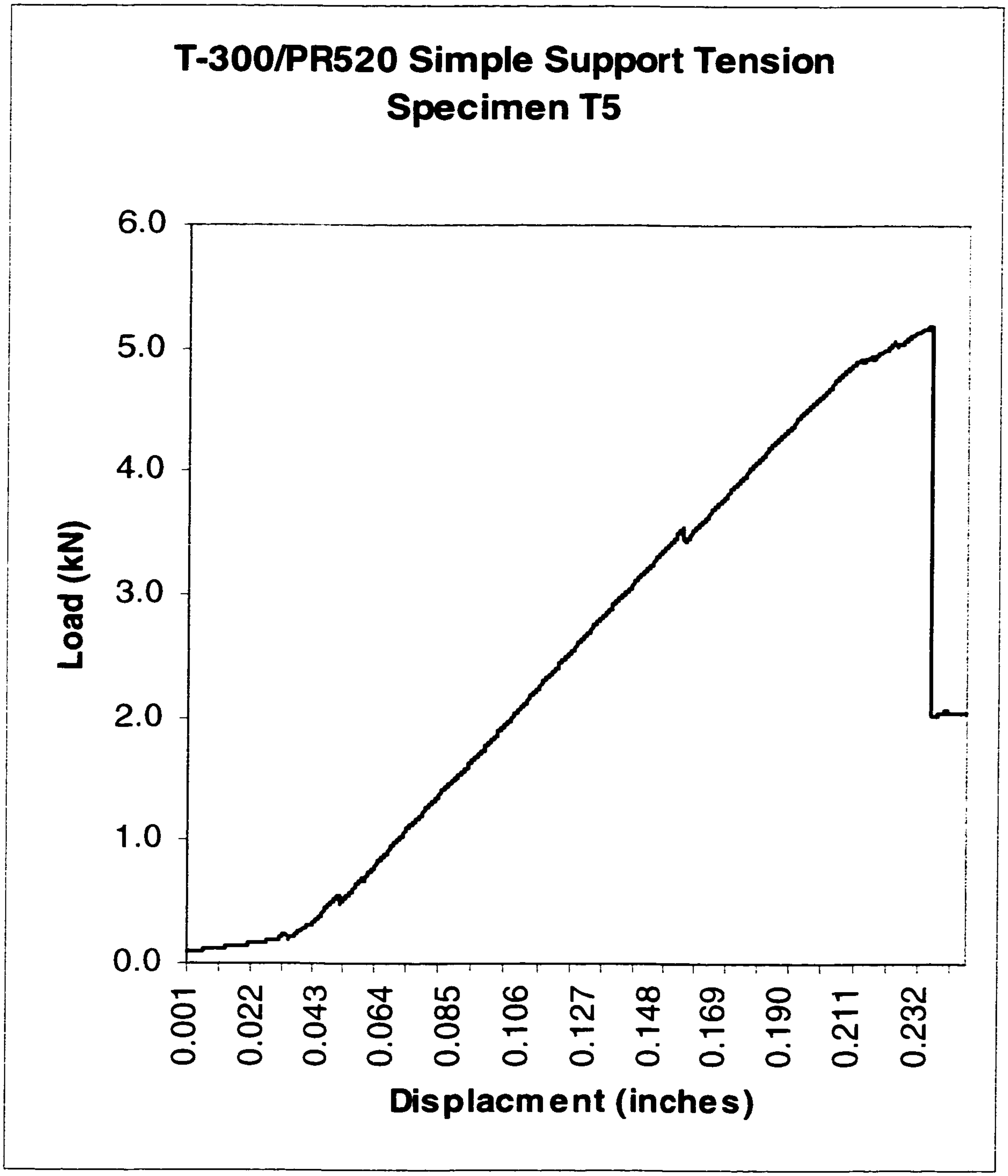

Figure E-29. T-Joint Simple Support Tension Load-Displacement Plot Specimen T5.

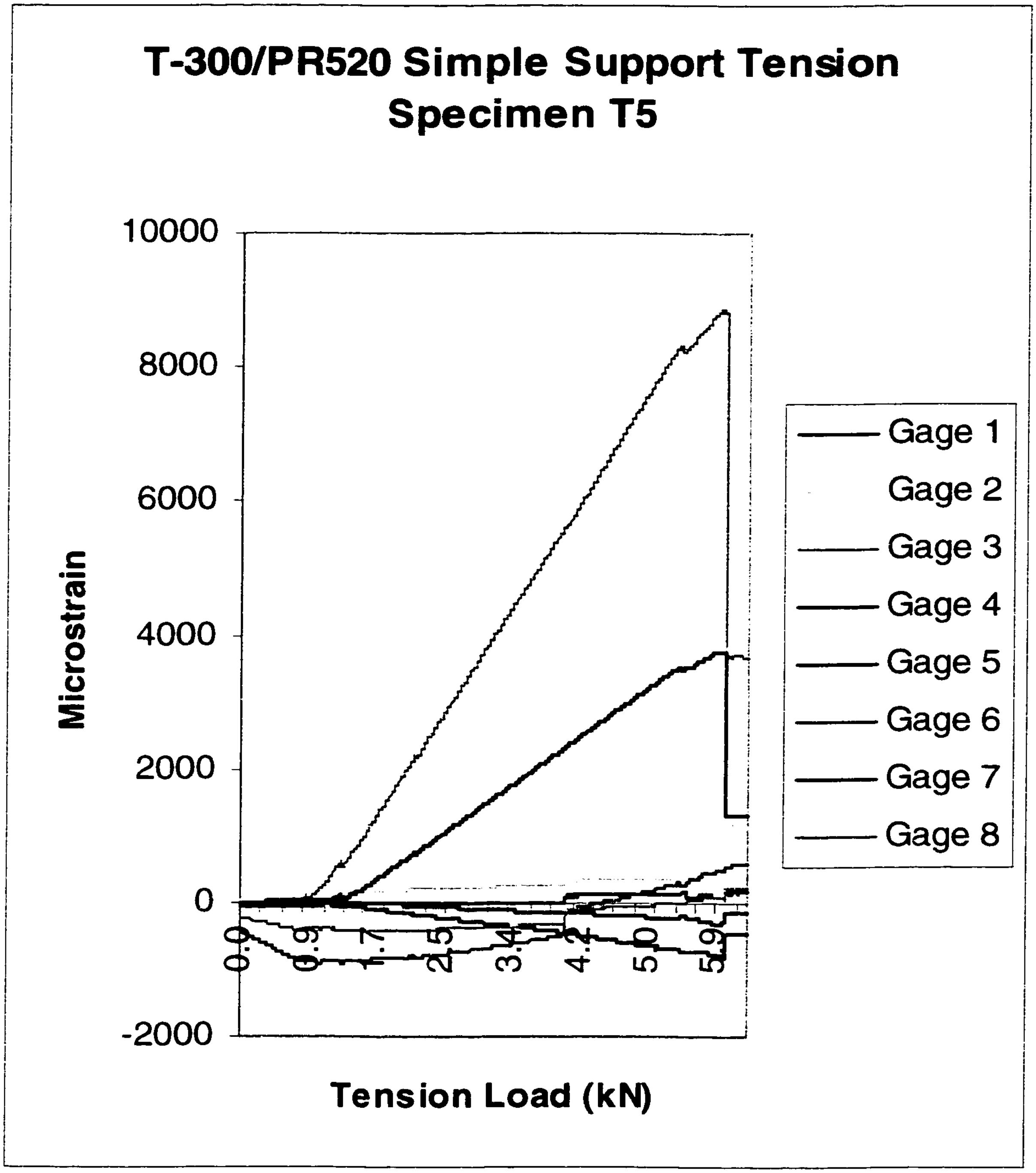

Figure E-30. T-Joint Simple Support Tension Strain-Load Plot Specimen T5.

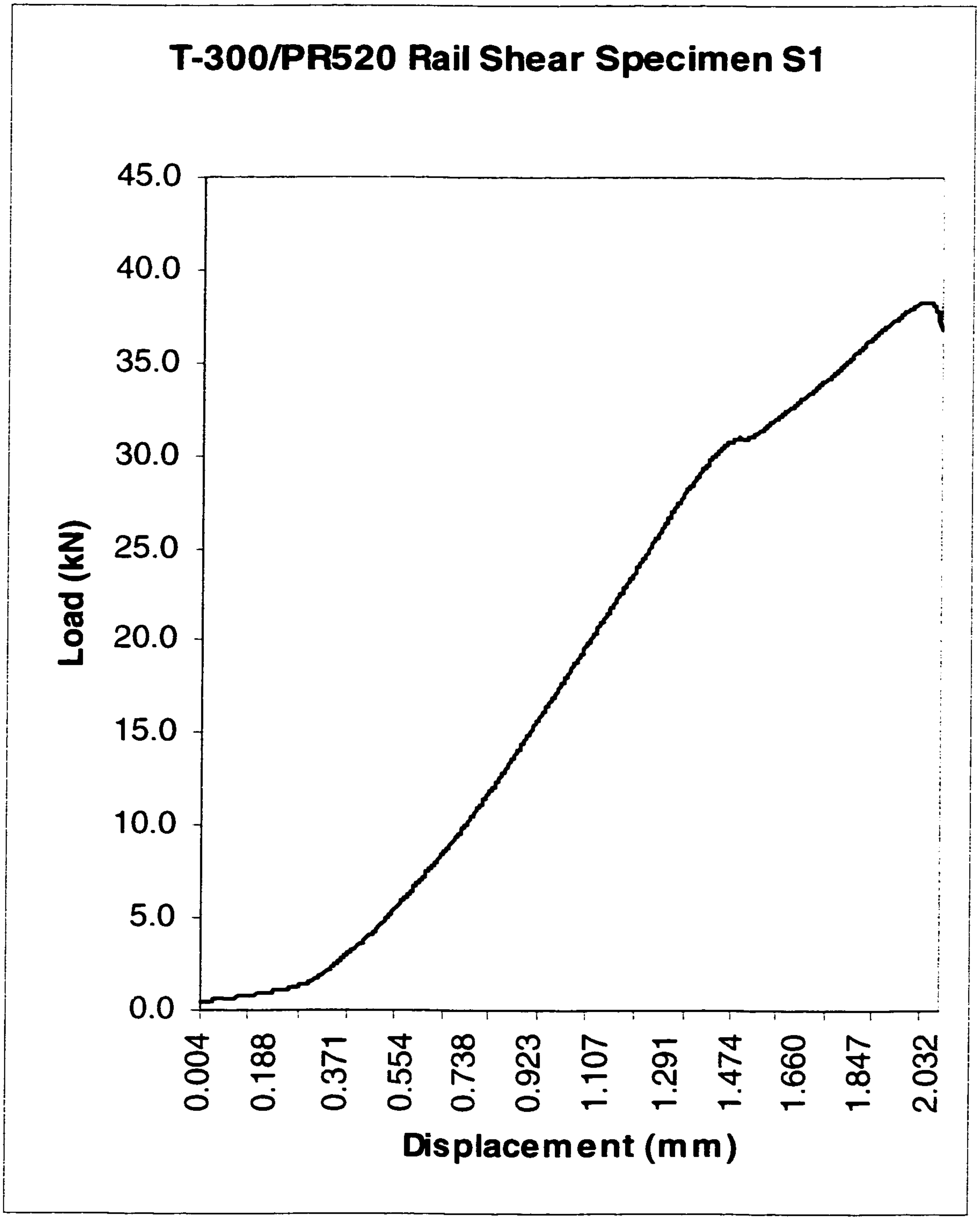

Figure E-31. T-Joint Rail Shear Load-Displacement Plot Specimen S1.

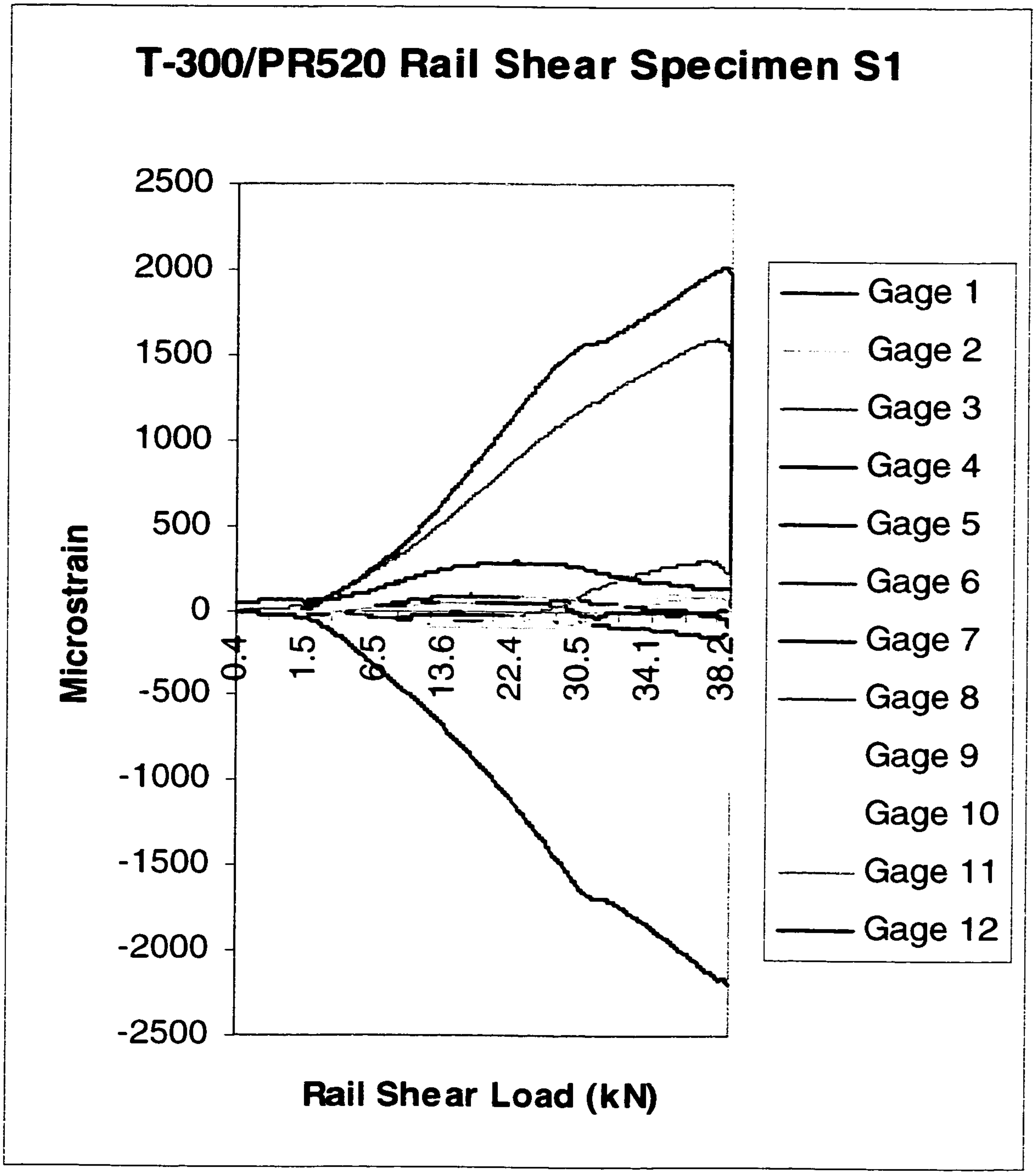

Figure E-32. T-Joint Rail Shear Strain-Load Plot Specimen S1.

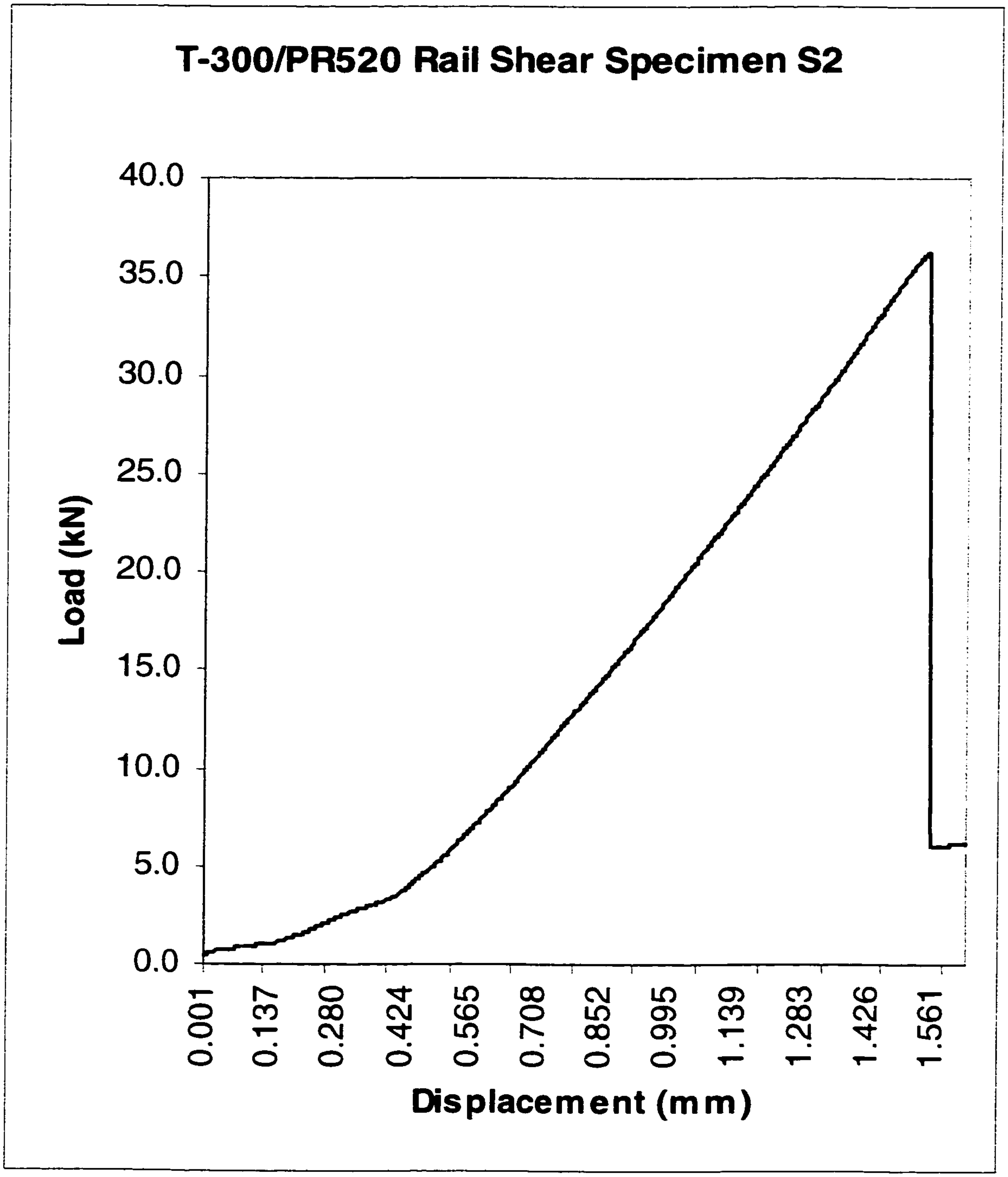

Figure E-33. T-Joint Rail Shear Load-Displacement Plot Specimen S2.

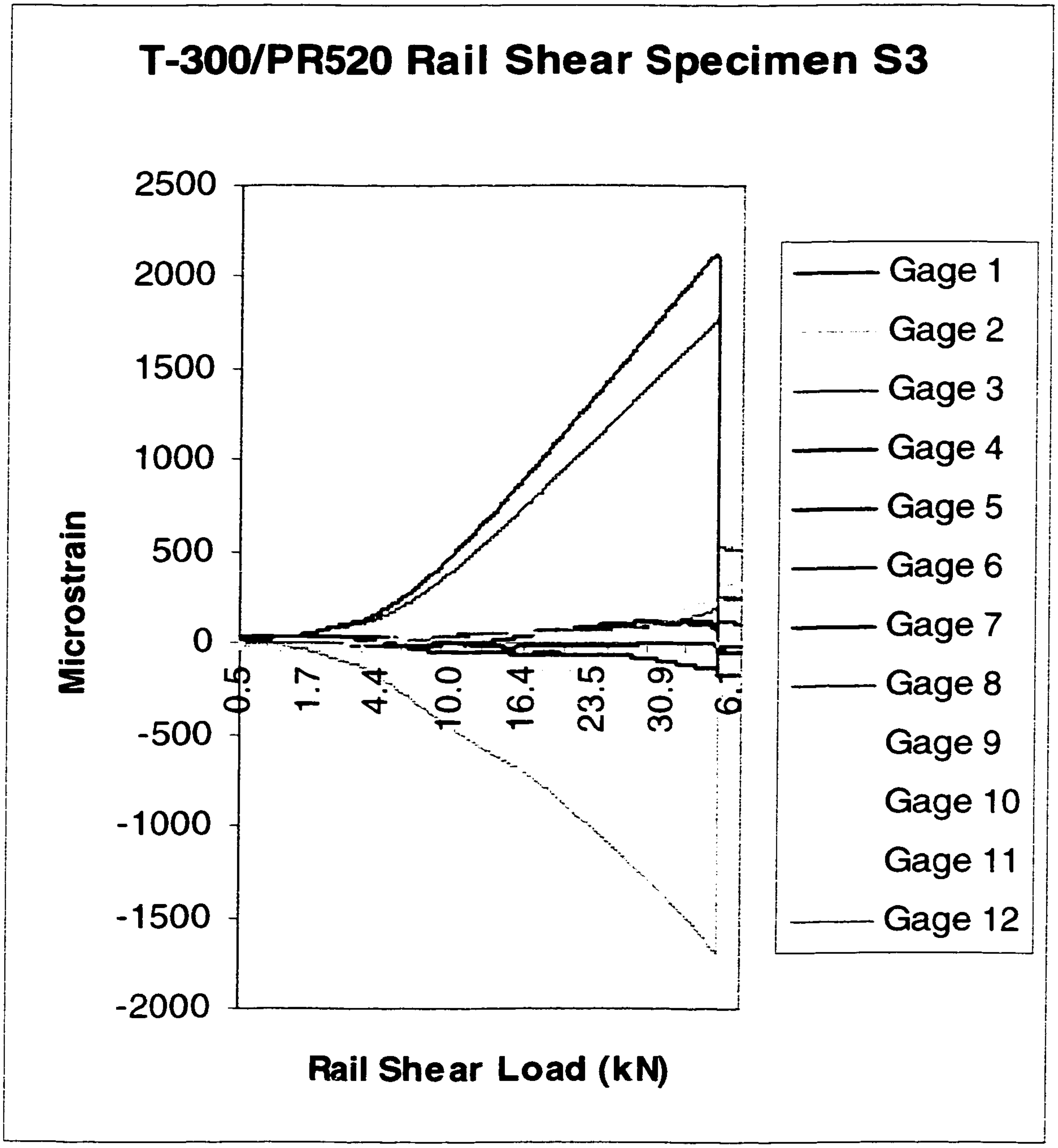

Figure E-34. T-Joint Rail Shear Strain-Load Plot Specimen S2.

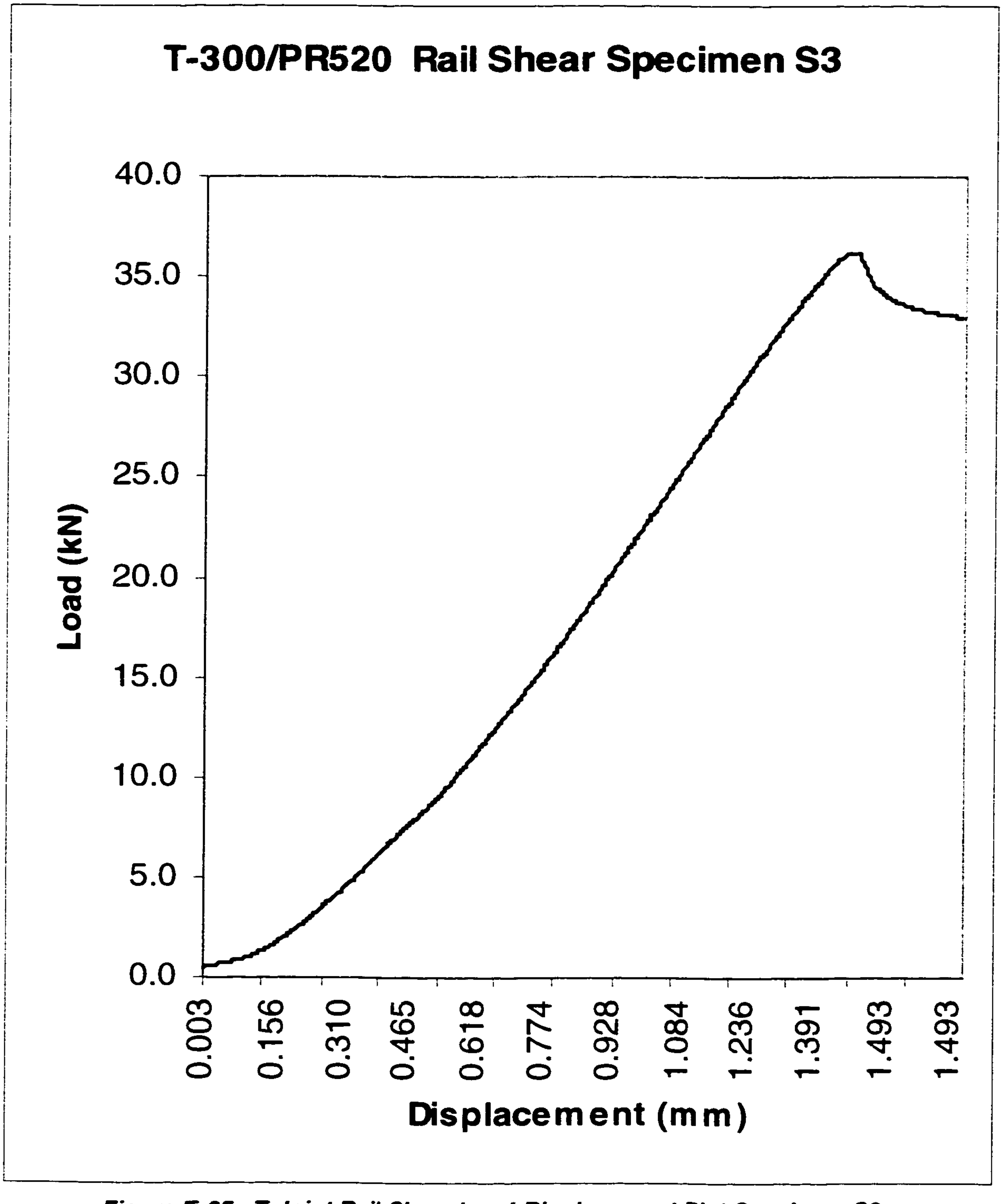

Figure E-35. T-Joint Rail Shear Load-Displacement Plot Specimen S3.

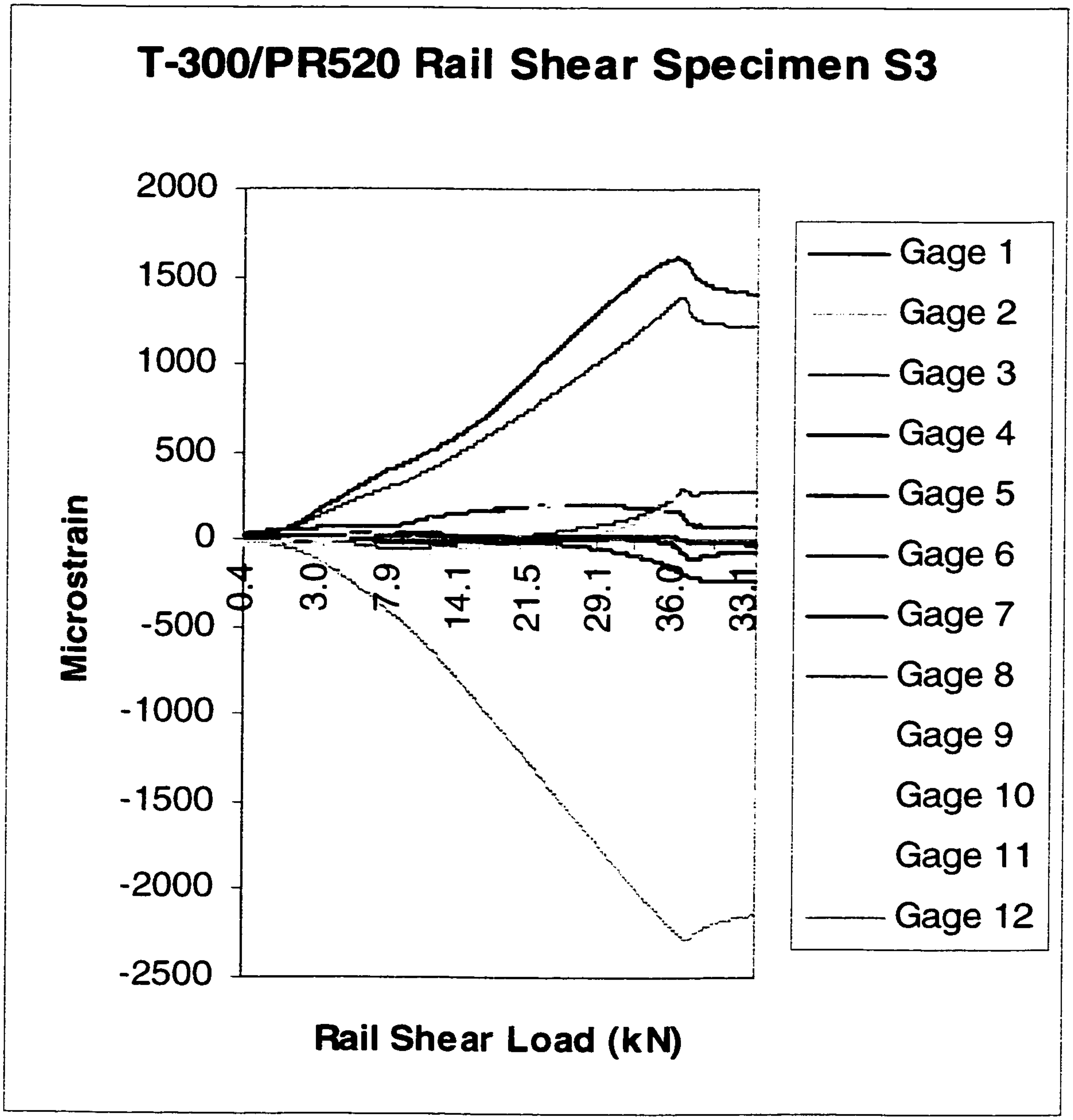

Figure E-36. T-Joint Rail Shear Strain-Load Plot Specimen S3.

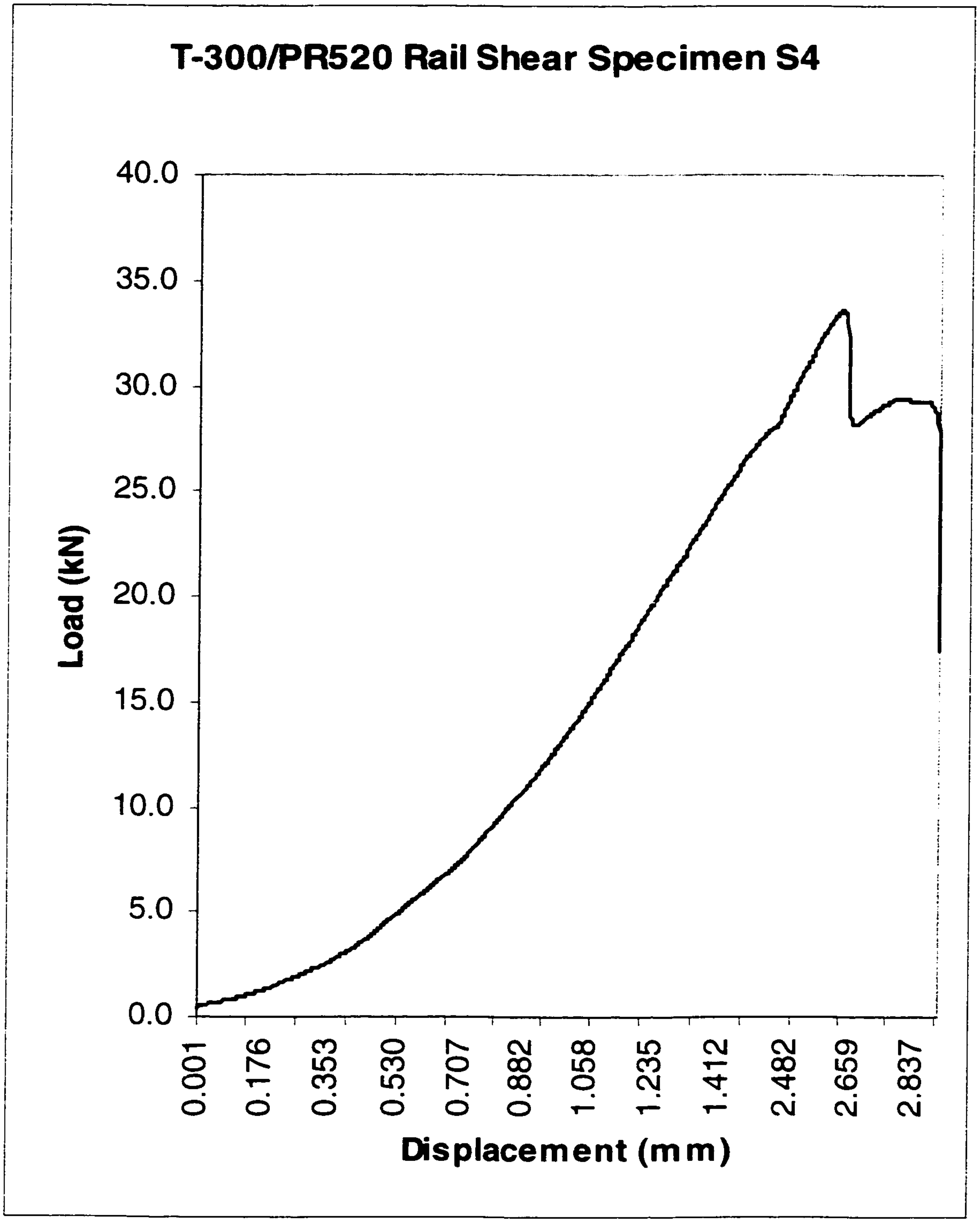

Figure E-37. T-Joint Rail Shear Load-Displacement Plot Specimen S4.

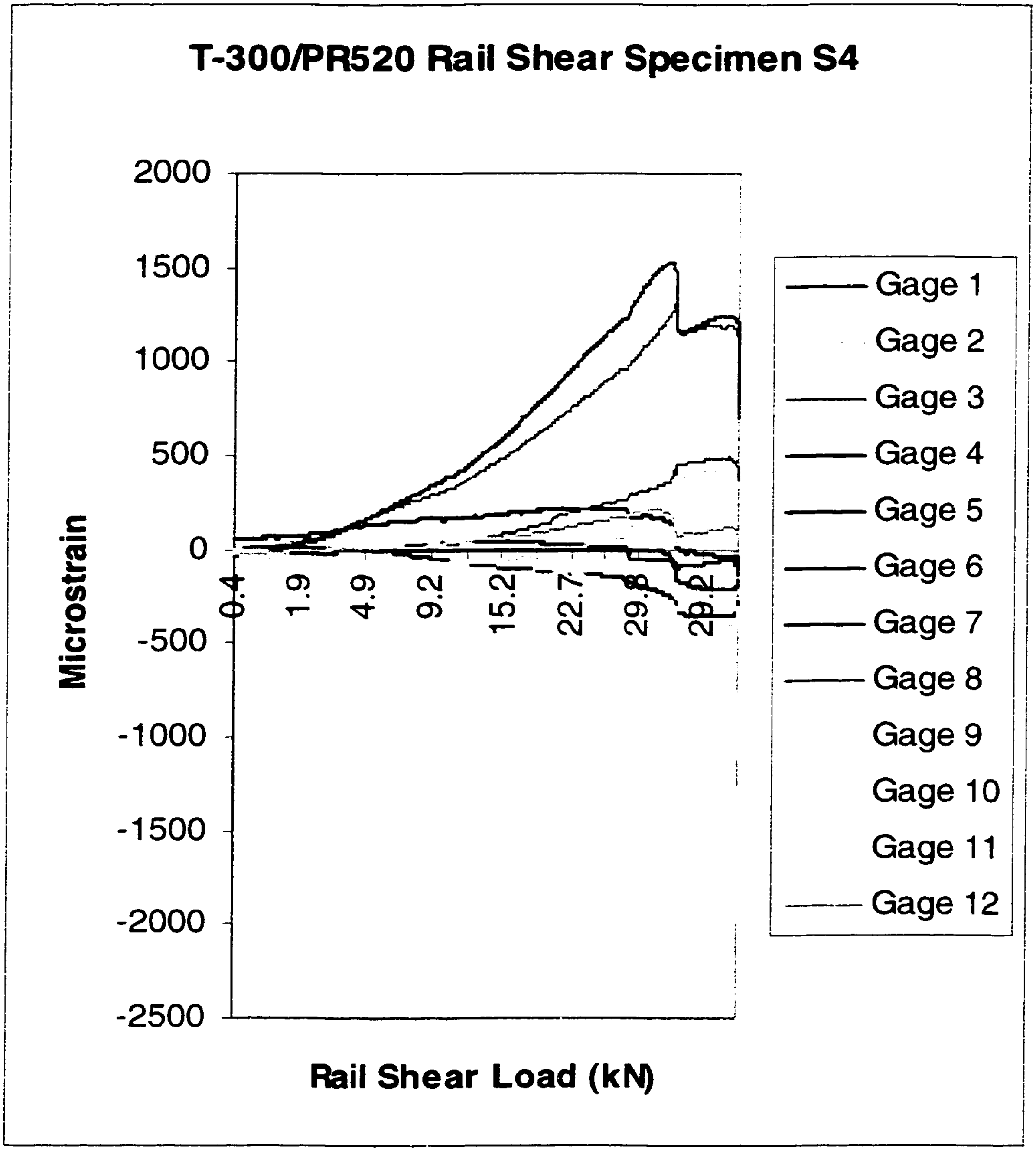

Figure E-38. T-Joint Rail Shear Strain-Load Plot Specimen S4.

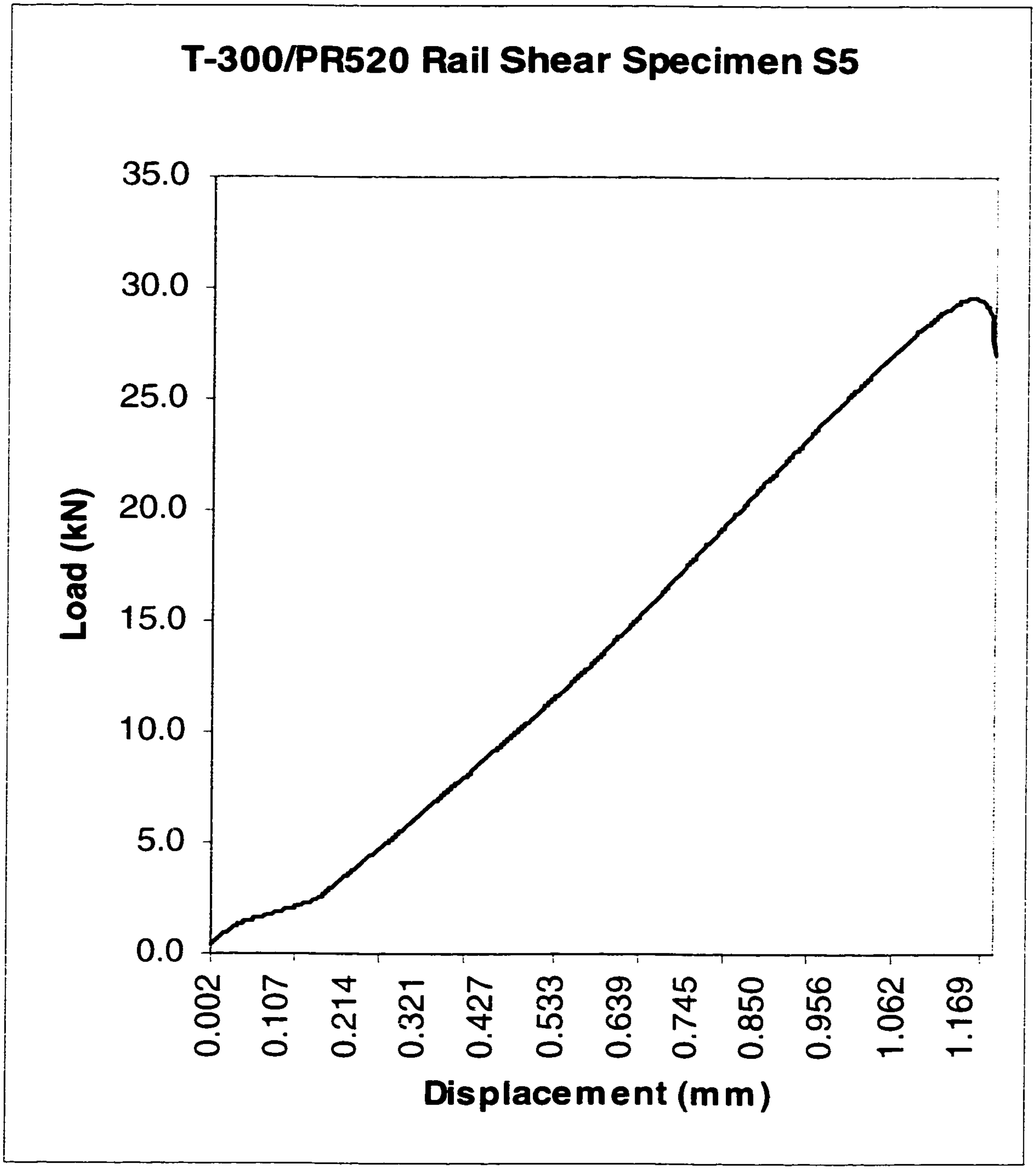

Figure E-39. T-Joint Rail Shear Load-Displacement Plot Specimen S5.

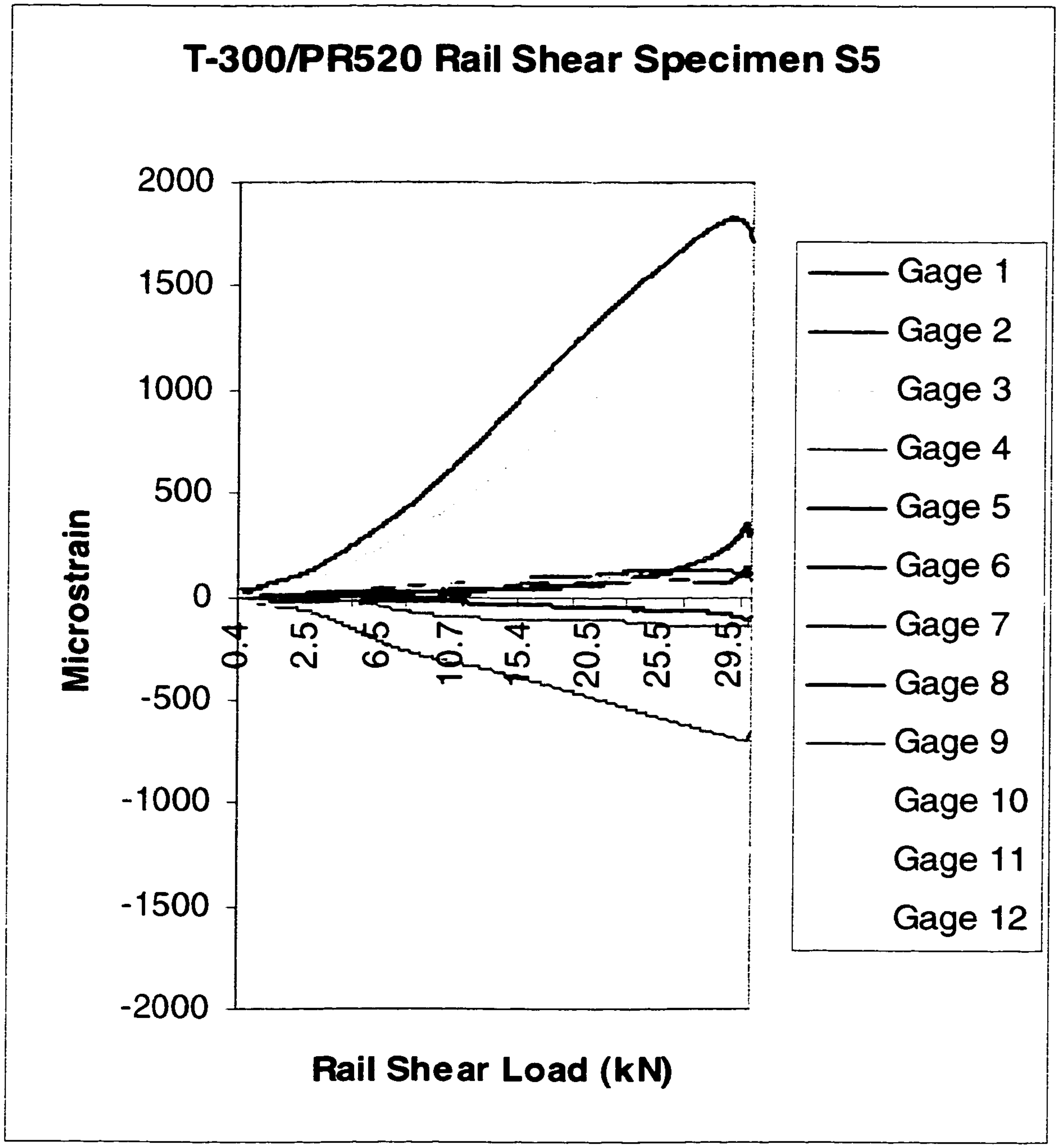

Figure E-40. T-Joint Rail Shear Strain-Load Plot Specimen S5.

APPENDIX F

INTERFACE THICKNESS EFFECTS

A linear elastic analytical analysis is performed on the T-joint under flexure, tension, and rail shear loading. Deflections are determined using a strength of materials approach.[85] Special consideration is given to the effect of matrix interface thickness on displacement. T-joint displacement under flexure loading is given by:

$$y_{max} = \frac{PL^3}{3EI}$$

where **P** is the load, **L** is the moment arm length, **E** is the modulus of elasticity, and **I** is the moment of inertia. Using the T-joint geometry and material properties, the load-displacement plot may be determined and is shown in Figure F-1.

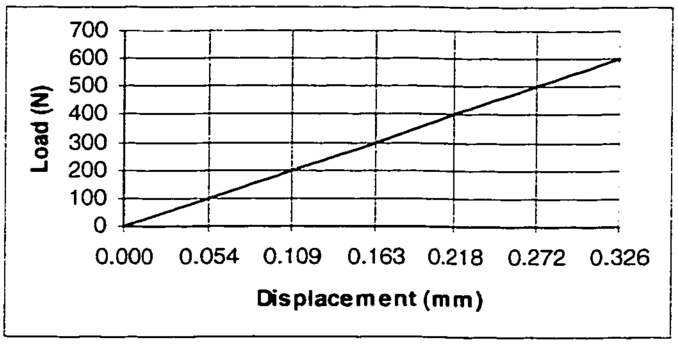

Figure F-1. T-Joint Flexure Analytical Analysis.

A flexure sensitivity analysis was performed to evaluate the deflection as a function of PR520 interface matrix thickness L2 (Figure F-2) at the initial damage load. Matrix thickness was shown to have a marginal effect on deflection at initial failure loads.

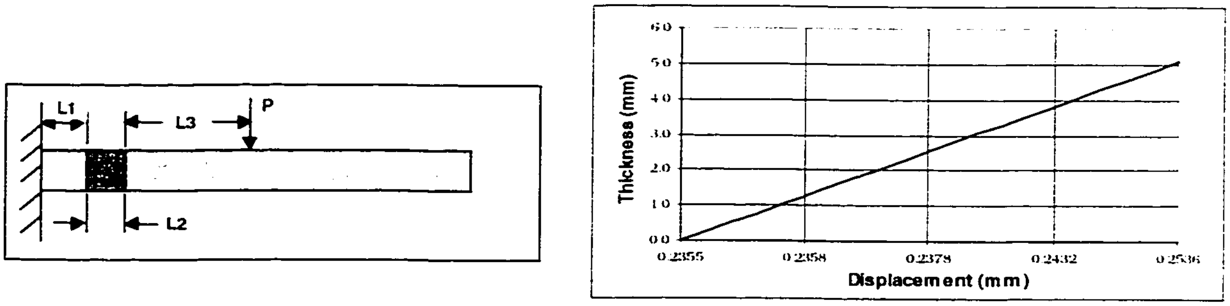

Figure F-2. T-Joint Flexure Interface Analysis: (a) Schematic and (b) Flexural Displacement as a Function of Resin Zone Thickness.

T-joint displacement under tension loading with simple support boundary conditions is given by:

$$y_{max} = \frac{PL^3}{48EI}$$

where **P** is the load, **L** is the moment arm length, **E** is the modulus of elasticity, and **I** is the moment of inertia. Using the T-joint geometry and material properties, the load-displacement plot may be determined and is shown in Figure F-3.

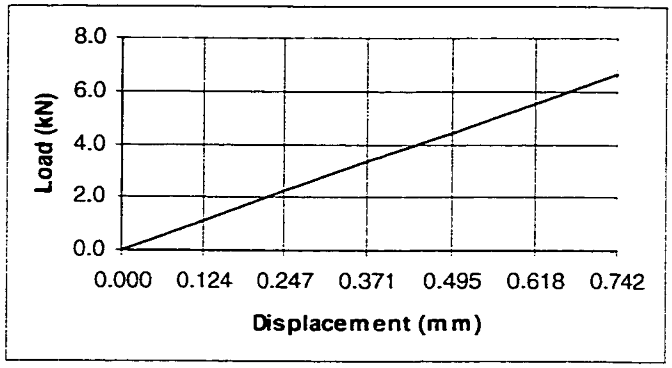

Figure F-3. T-Joint Tension Analytical Analysis.

A tension sensitivity analysis was performed to evaluate the deflection as a function of PR520 interface matrix thickness L2 (Figure F-4). Again, matrix thickness was shown to have a marginal effect on deflection at initial failure loads.

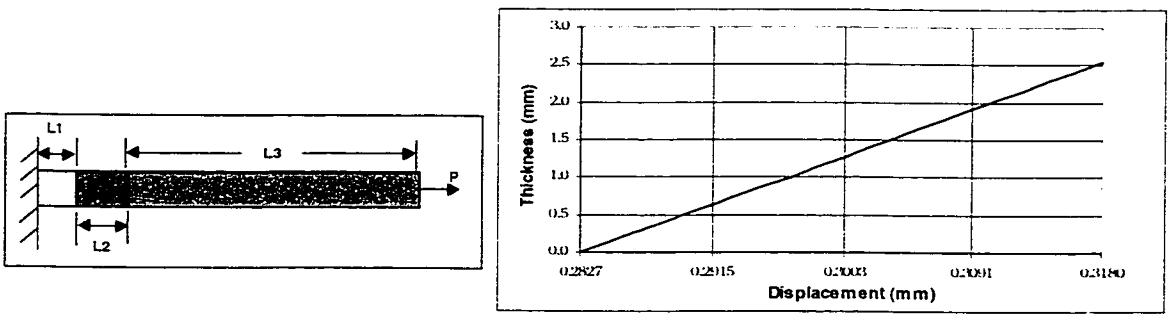

Figure F-4. T-Joint Tension Interface Analysis: (a) Schematic and (b) Tension Displacement as a Function of Interface Zone Thickness.

The T-joint maximum and average shear stress under pure shear loading is given by:

$$\tau_{max} = 1.5\frac{V}{wt} \qquad \tau_{Avg} = \frac{V}{wt}$$

where **V** is the load, **w** is the width and **t** is the thickness. The maximum shear stress under rail shear (pure shear) loading is shown in Figure F-5 and the average shear stress is shown in Figure F-6. Figure F-7 shows the maximum shear strain under rail shear loading.

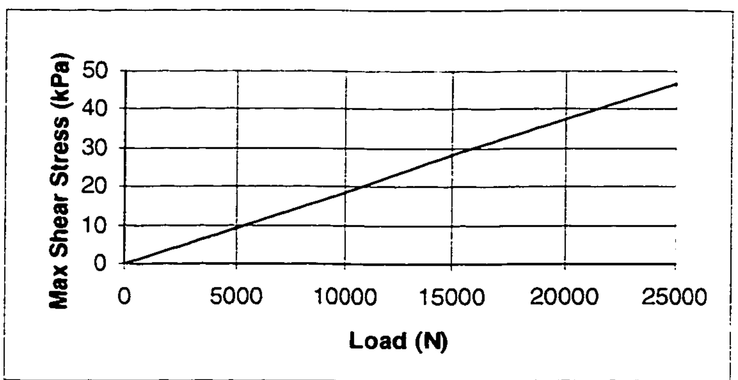

Figure F-5. T-Joint Rail Shear Max Stress.

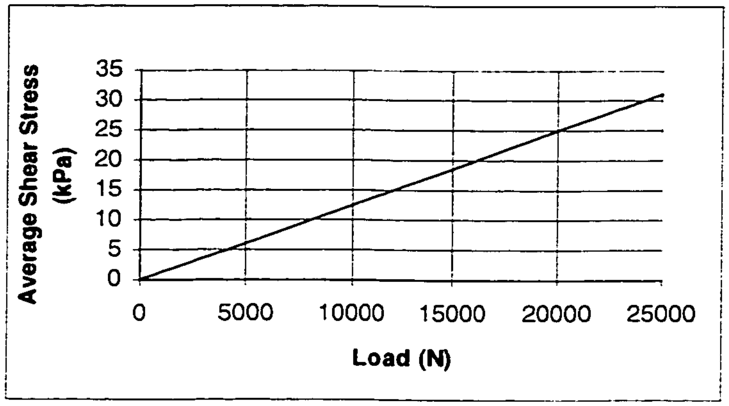

Figure F-6. T-Joint Rail Shear Average Stress.

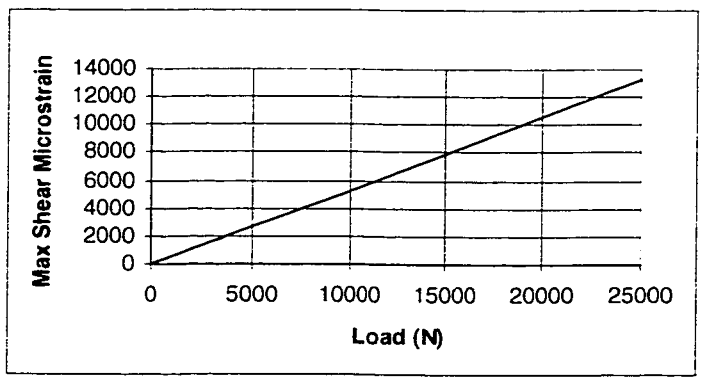

Figure F-7. T-Joint Max Strain Under Rail Shear Loading.

APPENDIX G

FEA INPUT FILES

```
/BATCH
/COM,ANSYS RELEASE  5.6.2  UP20000525        09:26:32    04/26/2001
/input,menust,tmp     ,,,,,,,,,,,,,,,,,1
/GRA,POWER
/GST,ON
/REPLOT,RESIZE
/TITLE,2D Composite T-joint Analysis
/REPLOT
/PREP7
!*
/NOPR
/PMETH,OFF,0
KEYW,PR_SET,1
KEYW,PR_STRUC,1
KEYW,PR_THERM,0
KEYW,PR_FLUID,0
KEYW,PR_ELMAG,0
KEYW,MAGNOD,0
KEYW,MAGEDG,0
KEYW,MAGHFE,0
KEYW,MAGELC,0
KEYW,PR_MULTI,0
KEYW,PR_CFD,0
/GO
!*
/COM,
/COM,Preferences for GUI filtering have been set to display:
/COM,  Structural
!*
ET,1,LINK1
ET,2,PLANE183
ET,3,PLANE2
!*
KEYOPT,2,3,2
KEYOPT,2,10,0
KEYOPT,3,3,2
KEYOPT,3,5,0
KEYOPT,3,6,0
!*
R,1,0.00045, ,
!*
UIMP,1,EX, , ,40000000,
UIMP,1,NUXY, , ,0.30,
UIMP,1,ALPX, , , ,
UIMP,1,REFT, , , ,
UIMP,1,MU, , , ,
UIMP,1,DAMP, , , ,
UIMP,1,DENS, , , ,
!*
```

```
UIMP,2,EX, , ,514000,
UIMP,2,NUXY, , ,0.38,
UIMP,2,ALPX, , , ,
UIMP,2,REFT, , , ,
UIMP,2,MU, , , ,
UIMP,2,DAMP, , , ,
UIMP,2,DENS, , , ,
!*
UIMP,3,EX,EY,EZ,6420000,1411000,6420000,
UIMP,3,PRXY,PRYZ,PRXZ,,,,
UIMP,3,NUXY,NUYZ,NUXZ,0.37,0.37,0.31,
UIMP,3,GXY,GYZ,GXZ,430000,430000,2398000,
UIMP,3,ALPX,ALPY,ALPZ,,,,
UIMP,3,REFT, , , ,
UIMP,3,MU, , , ,
UIMP,3,DAMP, , , ,
UIMP,3,DENS, , , ,
!*
UIMP,4,EX,EY,EZ,1411000,6420000,6420000,
UIMP,4,PRXY,PRYZ,PRXZ,,,,
UIMP,4,NUXY,NUYZ,NUXZ,0.37,0.31,0.37,
UIMP,4,GXY,GYZ,GXZ,430000,2398000,430000,
UIMP,4,ALPX,ALPY,ALPZ,,,,
UIMP,4,REFT, , , ,
UIMP,4,MU, , , ,
UIMP,4,DAMP, , , ,
UIMP,4,DENS, , , ,
!*
RECTNG,0,0.05,0,0.20,
RECTNG,0.05,0.1,0,0.2,
RECTNG,0.1,0.15,0,0.2,
RECTNG,0.15,1.75,0,0.2,
RECTNG,1.75,3.5,0,0.2,
RECTNG,0,0.05,0.2,0.25,
RECTNG,0.05,0.1,0.2,0.25,
RECTNG,0,0.05,0.25,0.7,
RECTNG,0.05,0.1,0.25,0.7,
RECTNG,0,0.1,0.7,1.5,
RECTNG,0,0.1,1.5,3,
!*
NUMMRG,KP, , , ,LOW
NUMCMP,ALL
!*
K,100,.15,.25,0,
LARC,8,15,23,.05,
LPLOT
FLST,2,3,4
FITEM,2,10
FITEM,2,20
FITEM,2,34
AL,P51X
!*
FLST,5,3,4,ORDE,3
FITEM,5,2
```

```
FITEM,5,17
FITEM,5,22
CM,_Y,LINE
LSEL, , , ,P51X
CM,_Y1,LINE
CMSEL,S,_Y
!*
CMSEL,S,_Y1
LATT,1,1,1, , , ,
CMSEL,S,_Y
CMDELE,_Y
CMDELE,_Y1
!*
FLST,5,5,5,ORDE,2
FITEM,5,1
FITEM,5,-5
CM,_Y,AREA
ASEL, , , ,P51X
CM,_Y1,AREA
CMSEL,S,_Y
!*
CMSEL,S,_Y1
AATT,       4,        1,    2,        0
CMSEL,S,_Y
CMDELE,_Y
CMDELE,_Y1
!*
FLST,5,2,5,ORDE,2
FITEM,5,6
FITEM,5,-7
CM,_Y,AREA
ASEL, , , ,P51X
CM,_Y1,AREA
CMSEL,S,_Y
!*
CMSEL,S,_Y1
AATT,       2,        1,    2,        0
CMSEL,S,_Y
CMDELE,_Y
CMDELE,_Y1
!*
/REPLOT
CM,_Y,AREA
ASEL, , , ,      12
CM,_Y1,AREA
CMSEL,S,_Y
!*
CMSEL,S,_Y1
AATT,       2,        1,    3,        0
CMSEL,S,_Y
CMDELE,_Y
CMDELE,_Y1
!*
FLST,5,4,5,ORDE,2
```

```
FITEM,5,8
FITEM,5,-11
CM,_Y,AREA
ASEL, , , ,P51X
CM,_Y1,AREA
CMSEL,S,_Y
!*
CMSEL,S,_Y1
AATT,       3,        1,    1,        0
CMSEL,S,_Y
CMDELE,_Y
CMDELE,_Y1
!*
```

APPENDIX H

FEA CONTOUR PLOTS

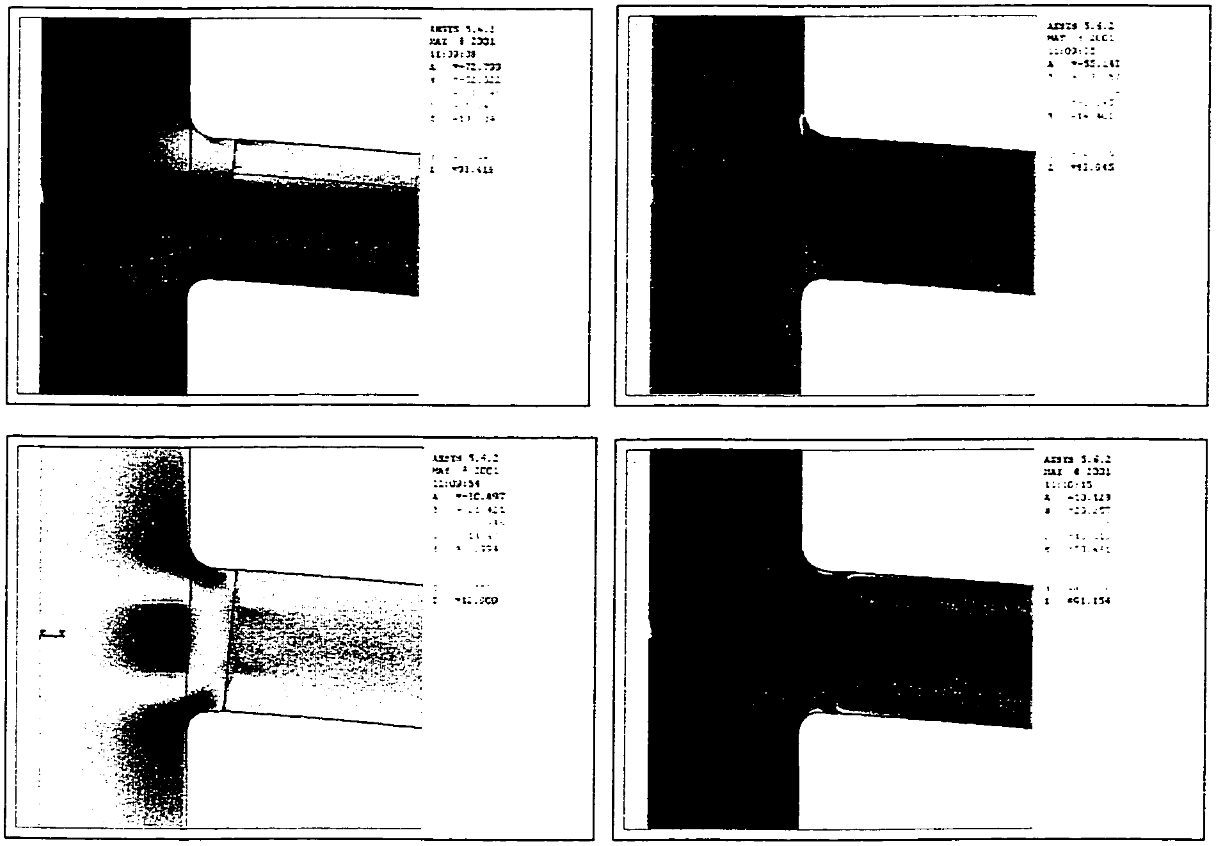

Figure H-1. Stress Contour Plots for Flexure Progressive Analysis Model 1 (MPa): (a) Normal Stress, σ_x, (b) Normal Stress, σ_y, (c) In-Plane Shear Stress, τ_{xy}, and (d) Effective Stress, σ_{eff}.

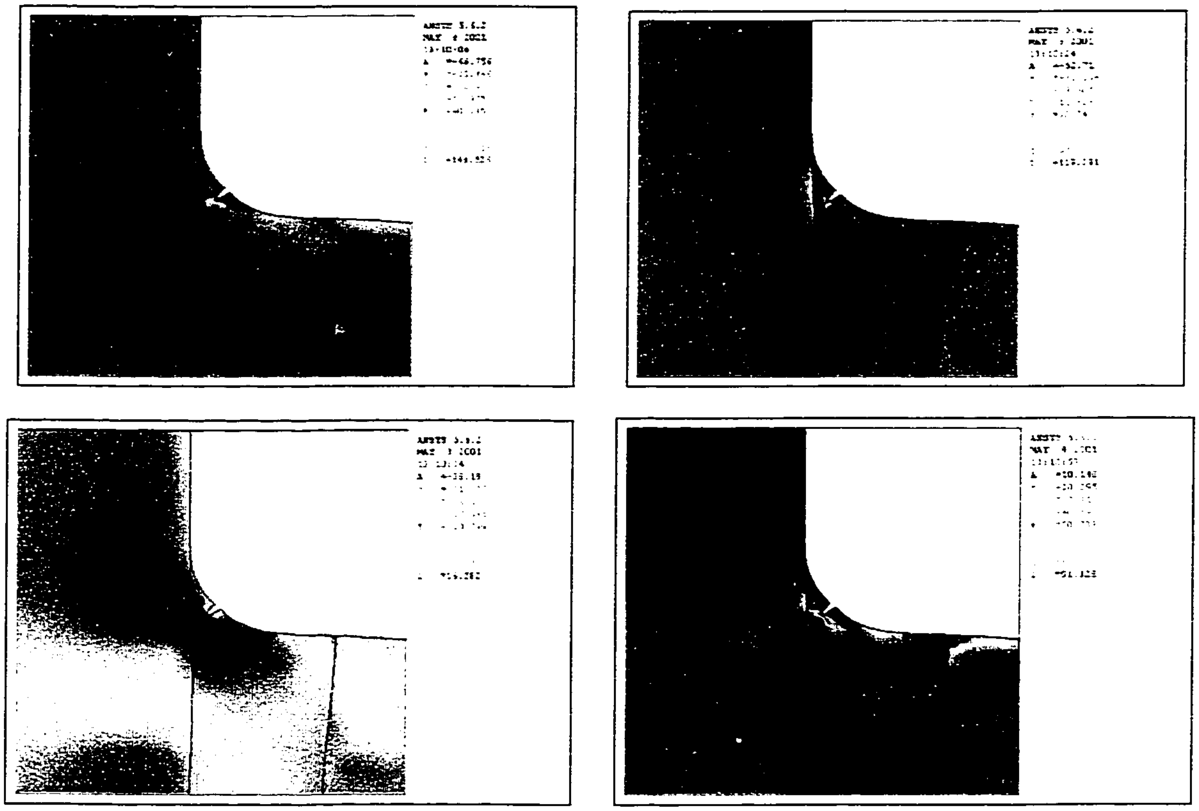

Figure H-2. Stress Contour Plots for Flexure Progressive Analysis Model 2 (MPa): (a) Normal Stress, σ_x, (b) Normal Stress, σ_y, (c) In-Plane Shear Stress, τ_{xy}, and (d) Effective Stress, σ_{eff}.

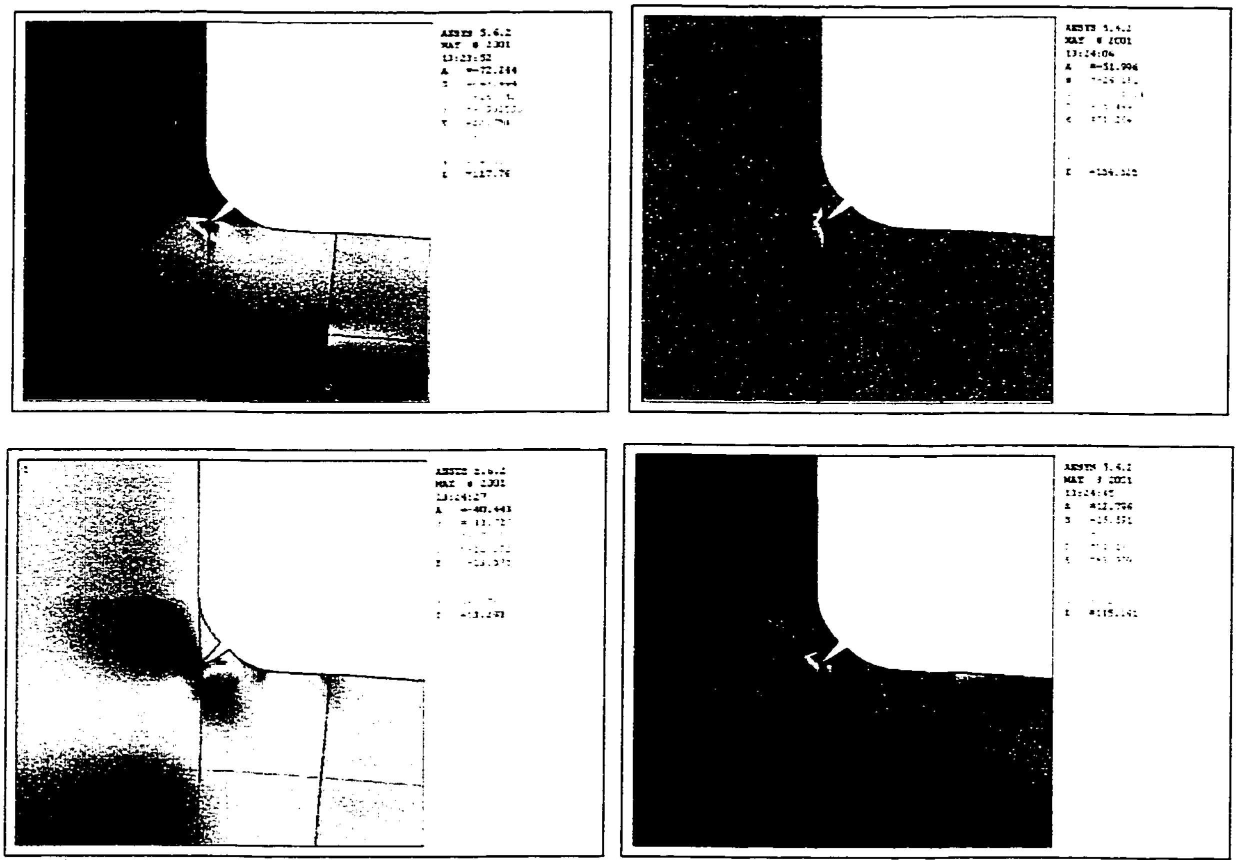

Figure H-3. Stress Contour Plots for Flexure Progressive Analysis Model 3 (MPa): (a) Normal Stress, σ_x, (b) Normal Stress, σ_y, (c) In-Plane Shear Stress, τ_{xy}, and (d) Effective Stress, σ_{eff}.

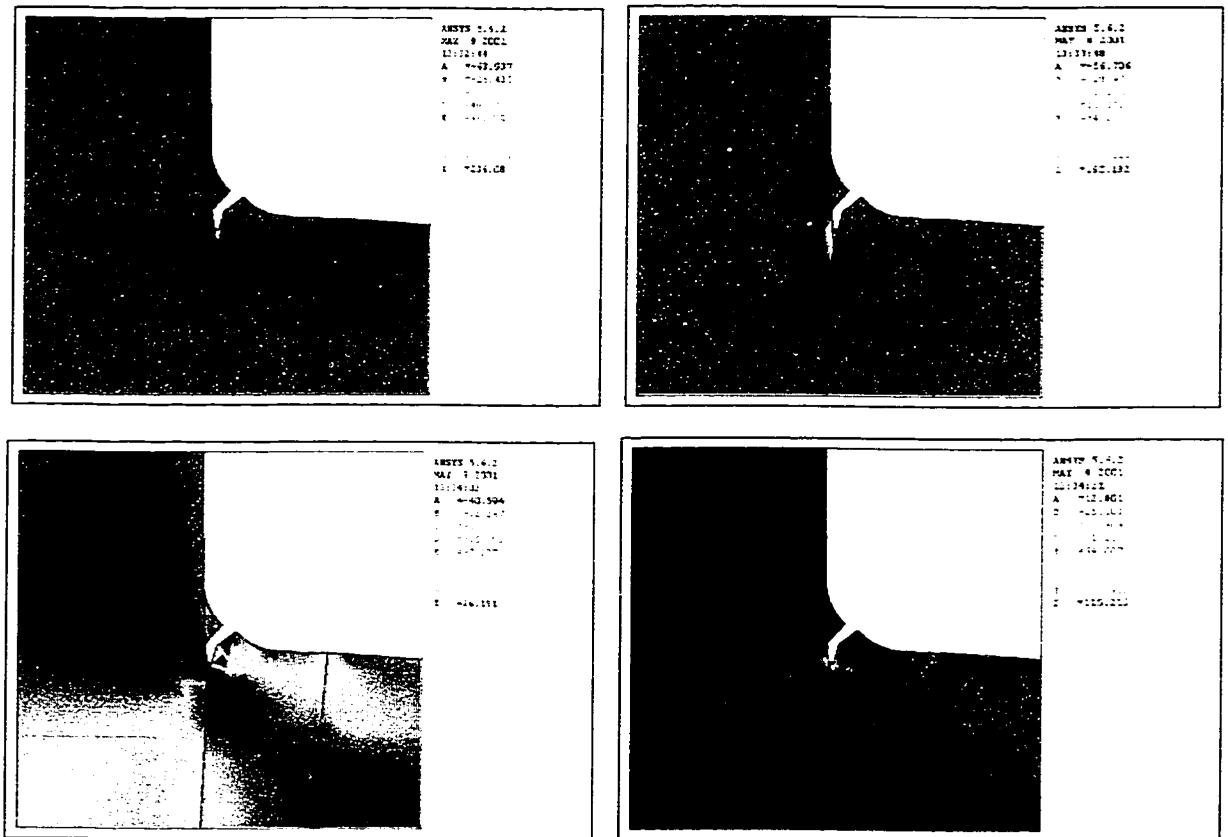

Figure H-4. Stress Contour Plots for Flexure Progressive Analysis Model 4 (MPa): (a) Normal Stress, σ_x, (b) Normal Stress, σ_y, (c) In-Plane Shear Stress, τ_{xy}, and (d) Effective Stress, σ_{eff}.

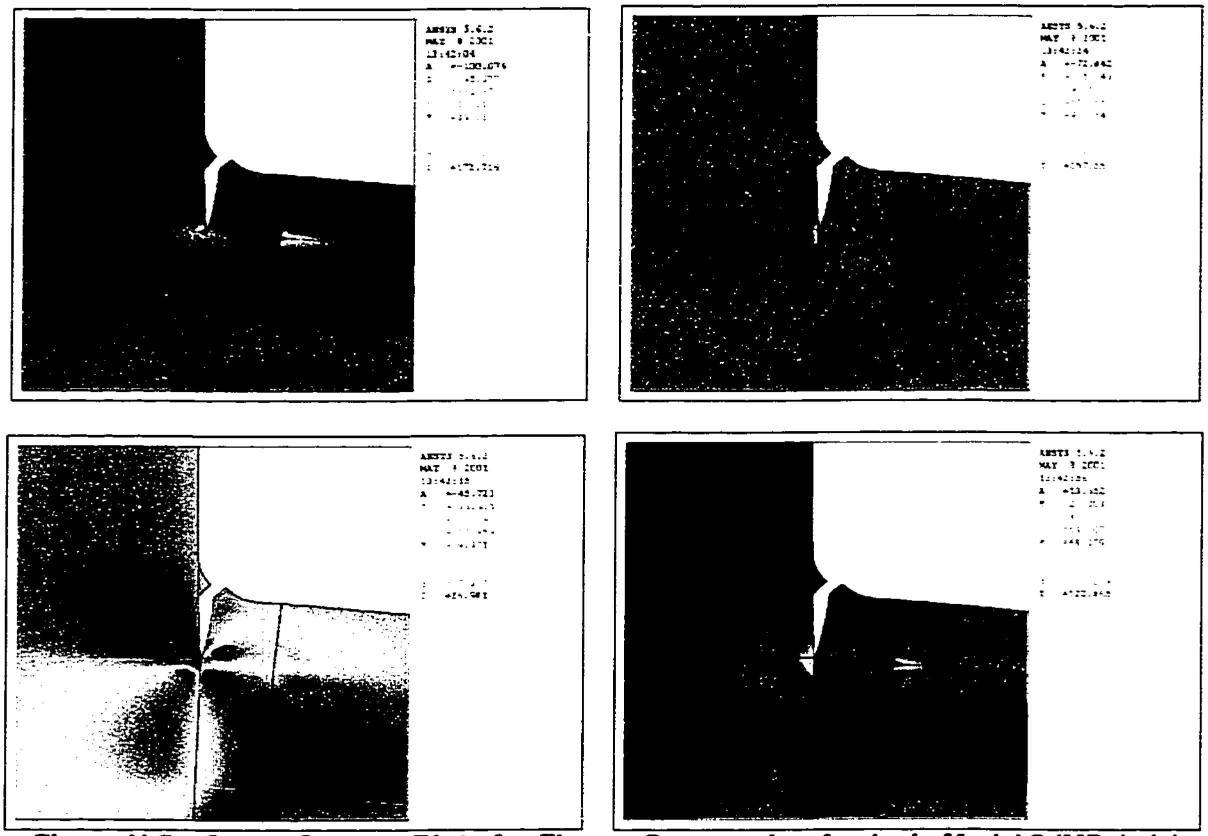

Figure H-5. Stress Contour Plots for Flexure Progressive Analysis Model 5 (MPa): (a) Normal Stress, σ_x, (b) Normal Stress, σ_y, (c) In-Plane Shear Stress, τ_{xy}, and (d) Effective Stress, σ_{eff}.

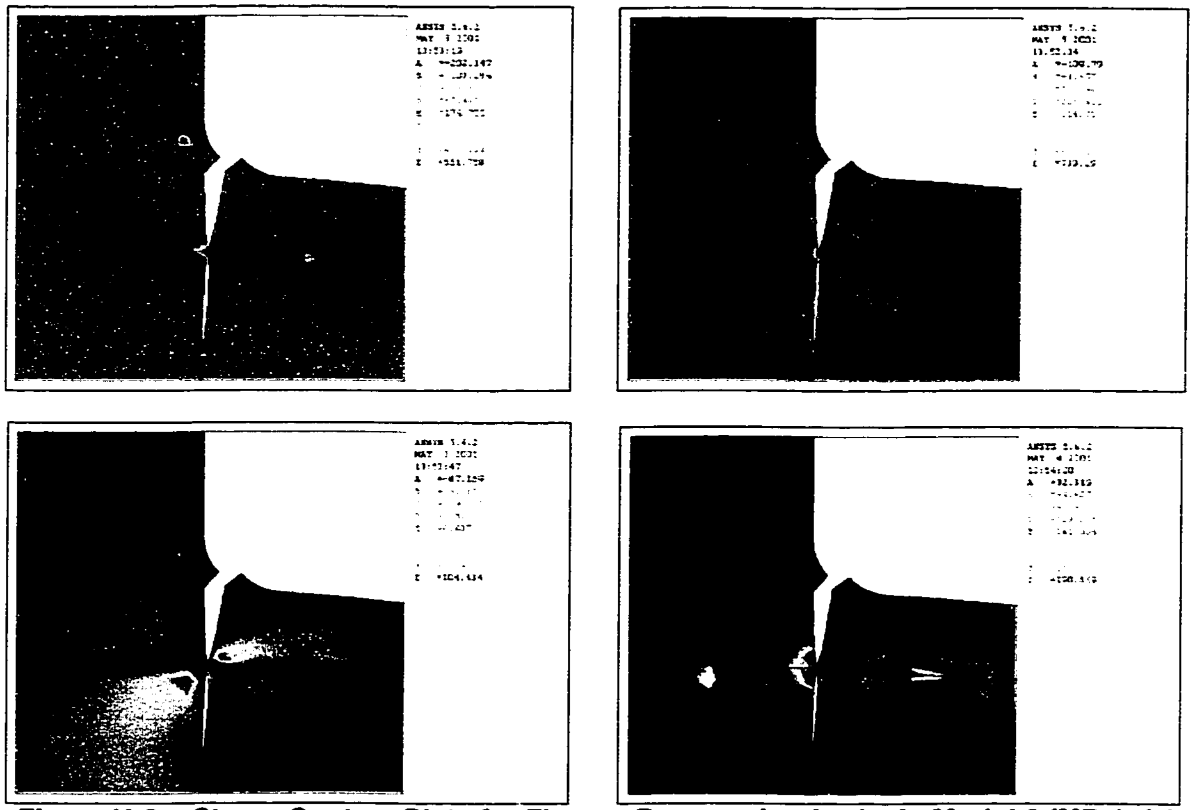

Figure H-6. Stress Contour Plots for Flexure Progressive Analysis Model 6 (MPa): (a) Normal Stress, σ_x, (b) Normal Stress, σ_y, (c) In-Plane Shear Stress, τ_{xy}, and (d) Effective Stress, σ_{eff}.

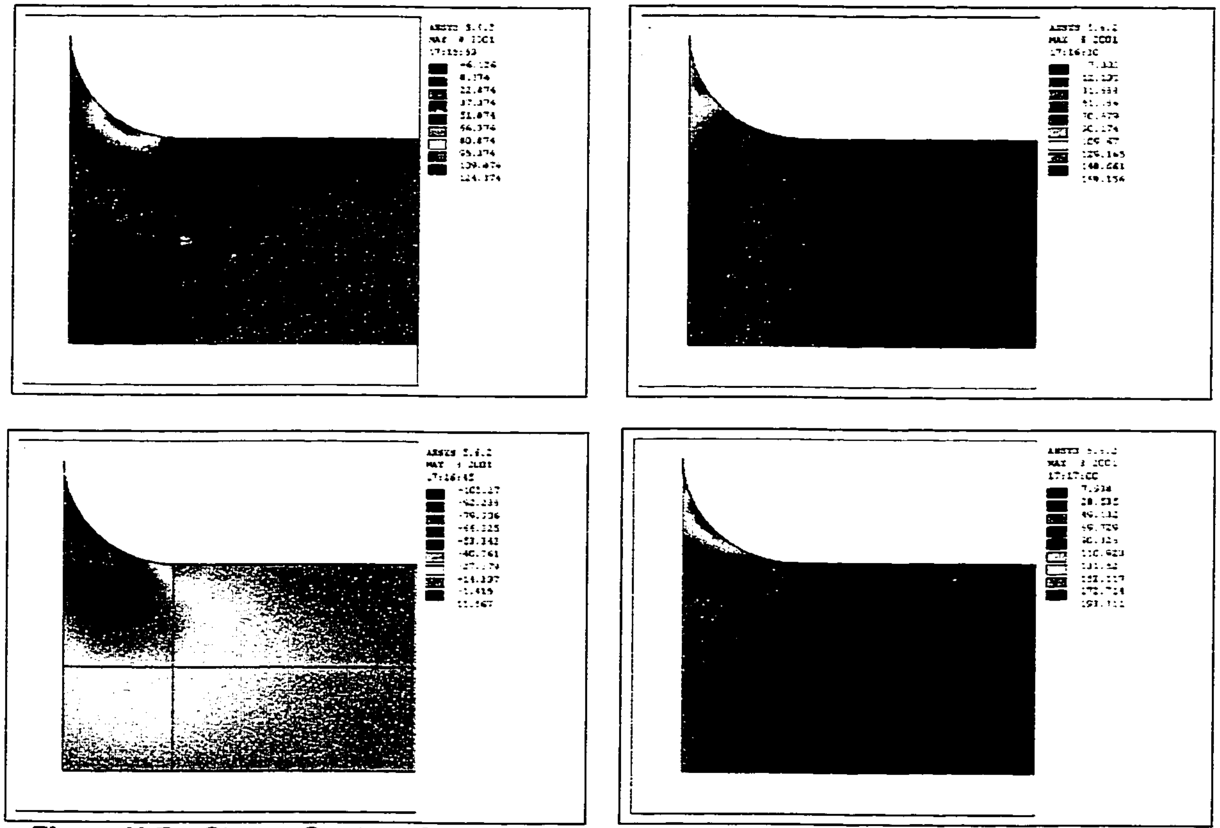

Figure H-7. Stress Contour Plots for Tension Progressive Analysis Model 1(MPa): (a) Normal Stress, σ_x, (b) Normal Stress, σ_y, (c) In-Plane Shear Stress, τ_{xy}, and (d) Effective Stress, σ_{eff}.

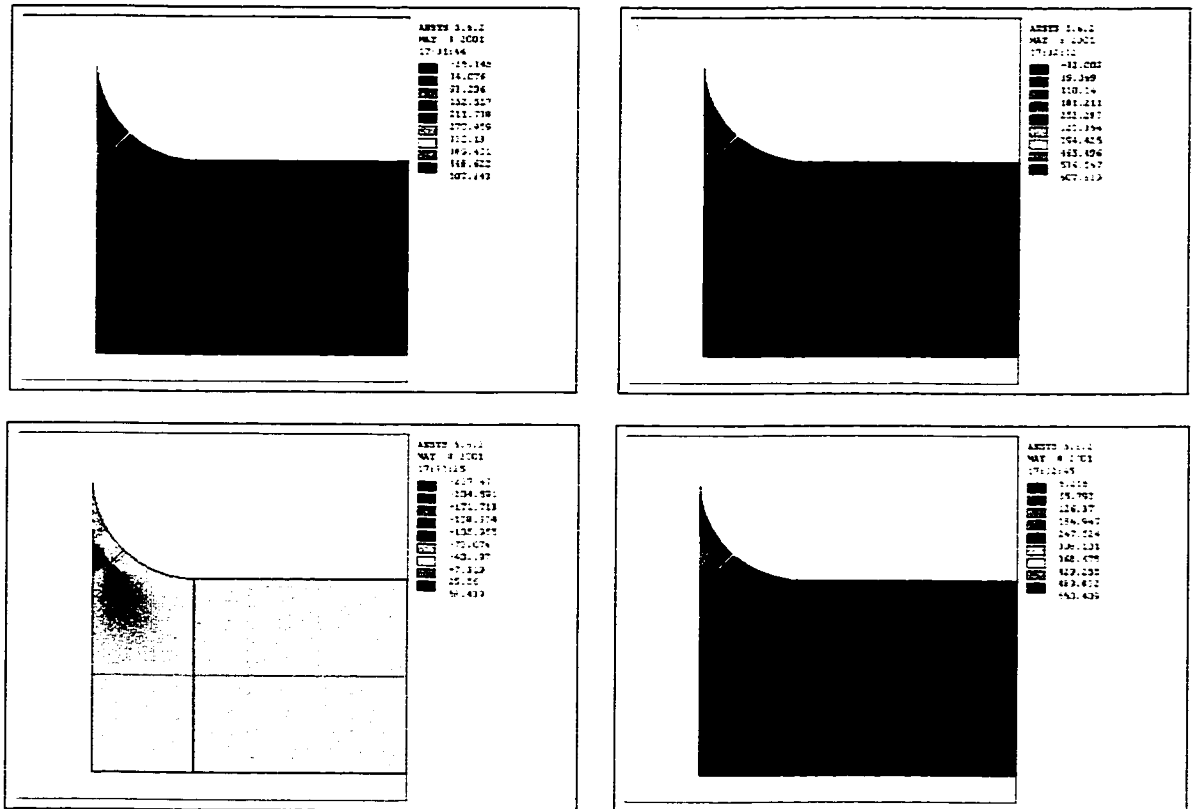

Figure H-8. Stress Contour Plots for Tension Progressive Analysis Model 2 (MPa): (a) Normal Stress, σ_x, (b) Normal Stress, σ_y, (c) In-Plane Shear Stress, τ_{xy}, and (d) Effective Stress, σ_{eff}.

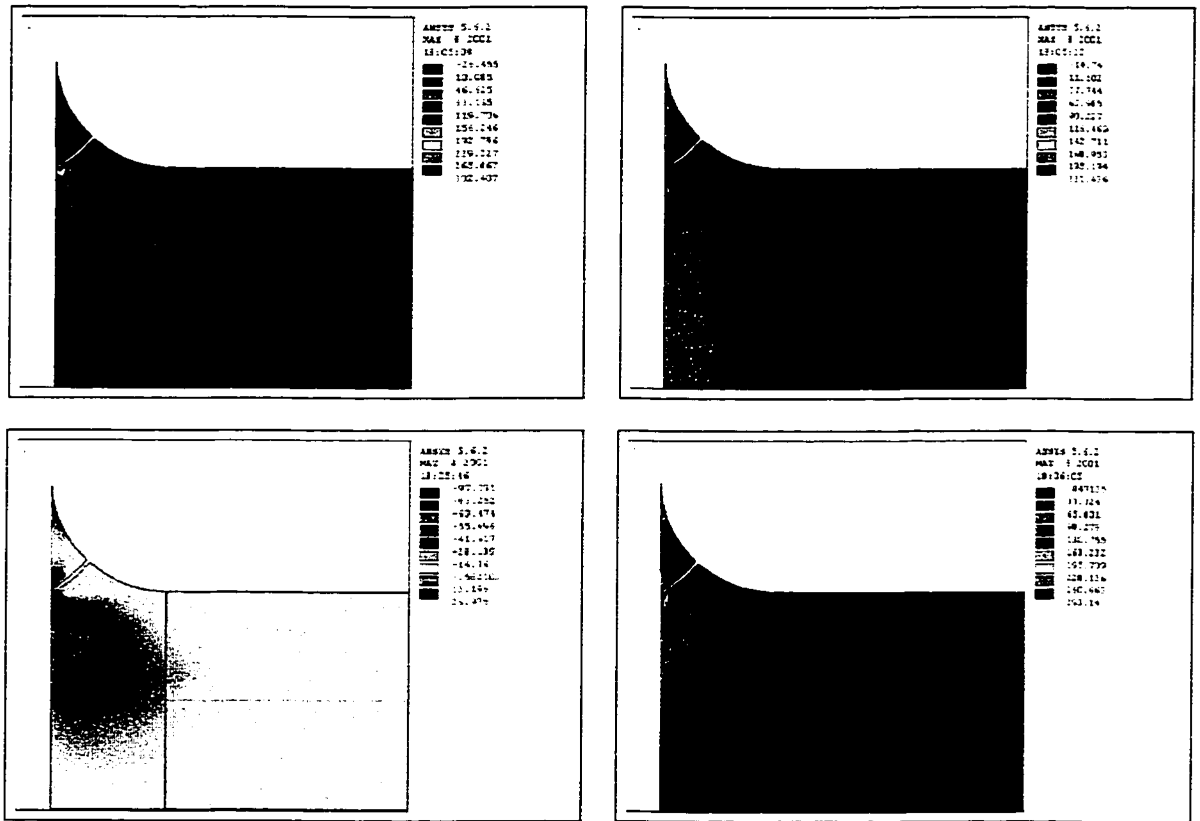

Figure H-9. Stress Contour Plots for Tension Progressive Analysis Model 3 (MPa): (a) Normal Stress, σ_x, (b) Normal Stress, σ_y, (c) In-Plane Shear Stress, τ_{xy}, and (d) Effective Stress, σ_{eff}.

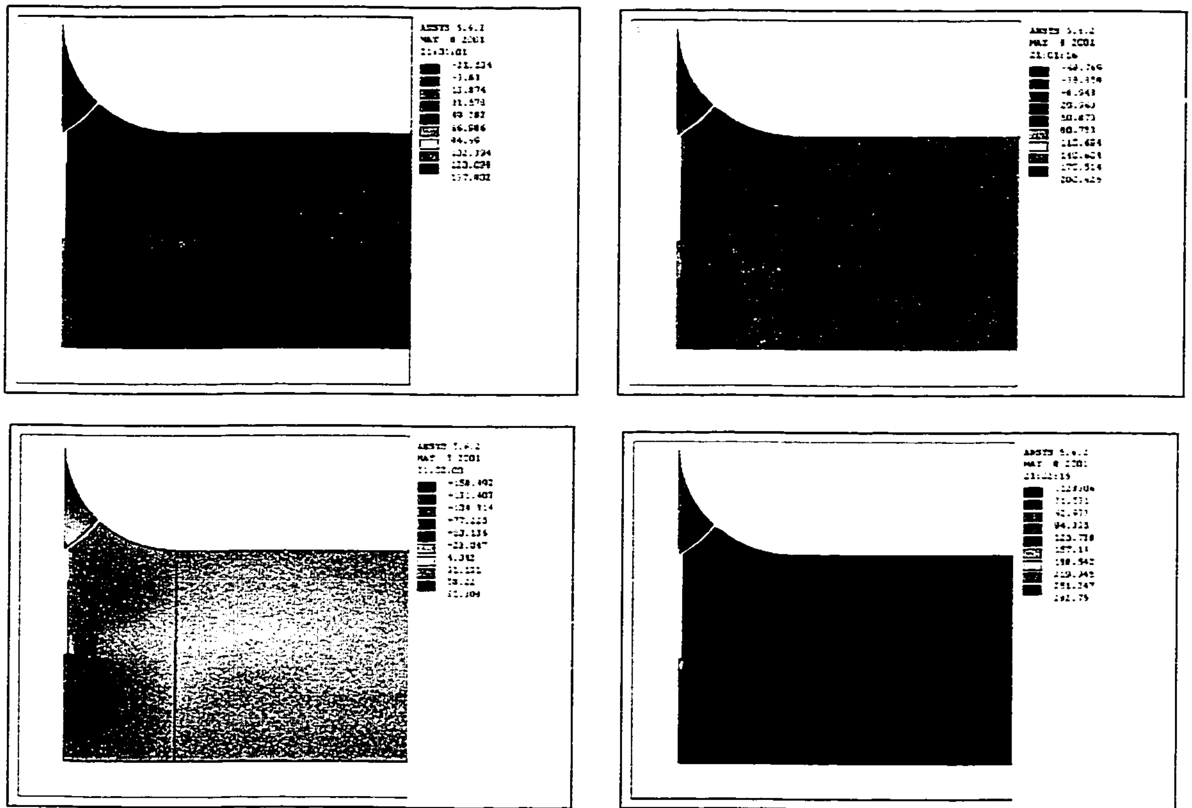

Figure H-10. Stress Contour Plots for Tension Progressive Analysis Model 4 (MPa): (a) Normal Stress, σ_x, (b) Normal Stress, σ_y, (c) In-Plane Shear Stress, τ_{xy}, and (d) Effective Stress, σ_{eff}.

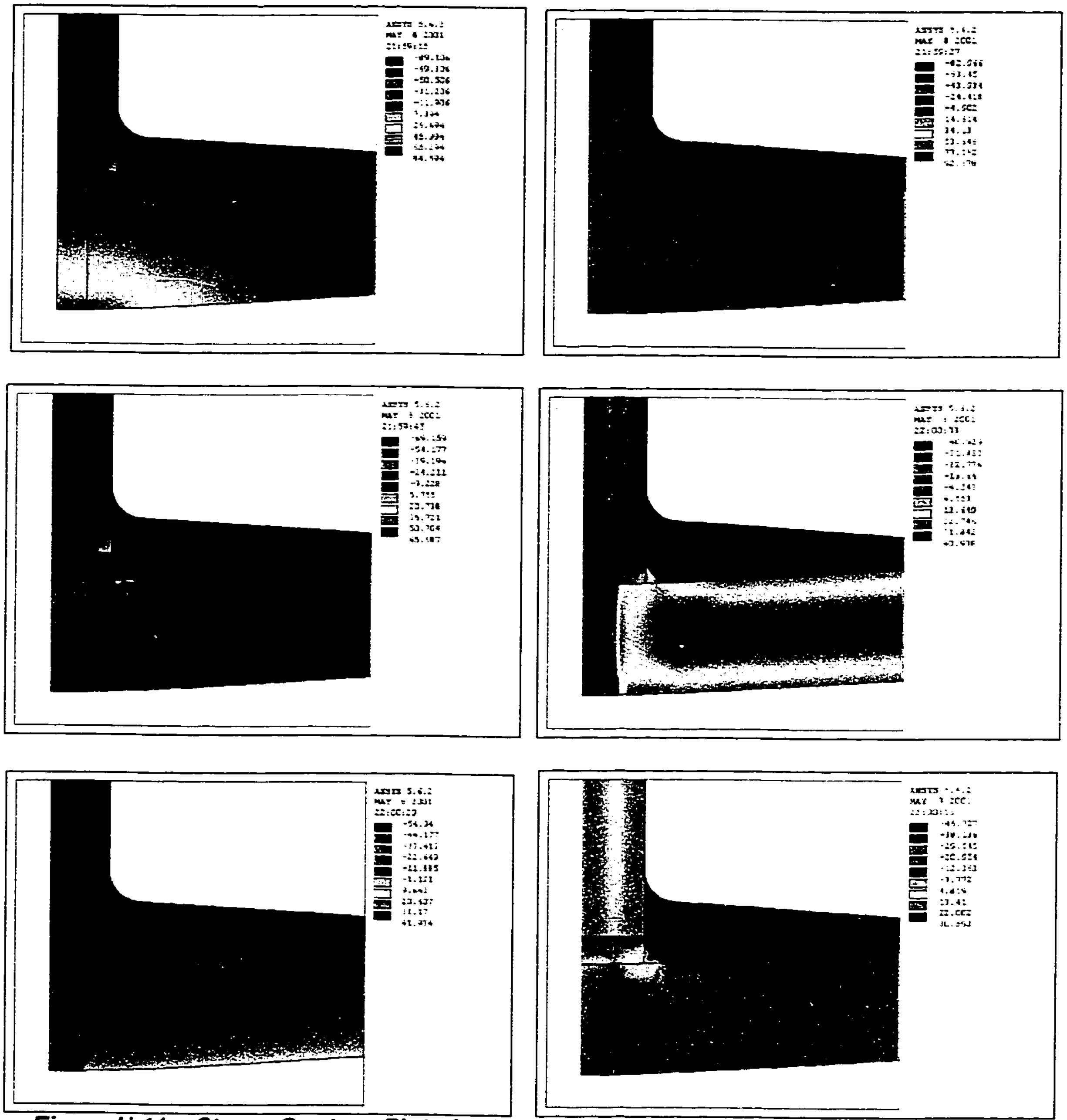

Figure H-11. Stress Contour Plots for 3D Linear Elastic Rail Shear (MPa): (a) Normal Stress, σ_x, (b) Normal Stress, σ_y, (c) Normal Stress, σ_z, (d) Shear Stress, τ_{xy}, (e) Shear Stress, τ_{yz}, and (f) Shear Stress, τ_{xz}.

APPENDIX I

OPTICAL MICROGRAPHS

Figure I-1. Optical Micrograph of Flexure Specimen F1.

Figure I-2. Optical Micrograph of Flexure Specimen F2.

Figure I-3. Optical Micrograph of Flexure Specimen F3.

Figure I-4. Optical Micrograph of Flexure Specimen F4.

Figure I-5. Optical Micrograph of Flexure Specimen F5.

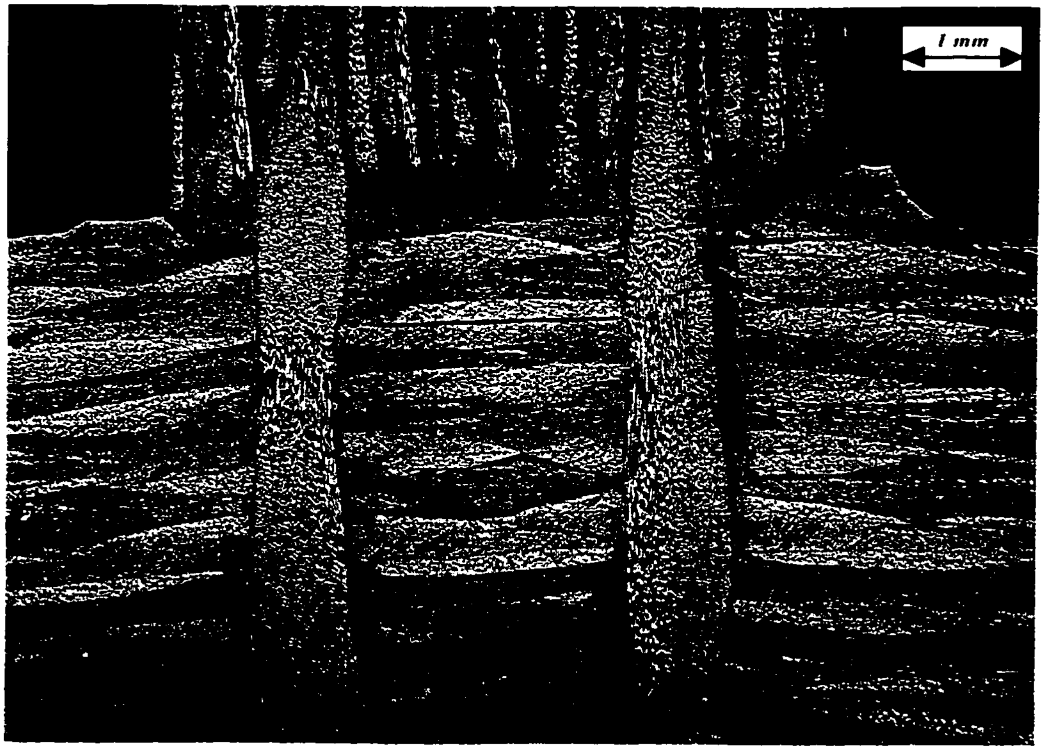

Figure I-6. Optical Micrograph of Simple Support Tension Specimen T2.

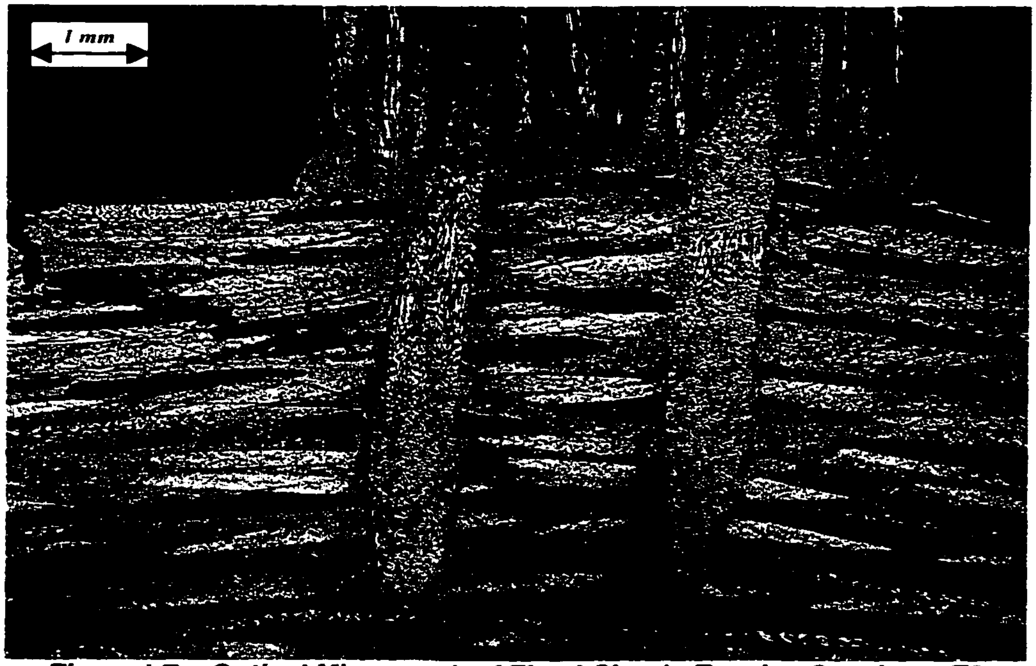

Figure I-7. Optical Micrograph of Fixed Simple Tension Specimen T3.

Figure I-8. Optical Micrograph of Fixed Simple Tension Specimen T4.

Figure I-9. Optical Micrograph of Fixed Simple Tension Specimen T5.

Figure I-10. Optical Micrograph of Rail Shear Specimen S3.

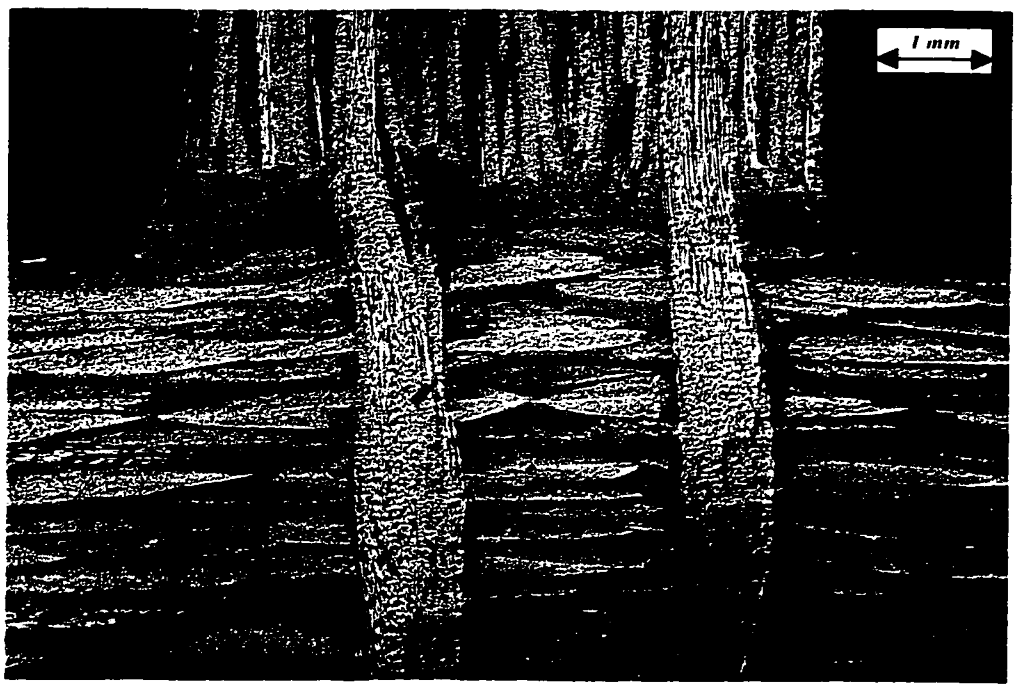

Figure I-11. Optical Micrograph of Rail Shear Specimen S5.

VITA

Patrick B. Stickler

Education:

Bachelor in Science in Industrial Engineering. Pennsylvania State University. State Collage, Pennsylvania, June 1987.

Master of Science in Manufacturing Systems Engineering. Lehigh University. Bethlehem, Pennsylvania, January 1990.

Master of Science in Mechanical Engineering. University of Washington. Seattle. Washington, August 1998.

Doctor of Philosophy in Mechanical Engineering. University of Washington. Seattle, Washington, June 2001.

Work Experience:

The Boeing Company: 11 years as a Research Engineering specializing in advanced composite structures design and analysis.

Professional Society Membership:

American Institute of Aeronautics and Astronautics (AIAA)

American Society of Mechanical Engineers (ASME)

American Society for Composites (ASC)

Society for the Advancement of Material and Process Engineering (SAMPE)

PUBLICATIONS ARISING FROM THE PRESENT RESEARCH

P.B. Stickler, M. Ramulu, and P.S. Johnson, "Experimental and Numerical Analysis of Transverse Stitched T-Joints in Bending," Composite Structures, Vol. 50 No. 1, (2000), pp.17-27.

P.B. Stickler, M. Ramulu, and B. Van West, "Transverse Stitched T-Joints in Bending With PR520 Resin: Initial Results," Journal of Reinforced Plastics and Composites, Vol. 20, No 1, (2001), pp. 65-75.

P.B Stickler and M. Ramulu, "Investigation of Mechanical Behavior of Transverse Stitched T-Joints with PR520 Resin in Flexure and Tension," Composite Structures, Vol. 52, No. 3-4, (2001), pp. 307-314.

P.B. Stickler, M. Ramulu, S.L. Coguill, and M.E. Tuttle, "Experimental Investigation of T-300/PR520 Laminate Properties and Failure Analysis," Submitted to Experimental Mechanics.

P.B. Stickler and M. Ramulu, "Experimental Study of Stitched Composite T-Joints Under Tensile Loading," Submitted to Experimental Mechanics.

P.B. Stickler and M. Ramulu, "Experimental Study of Stitched Composite T-Joints Under Rail Shear Loading," Submitted to Experimental Mechanics.

P.B. Stickler and M. Ramulu, "Damage Progression and Parametric Finite Element Analyses of Transverse Stitched Composite T-Joints Under Flexure Loading," Submitted to Materials and Design.